

Department of Precision and Microsystems Engineering

**Design of a 6-DoF Miniature Maglev Positioning Stage
for Application in Haptic Micromanipulation**

Name: Alexander Marijn Mulder

Report no: ME 11.021

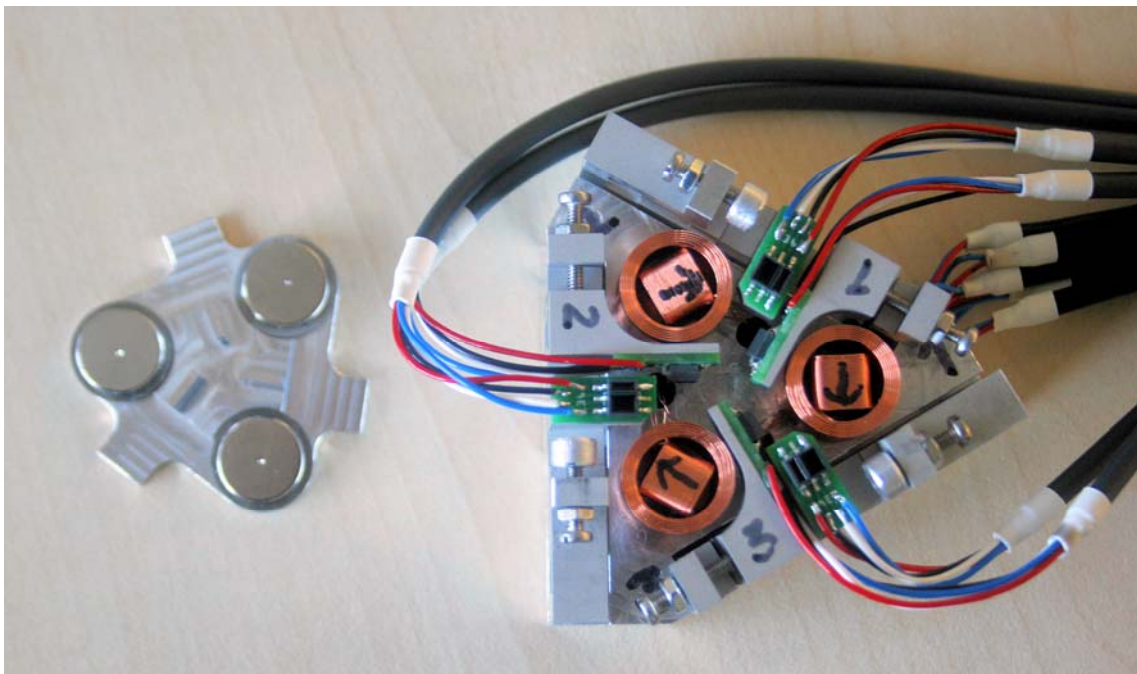
Coach: P. Estevez Castillo, MSc

Professor: Prof. Ir. R.H. Munnig-Schmidt

Specialisation: Mechatronic System Design

Type of report: Master Thesis Report

Date: 13-07-2011



Contents

Acknowledgement	4
Abstract	5
Note to the reader	6
1 Introduction	7
1.1 Haptic micromanipulation.....	7
1.2 The slave robot.....	8
1.3 Problem statement.....	9
2 Requirements of the slave robot	10
2.1 The human operator.....	10
2.2 General considerations.....	12
2.2.1 Cost and complexity.....	12
2.2.2 Application flexibility.....	12
2.2.3 Accuracy.....	12
2.2.4 Force resolution.....	12
2.3 The three steps of an assembly operation.....	13
2.3.1 Transport.....	13
2.3.2 Pre-alignment.....	13
2.3.3 Mounting.....	14
2.4 The two-stage approach.....	14
2.4.1 Comparison between the three assembly steps.....	15
2.4.2 Subdivision of the slave robot into two stages.....	16
2.4.3 The coarse stage.....	16
3 Fine stage concept	18
3.1 Possible fine stage concepts.....	18
3.2 Specifications.....	20
3.2.1 Movement range and resolution, translational.....	20
3.2.2 Movement range and resolution, rotational.....	20
3.2.3 Movement velocity and acceleration, translational.....	20
3.2.4 Movement velocity and acceleration, rotational.....	21
3.2.5 Force range and resolution, payload.....	21
3.2.6 Perturbation rejection.....	21
3.2.7 Overall size and mass.....	22
3.2.8 Accessibility.....	22
3.3 Fine stage technology selection.....	22
3.4 Overall topology and concept.....	24
3.4.1 Error budget.....	25
4 Sensors	27
4.1 Targeted sensor specifications.....	27
4.2 Possible sensor technologies.....	27
4.3 Optical sensors.....	29
4.3.1 Investigation of existing sensor systems.....	30
4.3.2 Sensor noise sources.....	32
4.3.3 Improved design of readout electronics.....	32
4.3.4 Sensor type selection.....	33
4.3.5 Design of three-channel circuit board.....	34
4.4 Final sensor and electronics specifications.....	34
4.5 Recommendations for further improvement.....	34

5	Actuators	36
5.1	Targeted actuator specifications.....	36
5.2	Possible actuator technologies	37
5.2.1	1-DoF reluctance actuator.....	37
5.2.2	2-DoF Lorentz actuator.....	38
5.3	Modelling	41
5.4	Current amplifiers	45
5.5	Final actuator design specifications	45
5.6	Recommendations for further improvement	46
6	System modelling	47
6.1	Electro-mechanical model.....	47
6.1.1	Mechanical model	47
6.1.2	Actuator model.....	47
6.1.3	Sensor model.....	48
6.1.4	Floor and suspension model.....	48
6.2	Control system	48
6.3	Noise.....	50
6.4	Environment.....	51
6.5	Assembly tolerances.....	52
6.6	Recommendations for further modelling	56
7	Mechanical design	57
7.1	Base structure	57
7.1.1	Sensor positions.....	58
7.1.2	Sensor alignment	58
7.2	Moving part	60
7.2.1	Eigenfrequency analysis	61
7.3	Assembly	63
7.3.1	Alignment tool.....	63
7.3.2	Sensor calibration and alignment.....	64
7.4	Recommendations for further improvement	64
8	Conclusion	65
8.1	Results	66
8.2	Recommendations	67
	References	68
	List of abbreviations	71
	Appendix	72
A	Literature summary: Existing micro-positioning stages	72
B	List of requirements for the three assembly steps	89
C	Actuator force distribution.....	98
D	Derivation of coordinate transformation matrices.....	105
E	Finite element modelling of reluctance actuators	110
F	Modal analysis of moving part	156
G	Sensor tests measurement data	165
H	Sensor readout board manual.....	184
I	Current amplifier board manual	193
J	System model.....	202
K	Mechanical design drawings	207

Acknowledgement

This thesis report and the work it describes would not have been possible without the help and support of many people. First and foremost of all I would like to express my thanks to my supervisor, Pablo Estevez Castillo, for his many useful suggestions, for his part in developing the microslave stage, for thorough proofreading and reviewing of my work, and of course for keeping me motivated. I'd like to thank Ir. Jo Spronck for useful suggestions and comments during the design process. Thanks are also due to Rob Luttjeboer of the PME lab for his aid and suggestions during the mechanical design phase. I would also like to thank Patrick van Holst and Harry Jansen for their assistance in manufacturing and assembling the microslave stage, and Marli Guffens and Corinne du Burck for their help with many practical and paperwork issues. My fellow students and neighbours at the TU Johan and Oscar provided me with welcome distraction and many helpful suggestions as well. My gratitude also goes out to my parents and family for their support, and of course to my "overbroers en -zusters" Wouter and Michiel, Joke and Silke.

The Haptic Micromanipulation research project, of which this thesis work is a part, receives financial support from MicroNed.

Abstract

This thesis presents the design of a six degree of freedom micropositioning stage. It is a part of a research project on haptic tele-operation, applied to micromanipulation, at the TU Delft. The micropositioning stage will be used as the fine range positioning stage of a slave robot, in a haptic tele-operated control scheme. The technology used to build the stage is magnetic levitation. The stage has a movement range of $200 \times 200 \times 200 \mu\text{m}$ and rotations of about $\pm 1^\circ$. The stage MIM (Minimum Incremental Motion) is designed to be $40 - 100 \text{ nm}$. The focus of this thesis is mainly on the modelling and design of the system and its components, the design of actuator and sensor electronics, and the mechanical design of the stage. Control aspects have been taken into account since the stage is open-loop unstable, but do not constitute a main topic.

The position sensors used in the micropositioning stage are infrared reflective sensors. These affordable sensors have previously been implemented in various projects at the TU Delft. Existing optical sensor readout electronics have been investigated; an improved version has been developed with lower noise levels. The achieved sensor noise is $14 - 28 \text{ nm}$, peak-to-peak over a measurement range of $200 \mu\text{m}$. A three-channel readout circuit board has been designed and tested. It can be used in other future applications as well as the current project.

The actuators are a novel Lorentz type actuator. They consist of two fixed coils and a permanent magnet attached to the moving mass. One actuator can generate two independent force components, namely a vertical force and a horizontal force. The actuator characteristics have been extensively investigated using FEM modelling. These characteristics are position dependent, and exhibit crosstalk and parasitic forces. The overall system modelling and actuator FEM modelling has shown that these effects are manageable over the motion and force ranges of the stage. The actuator can generate an 80 mN vertical force and a 10 mN horizontal force, continuously. A three-channel current amplifier circuit board has been designed and tested. It is used to drive the Lorentz actuators, but can also be used in other future applications.

Simulation diagrams have been developed of the mechanical system and its controller. The mechanical system is essentially a rigid free-floating mass that has 6 degrees of freedom. The eigenmodes of this mass have been investigated using FEM based modal analysis. Its eigenfrequencies lie far above the closed-loop system bandwidth, and are therefore not considered further. The control system is implemented as six independent SISO PD-controllers. The closed loop system bandwidth is 100 Hz .

Using the system model in a Monte Carlo-type simulation, the effect of manufacturing and assembly tolerances on stage performance have been investigated. The results showed that the stage can be built with standard manufacturing technology, provided that extra care is taken during assembly of the actuators to reduce misalignment of the actuator components. An alignment tool has been developed for this purpose.

A mechanical design has been made of the micropositioning stage. In this design the conclusions of the modelling phase and sensor and actuator characterisation have been taken into account. Fabrication drawings have been made, and all mechanical parts have been manufactured. The fine stage and its associated electronics have been fully assembled; the stage is currently in the test and characterisation phase.

Note to the reader

The work presented in this thesis consists of four topics that are more or less independent within the framework of the entire project. These are sensors, actuators, overall system modelling and mechanical design. For this reason each of these topics has its own chapter, including a specifications and a recommendations section per topic.

Chapter 1 is an introductory chapter explaining the framework of the thesis project itself, and the wider topic of tele-operated haptic micromanipulation of which it is a part. The focus of this project is the slave robot, especially the fine range positioning system. Chapter 2 discusses the requirements of the slave robot in detail, as well as the haptic micromanipulation process itself.

Detailed specifications of the fine range stage, the stage concept and technology selection are discussed in chapter 3.

The optical position sensors used in the stage are described in chapter 4. This chapter also discusses the electronic circuits needed to operate the sensors and their development.

The Lorentz actuators are discussed in chapter 5. They have been dimensioned and characterised by FEM analysis, this is also described in this chapter.

A simulation model of the complete system, with sensor and actuator nonlinearities, noise sources etc. has been developed to predict system performance. Chapter 6 provides a description of the model and its results. The mechanical design is discussed in chapter 7. Chapter 8 provides an overall conclusion.

1 Introduction

Current developments in the electronic and mechanical industry are ongoing miniaturisation, increasing complexity and functionality, and the introduction of MEMS devices. This requires the further development of micromanipulation technology, to enhance existing manufacturing techniques. Micromanipulation is used in the assembly of e.g. MEMS based sensors and actuators and opto-electrical systems that consist of several components that can not be made in a single production process. Micromechanical systems such as miniature motors and gear drives are also an application field for micromanipulation.

The manipulation and assembly of such micro parts (i.e. smaller than a millimetre) can be done in two ways with existing technology: either directly by hand by an operator, or in a fully automated process. The latter approach is useful for large production series with relatively simple assembly operations and part geometries. Examples of such automated systems have been developed at ETH-Zurich [20], Bern BFH-TI [21] and at Carnegie Mellon University [22]. The former approach allows much more complicated and varied assembly tasks owing to the great task flexibility of the human operator. Yield, consistency and precision are lower, however.

A recent development is the application of haptic feedback in micromanipulation tasks. The haptic micromanipulation scheme is a compromise between fully automated and manual operations. Such a scheme allows a human operator to work with the sub-micrometre precision achieved by automated equipment, while retaining his task flexibility. The intent of the haptic micromanipulation research project at the TU Delft is to develop a haptic micromanipulation system, targeted towards varied assembly tasks, in small production series and for prototyping purposes. This system should provide an affordable compromise between fully automated and manual operations.

1.1 Haptic micromanipulation

Several components are necessary in a haptic tele-operation system: a master robot, a slave robot, a computer control system, force sensors, and a visualisation system. In a haptic micromanipulation scheme, the operator has no direct contact with the parts to be assembled, but rather commands the slave robot to do the manipulation task, see fig. 1.1. The operator commands are issued via the master robot, and the slave robot follows these commands. In a haptic scheme, not only visual feedback is provided to the user through cameras and a screen, but also force feedback through sensors in the slave robot and actuators in the master robot.

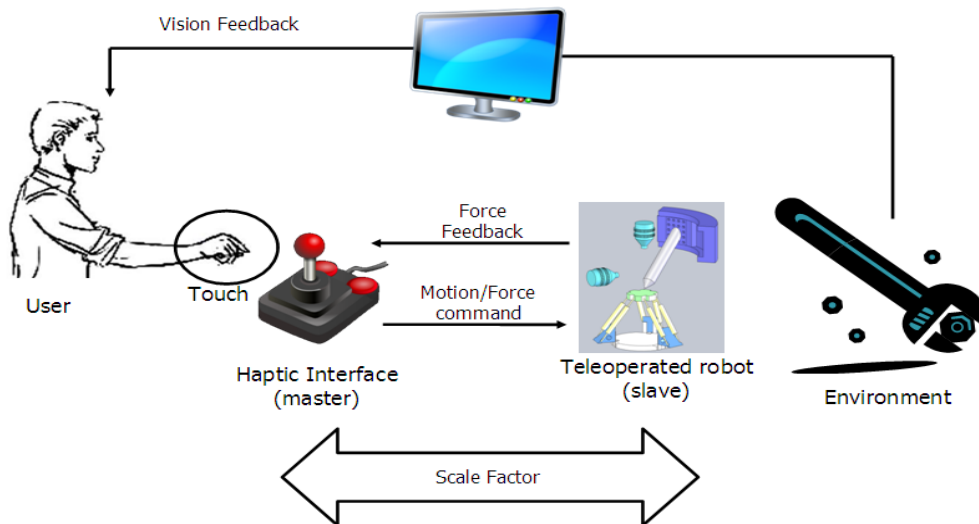


Figure 1.1. Haptic control scheme for micromanipulation tasks.

The operator commands can be scaled down, so more accurate positioning can be achieved than when the operations are performed directly by hand. Depending on the application and phase in the assembly process, the scale factor can be varied. This approach yields a flexible system that can be used in a variety of tasks. The haptic force feedback provides additional information to the operator, which improves performance (e.g. assembly time, precision).

Tele-operated micromanipulation systems without haptic feedback have been developed for instance in HUT-Finland [23] and Sabanci University-Turkey [24] and at several companies, like Scientifica Ltd. [25], Warner Instruments [26] and Zyvex Instruments [27]. The development of tele-operated systems with haptic feedback is very limited. At Klocke Nanotechnik, Germany, a 4-DoF system was developed with 1-DoF haptic feedback [28]. In KIST-Korea a 6-DoF system was developed with 3-DoF haptic feedback [29].

1.2 The slave robot

Since the slave robot is the focus of this thesis, we will take a closer look at it in this section. The slave robot is the part of a haptic system that carries out the actual manipulation and assembly operations. In general, it needs a motion range on the order of ten to several hundred millimetres to perform the manipulation operations, in at least two but usually three linear DoFs. Depending on the application additional rotational DoFs are provided. The resolution also depends on the application, but is usually in the range of tens to hundreds of nanometres. In addition to the actuators a haptic slave robot needs force sensors for all DoFs on which haptic feedback is to be provided to the operator.

For a slave robot with haptic feedback, there are several control strategies to provide force feedback to the operator and limit forces exerted on the delicate parts. One option is direct force control of the slave, or a force control loop around the position control loop can be implemented. Both strategies require a stiff slave, which is difficult to keep stable. Alternatively, a compliant slave can be used to implement position-position controllers (the feedback force is proportional to the difference in slave and master position). In the latter case, the slave robot itself will function as force sensor, by making use of its position sensors which are needed for the position control loop. A compliant slave can be used in a so-called 'hard master, soft slave' setup [30]. This research showed that stiff ('hard') masters enable detailed rendering of force feedback to the user, while compliant, damped slaves ensure stability and a delicate interaction with the environment. In general, it is also easier to implement 6-DoF position sensing in a stage than 6-DoF force sensing.

In this specific case, the manipulation tasks concern parts that have a 2.5 dimensional geometry. Examples of micromanipulation tasks include the assembly of micromechanical systems from individual components on a substrate, such as planetary gear drives [31], micro ball bearings [32],[33], watch mechanisms [34] and a micro rotor assembly [35]. Peg-in-hole tasks are also common [36],[37].

Many components in these micromanipulation tasks are 2.5 D as a result of the planar manufacturing techniques used to fabricate these components. A typical assembly step of a 2.5D part requires translation DoFs in two horizontal directions to move the part to its proper location, and a translation DoF in the vertical direction to stack parts or to insert parts into holes. A rotational DoF around the vertical axis is needed to align parts to each other. Finally, a gripping DoF is needed to handle the parts.

The largest component dimensions are on the order of a millimetre, and assembly tolerances generally lie in the area between 2 μm and 200 nm. The overall motion range of the slave robot should be about 20 x 20 x 20 mm. Two additional degrees of freedom with a small motion range are needed to correct tilting misalignments of the parts; these are the two rotations about the horizontal

axes. In the current research at the TU Delft, the slave robot will consist of two positioning stages, a coarse and a fine stage.

The coarse stage is a stiff (stepper motor) stage, the compliance of the slave robot will therefore be in the fine stage. The slave robot gripper or other end-effectors will be equipped with a 6-DoF MEMS force sensor to provide the haptic feedback. However, this option is still under investigation and an alternative is to use the compliant fine stage as the force sensor.

1.3 Problem statement

Using magnetic levitation technology for the fine stage allows a variable, low stiffness stage that can be used in for haptic micromanipulation of delicate parts. Existing 6-DoF maglev stages have been developed by, for example, Kim et al. [1],[2] and Li [8]. The physical size of these stages however is too large for the current application. This is a result of the relatively large payloads for which they have been designed (several kilograms). Other positioning stages are either too complicated and expensive for this application, such as Halbach motor stages [4],[5],[10] and [17], or are high stiffness mechanisms, such as piezo based stages [14],[18], or flexure based systems [11],[13] and [15].

The goal of this thesis is to design a miniature 6-DoF magnetically levitated stage, based on existing technology. Miniaturisation can be achieved if the payload of the stage is drastically reduced to several grams, and compact actuator and sensor geometries can be designed or selected. In view of the haptic micromanipulation project, this stage should be affordable and usable for a variety of assembly and manipulation tasks. The stage can be more affordable if certain requirements, such as absolute accuracy and bandwidth can be kept low, in accordance with the limited capabilities of the human operator in these areas.

This design project is performed within the wider research into the use of a magnetically levitated positioning stage as compliant slave in a haptic teleoperated micromanipulation scheme.

2 Requirements of the slave robot

In this chapter, the requirements of the slave robot will be discussed. Since the slave robot will be following a human operator's commands, the characteristics of these commands need to be taken into account. As stated in the introduction (section 1.2), the slave robot has to be able to handle 2½ dimensional parts which have dimensions of 1 mm or less. These should be positioned to within a tolerance of 2 µm - 200 nm relative to each other or a substrate, depending on the application. For example, in a peg-in-hole task, the hole will be 2 µm larger than the peg in coarser applications, down to 200 nm in the most precise applications.

The total movement range of the robot should be at least 20 mm x 20 mm in the xy-plane, to cover the area in which the parts are initially deposited. In the vertical (z-) direction, parts will have to be moved over or stacked on top of each other. Therefore, the movement range in this direction should be at least 1 mm, but a larger range of 5 – 10 mm will result in a more versatile device.

To achieve positioning within the required tolerances, the slave robot's Minimum Incremental Motion (MIM) should be several times smaller than this 200 nm in the most precise assembly operations. This MIM is required in all three directions (x-, y-, and z-direction). The MIM is defined as the smallest step a positioning system can reliably and repeatably make, and is therefore larger than its resolution. In noise limited stages, the MIM is measured as 2 times the peak-to-peak positioning noise [42].

In this application, range and MIM are the two most important requirements. Because of the way the slave robot is controlled, specifications such as accuracy and repeatability are less relevant. The reasons for this become clear when we take a closer look at how the haptic interface is used by the operator in a given micromanipulation task.

2.1 The human operator

The operator receives visual feedback through two (or more) cameras, whose images are magnified and displayed on a screen. During a haptic teleoperated micromanipulation operation, no exact measurements are presented to the user of the absolute positions of the parts to be assembled. The user commands are also not issued to the system in the form of quantitative displacements or positions instructions. Rather, the operator moves the master device in order to issue the commands, while using visual and haptic feedback (instead of or additional to numerical displays) to control the trajectory and interactions of the micro objects. The operator acts as an integrator in the feedback loop, minimising the position (or force) error.

Human operators are highly adaptable thanks to their learning ability. They are used and capable of dealing with inaccurate tools, as long as end-point feedback is available to them to correct for the errors introduced by the intermediate devices. In particular, this inaccuracy is present in their own limbs, which are a necessary link in the operation of haptic master devices. Feed-forward control of the arms (with closed eyes), for instance, generates error in displacements of around 10% of the commanded movements, while with visual feedback that error is only limited by the vision resolution and the tremor of the hand. When the operator issues a command through his limbs such a command is subject to this inherent inaccuracy. Therefore it is useless in this control scheme to follow the operator with an accuracy much higher than that of the limb. The final accuracy of the system will be achieved thanks to the control loop closed by the operator and not to the accuracy of the intermediate components. Conversely, in most existing applications of positioning stages, which are designed for automated operation, absolute positioning and therefore accuracy are much stronger requirements.

This scheme only works as long as the operator is still able to detect these errors, and for submicron tolerances this becomes a challenge. Visual (optical) techniques can resolve features of about 1.5 μm but not much smaller, due to the wavelength of visible light. This is why the haptic interface is especially important during the mounting operation. For instance, during a peg-in-hole task, the operator can scan the surface to determine the position of the hole, and sub-micron positioning can be achieved.

This is why an MIM that is several times smaller than the smallest tolerance is required. If the MIM is equal to this tolerance (200 nm) the part cannot always be positioned correctly, whereas if it is half the tolerance (100 nm) this is possible. To be able to scan the substrate surface for a hole position as described above, even smaller steps are required for a detailed haptic image of the substrate geometry. More specifically, a factor three is sufficient but a factor five would be preferable, if this MIM can be achieved.

Furthermore, the haptic interface should be transparent to the user. This leads to the additional requirements that the slave robot should be linear in its movements, and that motion tracking error stays within a percentage ($< 10\%$ of the considered distance) small enough that the operator can (intuitively) correct for this.

It is necessary to take the actuation and sensing capabilities of the average human into account when setting up requirements for the slave robot, especially those of the arm and hand. This subject has been extensively studied by various research groups. The characteristics that are most relevant to this application are listed below.

- The human operator can achieve, with a hand-operated master device, a MIM of about 1 mm over a range of 100 to 200 mm (ratio 100 : 1 – 200 : 1) when moving in free air, i.e. without obstacles. In the presence of stiffness (as would be the case for haptic feedback) a higher precision is possible [38].
- Motion tasks can be carried out with this precision up to a bandwidth of 1 – 2 Hz, in response to unexpected signals. When the motion is faster some of the precision and control are lost. In response to periodic signals and for periodic motion the bandwidth increases to 2 – 5 Hz, while for learned tasks and trajectories this can go up to a maximum of 5 Hz [39].
- Maximum acceleration for the human elbow flexion are observed to be 5g, whereas experts estimated typical accelerations in the order of 1.25g. Typical velocities that can be reached are 1.1 m/s [39].
- The human exerted force resolution depends on the exerted force, and at a force of 22.2 N a resolution of 0.3 N is reported. The relative force error increases as the required force goes down. The maximum finger force is about 45 N. This implies a force range-to-resolution ratio of about 75 : 1 – 100 : 1 [40]. However, 22 N is a large force for one finger, and the maximum force that can be comfortably and safely exerted is reported to be 7 N for the index finger [41].

From these characteristics we can conclude that the operator will be the limiting factor in the overall system performance, i.e. precision and bandwidth. Therefore, it will not be necessary to design a slave robot that has a very large bandwidth. The required velocity is low because of the low bandwidth, and the small scale at which the operations take place.

2.2 General considerations

Apart from the requirements following from the micromanipulation tasks themselves, additional considerations apply. These considerations follow from the design philosophy of the slave robot, and the intended application: The device will be used in the production of prototypes and small assembly series, and aims to provide a more economical solution than automation. Therefore it should be kept as simple and affordable as possible in order not to lose this comparative advantage. Many specifications can be kept low, such as bandwidth and velocity, because the human operator is the limiting factor for these performance figures. Furthermore, the key to a successful assembly operation without damaging the parts is a sufficiently low force resolution. This implies that actuator forces be kept low, and the moving parts should be optimised for low mass.

These considerations are what make the slave robot different from most existing positioning systems, which are usually designed for maximum accuracy, velocity and bandwidth. This will be explained further in the following paragraphs.

2.2.1 Cost and complexity

The haptic micromanipulation system is designed to be a relatively affordable, compact device. The entire system should fit on a table top, and will be used to enable the assembly of relatively small series of products. This puts limits on the complexity and cost of the system and its components. In particular for the slave robot, sensor systems such as laser interferometers would be too expensive and take up too much space. This also holds for actuation principles, such as Halbach array based magnetically levitated devices [4],[5],[10] and [17], although these could achieve the smallest required MIM over a large range. In short, because of these considerations certain technologies are ruled out for the slave robot. The performance of simpler actuation and sensing principles are justified also by the operator's limitations.

2.2.2 Application flexibility

Another consideration is that the system should be designed for flexibility in application. To set up the requirements a number of reference assembly tasks have been defined, but the system should by no means be limited to just these. Therefore it is useful to overspecify the slave robot where possible with regard to range and MIM. This will enable the operator to use the system with a larger number of scaling factors and to allow working with parts of different sizes and tolerances.

2.2.3 Accuracy

The most important requirements of the positioning of the slave robot are its step size (or MIM), positional stability, and perturbation rejection. In the requirement list no accuracy requirement is stated. This is done intentionally, since the complete haptic teleoperated system can't position the slave robot more accurately than the (relative) operator limb-transmitted commands.

A certain level of accuracy is still needed however. The controlled system should operate properly, and at least the 10 % linearity requirement should be met (section 2.1). This level of accuracy can be achieved with standard technology. Therefore, a tighter accuracy requirement is not needed and no closer attention is paid to this aspect.

2.2.4 Force resolution

Perhaps the most important requirement during operations involving contact between parts is force resolution. This resolution needs to be fine enough that small force increments will not lead directly to damage to parts, but rather will provide the user with haptic information about the assembly operation and position of parts.

To achieve this fine force resolution, the use of low-force actuators is advantageous. Furthermore, the moving mass should be as small as possible, to limit the inertia forces. This agrees well with the arguments that the slave robot should be a compact device, and that bandwidth and acceleration requirements are limited.

In some cases, the use of compliance, either in the parts themselves or in the tool or actuator, can generate similar results. For instance, parts can be made self-aligning in the rotational directions (within certain limits) this way. Nevertheless, other specifications of the system are compromised when stiffness is lowered. A variable stiffness system is an interesting option, given that it can dynamically adjust the tradeoffs of stiffness and other specifications (resonance frequencies, force ranges, accuracy, etc).

2.3 The three steps of an assembly operation

We have seen that the required motion range of the slave robot is 20 mm, and the MIM is less than 100 nm. This means that the range-to-MIM ratio of the system is greater than $2 \cdot 10^5 : 1$. Therefore, the system's specifications are far better than the performance of the operator, whose range-to-MIM ratio is at most 200 : 1 when commanding the master device in a hand-wrist operation. If an assembly task would be carried out in a single step, either the required range or accuracy could not be achieved, and the system would not perform satisfactorily.

To overcome this limitation, the operating range of the slave robot (and with it the assembly operation) can be subdivided into three steps, each with a range-to-MIM ratio compatible to the average operator's. These steps are the transport of parts to the assembly area (coarse), the pre-alignment of parts to their final position (mid-range), and the final mounting of parts (fine). In each consecutive step, the operator commands through the master device are scaled further down before being sent to the slave robot. Consequently, the active part of the travel range gets progressively smaller with each step and the MIM decreases. During the fine range step, fine contact operations take place. These include the actual mounting of parts, such as insertion, but also haptic (force) scanning of surfaces or holes, approaching and making contact between parts, etc. Conversely, transport and pre-alignment are mostly contact-free, risk-free and the motions are much coarser.

Tables listing more exact requirements and characteristics for each step are included in Appendix B. These tables have been adapted from [43].

2.3.1 Transport

The transport operation is a high velocity, low accuracy positioning. During this operation there should be no contact between the part in the gripper and the moving slave robot or other parts. Actual user force feedback is not needed, but some feedback could be used to provide the operator with extra information such as path following, collision avoidance and motion range limits. The operator commands are scaled down by a factor 10, so that the human operating range of about 200 mm is scaled to the slave robot's range of 20 mm.

The transport mode range is equal to the required total range and is at least 20 mm x 20 mm x 10 mm. To achieve a 200:1 operator range-to-MIM ratio for this step, the MIM is limited to a minimum of 100 μm . This is sufficient to bring the parts to within $1/10^{\text{th}}$ of the size of the assembly, after which the pre-alignment mode can take over.

2.3.2 Pre-alignment

After the part is transported to the assembly area, the camera zooms in and only a part of the full working area is used. This means that the haptic interface will scale the operator commands down

further than in the transport phase. In this pre-alignment phase, the part is positioned more accurately relative to the assembly so that any position errors left are small enough to be corrected within the range of the final mounting step. Also, the rotational orientation of the part can be corrected to within the rotational range of the final mounting step. In this phase there is mostly no contact between the part and the assembly. Some force feedback to the operator may be required, and the velocity and force range should be lower in this phase than during transport. In this way, collision and damage to parts can be avoided. The feedback can also help the operator in positioning the part accurately enough for the mounting operation.

The pre-alignment mode should have a range that is sufficient to correct the position error that is left after the transport operation, and to cover the assembly area. Therefore, this range should be about 1 mm x 1 mm x 1 mm, with an MIM of 20 μm . This implies a ratio of 500:1, which is overspecified with respect to the operator's ratio. However, this is necessary to ensure positioning in the middle of the mounting mode range. If needed, the scaling can be refined during the pre-alignment operation to let the operator make full use of the slave robot's capabilities.

2.3.3 Mounting

After the pre-alignment of the part is completed, the camera zooms in once more and the operator commands are scaled even further down. In this phase, the part is aligned to the assembly in all three rotational directions to within fractions of degrees, to ensure proper placement or insertion. Misalignment can be caused by gripping errors, part tolerances and, for rotations about the vertical axis, by errors left by the preceding steps. The slave robot should therefore be able to provide three rotational degrees of freedom in this phase, with sufficient resolution. In the previous phases, only a rotation about the vertical axis was needed.

In the mounting phase there will be contact between parts, and the operator has to receive force feedback from this interaction via the gripper force sensors. Mounting also requires a very fine resolution and control of the actuator forces, so the operator can position the parts precisely without damaging them.

The mounting mode should have a range that is several times larger than the positioning MIM of the pre-alignment mode. A range of 200 μm x 200 μm x 200 μm ensures that the part can always be brought to the correct final position, assuming the pre-alignment operation was successful, with some margin for error. The MIM of the mounting mode is equal to the overall MIM, namely 40 – 100 nm. This implies a 5000:1 – 2000:1 ratio, which is clearly an overspecification with respect to the user. However, the maximum accuracy of 200 nm is not needed for every assembly, and in those cases a coarser scaling can be used (for example, a 200 μm range with a 1 μm MIM). In other cases, the scaling could again be changed during the mounting operation, subdividing it into two steps, or the initial range could be chosen smaller. This is possible since the MIM of the pre-alignment operation is only 20 μm . In general, the larger the ratio between the range of one mode and the MIM of the mode preceding it, the easier it is for the user to switch between modes.

2.4 The two-stage approach

From the requirements for the three assembly steps a requirements list for the entire slave robot can be obtained. On this list a number of design concepts could then be based. However, it is interesting to first take a closer look at the three steps to see what they have in common and what the differences are. It will become apparent that the transport and pre-alignment steps have similar requirements and characteristics, and that the final mounting step is different from these two. This will be explained in more detail below, finally leading to a two-stage approach for the slave robot. The strategy to design for low moving mass, small size and fine force resolution further supports the development of a separate fine stage. The two stages will each have their own requirements, based

on the requirements of the three steps. These requirements will be listed. Since this thesis deals mainly with the design of the fine stage, its requirements will be discussed in greater detail.

2.4.1 Comparison between the three assembly steps

The main characteristics of the three steps are compared in table 2.1 below.

Requirement	Transport	Pre-alignment	Mount
Range, translation	20 x 20 x 10 mm	1 x 1 x 1 mm	200 x 200 x 200 μm
MIM, translation	< 100 μm	< 20 μm	40 – 100 nm
Range, rotation	360° (Θ_z)	360° (Θ_z)	2° x 2° x 2°
MIM, rotation	$\leq 1^\circ$	$\leq 1^\circ$	$\leq 0.002^\circ$
Number of Degrees of Freedom	4	4	6
Velocity, translation	> 10 mm/s	> 3.5 mm/s	> 1 mm/s
Acceleration, translation	> 30 mm/s ²	> 20 mm/s ²	> 5 mm/s ²
Perturbation rejection, translation	< 50 μm	< 5 μm	$\leq 7 - 35$ nm
Perturbation rejection, rotation	< 0.5°	< 0.5°	$\leq 0.0008^\circ - 0.002^\circ$

Table 2.1. Comparison between the characteristics of the three phases of a micro-assembly operation.

The transportation and pre-alignment steps have similar requirements, but the mounting mode requirements are different from these two. In particular, the transportation and pre-alignment steps both have a range of millimetre order of magnitude, with an MIM on the order of tens of micrometres. The final mounting step however has a range that is a fraction of a millimetre, with an MIM on the order of tens of nanometres, or a factor 10^3 smaller than the two previous steps. Furthermore, the first two operations require 4 degrees of freedom, with a large rotational range around the Z-axis. Conversely, the final mounting operation requires motion with the full six degrees of freedom, where the rotational range is merely a fine adjustment, of about $\pm 1^\circ$. The same conclusion can be drawn about the required velocities and perturbation rejection.

All in all, the requirements of the transportation and pre-alignment steps on one hand are contradicting those of the mounting step on the other. The first two steps require a positioner with a relatively large range and velocity, and one that doesn't need to be very precise. The final mounting step however requires a positioner with a short range and high precision.

Although it would be possible to construct or even buy a positioner that can meet all these demands at once, such a device would be complicated, expensive and bulky, and overspecified. The aim of this project is to design and build a compact device, that is relatively inexpensive and compact, and therefore affordable for use in the assembly of small series. Therefore, the idea of a single stage positioner is abandoned in favour of a two-stage approach. This approach acknowledges the differences between the requirement lists of the three steps. In addition, the small force resolution requirement of the mounting operation can be more easily met when a separate fine stage is used.

2.4.2 Subdivision of the slave robot into two stages

Following this analysis, the slave robot will consist of two positioning stages: a coarse and a fine stage. The fine stage will be mounted on top of the coarse stage to correct the last positioning errors. In this two-stage approach, the coarse stage will take care of both transport and pre-alignment operations, because these have similar requirements. The fine stage provides the final mounting operation. The coarse stage is then operated in two different modes, with a range of 20 mm for the transport mode, and a MIM for the pre-alignment mode of 20 μm . Owing to the relatively low precision requirements of the coarse stage, it can be implemented as a number of off-the-shelf stepper motor stages.

According to this subdivision, a simple control scheme will be used. Only one stage will be used at a time, depending on the mode in which the slave robot is operated. This scheme is the current control concept. However, sufficient overlap is provided between the range of the mounting step and the MIM of the pre-alignment step to be able to implement more advanced control schemes in the future. For example, if both stages are operated simultaneously, the coarse stage can follow the motions of the fine stage in a so-called transporter-following fine stage scheme. More advanced control schemes using both stages at once may also be needed to achieve the required perturbation rejection during the final mounting operation, when perturbations generated by the coarse stage will adversely affect the fine stage.

2.4.3 The coarse stage

The stepper motor stages comprising the coarse stage are already available in the group. They have been used in the first experiments with a haptic interface, and in the empirical characterisation of a dual Lorentz actuator that will be used in the fine stage. See fig. 2.1.

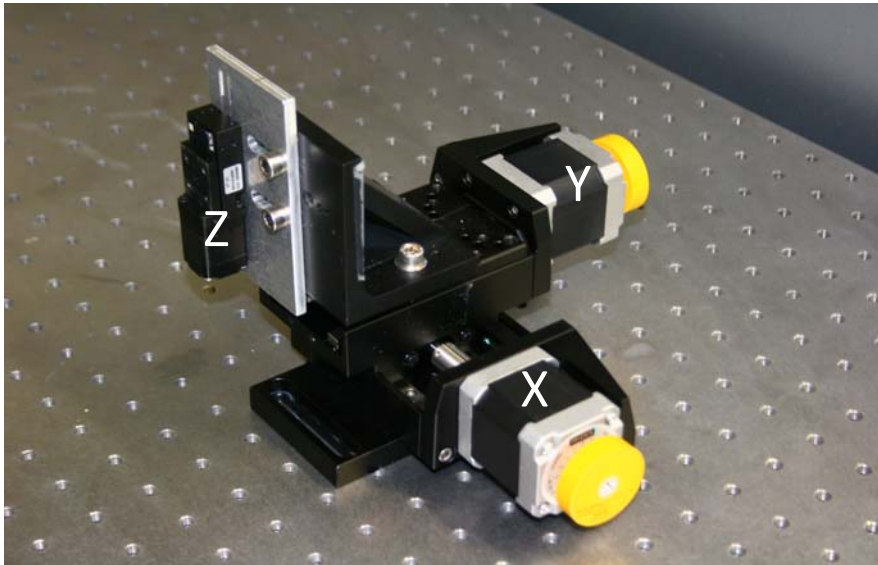


Figure 2.1. Overview of the coarse positioning stage. Three stepper motor-and-spindle stages provide the three translational DoFs. In future applications a fourth, rotational stage will be added to provide vertical rotation. The fine stage will be mounted to the moving part of the Z stage, left.

The x- and y-direction motions are provided by two MICOS LS-65 stages, which have a motion range of 26 mm each. The full-step resolution of these stages is 5 μm , meaning that this is the displacement corresponding to one step of the stepper motors. By using fractional steps this can in principle be improved down to 47 nm, but this is not very repeatable. The bidirectional repeatability of the stages is also 5 μm , due to backlash in the spindle. A 5 μm resolution and repeatability is more than adequate to meet the 20 μm MIM requirement for the coarse stage.

The vertical motion is provided by a third stage, a MICOS VT-21 S. It has a translation range of 10 mm with a 2.5 μm full-step resolution. The bidirectional repeatability is 4 μm , again sufficient to meet the MIM requirement. The maximum velocity is 5 mm/s, which is half the requirement. However, the vertical displacement that is needed in practise will be on the order of 1 – 2 mm with a velocity of 10 mm/s, so this is not a serious drawback. The stage has a weight of 0.1 kg and a load-bearing capacity of 10 N in all three directions. The torque-bearing capacity around all three axes is on the order of 0.5 Nm.

The mechanical design of the fine stage will be constrained by these load limits; the weight should be kept below 1 kg to prevent overloading. Also the torque load limitations will have to be taken into account. A further point to consider is the relatively small area that is available on the moving part of the vertical stage. The fine stage has to be mounted to this area, which is 24 mm by 22 mm. The fine stage itself can of course be larger than this.

The coarse stage in its current state has only the three translational DoFs. Later on in the research, an additional rotational stage will be inserted between the horizontal stages and the vertical stage to provide coarse rotation about the vertical axis. This is a MICOS DT-80 stage, which has a rotation range of 360° with a 0.01° full-step resolution and a bidirectional repeatability of 0.5°. Alternatively, the rotational stage could be mounted under the tool holder, so that the tool obtains a rotational DoF.

3 Fine stage concept

In this chapter the technologies that can be used for the design of the fine stage will be briefly described. The fine stage specifications, based on the “mounting step” requirements outlined in the previous section are presented, after which a technology selection is made and the fine stage concept is presented.

3.1 Possible fine stage concepts

The fine stage must be a six degree of freedom positioning stage with a 200 μm range and sub-micrometre resolution. A number of technologies exist that have been used in positioning stages, which could be of interest for the fine stage concept. These will be briefly described in this section.

A brief literature survey (see Appendix A) has been carried out to find the main characteristics and application areas of these technologies. The results of this survey are summarised below:

- **Piezo actuators and flexures**

Piezo actuators have usually small travel ranges, on the order of 50 – 100 μm [14],[18]. Motion amplifiers have to be used if larger ranges are required. Resolutions can be as fine as 15 nm [18]. Piezo actuators are characterised by a very high stiffness, and relatively large forces. A significant disadvantage is their considerable hysteresis and nonlinearity [1],[2]. They are usually implemented in a setup that has 1 – 3 degrees of freedom, the remaining degrees of freedom constrained by flexures and elastic hinges [14]. Typical applications are the positioning of samples and vertical actuation of the stylus in atomic force microscopes.

- **Lorentz actuators with linear guides**

Various types of Lorentz actuators exist, which vary from a single magnet and coil for short range actuators [13],[15] to linear motors [17]. These consist of a moving coil and a linear magnet array, or moving magnet and linear coil array. The single type has typical ranges of 100 μm to several mm, while linear motors can be made to any length. Resolutions can be as good as 10 nm, but are often less for larger range actuators. Lorentz actuators usually have zero stiffness in the direction of motion, and need bearings, guides or flexures to constrain the remaining degrees of freedom. Depending on size, large forces can be achieved and linearity is often good. Typical applications are micropositioning stages and wafer steppers.

- **Magnetic levitation**

In magnetic levitation devices, a moving plate is suspended in free air by magnetic forces. These forces can be generated by either Lorentz actuators or reluctance actuators. Lorentz actuators in these stages often are more linear than reluctance actuators, which have a distinct quadratic characteristic. The range of magnetic levitation stages is limited by the size of available magnets and coils (linearity) and can be 200 μm to several mm. Depending on the quality of the sensors and controllers used, resolutions can be as fine as 2 – 3 nm [1],[2]. Maglev stages usually have 5 or 6 degrees of freedom. In the latter case, no additional guides or supports are provided so the moving parts are entirely free-floating. A drawback is of course that the system is open loop unstable, and can be operated and tested only in closed loop configurations. However, the necessary control schemes are well-known [3],[6],[9]. The stiffness of the actuators is zero in open-loop, but the stiffness of the closed-loop system can be adjusted through the controller settings.

In positioning stages, magnetic levitation is still mostly in the experimental phase. However, in active magnetic (mainly rotating) bearings the technology is widely applied in high load, high precision and high speed applications [44].

- **Halbach array motors**

Halbach motors are a sub case of the maglev concept. They are essentially planar three-phase motors, based on a so-called Halbach magnet array. These devices usually have a long range, on the order of 20 – 200 mm, but this can be extended to any value by expanding the magnet array. Resolutions can be as fine as 10 nm [9], but 10 μm has also been reported [3]. The available forces and payloads are usually high, and the actuator stiffness is adjustable. Theoretically these devices are 6-DoF. However, vertical displacement and rotation about the vertical axis are usually limited, and tilting is avoided altogether [7].

The major drawback of this technology is its complexity, especially of the required controllers and sensors. Most devices are still in the experimental phase, but are intended for use in wafer steppers. 1-DoF Halbach motors are already in use in electron microscopes for sample positioning.

The key figures for a number of existing stages, namely travel range and resolution, are shown in fig. 3.1 (see also Appendix A). The stages are grouped according to the technology used. The red triangle shows the requirements of the slave robot fine stage, 200 μm range and 40 nm MIM.

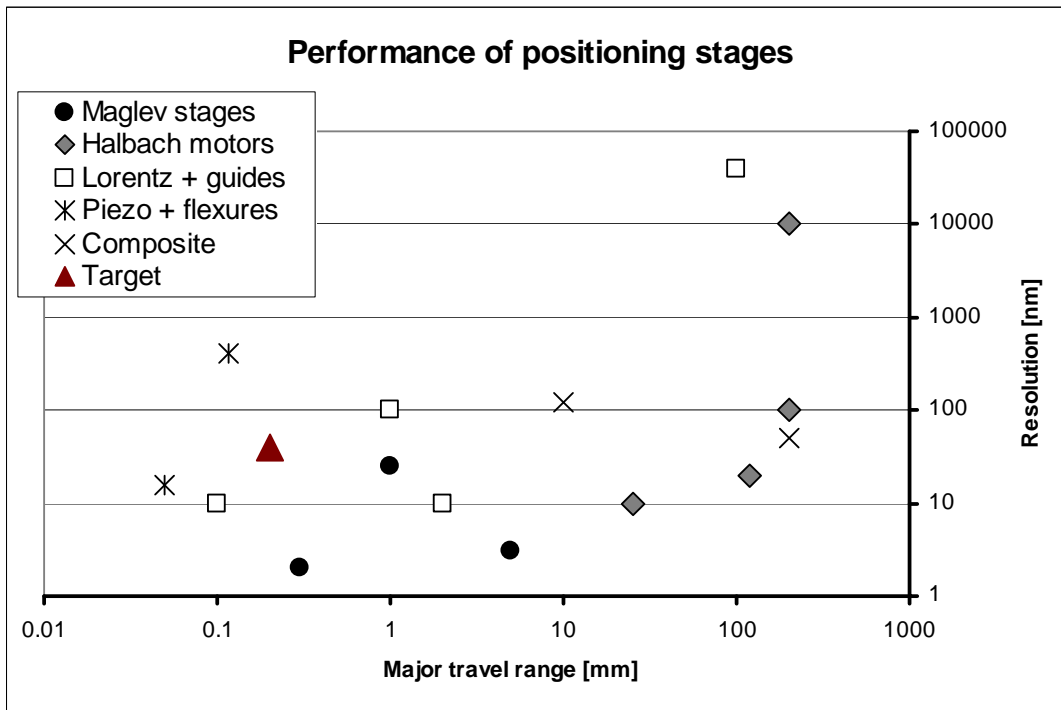


Figure 3.1. Overview of performance of existing micro-positioning stages.

Existing maglev and Halbach technology based stages have a moving mass on the order of several hundred grams (maglev) up to 25 kg (Halbach), while the payload generally is on the order of several kilograms. For the piezo actuated stages this is usually less, although exact numbers were not mentioned.

The available forces the stages can generate are usually on the order of 20 N for maglev stages, 20 – 150 N for Halbach stages and up to several hundred newtons for reluctance actuator and flexure based systems. Accelerations range from 10 to 70 m/s^2 . Piezo actuated stages have the lowest velocities, usually no more than 30 $\mu\text{m/s}$.

3.2 Specifications

The specifications of the fine stage follow from the requirements for the final step in the Microassembly process, the final mounting. These specifications are discussed in this section.

3.2.1 Movement range and resolution, translational

To provide sufficient overlap with the coarse stage MIM, the range of the fine stage should be 10 times the coarse stage MIM, namely 200 μm . However, a bigger overlap would improve flexibility and cooperation between the two stages. With a 40 nm MIM this means the fine stage is overspecified with respect to precision as far as the user is concerned (a ratio of 5000 : 1). However, when the full range of 200 μm is used, the MIM achievable by the user is 1 μm , so this falls in the middle of the range of part tolerances. For high precision positioning the fine stage could also work with a multistep scaling, subdividing the mount operation in the same way as the entire pick-and-place operation is divided into three steps. This would enable a more flexible way of operating the slave. Note that this 200 μm range is not only needed in the two horizontal directions of the fine stage, but should also be achieved in the vertical (z-) direction.

3.2.2 Movement range and resolution, rotational

The fine stage should be able to correct small angular alignment errors left by the coarse stage, part geometries, etc. about all three axes. The coarse stage is specified to have a 360° rotational range about the vertical axis, with a 1° MIM. To correct the rotational alignment errors caused by this relatively coarse MIM, the fine stage should have a rotational range of at least $\pm 1^\circ$. The rotational MIM around the z-axis also should be one fifth of the smallest part tolerance of 200 nm. For a 1 mm part this is $\arctan\left(\frac{0.2}{1000}\right) \cdot \frac{1}{5} = 0.002^\circ$.

To correct for tilt misalignment the rotational range about the horizontal axes of the fine stage should also be at least $\pm 1^\circ$ with the same MIM. This figure depends on the manufacturing of the parts. For instance DRIE etching results in parts with a 1° deviation of the sidewalls from vertical. Also errors left by the coarse stage and gripping errors need to be corrected.

To correct out-of-plane tilt errors in a peg-in-hole assembly operation, which are difficult to observe for the operator, compliance in some part of the system can be used to make the parts self-align. This compliance can be either in the gripper itself, or by a low stiffness actuator and suitable controller settings.

3.2.3 Movement velocity and acceleration, translational

If the entire range of the fine stage is to be traversed in one second, back and forth (representative of human operation), this bandwidth is 1 Hz, and the translational velocities and accelerations along all three axes have to be at least

$$\begin{aligned}x &= 0.1 \cdot \sin(2\pi t) \\ \dot{x} &= 0.2\pi \cdot \cos(2\pi t), \quad \dot{x}_{\max} = 0.2\pi = 0.6 \text{ mm/s} \\ \ddot{x} &= 0.4\pi^2 \cdot \sin(2\pi t), \quad \ddot{x}_{\max} = 0.4\pi^2 = 4 \text{ mm/s}^2\end{aligned}$$

where for simplicity a sinusoidal motion profile is assumed, with an amplitude of half the range, namely 100 μm . If the specifications have to be higher to accommodate the maximum human operator's actuating bandwidth of 5 Hz [39], these become 3 mm/s and 100 mm/s², respectively. These values are not including accelerations needed to achieve perturbation rejection in the control loop.

3.2.4 Movement velocity and acceleration, rotational

Similarly, the rotational velocities and accelerations (around the moving part centre of gravity) should be for an amplitude of 1° and 1 Hz bandwidth, $7^\circ/\text{s}$ and $43^\circ/\text{s}^2$, respectively. These values are approximately the same for rotation around all three axes.

For a 5 Hz bandwidth the velocities and accelerations are of course higher, namely $35^\circ/\text{s}$ and $1075^\circ/\text{s}^2$ respectively. These values are also not including accelerations needed to achieve perturbation rejection in the control loop.

3.2.5 Force range and resolution, payload

Interaction forces are typically on the order of 10 mN. These are the forces that should be exerted on the parts, to overcome friction, Van der Waals forces, capillary and electrostatic forces. Acceleration and control forces will have to be added to this force range, once the stage topology has been determined.

The force resolution should be as fine as 100 μN , to prevent damage to the small parts. A fine force resolution will also enable more detailed haptic feedback, and will allow the use of controller compliance for (partial) self-alignment of parts. When the interaction forces are on the order of 10 mN, this also corresponds with the range-to-resolution ratio of 100:1 of the human operator [39].

The payload of the stage will be on the order of a gram. This will increase the required acceleration forces somewhat, and will affect the control loop performance (the system control parameters are in part based on the estimated mass matrix of the moving part). However, in practise the micro parts will have a total mass that is negligible compared to the total moving mass.

3.2.6 Perturbation rejection

Perturbation rejection is important to ensure positional stability of the fine stage. For instance, during the lowering of a peg in a hole, the position of the assembly in the remaining 5 degrees of freedom should be stable enough that the peg does not hit the hole walls prematurely.

The rejection specification follows from the error budget (section 3.4.1), and is 14 – 35 nm, depending on the required MIM. The same reasoning applies to rotational perturbations; when a part size of 1 mm is assumed, a displacement of one end of 14 – 35 nm corresponds to a rotational perturbation rejection of 0.0008° – 0.002° .

Perturbations will be caused by vibration of the base structure of the device and of the floor on which it stands. For the controller to be able to compensate for these perturbations, the closed loop bandwidth has to lie above the bandwidth of the perturbations. This depends on the perturbation frequency spectrum. The power spectral density of floor vibrations was measured in previous work [45], it is shown in fig. 3.2.

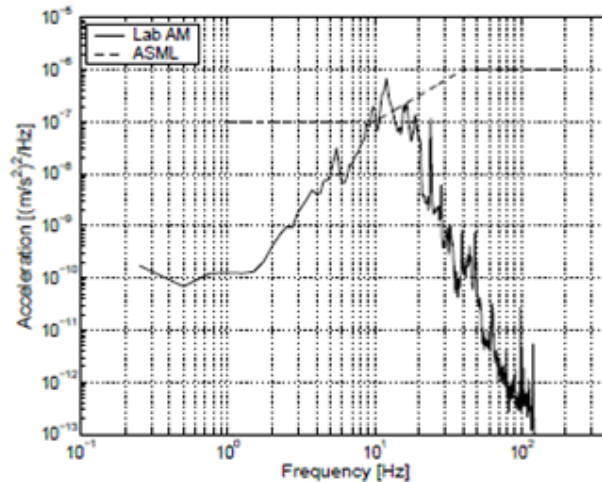


Figure 3.2. Power spectral density of floor vibrations, as measured in the lab of Advanced Mechatronics. Most of the frequency content of the floor vibrations lies around 10 Hz.

Modelling of the system has shown that the 10 Hz frequency content of the floor vibrations should be attenuated by a factor 100 (or 40 dB) at least in order to meet perturbation rejection specifications. This requires a 100 Hz closed loop bandwidth. See chapter 6 for more details.

The coarse stage will also introduce vibrations into the fine stage when it is active. Initially a simple control scheme is used, in which only one stage is active at a time. Therefore, coarse stage vibrations will not be considered further. However, when e.g. a transporter-following fine stage scheme is used this is no longer possible. The PSD of vibrations caused by the coarse stage should then be measured before the controllers can be designed.

3.2.7 Overall size and mass

The moving mass of the fine stage should be as low as possible to achieve the desired force resolution. This also goes for its moments of inertia, and so also the size of the moving part should be kept within certain limits. The upper limit on the moving mass is 10 grams. The entire fine stage will be mounted to the coarse stage, and this puts limits on the mass and size of the entire fine stage. The mass will have to be kept below about 0.5 kg, while the size limitation is on the order of 10 cm x 10 cm x 10 cm.

3.2.8 Accessibility

The fine stage should be constructed in such a way that the assembly area is as free from obstacles as possible. The tools and parts should be able to access this area from any direction. Therefore, in the ideal case the assembly area is the topmost part of the fine stage, there are no parts of e.g. sensors or actuators protruding above it. This forms a constraint on the design of actuators and sensors.

3.3 Fine stage technology selection

An important specification of the fine stage is its fine force resolution. A force resolution on the order of 100 μ N can be much more easily achieved when the total actuator forces are low. Therefore, actuators with low or zero stiffness are preferred, because then no actuator force is needed to deform high-stiffness suspension components (e.g. flexures) or to overcome friction (e.g. guides). Hysteresis and stick-slip, arising in some high-stiffness actuator principles, would also interfere with a fine force resolution. An actuator principle that is free of these phenomena will enable a more transparent haptic interface. Furthermore, when the actuators have zero stiffness, the closed loop

actuator stiffness can be adjusted by the controllers. This will help achieve the desired force resolution and can be used to assist the operator in compliance-based assembly tasks.

Additionally, assembly tasks can be either force or displacement controlled tasks. With high stiffness actuators position tasks are simple to control, but to deal with a force task, force sensors are required. Force sensors are not readily available with the required small size and fine resolution. On the other hand, with low stiffness actuators, force tasks are simple to control, and position tasks require position sensors, which are much more readily available with the right specifications.

A further consideration is whether the stage should be a parallel or serial configuration. In a serial configuration, the stage would consist of a stack of stages that each have one or a few degrees of freedom, similar to the coarse stage. This will not be easy to realise within the size restrictions, and could also lead to error propagation (hysteresis, play, alignment errors, etc.) from one stage to the next. A further disadvantage of such a serial configuration is that the moving masses increase, because the lower stages have to move the full mass of the stages on top of them. A free-floating mover naturally has 6 degrees of freedom, so the required motion ranges can be realised in a single, compact parallel stage. This parallel stage then has only one, low mass, moving part. An alternative 6-DoF parallel stage configuration would be e.g. a Stewart platform (hexapod) with six piezo actuators [18].

Piezo actuators are not suitable for the fine stage because of their high stiffness, nonlinear behaviour and the fact that they are not contact-free. Additionally, a 200 μm range is above the upper limit of current piezo actuated stage performance. A possible solution would be the use of Lorentz actuators combined with air bearings for the vertical support of the moving mass. This is a stable and contact-free solution. However, this would require additional equipment to provide and control the air pressure in the bearings, which increases size, cost and complexity. Additionally, such a device could not be used in a vacuum environment, which will be needed for specific assembly tasks. Halbach motors, as well as linear Lorentz motors, have typical motion ranges on the order of 20 – 200 mm with resolutions on the order of 10 nm. It would be possible with these specifications to make a single stage device, but the technology is bulky and complicated. With the two-stage approach the fine stage needs only a few hundred μm range. The added complexity, size and cost of these devices do not outweigh their better specifications. These three technologies will not be considered further.

Most existing stages found in the literature are high force and/or high mass devices. Conversely, the low force, low mass specification of the microslave stage asks for a miniaturised device. Technologies that can be miniaturised are magnetic levitation and Lorentz/reluctance actuator based stages. The main characteristics of existing stages and of the fine stage to be designed are summarised in the table 3.1.

Technology	Contact free	Open loop Stiffness	Linearity	Resolution	Range
Piezo	No	High	--	100 – 400 nm	50 – 100 μm
Lorentz	No	High / Zero	++	10 nm – 40 μm	100 μm – 100 mm
Maglev	Yes	Zero	+ / ++	2 – 20 nm	300 μm – 5 mm
Halbach	Yes	Zero	+	10 nm – 10 μm	20 – 200 mm
Microslave stage	Yes	Zero	++	40 – 100 nm	200 μm

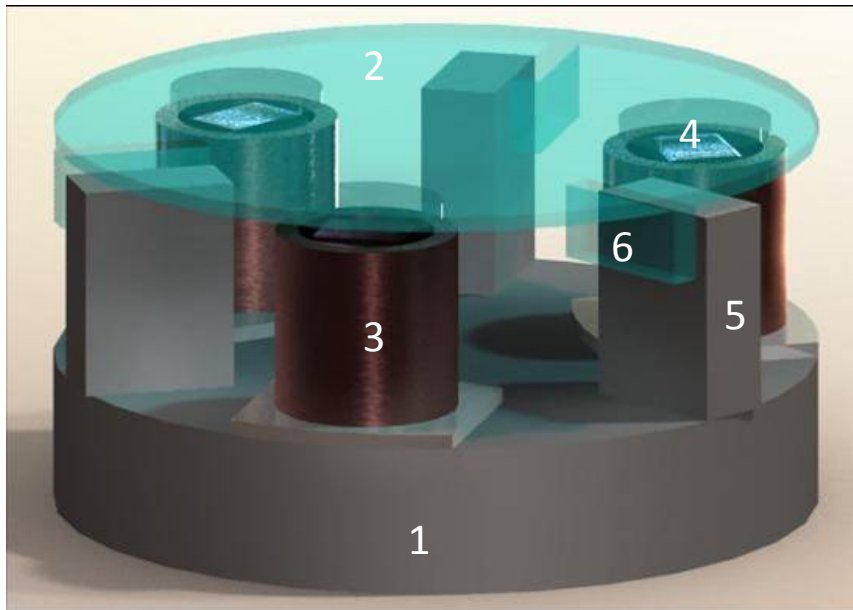
Technology	Complexity and cost	Control complexity	Suitable for miniature stage	Suitable for parallel stage
Piezo	+	+	+	++
Lorentz	+ / -	+	+	-
Maglev	+ / -	-	+	++
Halbach	--	--	-	+
Microslave stage	+	+	++	++

Table 3.1. Comparison of various existing technologies to the microslave stage requirements and specifications.

From the preceding considerations, magnetic levitation seems to be a suitable solution for the fine stage. Although other technologies could of course also be used, these all have some drawbacks. A maglev stage can deal with the required fine force and displacement resolutions, and can provide 6 degrees of freedom in a single stage.

3.4 Overall topology and concept

A concept for the fine stage based on magnetic levitation has been proposed in previous work [46]. This stage will consist of a magnetically levitated disk, actuated by three actuators. Each actuator can provide an electromagnetic force in two independent directions, so that all six degrees of freedom are actuated. On the levitated disk, targets are provided for the position sensors. A schematic overview of the fine stage topology is shown in fig. 3.3.



1. Base structure
2. Floating disk
3. Actuator coils
4. Actuator magnets
5. Sensor holders with sensors
6. Sensor targets

Figure 3.3. Concept sketch of the 6-DoF magnetically levitated microslave stage.

The base structure, which will be mounted to the coarse stage vertical actuator, supports the actuators and sensors. There are three actuators which are positioned at the corners of an equilateral triangle. The sensors to measure the six degrees of freedom will be mounted to the sensor holders, and are 1-dof optical reflective sensors (see chapter 4). The actuators each provide a Lorentz force to the levitated disk above them in a horizontal and a vertical direction (see chapter 5). This gives the disk the ability to move in all six degrees of freedom.

In this concept, there is no mechanical contact between the disk and the base structure when the stage is in operation. This meets the contact-free specification stated earlier. Another advantage of this configuration is that there are no components above the disk; its surface is entirely free. This allows access to the assembly area from any direction with any tool type, and makes the device much more flexible regarding possible applications.

3.4.1 Error budget

According to the definition of MIM for noise-limited stages, the maximum allowed peak-to-peak positioning noise is half the MIM, in this case 20 – 50 nm. There will be three main contributions to the noise, namely actuator noise, sensor noise and external perturbations. These can each be subdivided into specific component noise contributions, and this way an error budget (see fig. 3.4) can be defined. Since it is assumed here that the noise from each component is a random, independent error source, the sum of noise contributions is defined as the square root of the sum of the squares of all contributions.

The external perturbations are given the largest part of the error budget, because these are the hardest to get under control. Note that the amplitude of these perturbations is for the closed loop system, i.e. after perturbation rejection by the controller. This means that the overall perturbation figure defines the perturbation rejection specification.

The actuator noise is distributed over amplifier and controller noise, noise generated by the actuator coils themselves and D/A converter noise. These last two are expected to be low, since the coil has a low impedance and modern D/A converters have a high resolution. The remaining noise budget is distributed evenly between amplifier and controller.

The sensor noise is distributed over the sensor itself, the readout electronics and the A/D converter. The latter is assumed to be low, since even a 16-bit ADC will give a resolution of about 3 nm over a 200 μm range, and many modern ADCs have better resolution than this. The remaining noise budget is again distributed evenly between sensor and readout.

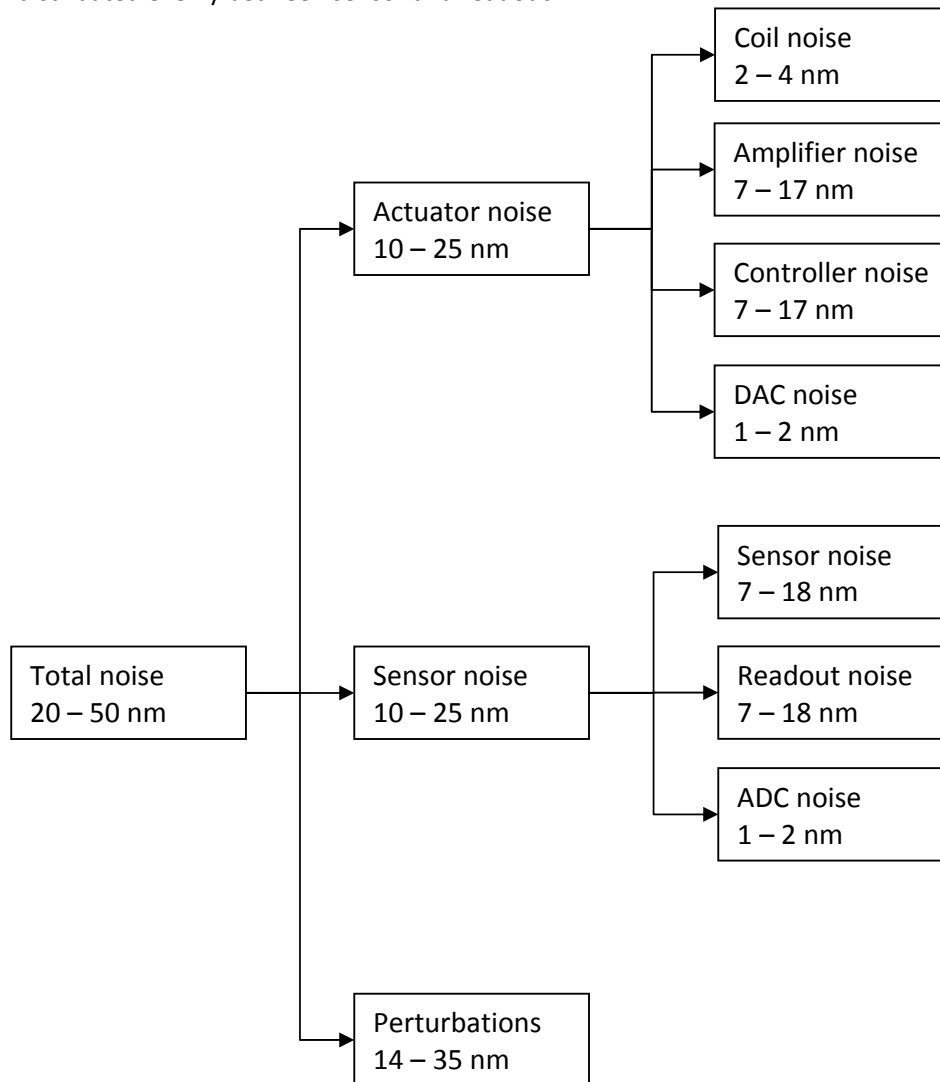


Figure 3.4. Error design budget for the microslave stage.

4 Sensors

The sensors will measure linear displacements, in six independent directions. These are three vertical displacements, and three horizontal displacements. From these, the three centre of gravity displacements X , Y and Z and three rotations ϕ , θ , and ψ are calculated, using a coordinate transformation matrix. Like the actuators, they will be placed at the corners of an equilateral triangle. To ensure observability, especially of the rotations, the sensors should be placed a minimum distance apart, and the horizontal displacement directions that are measured should not go through the same point. Because the slave robot will essentially be used as a motion tracking device, the position measurements need not be absolute.

4.1 Targeted sensor specifications

- Range at least 200 μm
- Peak-to-peak noise (6-sigma, including readout electronics and ADC) max. 25 nm
- Nonlinearity better than 5% relative to full scale over the entire range
- Bandwidth 1 kHz (for a control loop BW of 100 Hz)
- Contactless
- Position measurement may be relative

4.2 Possible sensor technologies

For the vertical displacements, the bottom surface of the levitating disk is used as a target. Depending on the type of sensor used, the target areas may have to be coated with a material of the right properties (e.g. reflectivity, conductivity, magnetic permeability). For the horizontal displacements, three vertical targets are needed. These will be made as three vertical protrusions on the disk's underside. They should be designed such that they do not introduce low (< 5 kHz) eigenfrequencies to the disk.

Each sensor should have a range of at least 200 μm , preferably more, with a sensor noise of at most 20 nm. The sensors should be insensitive to tilting of their targets over a range of $\pm 1^\circ$, and lateral displacements of the targets over the 200 μm range. The sensors should be as small as possible. The sensing principle should of course be contact-free. To enable easy exchange of disks and keep the disk completely contact-free the sensors should preferably be of a type that does not require a grounding cable to the sensor targets or disk.

Possible sensor principles are listed below, along with their advantages and drawbacks for this application.

- Capacitive sensing
 - Variable capacity by changing distance between electrodes
 - + Disk itself can be used as moving electrode
 - + Available in small size
 - + Available with required range
 - + High bandwidth, fine resolution
 - Requires ground connection to moving disk
 - Expensive [47]
 - Variable capacity by changing overlap between electrodes
 - Requires electrode structure on disk, and connecting cables
 - Difficult to realise in a 6-DoF system, sensitive in multiple directions
 - Not commercially available

- Inductive sensing
 - Eddy current sensing (conductive target)
 - + Disk itself can be used as moving electrode
 - + Available with required range and resolution
 - + Less expensive
 - Requires ground connection to moving disk
 - Too large size
 - May cause interference with actuators and vice versa
 - Variable inductance by changing distance to a ferromagnetic target
 - + Available with required range and resolution
 - + Less expensive
 - Requires additional material on disk, adds weight
 - Too large size
 - May cause interference with actuators and vice versa
 - Poor linearity

- Optical sensing
 - Reflective sensing (interferometer)
 - + High bandwidth, fine resolution
 - + Long range
 - Complicated and expensive equipment
 - Requires mirror surfaces on moving disk
 - Too large size
 - Reflective sensing (laser sensor)
 - + Available with required range and resolution
 - + Less expensive
 - + Disk itself can be used as target
 - Sensitive to target tilting
 - Too large size
 - Reflective sensing (LED and phototransistor)
 - + Very affordable
 - + Small size
 - + Available experience from previous research
 - + Disk itself can be used as target
 - Range and resolution not well described
 - Not available as off-the-shelf system
 - May be sensitive to target tilting
 - Photo-interrupter (LED and phototransistor)
 - + Very affordable
 - + Small size
 - + Available experience from previous research
 - Range and resolution not well described
 - Not available as off-the-shelf system
 - Requires more complicated target geometry

Based on these considerations, where low cost and complexity and small size were the most important, optical reflective sensors and photo-interrupters were investigated further.

4.3 Optical sensors

Two types of simple optical sensors have been used in previous research at the PME department. Both operate on a similar principle: An infrared LED functions as light source, and a phototransistor receives part of this light. The amount of received light varies with displacement of a target and results in varying conduction of the phototransistor (PHT).

The two sensor types are:

- A reflective sensor (Osram type SFH-9201), used in the Contactless Air-film Waferstage of Jasper Wesselingh [48] and the Smart Air Bearing investigated by Rein Boshuisen [49]. In this sensor, LED and PHT lie in the same plane, light is emitted upwards and reflected by a target at some distance z above this plane (see fig. 4.1). When z is zero, no light is reflected and the PHT is cut off. This also happens when z is very large. A PHT conduction maximum lies somewhere around $z = 500 \mu\text{m}$, and there are two measurement ranges with a different slope (see fig. 4.2). The linear part of the “near” range is approximately $200 \mu\text{m}$ long.

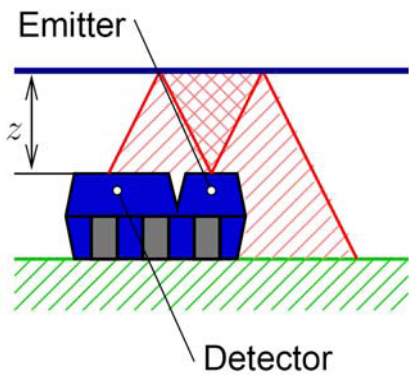


Figure 4.1. Sensing principle of the SFH-9201 reflective position sensor.

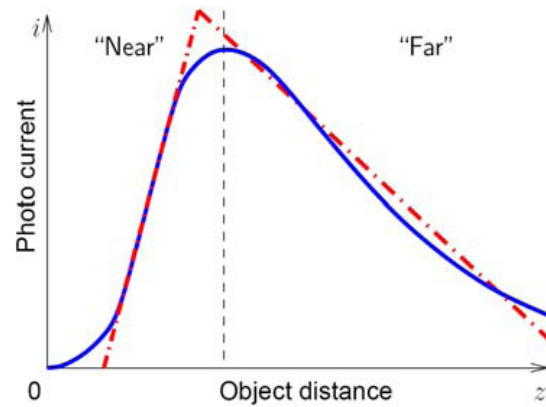


Figure 4.2. Theoretical near and far measurement ranges of the SFH-9201. The peak occurs approximately at $z = 500 \mu\text{m}$. [49]

- A miniature version of the well-known photo-interrupter (Rohm type RPI-122), used as angle sensor in the 1-DoF Haptic Gripper of Ton de Boer [50]. The LED and PHT are mounted opposite from each other, and a target moves between them to block the light from the LED depending on position (fig. 4.3). The linear part of the range is approximately $200 \mu\text{m}$ long (fig. 4.4).

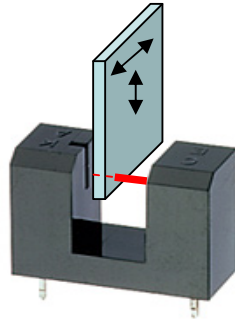


Figure 4.3. Sensing principle of the RPI-122 photo-interrupter.

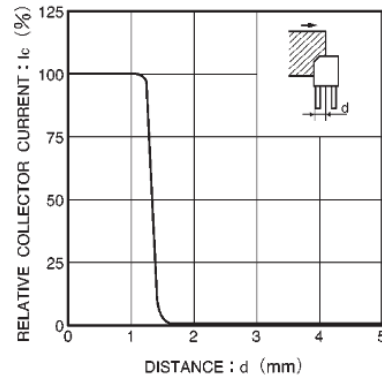


Figure 4.4. Theoretical sensor characteristic of the RPI-122, sideways motion of the target. The linear part of the range is approximately 200 μm long. [51]

4.3.1 Investigation of existing sensor systems

Sensor readout boards were available from the previous research, these have been tested in a setup with a manually operated 1-DoF translation stage and an inductive sensor as reference (fig. 4.6). Both boards have a similar electrical topology (fig. 4.5): The infrared LED is fed by a one-transistor constant current source (CCS) that has a green LED as voltage reference. The PHT photocurrent is converted to a voltage by an emitter resistor, followed by an opamp voltage amplifier and a 2nd order Sallen-Key filter with Butterworth characteristic. The CCS is needed to compensate the strong temperature dependency of the LED forward voltage, while the filter blocks HF noise and prevents aliasing of the ADC. The supply voltage in both cases was 5 V.

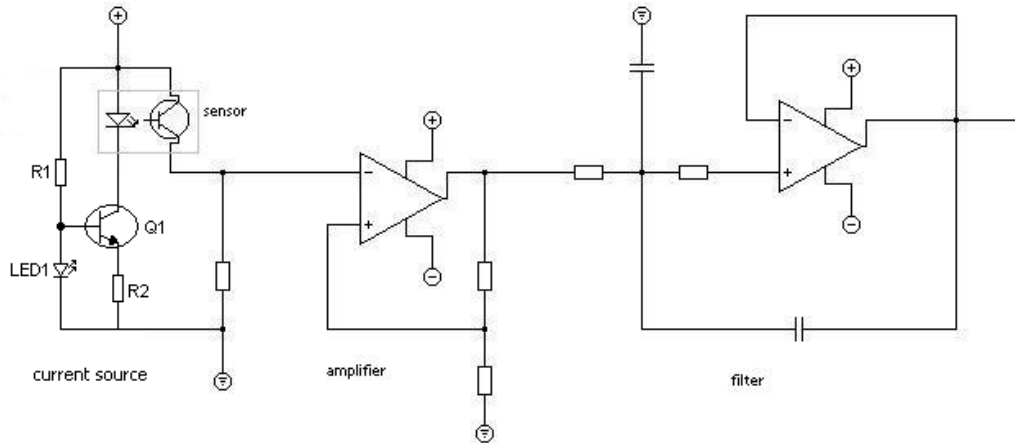


Figure 4.5. Schematic diagram of the existing optical sensor readout boards. In the board used in the Haptic Gripper project the amplifier and filter were built with a single opamp [49].

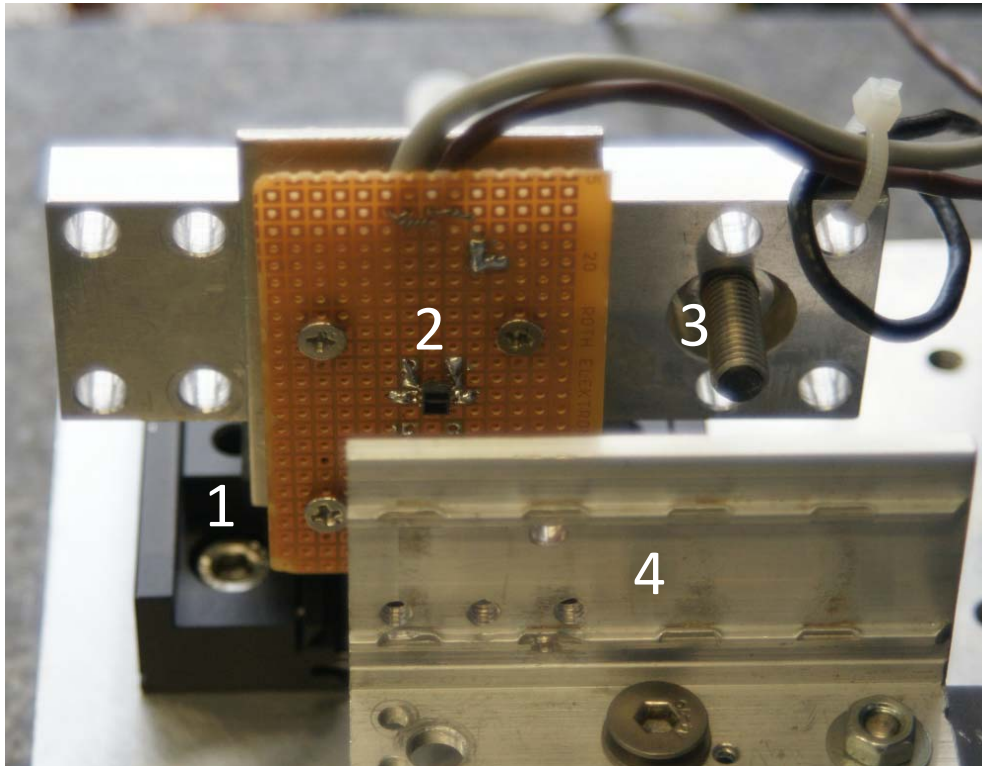


Figure 4.6. Test setup to investigate sensor performance.

1. Manual 1-Dof positioning stage
2. Optical sensor
3. Inductive sensor (Reference sensor)
4. Aluminium sensor target

The photo-interrupter was tested with the target moving in from two different directions, frontal and sideways (see fig. 4.3). Two different characteristics can then be observed, as a result of the photo-interrupter slit geometry. The initial test results are given in table 4.1, the measurement data from which these values are derived can be found in Appendix G. Note that the noise levels indicated are for an unshielded setup, with some interference from other equipment. Without this interference, the noise varies from approx. 50 – 100 nm_{pp}.

Sensor	Range [μm]	Position noise in the lower part of the range [nm, p-p]	Position noise at mid-range [nm, p-p]	Position noise in the upper part of the range [nm, p-p]
SFH-9201	120	106	124	169
RPI-122 Frontal	100	115	135	154
RPI-122 Sideways	80	110	88	120

Table 4.1. Results of initial optical sensor range and noise tests.

These results show that the sensors with their original readout electronics are not suitable for this application; the measurement ranges are too small and the noise level too high. The small ranges are due to amplifier and PHT saturation; this could easily be extended by decreasing the amplifier gains and selecting smaller values for the emitter resistors. The noise was more difficult to reduce, since there are a number of noise sources in the circuit. These are listed in the following paragraph.

4.3.2 Sensor noise sources

- **Noise in the power supply.** Since the supply directly feeds the PHT, this noise shows up in the (amplified) output signal. This can be reduced with a series regulator IC, but it has to be a low-noise type. The IC used in [50] was found to actually add noise.
- **Noise in the CCS.** This can be a result of power supply noise, noise in the CCS transistor and noise in the reference voltage. Since this noise modulates the LED light intensity, it also shows up in the output signal, and with considerable gain.
- **Noise generated by the amplifier and filter.** Every opamp produces some noise, depending on opamp type and impedance of the input and feedback components. In a well-designed system this should be on the order of microvolts.
- **Thermal noise in passive components.** This can only be reduced by choosing low impedance components.
- **Noise generated by the sensor itself.** This can only be influenced by selecting another type of sensor.
- **A/D conversion noise.** This depends on the resolution of the ADC used. The ADC itself also adds noise to the signal in its amplifiers or through its power supply. This is especially true for the USB based NI acquisition boards.
- **RF interference.** Although this lies far outside the sensor bandwidth, aliasing in the ADC can cause it to decrease the SNR of the sensor. Shielding reduces it, as well as using an ADC board with integrated anti-aliasing filters.
- **Mains interference.** Shows up as a 50 Hz peak in the noise spectrum. Since this lies within the bandwidth it cannot be filtered out. Shielding and avoiding earth loops are necessary to reduce it.
- **Stray light.** Light from electric sources causes a 100 Hz peak in the noise spectrum (rectified mains frequency). The built-in IR filter of the sensors reduces this. It was found that because of the small distances between sensor and target, the amount of stray light that enters the PHT is negligible.

4.3.3 Improved design of readout electronics

To reduce the noise levels a number of improvements have been made to the existing readout electronics. These are based on the above observations about noise and many experiments. Tests have been made with all three sensor configurations. Lab reports and measurement results of these experiments are listed in appendix G. The resulting improvements are listed below.

- **Power supply.** The power supply voltage was increased from 5 V single-ended to ± 15 V. This enables an output signal of at least ± 10 V, so that the standard input range of most available ADC boards can be fully used and no resolution is lost. Noise generated by the amplifier and filter also has less impact on the SNR when the output voltage range is increased to 20 V. With an output range of 20 V and measurement range of 200 μm , the sensitivity is then 100 mV/ μm . Furthermore, the noise on the power supply lines was reduced by low-noise series stabiliser IC's. These are the LT1962 for the positive voltage and LT1964 for the negative voltage. According to the manufacturer's specifications the output voltage noise should be on the order of 20 – 30 μV_{rms} . Decoupling capacitors have been added to each opamp to reduce crosstalk between channels on the final sensor readout board. The use of ceramic capacitors has been avoided here and in the filter, because these can exhibit piezo-electric effects and their capacitance greatly varies with the capacitor voltage [52],[53].
- **Constant current source.** Most noise in the output signal derives from noise in the CCS. This can be concluded from the fact that the noise levels are higher in the upper part of the measurement range, i.e. when more light reaches the PHT. This was found for all sensor configurations and measurements. The gain from LED current noise to output voltage is, depending on configuration, 400 – 1200 mV/mA. This means that the current noise should be

less than $2.5 - 0.8 \mu A_{pp}$ if the sensor noise has to be $<10 \text{ nm}_{pp}$. The one-transistor CCS was found to be too noisy and very sensitive to thermal fluctuations, resulting in drift. Especially the latter problem could effectively be solved by implementing an opamp-controlled CCS. The relative impact of current noise can be further reduced by increasing the CCS current, although at the expense of thermal dissipation.

- **Voltage reference.** A further improvement of the CCS was made by replacing the green LED voltage reference with a series combination of a diode and a 5.6 V zener. This combination has a very low thermal coefficient, and this was also found to reduce thermal drift in the circuit. A bypass capacitor was added to further reduce noise on the reference voltage.
- **Amplifier.** The existing configuration consisting of an emitter resistor and non-inverting amplifier was abandoned in favour of a so-called transresistance amplifier. In this configuration the PHT output (current) is directly connected to the virtual earth node of an inverting amplifier, and converted to an output voltage by the opamp's feedback resistor. This configuration keeps the PHT collector-emitter voltage always at the same level, regardless of the current, resulting in a more linear behaviour. Additional benefits are that the PHT can be fed from the same supply as the rest of the circuit, and that the zero and gain of the amplifier can easily be adjusted.
- **Filter.** The filter topology of the existing boards (2nd order low-pass Sallen-Key with Butterworth characteristic) has been kept. It has been redesigned for lower noise and a 1 kHz bandwidth. The noise added by the filter can be reduced by lowering the filter impedance and selecting an opamp optimised for low noise with this impedance. The LT1007 was found the most suitable.
- **A/D converter.** The standard NI USB-type boards were found to be too noisy for this application, even though their resolution (16 bit) is theoretically sufficient. Other DAQ systems will have to be used, such as NI cRIO-based systems.

4.3.4 Sensor type selection

During the experiments, the photo-interrupter type sensors were found to have considerable drawbacks:

- **Difficulties with aligning the sensors to their targets.** Since the target is a small metal vane moving in and out of the sensor, it has to be aligned such that it does not make contact with the sensor anywhere. Otherwise, the ensuing stick-slip will result in erroneous sensor readings. The available clearance for this is about 1 mm, so this puts extra demands on manufacturing tolerances or requires extra alignment mechanisms. In addition, the metal vanes will complicate the final stage design as well as its assembly procedure, and may introduce unwanted structural modes to the moving part.
- **Sensitivity to dirt and dust.** The sensor body has a narrow optical slit to increase its positional sensitivity, which is a few hundred μm wide. It can easily get blocked by dust getting into it, which is then almost impossible to clean out again.
- **Greater sensitivity to thermal fluctuations of the sensor body.** Even with the improved CCS, the photo-interrupters showed drift when exposed to airflow, possibly as a result of deformation of the sensor body and/or thermal coefficient of the PHT.
- **Smaller linear range.** The available sensor types had a linear range of less than 200 μm . Other types could be chosen that have larger ranges, but the above drawbacks still hold and they have generally a larger physical size.

The reflective type sensor does not have the first two drawbacks mentioned. It also suffers considerably less from thermal drift and has a 200 μm range. For these reasons, the SFH-9201 was chosen as position sensor in the microslave stage. The noise figures listed in table 4.2 were measured for this sensor after all the above improvements had been made:

Range	RMS position noise [nm]	Peak-to-peak position noise [nm]
Full	3.3	28
Mid	2.5	20
Low	1.6	15

Table 4.2. Results of final noise tests, SFH-9201 reflective sensor with improved readout electronics.

4.3.5 Design of three-channel circuit board

Based on the prototype that resulted from the experiments, a sensor readout board has been designed. It contains electronics for three complete sensor channels and a low-noise power supply. Although it has primarily been designed for application in the microslave stage, it can also be used in applications with other sensor types based on a LED and phototransistor. To accommodate such applications, the LED current, amplifier gain and zero setting have been made adjustable. The filter characteristic can be adapted by changing component values. The board and its schematic diagram are described in detail in appendix H. It has been tested and its specifications are listed in the following section. Fig. 4.7 shows a simplified schematic diagram of the final sensor readout circuitry.

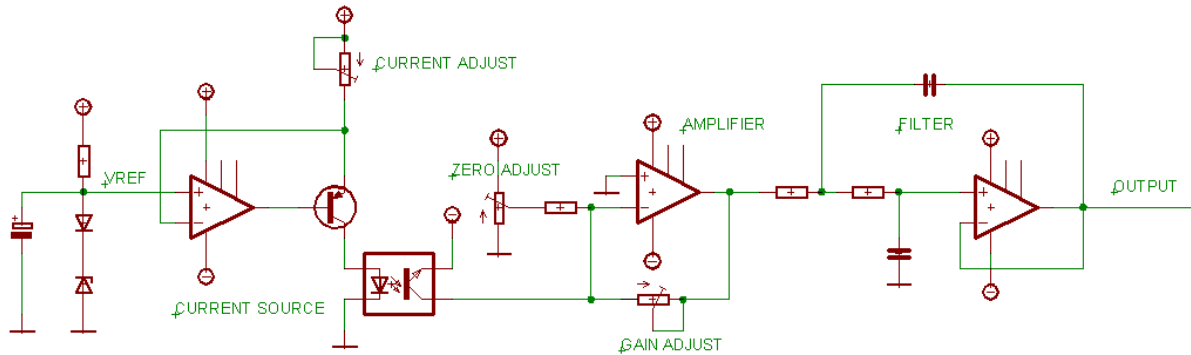


Figure 4.7. Simplified schematic diagram of sensor readout circuitry.

4.4 Final sensor and electronics specifications

- The final specifications of the optical sensor, in combination with its readout board are as follows:
- Range 200 μm
- Peak-to-peak noise (6-sigma, including readout electronics and ADC) 14-28 nm, depending on position
- Nonlinearity 2.5% relative to full scale over the full range
- Bandwidth 1 kHz
- Filter phase shift at 100 Hz -8° (calculated value)
- Sensor phase shift at 100 Hz -2° (calculated value)
- Supply voltage ± 15 V
- Output voltage range ± 10 V
- Output sensitivity 100 mV/ μm

4.5 Recommendations for further improvement

- The constant current source can be further improved by replacing the output transistor with a darlington or mosfet type. This will eliminate the last traces of temperature dependency. Additionally, an integrated circuit type CCS with low noise can be used. The LT3092 has been tested but was found to generate more noise than the existing circuit.

- The reference voltage noise level can possibly be lowered if low-noise IC voltage references are used instead of the diode/zener combination. This has not been investigated.
- The CCS noise contribution in the output signal can be eliminated if the sensor output signal is normalised with respect to the CCS current, i.e. divided by the voltage across the CCS current measurement resistor. A connector is available for this purpose on the circuit board, but it does require a DAQ system with six extra inputs.
- A sensor that is linear over a range larger than 200 μm yields a more robust and easier to manufacture stage, and will increase the rotation ranges. Other reflective sensor types with larger ranges should be investigated to achieve this.

5 Actuators

The actuators will be electromagnetic actuators, and to actuate the six DoFs six independent forces in six directions are needed. These forces will not be exerted in the centre of gravity of the moving part, since the actuators are situated at the points of an equilateral triangle. Therefore a transformation matrix is needed in the controller to convert from required CG forces to actuator forces. To ensure controllability the horizontal forces should not go through the same point.

The microslave moving part has a total mass of 7.5 gram, and its moments of inertia are approximately 500 gmm² about the horizontal axes (x,y) and 1000 gmm² about the vertical axis (z). There are four different functions of the microslave stage that require forces:

- Motion tracking of the user commands over the full operating range at 1 – 5 Hz. The accelerations required by motion tracking are maximum 100 mm/s² and 1075 °/s². This corresponds to total actuator forces of 0.75 mN (x,y,z) and torques of 0.5 mNm (x,y) and 1 mNm (z)
- Perturbation rejection over a 100 Hz bandwidth. The greater bandwidth of perturbation rejection implies greater accelerations and forces. However, perturbations such as floor vibrations will not be on the order of the stage motion range. If we assume that amplitudes of 2 µm and 0.02° are needed with a 100 Hz bandwidth, the required accelerations are 800 mm/s² and 7900°/s² respectively. This corresponds to total actuator forces of 6 mN (x,y,z) and torques of 4 mNm (x,y) and 8 mNm (z)
- Interaction forces between parts during assembly. These are assumed to be around 10 mN (x,y,z), without torques acting.
- Gravity compensation. If the moving mass together with payload is assumed to be 7.5 g, a total gravity compensation force of about 75mN is required (z). An inclination of the moving part of 1° requires a horizontal force of about 1 mN (x,y).

5.1 Targeted actuator specifications

The required forces and torques and the force distribution equations (Appendix C) yield the worst case forces for the horizontal and vertical actuators. These are as follows:

- Vertical:
 - 0.25 mN dynamic load (z translation motion tracking)
 - 0.5 mN dynamic load (x/y rotation motion tracking)
 - 2 mN dynamic load (z translation perturbation rejection)
 - 3.3 mN dynamic load (x/y rotation perturbation rejection)
 - 3.3 mN interaction force (z translation)
 - 25 mN static load (gravity compensation)
- Horizontal:
 - 0.44 mN dynamic load (x/y translation motion tracking)
 - 0.5 mN dynamic load (z rotation motion tracking)
 - 4 mN dynamic load (x/y translation perturbation rejection)
 - 4 mN dynamic load (z rotation perturbation rejection)
 - 6.6 mN interaction force (x/y translation)
 - 0.66 mN quasi-static load (gravity compensation at 1° inclination)

Adding all contributions up and adding a safety margin leads to the following minimum force specifications (per actuator):

- Actuator force
 - Vertical: >30 mN continuous, >40 mN peak
 - Horizontal : >10 mN continuous, >20 mN peak

Additional specifications are:

- Actuator range: $\pm 100 \mu\text{m}$ around operating point in X, Y and Z
- Bandwidth: > 100 Hz
- Force resolution: no coarser than 100 μN in all directions
- Force variation due to tilting of the target ($\pm 1^\circ$) less than 1% of full range
- Size less than 15 x 15 x 15 mm per actuator
- Actuator target area less than 100 mm^2 per actuator
- Actuator target mass less than 1 g per actuator

5.2 Possible actuator technologies

Two main actuator principles exist that generate electromagnetic forces. One is the Lorentz actuator, in which forces occur between current-carrying conductors (coils) and permanent magnets. These forces can be in two directions, i.e. attracting and repelling. The other principle is the reluctance actuator, where forces arise between an electromagnet and a ferromagnetic target. These forces can be in one direction only, namely attractive. In order to generate forces in both directions, a differential actuator will have to be used.

Two possible actuator concepts have been investigated extensively in a previous assignment. These are a 1-DoF reluctance actuator and a dual Lorentz actuator. They will be briefly described in the following sections. Appendix E contains the results of this assignment.

5.2.1 1-DoF reluctance actuator

The reluctance actuator shown in fig. 5.1 is a differential type actuator. It consists of two iron electromagnetic yokes with copper coils around them. When current is applied to these coils, a reluctance (attractive) force appears between the yokes and their iron targets. The levitated disk is attached between the two targets. The two yokes are operated in differential mode, which means that if the current through one is increased, the current in the other is decreased by the same amount. This makes the actuator force characteristic more linear. Both yokes receive bias flux from permanent NdFeB magnets, to reduce the quiescent current consumption. These magnets also have a low ferromagnetic permeability, and therefore function as additional air gaps in the magnetic circuit. This further linearises the actuator characteristic, at the expense of available force. The two yokes are different in shape, so that one is positioned below the moving disk and the other beside it, rather than above it. This is done to minimise the area of the disk that can't be accessed by the gripper.

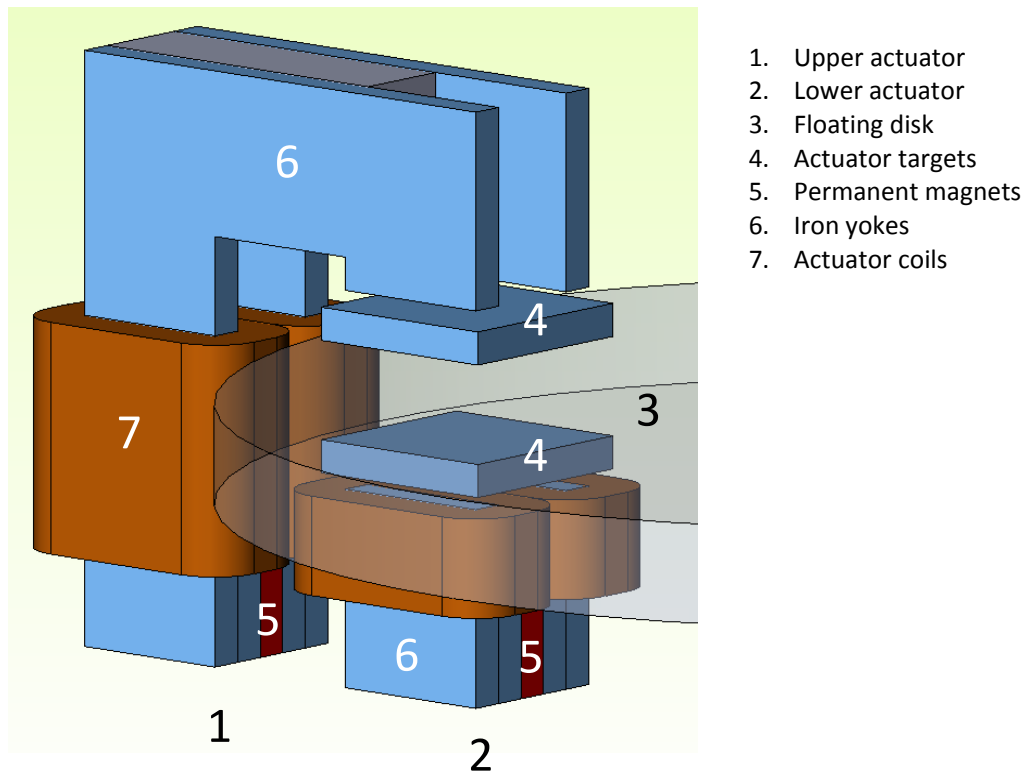


Figure 5.1. 3D CAD model of the reluctance actuator concept.

An actuator based on this principle was designed, optimized and extensively investigated for this application through FEM simulations. Details about this research can be found in appendix E. The overall sizes of the actuator pair shown are 18 mm x 8 mm wide and 18 mm high. The actuator should be able to generate a force of at least 50 mN in both directions, over a displacement range of $\pm 100 \mu\text{m}$ according to the FEM model. For the horizontal forces, a similar, but smaller actuator pair could be used. No practical experiments have been carried out with this actuator type.

The advantages of this actuator are:

- Negligible stray flux
- Small actuator target size (6 x 6 mm)
- Force characteristic not affected by horizontal displacements
- Force characteristic fairly linear

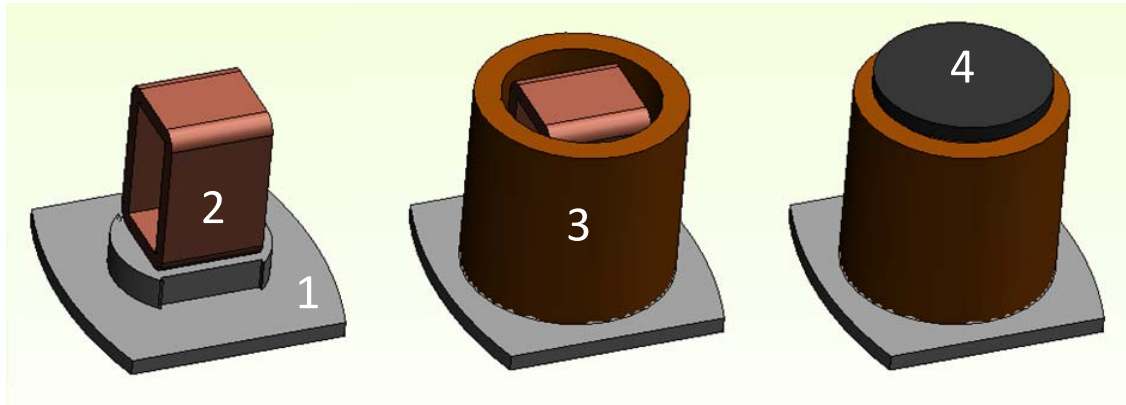
The disadvantages of this actuator are:

- Provides force in only one linear direction, so that six actuators are needed in total
- A total of 12 actuator targets are needed, which may need a large overall surface area
- Part of the actuator geometry is above the disk's surface:
 - This can be an obstacle for the tool during assembly operations
 - Makes exchanging of disks more difficult
- Two controller outputs required per degree of freedom
- Actuator dimensions slightly bigger than specification allows

5.2.2 2-DoF Lorentz actuator

The Lorentz actuator shown in fig. 5.2 is a dual type actuator, capable of supplying a force in a horizontal and the vertical direction. It consists of an aluminium base structure, to which a square coil is mounted. This coil provides the horizontal force. Around this coil a second, cylindrical coil is

placed, which provides the vertical force. The actuator target, attached to the moving disk, is a cylindrical NdFeB permanent magnet, which is kept floating a few hundred μm above the coils. This magnet is axially polarised, meaning that the magnetic field lines around it are mostly oriented in the vertical direction.



1. Base structure
2. Square coil
3. Cylindrical coil
4. Permanent magnet

Figure 5.2. 3D CAD model of the Lorentz actuator concept.

The horizontal force is generated by the current flowing in the top section of the square coil. This current flows mainly perpendicular to the (vertical) magnetic field at the magnet pole, in fig. 5.2 the current direction is front to back. Refer also to the cross-section view in fig. 5.3. The Lorentz force acting on this part of the coil is therefore directed left to right. The Lorentz forces acting on the vertical sections of the square coil are due to horizontal components in the magnetic field, but these cancel out when the magnet is centred. Finally, the Lorentz force acting on the lower section of this coil is opposite in sign to the horizontal force of the upper section, but much smaller due to the larger distance to the magnet. Therefore, there is a net horizontal Lorentz force acting on the square coil, and therefore an opposite reaction force acting on the magnet.

The vertical force is generated by the current flowing in the cylindrical coil. The magnetic field of the magnet intersects this current at right angles, see fig. 5.3. The resulting Lorentz force contributions are directed upwards and outwards. In this case, vertical components add up to a net vertical force. When the magnet is centred above the coil, horizontal force contributions cancel out due to the axial symmetry.

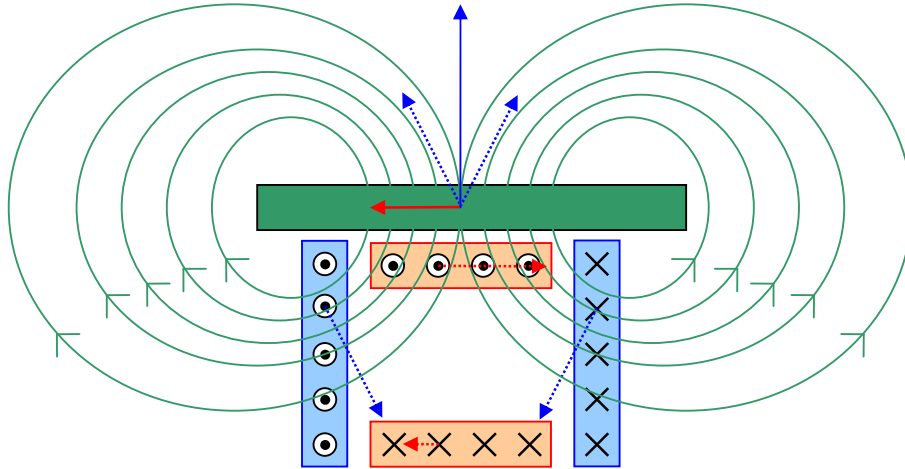


Figure 5.3. Schematic cross-section of the dual Lorentz actuator. The permanent magnet and its field lines are shown schematically in green. The vertical (cylindrical) coil and its associated force components are shown in blue, the horizontal (square) coil and its force components in red.

This actuator has also been characterised by means of extensive FEM modelling in [54], and its dimensions have been optimised for this application. For a given actuator force, there is a trade-off between the dimensions of the coil and the magnets. A smaller magnet reduces the moving mass, but also requires bigger coils. This increases their footprint on the base structure, and consequently the moving part size and mass. Further, in this concept the square coil must fit inside the round one, creating an additional trade-off between their sizes. Increasing the height of the coils has no negative effects: a taller round coil generates more force while in a taller square coil the counter force of the lower section is reduced. However, above a height of 10mm further increasing the height has negligible effect. Therefore the height was fixed at that value.

These trade-offs were explored in order arrive to the final coil and magnet dimensions. FEM simulations were made while varying magnet and coil dimensions and testing for the maximum force value, and for an approximate moving mass. Final dimensions were selected such that the assembly would remain small, and generate forces above the requirement while keeping the moving mass small. A complete optimization was however not made, since many other design parameters play a role in the final performance. The final dimensions are as follows: The vertical coil has an external diameter of 12 mm and a height of 10 mm. The target magnet is 1 mm thick and has a 10 mm diameter. The available vertical force is theoretically about 100 mN, and the horizontal force about 10 mN.

FEM modelling and practical experiments further showed that this actuator has a position-dependent force characteristic (in all directions) due to the non-homogeneous field of the permanent magnet and coils. This is especially apparent for large displacements ($> 100 \mu\text{m}$). Additionally, the actuator exhibits some crosstalk between the horizontal and vertical coils, which leads to parasitic forces. This effect is also stronger as the magnet is displaced further from its central position.

The advantages of this actuator are:

- Provides force in two directions, enables compact fine stage design
- Dimensions smaller than specifications
- Only one controller output needed per degree of freedom
- All actuator parts are situated under the moving disk, nothing gets in the way during assembly operations

The disadvantages of this actuator are:

- Force characteristics are less linear and exhibit crosstalk
- Considerable stray flux from the magnet, needs to be shielded
- Larger and heavier actuator targets, although only three are needed, reducing the required floating disk area

Considering the advantages and disadvantages of both actuator types, the dual Lorentz type has been selected for further development. Especially the more compact stage design and the fact that the top surface of the disk remains entirely free for assembly operations were considered to be strong arguments in favour of the Lorentz actuator.

5.3 Modelling

A COMSOL model of the actuator has been made to investigate its force-displacement characteristic. The model consists of the two coils, the magnet and a steel disk on top of the magnet. The steel disk is used to shorten the flux path, thereby shielding the assembly area from stray flux and increasing flux density in the actuator coils. By moving the magnet and disk relative to the coils, the forces can be calculated in each point in space. A displacement range of $1 \times 1 \times 1$ mm centred about the operating point has been investigated this way, for a total of $7 \times 7 \times 7$ data points. The meshed model consisted of about 15,000 elements, with about 100,000 degrees of freedom. Mesh dependency is less than 1% when the number of elements is halved. A current density of 4 A/mm^2 was assumed in both coils simultaneously. This is a somewhat optimistic value, since the coil fill factor is less than unity, but in practise the maximum current will not flow continuously. Since there is no magnetic saturation occurring as a result of the coil magnetic field, the force-current relation has been assumed linear.

In each point the Lorentz force contribution was integrated over the square and cylindrical coils separately, the reaction force on the target is then the sum of these two. The reaction torques are not the same as the sum of Lorentz torques on the coils because of the distance between the coils CG and the magnet CG. The resulting error is on the order of $100 \text{ }\mu\text{Nm}$. Theoretically a better approach would be to integrate the Maxwell stress tensor over the outer surfaces of the magnet and iron disk, giving the forces and torques on the target directly. However, this is a relatively coarse method in COMSOL, leading to FEM errors that are an order larger than the forces being investigated. Additionally, with the Lorentz approach the forces due to both coils can be found in the same modelling run.

The resulting force-displacement graphs for constant current are shown in fig. 5.4 for the vertical (cylindrical) coil and fig. 5.5 for the horizontal (square) coil. The magnitude of forces and torques is plotted in each graph in seven planes corresponding to the seven vertical (z-)positions from 0.25 to 1.25 mm that have been investigated, against displacement in the x- and y-directions. All displacements in the x- and y- directions are relative to the operating point: magnet centred with respect to the cylindrical coil.

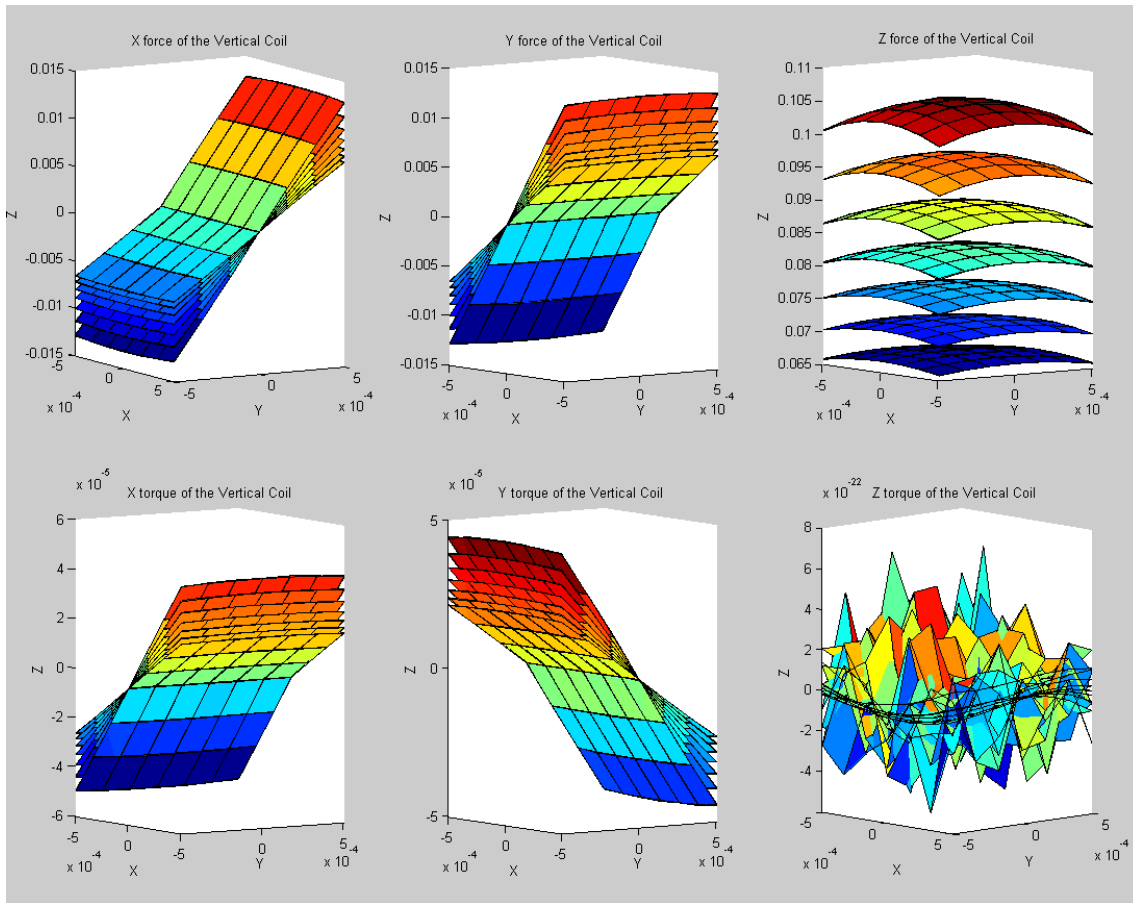


Figure 5.4. Force-displacement characteristic of the vertical coil as calculated by the FEM model. Units on the x- and y-axes are [m], units on the vertical (z-) axis are [N] for the upper row and [Nm] for the lower row.

For the vertical coil, the Z force is the desired force. It is about 90 mN in the operating point and decreases with increasing distance to the target. Force variations resulting from lateral (x and y) displacements are smaller. All other force components in this coil are parasitic. The horizontal parasitic forces (X and Y forces) are zero in the operating point but increase strongly with lateral displacement, due to the inhomogeneous magnetic field. At 500 μm displacement they are on the same order as the horizontal coil force, but this point is never reached in practise, and the vertical coil will generally not be running at full current. This means that the parasitic forces are practically manageable, but not negligible. The coil and magnet should be axially aligned to within about 100 μm to keep them acceptably low.

Horizontal parasitic torques are on the order of 50 μNm and can easily be compensated. They show a similar characteristic as the horizontal parasitic forces. Parasitic torques about the z-axis are negligible (order 10^{-22} , due to FEM errors).

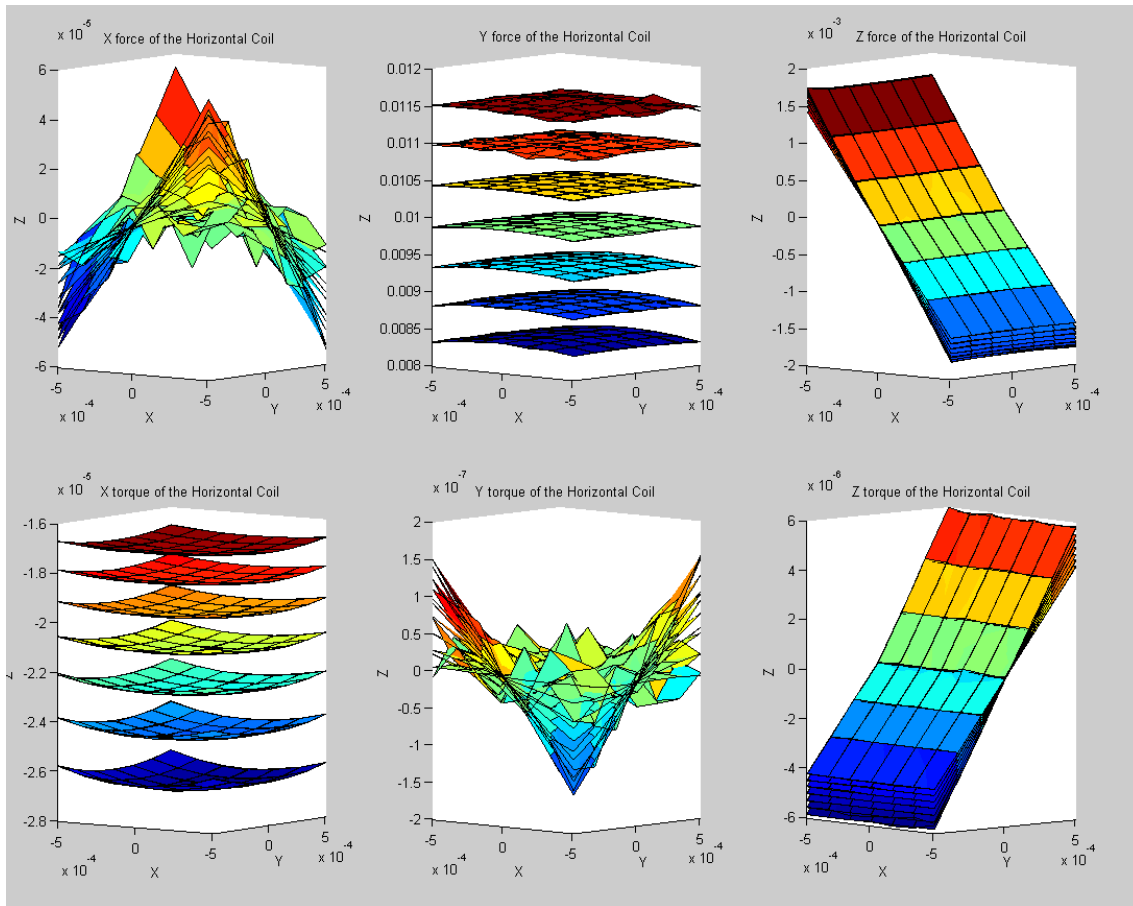


Figure 5.5. Force-displacement characteristic of the horizontal coil as calculated by the FEM model. Units on the x- and y-axes are [m], units on the vertical (z-) axis are [N] for the upper row and [Nm] for the lower row.

For the horizontal coil, the Y force is the desired force. It is about 10 mN in the operating point and is almost constant with lateral displacement. It varies more strongly with vertical (Z) displacements. The parasitic force in X direction is negligible (order 10^{-5} , again mostly due to FEM errors), and the parasitic Z force is on the order of millinewtons. This can easily be compensated by the vertical coil. Parasitic torques about the x- and z-axes are on the same order as the vertical coil parasitic torques, while the parasitic Y torque is negligible.

Using the same model, the influence of tilting the magnet relative to the coils has also been investigated. A tilt angle of $+1^\circ$ and -1° about both x- and y- axes was tested at the outer and middle points of the $1 \times 1 \times 1$ mm displacement space, leading to a total of $2 \times 2 \times 3 \times 3 \times 3$ data points. This gives an indication of the influence of tilting in all extreme displacement cases. The actuator is assumed to be insensitive to rotation of the magnet about the z-axis, since it is cylindrical. Shown in tables 5.1 and 5.2 are the biggest differences between two orientations in the same XYZ position, both absolute and relative to the non-rotated configuration.

Cylindrical coil						
Z = 250 μm	Fx	200 μN 1.5 %	Fy	850 μN 6.5 %	Fz	400 μN 0.4 %
	Tx	18 μNm 30 %	Ty	15 μNm 30 %	Tz	-
Z = 750 μm	Fx	60 μN 0.6 %	Fy	640 μN 7 %	Fz	200 μN 0.3 %
	Tx	12 μNm 30 %	Ty	10 μNm 30 %	Tz	-
Z = 1250 μm	Fx	50 μN 0.8 %	Fy	440 μN 6.5 %	Fz	130 μN 0.2 %
	Tx	8 μNm 30 %	Ty	7 μNm 30 %	Tz	-

Table 5.1. Maximum force and torque differences due to magnet tilting, in absolute and relative figures, shown for the vertical (cylindrical) coil.

Square coil						
Z = 250 μm	Fx	140 μN -	Fy	370 μN 3 %	Fz	850 μN 40 %
	Tx	0.28 μNm 1 %	Ty	0.35 μNm -	Tz	0.67 μNm 11 %
Z = 750 μm	Fx	100 μN -	Fy	200 μN 2 %	Fz	600 μN 30 %
	Tx	0.25 μNm 1 %	Ty	0.40 μNm -	Tz	0.42 μNm 8 %
Z = 1250 μm	Fx	80 μN -	Fy	150 μN 2 %	Fz	440 μN 25 %
	Tx	0.22 μNm 1 %	Ty	0.20 μNm -	Tz	0.20 μNm 5 %

Table 5.2. Maximum force and torque differences due to magnet tilting, in absolute and relative figures, shown for the horizontal (square) coil.

The torque differences can be disregarded safely. The force differences are on the order of fractional mN's. The parasitic forces show the largest relative change, while the (wanted) vertical force of the cylindrical coil varies by only 0.4 %. The most problematic one is probably the (wanted) horizontal force of the square coil, which varies by up to 3%. The relative changes are small enough that they can be neglected, especially when tolerances are considered. However, in absolute figures, force changes of 800 μN or more as the target is rotated from -1° to $+1^\circ$ can interfere with the requirement of a 100 μN force resolution. That said, a lot of the differences observed here are probably on the order of, or smaller than, FEM accuracy.

A test was also made to model crosstalk between actuators. For this test, the model was run with the target displaced by 15 mm, corresponding to the approximate position of a second actuator target in the complete stage. This way, the resultant Lorentz forces found acting on the coils are the crosstalk

forces: the currents in one coil acting on the target of another. They were found to be on the order of 200 – 300 μN at most. These values are also negligible and therefore the assumption of zero crosstalk between coils holds (at least for DC, but at 1 kHz the inductive coupling between coils is very small.)

5.4 Current amplifiers

To drive the coils, current amplifier boards have been designed. The circuit used is a Widlar bidirectional current source [56] built around an OPA551 power opamp. A schematic diagram of this amplifier is shown in fig. 5.6.

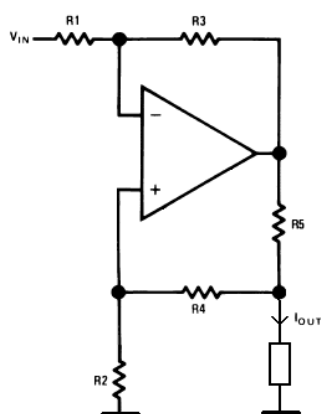


Figure 5.6. Widlar bidirectional current source. The input voltage V_{in} is converted with a fixed gain to a load current I_{out} , independent of voltage variations across the (in this case inductive) load.

This circuit converts an input voltage in the range $-10\text{ V} - +10\text{ V}$ to a constant coil current within a certain range. The wire diameter of the coils is 0.4 mm, so at 4 A/mm^2 the maximum continuous current is 60 mA. To supply transient forces (System BW 100 Hz), the current range should be chosen larger than this. The current range can be selected by means of a jumper to be either $\pm 100\text{ mA}$ or $\pm 150\text{ mA}$.

The opamp has been chosen such that the bandwidth of the amplifier is several orders larger than that of the coil. As long as the amplifier does not saturate (i.e. sufficient output voltage swing), current changes are virtually instantaneous. This means that the electrical time constant of the actuator does not play a role in the system dynamics anymore, and the actuators are current controlled. Tests show that this is indeed the case.

From the overall system modelling (see chapter 6) it was found that the current noise on the actuator coils should be on the order of 75 μA at most, to achieve the desired position noise levels in the stage. This figure has been achieved with this circuit in initial tests. A more detailed description of the current amplifiers is given in Appendix I.

5.5 Final actuator design specifications

- Actuator force
 - Vertical: 80 mN continuous, 160 mN peak
 - Horizontal : 10 mN continuous, 20 mN peak
- Actuator range: $\pm 100\text{ }\mu\text{m}$ around operating point in X, Y and Z
- Electrical properties
 - Vertical coil resistance 25 Ω
 - Horizontal coil resistance 9 Ω
 - Vertical coil self-inductance 2900 μH

- Horizontal coil self-inductance 375 μH
 - Bandwidth
 - Vertical coil: 8 kHz
 - Horizontal coil: 24 kHz
 - Force resolution
 - 100 μN vertical due to amplifier and DAC noise
 - 13 μN horizontal due to amplifier and DAC noise
 - Actual performance may be worse due to parasitic forces, crosstalk and target tilting
 - Force variation due to tilting of the target ($\pm 1^\circ$)
 - Vertical: 0.4 % of maximum continuous force
 - Horizontal: 3% of maximum continuous force
 - Actuator dimensions $\varnothing 12 \times 12$ mm high, including target magnet
 - Actuator target area 80 mm^2 per actuator
- Actuator target mass 0.6 g per actuator

5.6 Recommendations for further improvement

- The actuator characteristic will become less position dependent when the magnet diameter is enlarged. However, this makes the moving part heavier, requiring more force. This is a trade-off in the size of the magnet, which has not been optimised.
- Parasitic horizontal forces can be significantly reduced if the vertical actuator force is reduced. Since most of the actuator force is needed for gravity compensation and not for positioning or part interaction, this could be accomplished by adding a passive gravity compensator (consisting of permanent magnets). This would increase the moving mass and may introduce additional instabilities, but may still be an improvement. This option has not been investigated.
- During the dimensioning of the actuator coils, a continuous vertical force capability of 100 mN was assumed. In later calculations this value was found to be on the high side, 40 mN suffices. Taking this into account when redesigning the actuators can lead to different actuator dimensions. Specifically, if the vertical coil needs to supply a smaller force, it can be made smaller and its parasitic horizontal forces will be reduced.
- More force can be generated with the same coil and magnet dimensions if magnets with a greater remanent flux density are used. The FEM model assumes a remanent flux density of 1.17 T, magnets with 1.4 T are available.
- More force can also be generated with the same coil dimensions if magnet height is increased, e.g. to 1.5 mm. This increases the moving mass, which indicates another trade-off that can be optimised. 1.5 mm magnets have been used in the first prototype of the stage, FEM modelling showed that these magnets will increase the available forces by a factor 1.5.

6 System modelling

A model has been made of the complete system using the SimMechanics package of Simulink. This model includes the mechanical properties of the stage, the electrical and force characteristics of the actuators, a model of the sensors and external disturbance forces (i.e. floor vibrations and assembly interaction forces). This model will be briefly described in this chapter, as well as the aspects of the stage that have been investigated with it. The Simulink diagrams of the model and its subsystems are given in Appendix J. A simplified diagram of the model is shown in fig. 6.1 below.

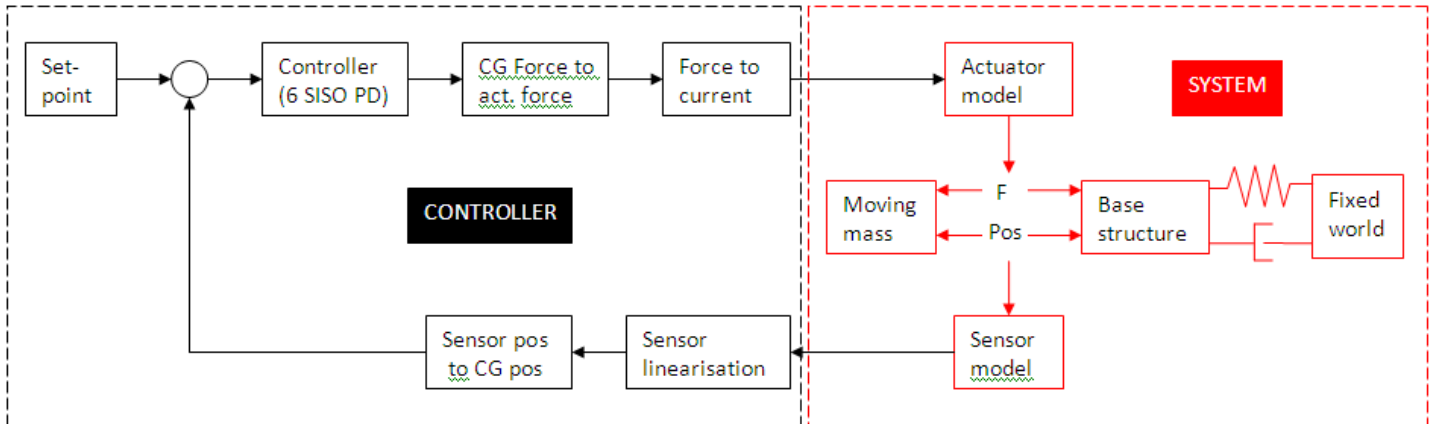


Figure 6.1. Simplified Simulink model of the microslave stage. The controller (left) consists of six SISO PD controllers and coordinate transformation matrices. The system (right) consists of the moving mass, a base structure mass that is flexibly linked to the fixed world, and actuator and sensor models.

6.1 Electro-mechanical model

In the following paragraphs the subsections of the overall electro-mechanical model are described. Refer also to fig. 6.1.

6.1.1 Mechanical model

The mechanical part of the system has been modelled as two rigid masses, namely the floating disk with a mass of 10 g and the base structure. Internal dynamics have not been taken into account, since the first resonance frequencies lie far beyond the system closed loop bandwidth. In the initial versions of the model the base was rigidly linked to the fixed world, while in the final versions a suspension was used. The moving mass has of course six degrees of freedom, and has three actuator ports and six sensor ports, corresponding to the actual placement of actuators and sensors. The absolute position of the moving mass can be measured, to compare it to setpoint and position as observed by the controller.

6.1.2 Actuator model

Each of the three actuators is modelled as a 6-DoF force actuator acting on a 6-DoF zero stiffness joint. The forces, including the parasitic forces, are calculated from the controller output current using the force-displacement characteristics found with the COMSOL model. To do this, a position sensor in the model measures the relative displacement of actuator target and coils, and this is fed back to the actuator characteristic. White noise (band-limited by the model step frequency of 10 kHz) is added to the actuator current to investigate its influence on the position noise. This version of the model is the current controlled actuator (see section 5.4), a second version was also made that

includes the actuator electrical dynamics (voltage control scheme). The actuator models include saturation of the actuator current and voltage.

6.1.3 Sensor model

Each of the six sensors is modelled as a 1-DoF position sensor acting on a 6-DoF zero-stiffness joint between the moving disk and base. The output of this sensor (position) is then translated to an output voltage, including the measured nonlinearity of the actual optical sensor. This is done using a fifth-order polynomial that was fitted to the sensor measurement data. White noise is added to the signal that has the same amplitude as the actual sensors, including position dependency of this amplitude. Also included in the sensor model are output voltage saturation and the 2nd order Butterworth 1 kHz low-pass filter that is part of the readout board.

6.1.4 Floor and suspension model

In later versions of the model the base structure is no longer rigidly linked to the fixed world, but rather attached to it via a spring and damper. To model a vibration isolation table, the mass of the base structure was increased significantly (assuming a rigid link between table mass and base structure) to 10 - 100 kg. The suspension characteristics were set for a low-frequency resonance (1 Hz) with relative damping of 0.5 - 0.7. To model floor vibrations, an acceleration profile was first modelled by filtering white noise through an experimentally determined transfer function until it matched floor vibration measurements (section 3.2.6) . A (infinite stiffness) position actuator was then inserted between the 'lower' end of the suspension spring and fixed world, and controlled with this acceleration signal and the derived velocities and positions.

6.2 Control system

The focus of this thesis is not on the control of the fine stage. Nevertheless, a control system is indispensable for both the model and the actual system, since it is inherently open-loop unstable. The system is a 6-DoF MIMO system with considerable crosstalk present. However, for simplicity during the initial testing, the controller is implemented as six independent SISO controllers. This approach is also taken in the control of existing 6-DoF maglev stages by various research groups (See Appendix A, for example [1],[2],[7]). If this should lead to insufficient performance, a MIMO controller can always be added since the controller is fully digital.

The six controllers used in the model are SISO PD controllers with gain limiting. There is no integrator present in the controller since this may cause high actuator forces, leading to possible damage to parts and tools. The virtual stiffness of the closed loop system should be low to avoid this, and that is not possible at low frequencies with an integrator. The differentiator is necessary to provide damping to the closed loop system and to increase the phase margin. It is tuned so that the maximum phase lead occurs around the 0 dB point of the closed loop. Differentiator gain limiting is provided to reduce the gain at high frequencies (noise). Bode plots of the controller, moving mass and closed-loop system are shown in fig. 6.2. These are linearised transfer functions for one channel (translation) only, and assuming no sensor or actuator dynamics, to give an indication of the control system.

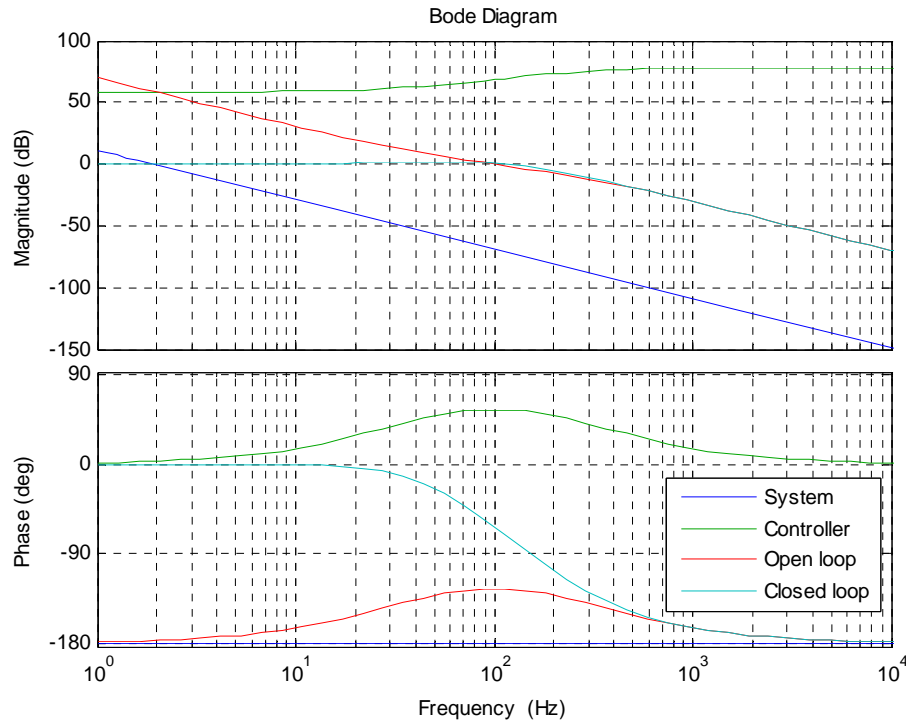


Figure 6.2. Bode plots of the simplified, linearised system model. Closed loop bandwidth is about 100 Hz.

Using a 1-DoF model [57] it was determined that the closed loop bandwidth should be about 100 Hz to provide sufficient floor vibration rejection. The six PD controllers in the model have been tuned to this bandwidth, see also fig. 6.2. Note that the model can be used to investigate step response, but that in practise this will never occur because of the limited bandwidth of user commands (10 – 20 Hz). For this reason, a 20 Hz input low-pass filter has been implemented in the model. The model also has a feedforward block, to investigate control schemes using feedforward control in addition to feedback control. It simply takes the setpoint and multiplies it by the inverse system dynamics, ms², and an adjustable gain factor.

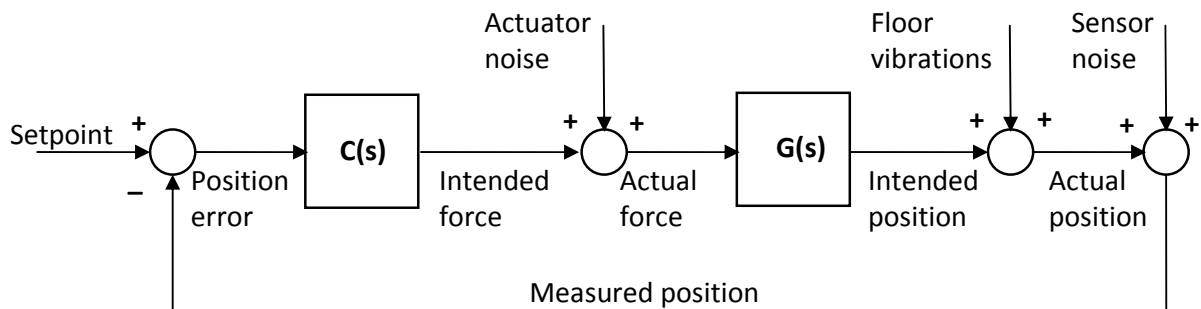


Figure 6.3. Simplified, linearised control loop with noise sources.

The controller is designed for forces and torques acting on the moving part's CG, and for sensor measurements in the same position. The setpoint (Zero reference plus user commands) is also in CG coordinates. Since the actuators and sensors are not situated in the CG, transformation matrices are needed. The measured sensor positions are first translated to CG positions via a coordinate transformation matrix (See appendix D). A second transformation matrix translates the CG forces to

actuator forces, and a force-to-current matrix translates that to actuator currents. The latter matrix is diagonal (parasitic forces are not considered, but the controller treats them as external disturbance forces) and can be made position dependent to account for the position-dependent actuator characteristic. The sensor position signals are linearised using a fifth-order polynomial fitted to the inverse sensor output characteristic. During modelling this was found to significantly reduce steady-state position error.

6.3 Noise

The error budget (section 3.4.1) shows two main sources of noise that are inherent to the system: actuator noise and sensor noise. These are indicated in the simplified control loop diagram of fig. 6.3. The sensor noise components above the system bandwidth of 100 Hz are attenuated by the control loop. The gain from sensor noise to actual position is the system complementary sensitivity function

$\frac{C(s)G(s)}{1+C(s)G(s)}$ which is smaller than unity above 100 Hz, see fig. 6.4. According to the model, the measured sensor noise of 15 – 28 nm_{pp} (1 kHz noise BW) is attenuated by the closed loop system to a position noise of about 6 – 11 nm_{pp}.

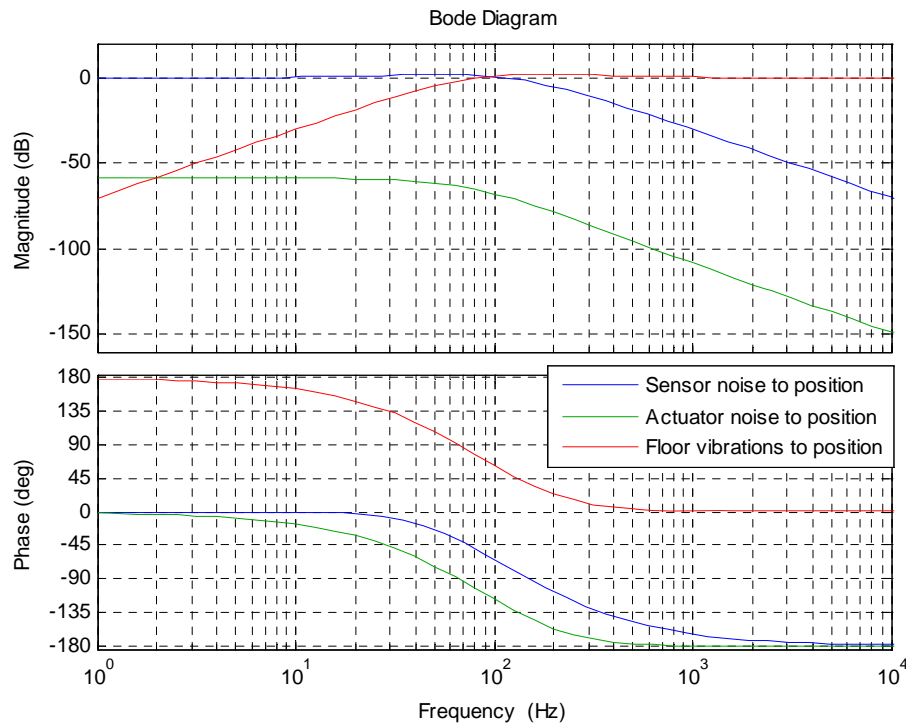


Figure 6.4. Bode plots of transfer functions from noise sources to moving mass position for the simplified system.

Similarly, the gain from actuator noise to actual position is given by $\frac{G(s)}{1+C(s)G(s)}$ which also falls

with increasing frequency above the bandwidth. This means that actuator noise is also attenuated by the control loop, and high frequency content does not show up in the moving mass position. The model shows that a 75 μ A_{pp} noise current (10 kHz noise BW) in the coils causes a position noise of about 10 nm_{pp} in the vertical direction and less than a nm peak-peak in the horizontal directions (due to the factor 10 smaller current-to-force gain of the horizontal coils). The current amplifiers have been designed to stay within this noise limit.

Position noise due to sensors and actuators is lower than initially allowed for in the error design budget (section 3.4.1) because these are filtered by the control loop. Therefore, the microslave stage can cope with somewhat greater floor vibrations, as indicated in the new error budget in fig. 6.5.

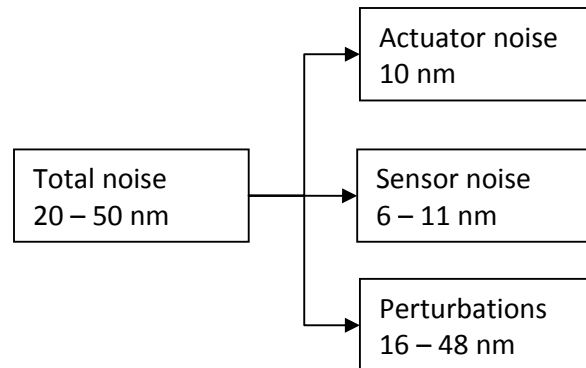


Figure 6.5. Error budget after sensor improvements and modelling phase. The noise figures mentioned are peak-to-peak, for the closed loop system.

6.4 Environment

The third noise source in the error budget is an external source of noise, namely floor vibrations. . The gain from floor vibrations (essentially external disturbances) to actual position is the system sensitivity function $\frac{1}{1+C(s)G(s)}$, see also fig. 6.4. The sensitivity is smaller than unity below the

bandwidth, meaning that only low frequency vibrations are attenuated by the closed loop system. According to preliminary measurements most noise power is present in a narrow frequency range around 10 Hz. At 10 Hz the vibration rejection is 30 dB. The complete system model confirms this value for disturbance rejection. However, there is of course still an upper limit to the vibrations amplitude. With 30 dB rejection and an error budget of 16 – 48 nm the maximum allowable base structure vibration is 0.5 – 1.5 μm_{pp} at 10 Hz. Modelling has shown that a vibration isolation table remains a necessity to achieve this value. A rigid table, even with a heavy top, passes too much of the floor vibration to the microslave stage. Table 6.1 sums up the resulting achievable MIM with and without floor vibrations. If the perturbation rejection can be increased to 40 dB as originally specified, the translational MIM of the microslave stage is within specification even without an isolation table.

Specification	Design target	Achieved, theoretical value	Remarks
Translation MIM	40 – 100 nm	30 nm	Without floor vibration
		50 nm	With vibration isolation table
		240 nm	Without vibration isolation table
Rotation MIM	0.002°	0.00012°	Without floor vibration
		0.0002°	With vibration isolation table
		0.0004°	Without vibration isolation table

Table 6.1. Theoretically achievable MIM, with and without a vibration isolation table.

6.5 Assembly tolerances

The most important aspect that was investigated with the system model is that of assembly tolerances. The coordinate transformation matrices mentioned in section 6.2 assume perfect alignment of sensors and actuators, and any deviation will cause steady state position errors. Furthermore, misalignment of the magnets relative to the actuator coils will cause extra parasitic forces and gain errors, due to the position dependent actuator characteristics.

Using a Monte Carlo inspired method, the model was called from a loop. Every iteration normally distributed random misalignments were added to all sensor and actuator positions, as well as the relative positions of the magnets with respect to the coils and the number of turns of the coils. The misalignments are in all directions, linear and angular, except for the measurement directions of the sensors. These will be equipped with adjustment screws, so any assembly tolerances can be eliminated to within a few μm . The misalignments were defined to lie within three-sigma intervals of 50, 100, 200, 400 and 800 μm , while the corresponding rotations were 0.5, 1, 2, 2 and 2 degrees. Per interval 10 sets were generated, and an extended test of 250 for the 200 μm / 2° interval.

Every set of misalignments generated in this way was tested with step inputs (filtered at 20 Hz) on each DoF individually, in both positive and negative directions. For each setpoint, twelve per set in total, the vector norm and absolute angle of the resulting final position errors were determined. Instability and saturation were also tested for each case, but these never occurred.

The resulting position errors are shown in figures 6.6 and 6.7. In later tests, the influence of pure translational and pure rotational misalignments was also investigated, as well as the influence of misalignments of individual system components.

A final feature that was tested is the position dependent gain (PDG), or inverse actuator characteristic. In a perfectly aligned device, the exact position of all magnets is known, relative to their coils. Therefore it is possible to exactly compensate the position dependent actuator characteristics by multiplying the actuator current by the inverse characteristic. In a practical device however, exact positions are not known because of tolerances on the order of the actuator displacements. This means that the PDG control scheme may deteriorate system performance.

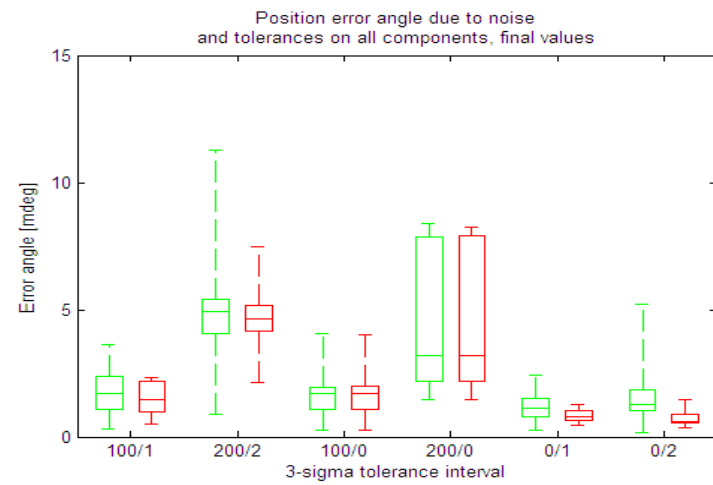
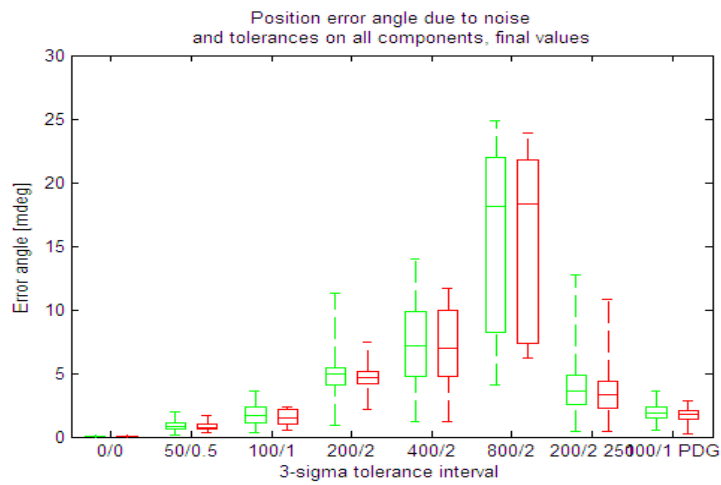
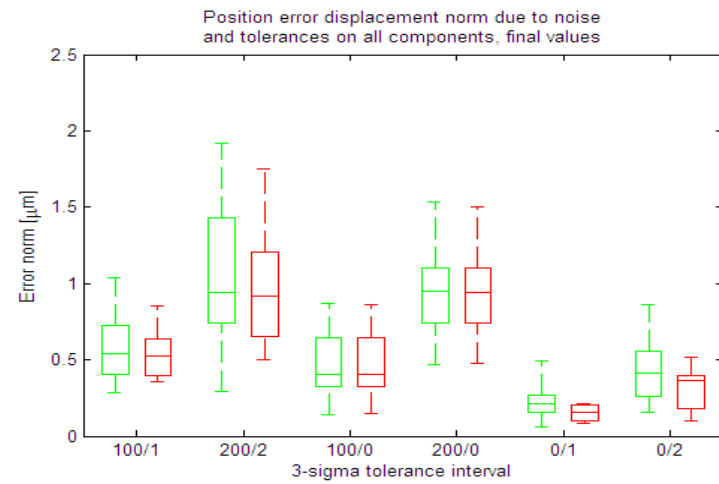
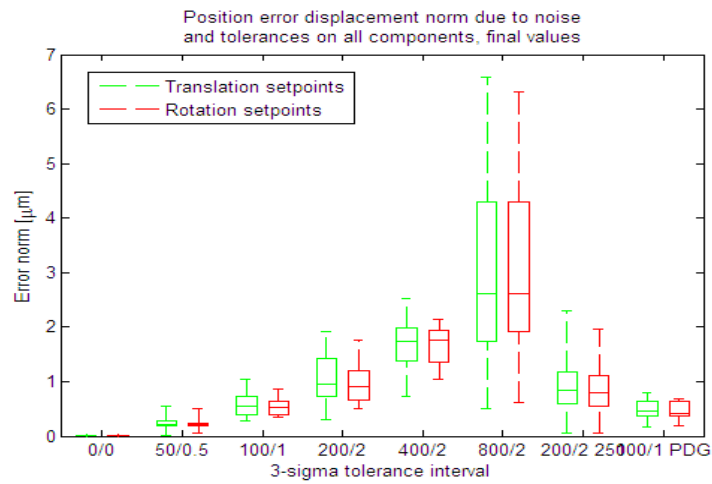


Figure 6.6. Error norm and angle as a result of misalignments on all components, for various tolerance intervals.

In the left-hand side of fig.6.6 the results of the simulations with tolerances on all components are shown. From left to right these are a reference run assuming perfect alignment, five runs with tolerance intervals increasing from $50\ \mu\text{m} / 0.5^\circ$ to $800\ \mu\text{m} / 2^\circ$, an extended run with tolerance interval $200\ \mu\text{m} / 2^\circ$ and a test run with the position dependent gain control scheme.

The simulation run with noise, but without tolerances (labelled 0/0), shows that the noise alone results in final position errors smaller than $8\ \text{nm} / 30\ \mu\text{deg}$. This is negligible with respect to the position errors caused by misalignments and crosstalk, but does limit MIM.

Subsequent simulation runs with increasing tolerances show increasing position errors. The run with a tolerance interval of $200\ \mu\text{m} / 2^\circ$ (labelled 200/2) is probably representative for the actual device. This run yielded position errors of about $2.5\ \mu\text{m} / 12\ \text{mdeg}$. Similar values are also found in the extended run of 250 iterations (labelled 200/2 250, second from the right), showing that a run of 10 iterations gives a good indication of the error order of magnitude.

The rightmost plot (labelled 100/1 PDG) shows position errors with the position dependent gain control scheme enabled, for a tolerance interval of $100\ \mu\text{m} / 1^\circ$. The errors are on the same order of magnitude as with PDG disabled, indicating that this control scheme does not have much effect when there are misalignments.

The right-hand side of fig. 6.6 shows the results of the simulation runs with pure translational and pure angular tolerances only. The leftmost two are repeated box plots of the $100\ \mu\text{m} / 1^\circ$ and $200\ \mu\text{m} / 2^\circ$ simulation runs, for comparison. Then, from left to right, two runs with pure translational tolerances ($100\ \mu\text{m}$ and $200\ \mu\text{m}$ intervals), and two runs with pure angular tolerances (1° and 2° intervals).

Pure translation misalignments cause position errors that are almost as big as combined translational/angular tolerances. Pure rotation misalignments on the other hand, cause position errors that are almost half this value. It is therefore the best strategy to try to minimise the translation misalignments, the angles are less critical.

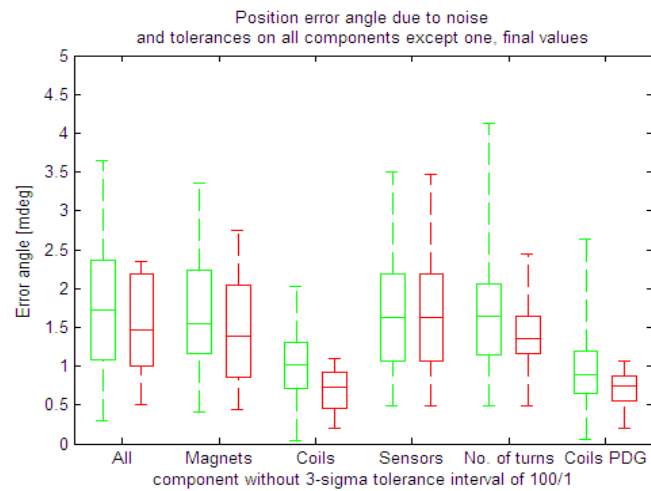
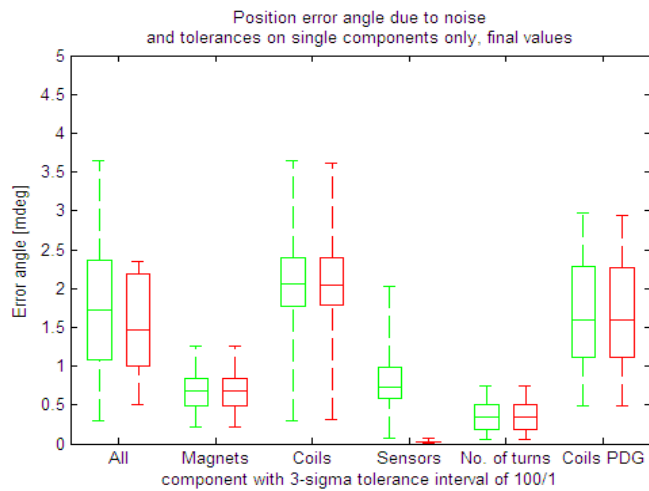
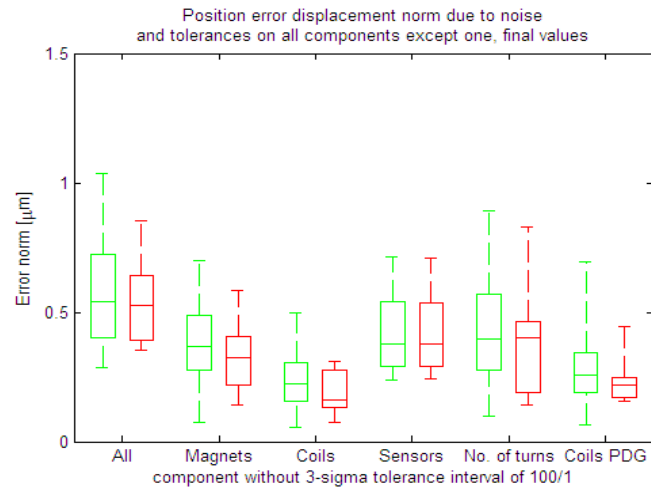
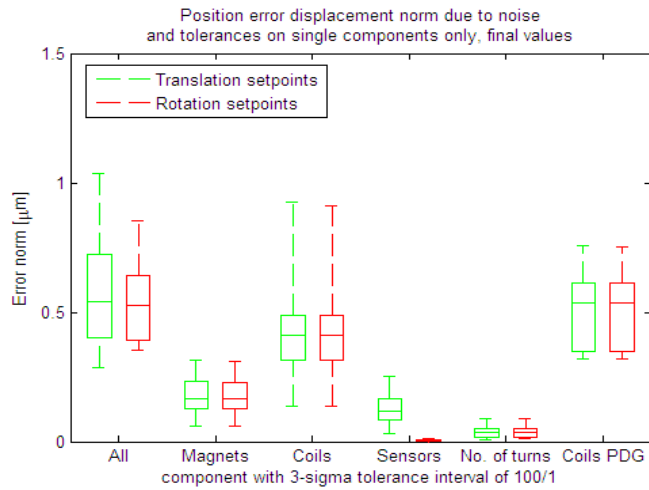


Figure 6.7. Error norm and angle as a result of misalignments on single components (left), and all components but one (right) for a tolerance interval of $100\mu\text{m}$, 1° 3-sigma.

The left-hand side of fig.6.7 shows the results of simulation runs with all components of the stage perfectly aligned except one. The tolerance interval is in all cases $100\ \mu\text{m} / 1^\circ$ three sigma. The leftmost box plot shows the results of the simulation run with tolerances on all components, for reference. Then, from left to right the box plots show results of tolerances on the actuator position only, the relative position of coils and magnets, sensor position only, and number of coil turns. The rightmost plot shows position errors resulting from relative misalignments between coils and magnets only, with the position dependent gain control scheme (labelled 'Coils PDG').

It appears that the relative misalignment between coils and magnets gives the largest contribution to the position error. In fact, when all other components are perfectly aligned, the error is hardly smaller than with tolerances on all components. Enabling position dependent gain reduces this somewhat, but the effect is not strong. Other interesting effects are that sensor misalignments do not cause coupling between rotation motion and position error, and that the number of turns of the coils is not very critical.

The right-hand side of fig.6.7 shows the results of simulation runs with only one component of the stage perfectly aligned, and tolerances on all others. The tolerance interval is in all cases $100\ \mu\text{m} / 1^\circ$ three sigma. The leftmost box plot again shows the results of the simulation run with tolerances on all components, for reference. Then, from left to right the box plots show results of perfect alignment of the actuator position only, the relative position of coils and magnets, sensor position only, and number of coil turns. The rightmost plot shows position errors resulting from perfect alignment between coils and magnets only, with the position dependent gain control scheme. This yields similar results as the previous simulations. A perfect alignment of the coils to the magnets gives the biggest position error reduction. Aligning magnets or sensors better also reduces position error, but the effect is not as strong. Enabling position dependent gain increases the position error somewhat in this case.

Concluding, minimising the misalignments between coils and magnets is the most effective way to reduce the stage position error. The absolute positions of the magnets are not very important, as long as the coils are in exactly the same places. However, this is of course also the hardest to realise, since the coils and magnets are mounted to two completely independent subassemblies (base and disk). Since the position dependent gain scheme shows no strong reduction of position errors at best, and in some cases even increases this error, it will not be used in the controller of the actual stage.

6.6 Recommendations for further modelling

- Include sensor phase delay in the model (estimated to be 2° at 100 Hz, $\frac{1}{4}$ of the filter delay).
- Optimise PD controller parameters. The controllers have been tuned for a 100 Hz bandwidth with an acceptable step response, but have not been optimised.
- Disturbance rejection could be improved. Without a derivative gain in the controller the disturbance rejection is more than 40 dB at 10 Hz. The derivative gain is needed to provide sufficient damping, but there is a trade-off with disturbance rejection that has not been optimised.
- Investigate MIMO controller architecture: The controller matrix is diagonal in all versions of the model so far.
- Investigate feedforward control. This has been included in the model but not extensively tested or optimised.
- Investigate parts assembly interaction forces (waveforms, magnitude) and include these in the model. An option has been provided for this but it has not been used yet.
- Measure vibrations caused by the coarse stage, and include these in the model to determine the position noise caused by these vibrations (Necessary for future control schemes using both stages simultaneously).

7 Mechanical design

The sensor concept has been developed into a detailed mechanical design and corresponding fabrication drawings (see Appendix K for the latter). The design and the considerations leading to it will be described in this chapter. Figure 7.1 gives an overview of the final design of the microslave stage.

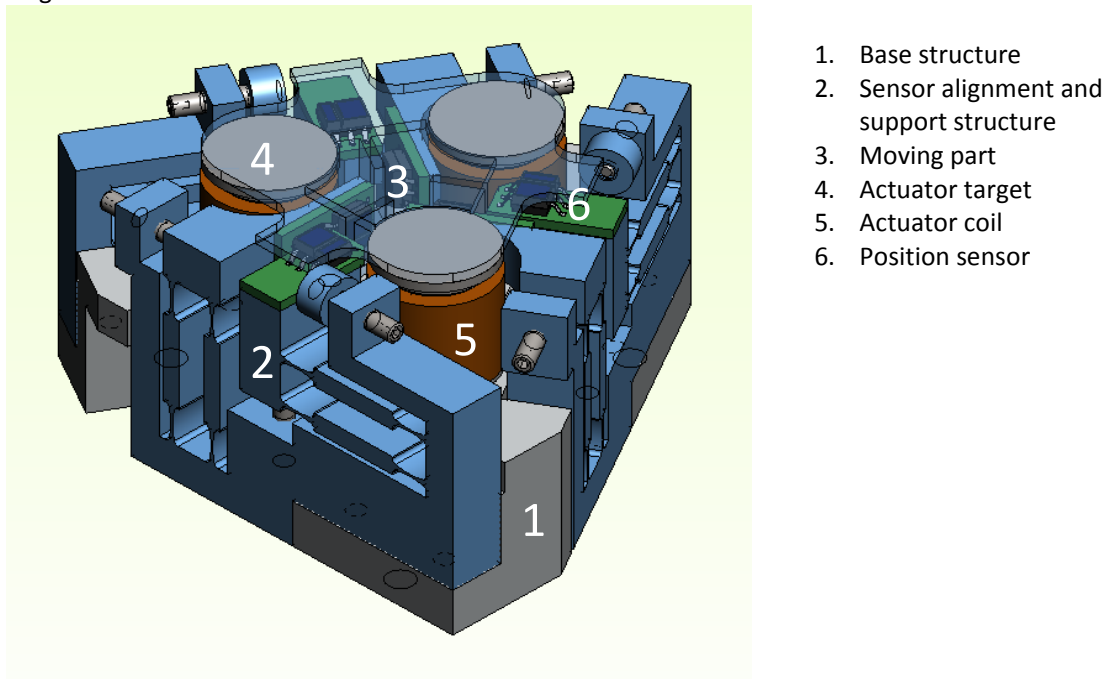


Figure 7.1. Overview of the microslave stage mechanical design.

7.1 Base structure

The base structure, shown in fig. 7.2, holds the three sets of actuator coils. It is a single aluminium part that will be fabricated by means of 5-axis CNC milling. The coil positions are defined by protrusions on the upper face of the part. These protrusions are designed to exactly fit the cylindrical coil internal diameter and the square coil winding height, since these are well-defined coil dimensions. The three coil sets lie on a circle with a 24 mm diameter. Slots and through holes are provided for the connecting wires. These will be soldered to a connection circuit board located in the hollow underside of the base part.

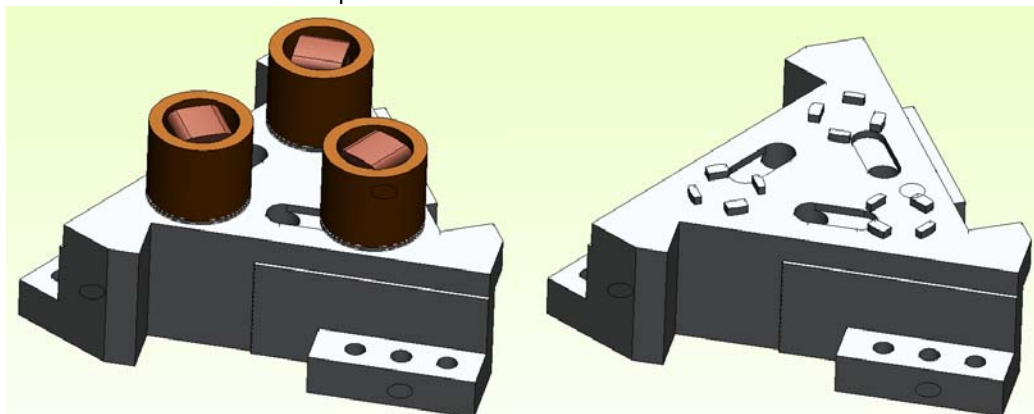


Figure 7.2. Base structure of the microslave stage, shown with actuator coils on the left, and without coils on the right.

The base structure further has three rectangular cut-outs for the sensor support structures, described in the following section. It can be mounted to either an optical table or the coarse positioning stage using adapter brackets and three M3 screws.

7.1.1 Sensor positions

Ideally, the six sensors are all mounted at the same distance from the centre of the moving part. This distance determines the magnitude of rotations around the moving part CG that can be measured with the $\pm 100 \mu\text{m}$ sensor range: $\tan \theta = \frac{\pm 100 \mu\text{m}}{R}$. In order to have a $\pm 1^\circ$ range around all three

axes, the sensors have to be on a circle with a maximum diameter of 5.7 mm. However, due to the physical size of the sensors and space restrictions this is not feasible. In practise, the position of three sensors lie on a circle of about 5 mm radius, and the other three on a larger, concentric circle of about 12 mm radius. This means that not all rotation ranges can be the full $\pm 1^\circ$, and that this specification can not be attained in the current design with this type of sensor.

The most important rotation motion in this design is the one about the vertical axis. This rotation is actively controlled by the user with the master robot, and should have the largest possible range. The rotations about the horizontal axes are only necessary to allow 6-DoF position stability and automatic tilting alignment if needed. The vertical rotation measurement derives from the horizontal sensors, therefore these should be located on the smaller, inner circle. The horizontal rotations, which are measured by the vertical sensors, will then be limited to about $\pm 0.5^\circ$.

7.1.2 Sensor alignment

Since the sensor range is no greater than the specified movement range of the stage, it is important that the sensors are accurately aligned to their targets, i.e. the movement range and measurement range should fully overlap to within a few μm . Because of component and assembly tolerances an alignment mechanism is needed, that can compensate for these tolerances and keep the sensor parallel to its target otherwise. A hole hinge based parallel guide has been designed for this purpose.

According to manufacturer data, the tolerance on the sensor body height is $400 \mu\text{m}$. At least $100 \mu\text{m}$ will be added to this for the glue layer between sensor PCB and support structure, another $100 \mu\text{m}$ for the solder between sensor and PCB, and the manufacturing tolerances on sensor targets and the base structure will add another few $100 \mu\text{m}$. All in all, an adjustment range of 1 mm is required. Because of size limitations of the microsclave stage, the beam length (i.e. distance between two hole hinges) is limited to 14 mm or so. This implies a rather large angular rotation ψ of the hinges of $\arctan\left(\frac{1}{14}\right) \approx 4^\circ$.

This hole hinge design is limited by the allowable bending stress in the bridge between the holes. The material used is high-strength aluminium alloy 7075, which has a yield strength of 470 MPa. According to the design chart in [57] for a maximum bending stress of 400 MPa, a rotation angle $\psi = 4^\circ$ and Young's modulus $E_{Al} = 70 \text{ GPa}$, the ratio between hole diameter D and bridge thickness h should be $\frac{h}{D} \leq 0.0144$. This implies a hinge with a long, slender bridge. The sensor support structure will be fabricated by a combination of CNC milling and wire EDM. The latter manufacturing technique places a lower limit on the bridge thickness of about 0.15 mm. When 0.2 mm is taken as a practical limit, the holes should be 14 mm in diameter.

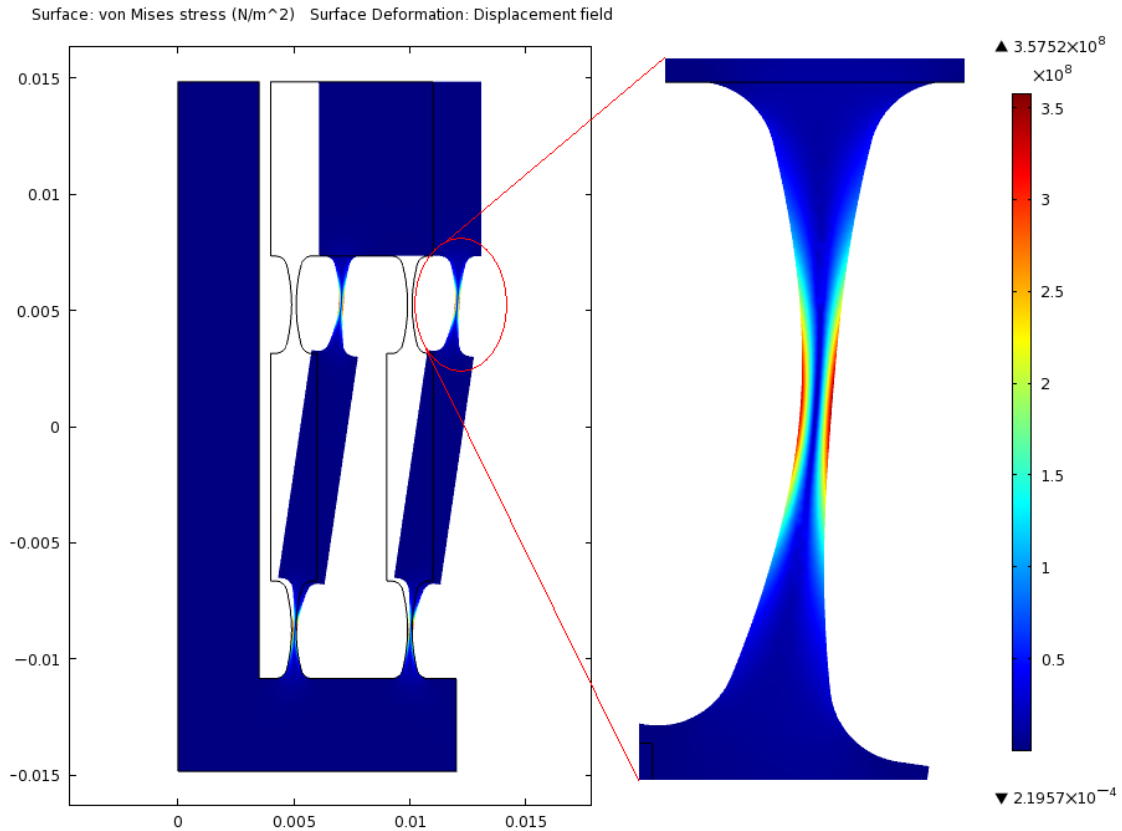


Figure 7.3. FEM analysis of flexure-based parallel guide for sensor alignment. For a deflection of 1 mm the maximum Von Mises stress (358 MPa) stays well below the yield strength of Aluminium Alloy 7075 (470 MPa).

To reduce the required space, the holes will be implemented as partially cylindrical holes. The abovementioned design chart is valid for hole angles $> 60^\circ$. However, the available space required this angle to be reduced to 35° , so the final design is a compromise between a hole hinge and a flexible beam. This means that FEM analysis had to be used to check the stresses occurring in the beams. A deformed shape and Von Mises stress plot of the final design is shown in fig. 7.3. The FEM analysis showed that the maximum bending stress is about 405 MPa, while the maximum Von Mises stress is 358 MPa. This seems to indicate that the design chart gives a good approximation, even for this non-typical case. The 2D FEM model consisted of 27,000 elements, with 115,000 degrees of freedom. The solution showed mesh convergence. A detail of the flexure hinge meshing is shown below in fig. 7.4.

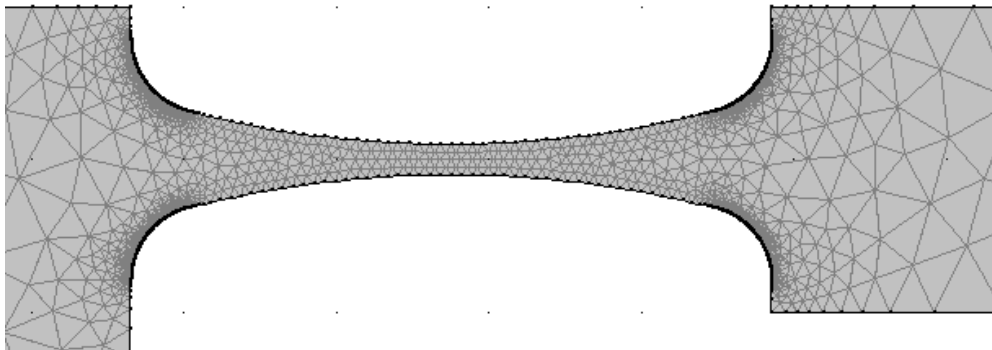
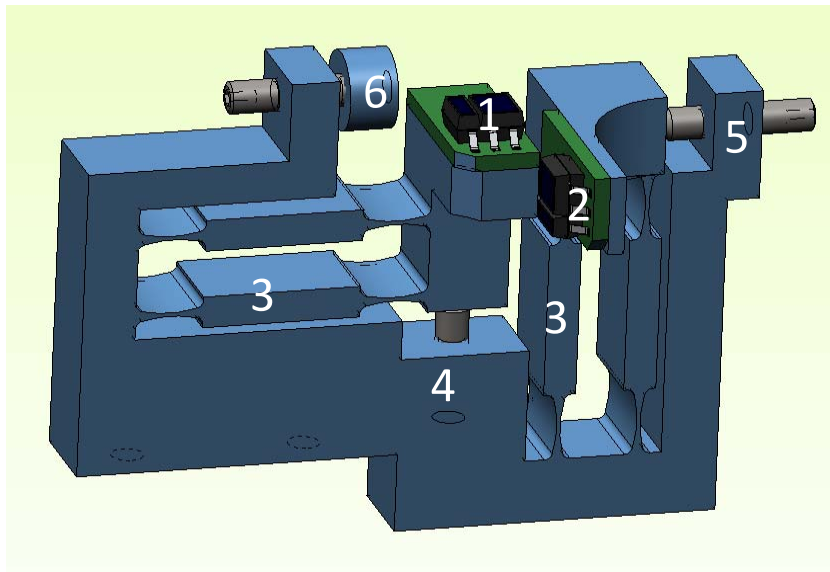


Figure 7.4. Detail of FEM meshing of the 2D model of a flexure hinge, used to compute the mechanical stresses.



1. Vertical position sensor
2. Horizontal position sensor
3. Parallel guide alignment mechanisms
4. Vertical sensor adjustment screw
5. Horizontal sensor adjustment screw
6. Horizontal end stop

Figure 7.5. Sensor support and alignment structure, consisting of two identical parallel guide adjustment mechanisms. The adjustment screw in the upper left corner is an end stop.

Two of these parallel guides are combined into a single block, which holds a vertical and a horizontal sensor, see fig. 7.5. Three of such blocks are needed for the entire stage. Protrusions are added to the moving parts of the parallel guide mechanisms to hold the sensors in the appropriate positions. The sensors are soldered to small circuit boards, which are glued to these protrusions. The sensor adjustment is made by means of an M2 adjustment screw. The thread pitch of these screws is $400\ \mu\text{m}$, so that a displacement of $1.1\ \mu\text{m}$ per degree rotation is obtained. An adjustment resolution of a few μm is then realisable. An adjustable end stop is provided to constrain horizontal motion to the measurable range.

7.2 Moving part

The moving part of the microslave stage contains the actuator magnets, magnetic shielding for these magnets and the optical sensor targets. Its mass should be 10 g at most and preferably less than 7 g. Eigenfrequencies of the moving part should lie far above the overall system bandwidth, in practise the lower limit is about 5 kHz. This prevents internal dynamics of the moving part from negatively affecting the control loop performance.

The final moving part design is shown in fig. 7.6. The structure consists of a single piece of aluminium that has six 'flaps' that serve as horizontal and vertical sensor targets. The vertical targets also function as contact edge for the adjustable end stops. The sensors themselves function as end stops in the other directions. The structural part is manufactured by means of CNC milling of a thick aluminium block. The resulting shape is then cut by wire EDM to obtain a final plate thickness of 1 mm.

Magnetic shielding is provided by three 1 mm thick steel disks. These parts constitute the largest fraction of the moving part mass, together with the magnets.

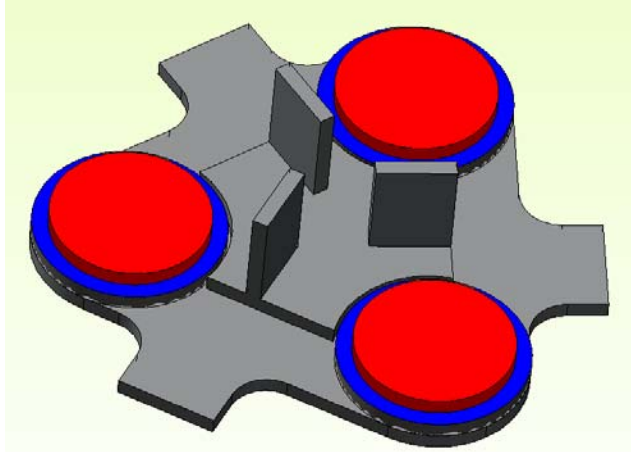


Figure 7.6. Overview of the microslave stage moving part. The aluminium structure is shown in light grey, the magnets in red and the steel shielding disks are shown in blue.

7.2.1 Eigenfrequency analysis

During the design phase of the moving part, the eigenfrequencies have been evaluated using FEM analysis. This was done for every major change in the design, the results of this analysis are given in appendix F. The design started with a 2 mm thick aluminium disk of 36 mm diameter. This disk has a mass of 5.5 g and a first eigenfrequency of 7.9 kHz. The first nine mode shapes and corresponding eigenfrequencies are shown in fig. 7.7. These are all bending modes, i.e. the displacement is out-of-plane (The first in-plane mode shape has a frequency of 64 kHz). The model consisted of 6,600 elements with 34,000 degrees of freedom. The eigenfrequencies varied by less than 1% when 3,400 elements were used instead as a check on mesh convergence.

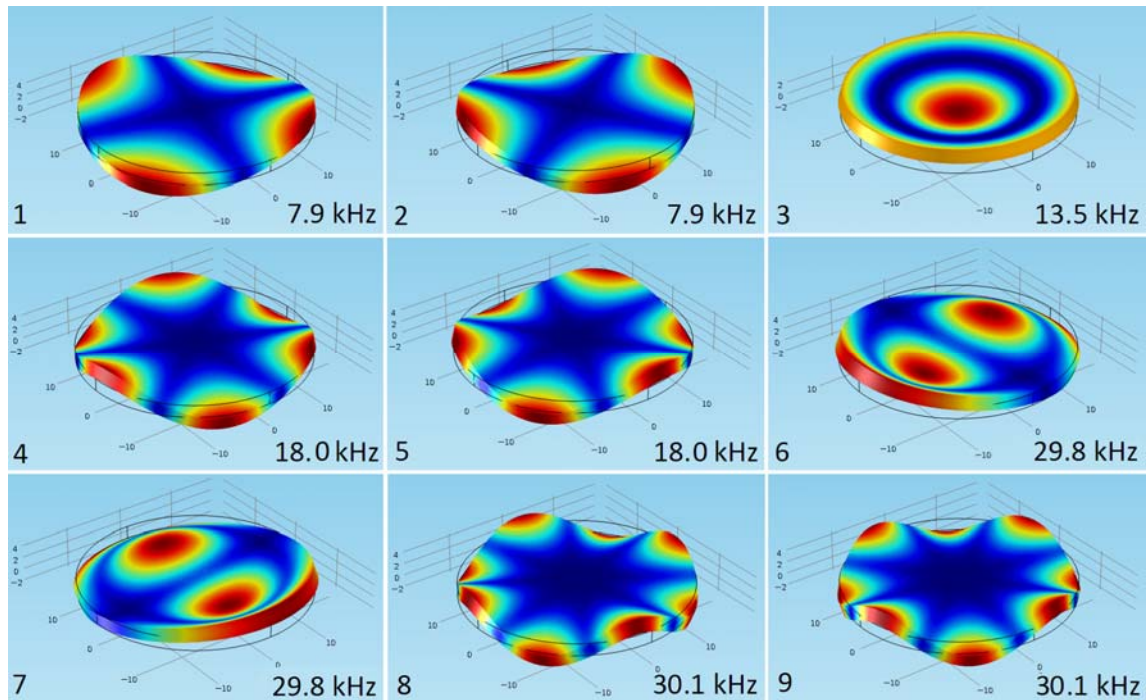


Figure 7.7. First nine mode shapes of a free-floating aluminium disk. Diameter = 36 mm, thickness = 2 mm. Because of the symmetry of the disk all modes (except the 3rd) occur twice.

In the final moving part design, as much material as possible has been removed to reduce the mass. Removing material along the disk's edge will increase stiffness and raise the eigenfrequencies, reducing the thickness will decrease stiffness. To retain some stiffness, the middle part of the disk is left 2mm thick. The total mass of the moving part with magnets and magnetic shielding is 7.5 grams.

Some of the aluminium has been replaced by the steel magnetic shielding. The disk bending stiffness will be reduced significantly because the edges of the magnetic shields are kept loose from the aluminium structure (This is necessary to obtain sufficient alignment space for the magnets). Adding the magnets will further lower the eigenfrequencies, since this increases the mass at specific locations.

The aluminium 'flaps', that are needed as sensor targets, will introduce extra eigenmodes to the moving part. Because of their small sizes, these have high eigenfrequencies. A FEM analysis with zero displacement boundary conditions applied to the appropriate surfaces was made to investigate this. The first (bending) modes of the targets alone have frequencies of about 22 kHz for the vertical sensor targets and 24 kHz for the horizontal targets.

The first nine mode shapes of the free floating moving part and the corresponding eigenfrequencies are shown in fig. 7.8. The model consisted of 6,200 elements with 33,000 degrees of freedom. The eigenfrequencies varied by less than 1% when 3,300 elements were used instead as a check on mesh convergence.

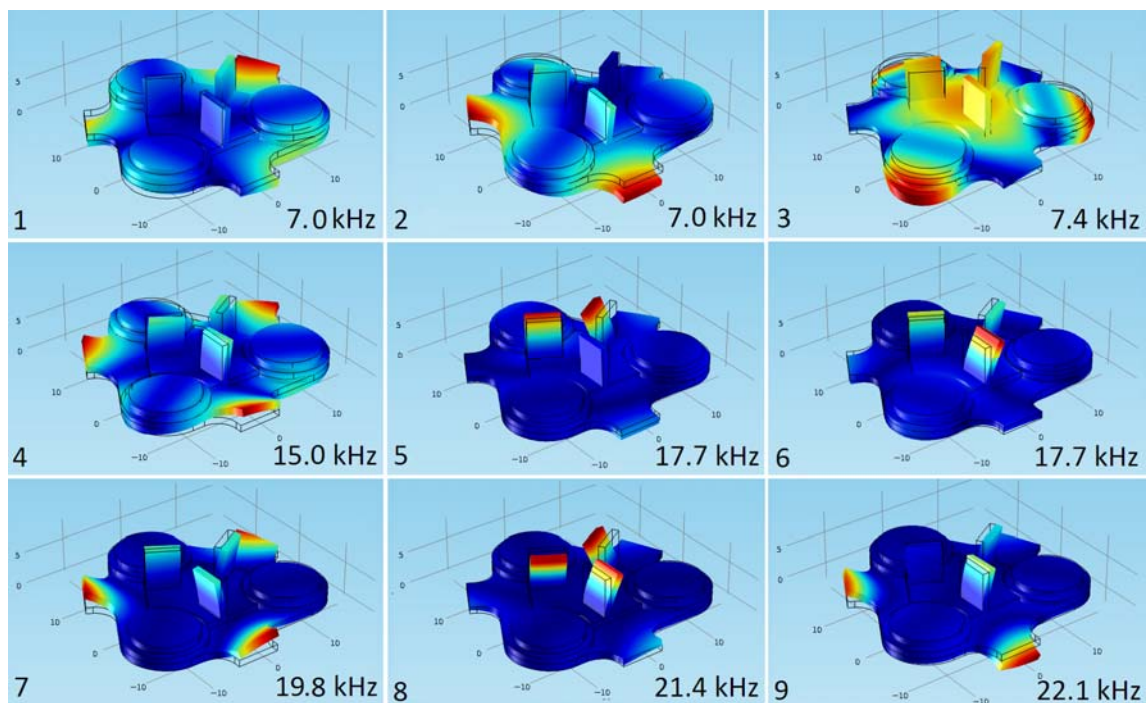


Figure 7.8. First nine mode shapes of the free-floating moving part, as designed for the microslave stage.

The first two mode shapes are very similar to the first two of the disk, with the same four-fold symmetry and only slightly lower eigenfrequency. For these modes the abovementioned effects largely cancel out. The third mode is also similar, but the eigenfrequency is half that of the disk's 3rd eigenfrequency. This is a result of the added mass of the magnets and reduced stiffness between the magnet/shield masses and central mass.

Modes 5 and 6 are similar to modes 6 and 7 of the disk, but the frequency is lower and the displacement of the disk is amplified at the ends of the horizontal sensor targets. Modes 4 and 7

show the same six-fold symmetry as the disk modes 4 and 5. Modes 8 and 9 are mainly bending modes of the sensor targets.

The mode shapes show that displacement is largest in the sensor targets. This will however not affect the system performance since:

- The lowest eigenfrequency is 7 kHz, and lies far outside the closed loop bandwidth (100 Hz) and sensor filter bandwidth (1 kHz). At 7 kHz the amplitude is so small that phase shift and resonance effects are negligible.
- The system bandwidth of 100 Hz ensures that the actuators can not excite the moving part's structural modes, only in the event of collision can this occur.

7.3 Assembly

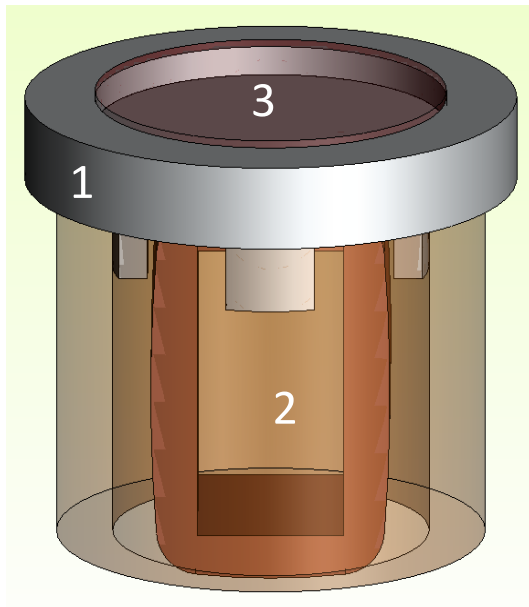
The assembly procedure of the microslave stage is in the following order:

- Base structure
 - The three sets of coils are glued to the base structure, using the protrusions on its surface to define the coil positions. Non-conductive foil is wrapped around the inner, square coil to centre it within the cylindrical coil. The coil wires are led through the wire slots to the underside of the base.
 - A circuit board is glued to the underside and connecting cables are soldered to it to make contact with the coils.
- Moving part
 - The magnets are glued to the steel disks that serve as magnetic shielding. They should be centred to each other.
 - Alignment tools are used to align the positions of the magnet/ steel subassemblies to the coil positions. Then, the magnet/steel subassemblies are glued to the aluminium structure of the moving part.
- Sensor support structure
 - The sensors are soldered to the sensor PCBs, keeping them as much aligned as possible.
 - The sensor boards are glued to the appropriate surfaces of the alignment mechanisms and connecting cables are soldered to them.
 - The entire sensor subassembly is mounted to the base structure with 2 M2 screws.

7.3.1 Alignment tool

Modelling of the effect of assembly tolerances (section 6.5) showed that the *relative* misalignment between magnets and coils has the biggest impact on position error and on force magnitude. The position of the actuators is not so critical, as long as coils and magnets lie directly above each other (when the stage is at zero position). To reduce this misalignment, an alignment tool has been designed, shown in fig. 7.9.

The alignment tool has a chamber that is made to fit the outer diameter of the actuator magnet. On the other side four protrusions are made that fit in the inner diameter of the actuator cylindrical coil. The cylindrical outer surface of these protrusions and the chamber can be made in the same operation on a lathe, thus ensuring concentricity of these features. When three alignment tools are used in this manner during gluing of the magnets to the moving part structure, the relative position misalignment of coils and magnets will be reduced.



1. Alignment tool
2. Actuator coils
3. Actuator magnet

Figure 7.9. Alignment tool for actuator assembly and sensor alignment. The actuator tool is shown inserted in the actuator coils, holding the permanent magnet during assembly of the moving part.

7.3.2 Sensor calibration and alignment

To calibrate and align the sensors, the following procedure should be followed:

- The readout electronics of the six sensors is calibrated by mounting each sensor in turn in a setup with reference sensor like the one used for the sensor tests described in chapter 4. The amplifier gain and zero are adjusted such that the output sensitivity is $100 \text{ mV}/\mu\text{m}$, and the 0 V point lies in the middle of the linear part of the sensor characteristic.
- When the stage is assembled, $500 \mu\text{m}$ thick shims or foil is inserted between the coils and magnets and the moving part is pressed to the base structure. The vertical sensor targets are now in the operating point of the stage. The three vertical sensors can then be aligned using the set screws of their flexure mechanisms, until the outputs read 0 V.
- The foil is removed and the alignment tools are again inserted between coils and magnets. The horizontal sensor targets are now in the operating point of the stage, and the horizontal sensors can be aligned in the same way.

7.4 Recommendations for further improvement

- Alignment of the sensors in directions other than their measurement direction is not very accurate, because of the relatively large manufacturing tolerances of the sensor PCB and soldering process. Although modelling showed that this is not a serious issue, it will result in position errors. An alignment procedure or tool should be developed to reduce the sensor misalignments.
- In future versions of the stage, sensor wire connections should be redesigned. The sensor connecting wires are rather stiff, and will transmit vibration to the sensor alignment mechanisms. A possible solution is the use of flexible printed circuits, that replace the sensor PCB and the wires leading to it.
- The possibilities of simplifying the geometry of base structure and sensor alignment structure should be investigated. This will yield a design that is easier and more economical to manufacture, especially if the microslave stage has to be taken into production.
- A looser fit has to be specified on the components that should fit the inside diameter of the cylindrical coil (Base structure and alignment tool). These were found to fit rather tightly, causing possible damage to the coil wires.

8 Conclusion

Based on existing maglev technology and a novel Lorentz actuator design, a miniaturised 6-DoF positioning stage has been designed. Modelling of the stage showed that it is possible to build a stage with the required small sizes and payload. Table 8.1 summarises the main specifications of the microslave stage and its components, both the design and achieved values. Most 'achieved' values are still only theoretical, i.e. modelling results. This is due to the fact that the microslave stage is still in the manufacturing and testing phase. All electronic components have been assembled, and all mechanical components have been fabricated. The stage is fully assembled and first tests have been performed (open-loop). The moving part can be levitated and forces and torques can be applied in all directions. Closed-loop tests are currently being carried out.

Specification	Design target	Achieved, theoretical value	Achieved, measured value	Remarks
Translation range	200 x 200 x 200 μm	200 x 200 x 200 μm	-	Smaller range when tilted
Translation MIM	40 – 100 nm	30 nm	-	Without floor vibration
		50 nm	-	With vibration isolation table
		240 nm	-	Without isolation table
Rotation range	$\pm 1^\circ$, three axes	$\pm 1^\circ$, vertical $\pm 0.5^\circ$, horizontal	-	Not simultaneous
Rotation MIM	0.002°	0.00012°	-	Without floor vibration
		0.0002°	-	With vibration isolation table
		0.0004°	-	Without isolation table
Translation velocity	3 mm/s	40 mm/s vertical 12 mm/s horizontal	-	100 μm step response
Rotation velocity	35 °/s	60 °/s vertical 160 °/s horizontal	-	0.1° step response
Force range	10 mN	10 mN	-	Interaction force
Force resolution	100 μN	100 μN vertical 13 μN horizontal	-	amplifier and DAC noise only
Payload	1 g	>3 g	-	
Perturbation rejection	40 dB at 10 Hz	30 dB at 10 Hz	-	
Overall size	10 x 10 x 10 cm	-	6 x 6 x 4 cm	
Overall mass	500 g	-	<100 g	
Moving mass	7 g	-	7.5 g	

Specification	Design target	Achieved, theoretical value	Achieved, measured value	Remarks
Moving part resonance frequency	>5 kHz	7 kHz	-	
Sensor range	>200 μm	-	200 μm	
Sensor noise	10 – 25 nm pp	-	15 – 28 nm pp	
Actuator force	>40 mN peak vertical >20 mN peak horizontal	160 mN peak vertical 20 mN peak horizontal	-	

Table 8.1. Overview of target and final specifications of the microslave stage and its components

8.1 Results

- A requirements and specifications list has been set up for a miniature 6-DoF maglev positioning stage. The specifications are targeted towards application of the stage in a haptic micromanipulation setup, and an affordable solution. The stage will be used both as a fine positioner and as a variable stiffness force sensor in haptic micromanipulation.
- Existing optical sensors have been investigated, and improved readout electronics have been designed, built and tested. With the improved circuitry, the position noise of a reflective position sensor has been reduced from 50 – 100 nm_{pp} to 15 – 28 nm_{pp}. As a result, the reflective sensor can be applied as position sensor in the miniature maglev stage. For the readout electronics a three-channel board has been designed, that can also be used in other applications and with other sensor types.
- Miniature electromagnetic actuators have been investigated. FEM models have been made of a reluctance actuator and a novel two-coil Lorentz actuator. The Lorentz actuator was found most suitable; it has been further investigated to find its force characteristics. Within the given size and mass limitations, the actuator can generate sufficient forces for application in the maglev stage. Nonlinearities and parasitic forces in the actuators are not negligible in this design, but their effects are manageable. Current amplifiers have been designed and tested for these actuators. A three-channel amplifier board has been designed, that can also be used in other applications and with other miniature electromagnetic actuators.
- A detailed Simulink model of the stage, its sensors, actuators and control system has been made. This model was used to investigate various aspects such as position noise, perturbation rejection, the effect of actuator nonlinearities and crosstalk, and assembly and manufacturing tolerances. The stage can be built with the assembly tolerances of standard manufacturing technology. Perturbation rejection is on the low side, but MIM specifications can be achieved when a vibration isolation table is used.
- A complete mechanical design of the stage has been made. The components have been fabricated and the stage has been fully assembled. The stage is currently in the test phase, levitation has been achieved. The mechanical design meets the mass and size specifications, and the resonance frequencies of the moving part are sufficiently high.

8.2 Recommendations

- The optical sensor linear range is the minimum possible range, namely 200 μm . This is a property of the sensor type. As a consequence, the alignment of the position sensors is critical, and the achievable rotations are smaller when the moving part is not in the centre of its translation range. A sensor with a larger linear range would improve these points significantly, and would also allow horizontal rotations of more than $\pm 0.5^\circ$. The 'far' range of the optical sensors could be used since it is longer, but it is far more nonlinear.
- The Lorentz actuator is theoretically capable of generating far more vertical force than needed. This allows a larger vertical velocity and payload, but at the expense of parasitic forces and force resolution. The actuator geometry could be redesigned for lower vertical forces, also making the actuator smaller.
- The controllers need to be optimised, or more advanced control architectures need to be considered, to increase the perturbation rejection. At the moment it is 10 dB too low, resulting in greater sensitivity to floor vibrations and the need for a vibration isolation table. It is therefore also not yet possible to operate the coarse and fine stage simultaneously.
- The possibilities of simplifying the geometry of the stage should be investigated. This will yield a design that is easier and more economical to manufacture, especially if the microslave stage has to be taken into series production.

References

1. Gu, J., W.-j. Kim, and S. Verma, *Nano scale Motion Control With a Compact Minimum-Actuator Magnetic Levitator*. Journal of Dynamic Systems, Measurement, and Control 2005. **127**: p. 433-442.
2. Kim, W.-j., S. Verma, and H. Shakir, *Design and precision construction of novel magnetic-levitation-based multi-axis nano scale positioning systems*. Precision Engineering 2007. **31**: p. 337-350.
3. Verma, S., H. Shakir, and W.-J. Kim, *Novel Electromagnetic Actuation Scheme for Multiaxis Nanopositioning*. IEEE TRANSACTIONS ON MAGNETICS, 2006. **42**(8): p. 2052-2062.
4. Yu, H., *Design and control of a compact 6-degree-of-freedom precision positioner with linux-based real-time control*. 2009, Texas A&M University.
5. Jansen, J.W., *Magnetically levitated planar actuator with moving magnets: Electromechanical analysis and design*. 2007, TU Eindhoven: Eindhoven.
6. van Lierop, C.M.M., *Magnetically levitated planar actuator with moving magnets: Dynamics, commutation and control design*. 2008, TU Eindhoven: Eindhoven.
7. Lai, Y.-C. and J.-Y. Yen, *Design of a novel 6-DOF planar maglev system*. Journal of Magnetism and Magnetic Materials, 2006. **304**: p. e386-e390.
8. Li, D., *Modelling and Control of a High Precision 6-DOF Maglev Positioning Stage With Large Range of Travel*. 2008, Florida Institute of Technology.
9. Nielsen, C., C. Fulford, and M. Maggiore, *Path Following Using Transverse Feedback Linearization: Application to a Maglev Positioning System*. Automatica, 2010.
10. Yu, H. and W.-J. Kim, *Controller design and implementation of six-degree-of freedom magnetically levitated positioning system with high precision*. J. Systems and Control Engineering, 2008. **222**: p. 745-756.
11. Chen, M.-Y. and H.-W. Tzeng, *Implementation of a novel large moving range submicrometer positioner*. Mechatronics, 2009. **19**: p. 1143-1151.
12. Holmes, M., R. Hocken, and D. Trumper, *The long-range scanning stage: a novel platform for scanned-probe microscopy*. Journal of the International Societies for Precision Engineering and Nanotechnology, 2000. **24**: p. 191-209.
13. Cuff, D.P., *Electromagnetic Nanopositioner*. 2006, MIT.
14. Li, Y. and Q. Xu, *Development and Assessment of a Novel Decoupled XY Parallel Micropositioning Platform*. IEEE/ASME TRANSACTIONS ON MECHATRONICS, 2010. **15**(1): p. 125-135.
15. Kang, D., et al., *Optimal design of high precision XY-scanner with nanometer-level resolution and millimeter-level working range*. Mechatronics, 2009. **19**: p. 562-570.
16. Ozturk, O., *Multi-Scale Alignment And Positioning System II*. 2008, University of North Carolina.
17. Dejima, S., et al., *Precision positioning of a five degree-of-freedom planar motion stage*. Mechatronics, 2005. **15**: p. 969-987.
18. Lin, K.-H. and Y.-H. Hu. *The Design, Analysis and Fabrication of a Six-Axis Micropositioning Stage*. in *International MultiConference of Engineers and Computer* 2008.
19. Li, D. and H. Gutierrez, *Precise Motion Control of a Hybrid Magnetic Suspension Actuator with Large Travel*. Industrial Electronics, 2008.
20. Probst, M., et al., *A Microassembly System for the Flexible Assembly of Hybrid robotic Mems Devices*. International Journal of Optomechatronics, 2009. **3**(2): p. 69-90.
21. Sébastien, P., C. Alain, and M. Yves. *PocketDelta : a miniature robot for microassembly*. in *5th International Workshop on MicroFactories (IWMF'06)*. 2006.
22. Hollis, R.L., et al. *Vision guided pick and place in a minifactory environment*. in *5th International Workshop on MicroFactories (IWMF'06)*. 2006.
23. Zhou, Q., et al., *Microassembly system with controlled environment*. Journal of

- Micromechatronics, 2002. **2**: p. 227-248.
24. Bilen, H. and M. Unel, *Micromanipulation Using a Microassembly Workstation with Vision and Force Sensing*, in *Advanced Intelligent Computing Theories and Applications With Aspects of Theoretical and Methodological Issues*. 2008, Springer. p. 1164-1172.
 25. Scientifica. *Manipulators*. 2011; Available from: <http://www.scientifica.uk.com/products/manipulators>.
 26. Warner Instruments. *Ultraprecise Motorized Micromanipulator*. 2011; Available from: http://www.warneronline.com/product_info.cfm?id=627.
 27. Zyvex. *Nanotechnology at Zyvex*. 2011; Available from: <http://www.zyvex.com/>.
 28. Klocke Nanotechnik. *Nanomotor*. 2011; Available from: <http://nanomotor.de/>.
 29. Kim, B., et al., *A flexible microassembly system based on hybrid manipulation scheme for manufacturing photonics components*. *The International Journal of Advanced Manufacturing Technology*, 2006. **28**(3): p. 379-386.
 30. Christiansson, G.A.V. and F.C.T.v.d. Helm, *The Low-Stiffness Teleoperator Slave -- a Trade-off between Stability and Performance*. *The International Journal of Robotics Research*, 2007. **26**: p. 287-299.
 31. Xie, H., W. Rong, and L. Sun, *A Flexible Experimental System for Complex Microassembly under Microscale Force and Vision-Based Control* *International Journal of Optomechatronics*, 2007. **1**(1): p. 81-102.
 32. Lambert, P., et al., *A case study of surface tension gripping: the watch bearing* *Journal of Micromechanics and Microengineering*, 2006. **16**(7): p. 1267-1276.
 33. Clévy, C., et al., *Design, Fabrication and Characterization of a Flexible System Based on Thermal Glue for in Air and in SEM Microassembly* *Precision Assembly Technologies for Mini and Micro Products* 2006. **198**(21-31).
 34. Chollet, S.K., et al. *A Flexible Microassembly Cell for Small and Medium Sized Batches*. in *33rd ISR (International Symposium on Robotics)*. 2002.
 35. Chia, L.K. and D.H. Jing, *Joint design and fabrication for mechanical elastic self-deformation micro-assembly technology*. *Materials Science Forum*, 2006. **505-507**: p. 829-834.
 36. Jing, D.H. and L.K. Chia, *Pin-plate micro assembly by integrating micro-EDM and Nd-YAG laser*. *International Journal of Machine Tools & Manufacture*, 2002. **42**: p. 1455-1464.
 37. Jones, J.F., D.M. Kozlowski, and J.C. Trinkle, *Micro Scale Force Fit Insertion*. *Journal of Micromechatronics*, 2002. **2**(3-4): p. 185-200.
 38. Kroemer, K.H.E., H.B. Kroemer, and K.E. Kroemer-Elbert, *Ergonomics: How to design for ease and efficiency* 1994, Prentice Hall.
 39. Brooks, T.L. *Telerobotic response requirements*. in *IEEE International Conference on Systems, Man and Cybernetics*. 1990.
 40. Tan, H.Z., et al., *Human factors for the design of force-reflecting haptic interfaces*. *Dynamic Systems and Control*, 1994. **55**(1).
 41. Shimoga, K.B. *A survey of perceptual feedback issues in dexterous telemanipulation. II. Finger touch feedback*. in *Virtual Reality Annual International Symposium*. 1993.
 42. Newport. *Motion Basics and Standards*. 2011; Available from: <http://www.newport.com/Motion-Basics-and-Standards/140230/1033/catalog.aspx>.
 43. Estevez, P. and H. Langen, *Internal report: Requirements*. 2010.
 44. Schweitzer, G. and E.H. Maslen, eds. *Magnetic Bearings: Theory, Design, and Application to Rotating Machinery*. 2009, Springer.
 45. Jabben, L. and D. Laro, *Internal report: Floor vibration measurements*. 2010.
 46. Estevez, P., *Internal report: Maglev Concepts*. 2010.
 47. IBS Precision Engineering, *Quotation for 6-DoF Capacitive Sensor System*. 2010.
 48. Rij, J.v., et al. *Planar Flat Product Transport Using Viscous Traction*. in *International Joint Tribology Conference* 2008.
 49. Boshuisen, R., *Smart Air Bearing With Optical Sensor*. 2009.
 50. de Boer, T., *Design and Testing of a Haptic Microgripper for Microassembly Applications*, in

- PME*. 2010, TU Delft: Delft.
51. ROHM, *Datasheet: RPI-122 Photointerrupter*. 2009.
 52. Linear Technology, *Datasheet: LT1962 Micropower regulator IC*. 2000.
 53. Texas Instruments, *Analysis of the Sallen-Key Architecture*. 2002.
 54. Estevez, P. and A. Mulder, *Internal report: FEM characterisation of 2-DoF Lorentz actuator*. 2011.
 55. Widlar, R.J., *IC Op Amp Beats FETs on Input Current*. National Semiconductor Application Note, 1969. **29**.
 56. Koster, M.P., *Design Principles for Accurate Motion and Positioning*. 1996.
 57. Estevez, P., *Internal report: Bandwidth Estimation for Perturbation Rejection*. 2010.

List of abbreviations

A/D	Analog / Digital
ADC	Analog-to-Digital Converter
BW	Bandwidth
CAD	Computer Aided Design
CCS	Constant Current Source
CG	Centre of Gravity
CNC	Computer Numerical Control
cRIO	Compact Reconfigurable Input/Output
D/A	Digital / Analog
DAC	Digital-to-Analog Converter
DAQ	Data Acquisition
DC	Direct Current (Zero Hz)
DoF	Degree of Freedom
DRIE	Deep Reactive Ion Etching
EDM	Electrical Discharge Machining
FEM	Finite Element Method
HF	High Frequent / High Frequency
IC	Integrated Circuit
IR	Infrared
LED	Light Emitting Diode
maglev	Magnetic levitation / magnetically levitated
MEMS	Micro Electro-Mechanical System
MIM	Minimum Incremental Motion
MIMO	Multiple Input, Multiple Output
NdFeB	Neodymium-Iron-Boron alloy
NI	National Instruments
PCB	Printed Circuit Board
PD	Proportional Differential
PDG	Position Dependent Gain
PHT	Photo-Transistor
PI	Proportional Integral
PID	Proportional Integral Differential
PP	Peak-to-peak
PSD	Power Spectral Density
SISO	Single Input, Single Output
SNR	Signal-to-Noise Ratio
TLA	Three-Letter Acronym
USB	Universal Serial Bus

Appendix

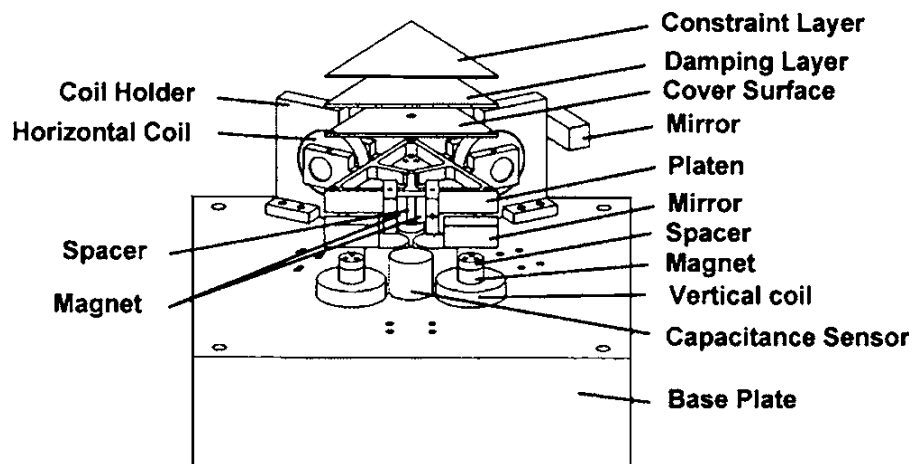
A Literature summary: Existing micro-positioning stages

1. Nano scale Motion Control With a Compact Minimum-Actuator Magnetic Levitator

Jie Gu, Won-jong Kim, Shobhit Verma

Journal of Dynamic Systems, Measurement, and Control SEPTEMBER 2005, Vol. 127
p.433-442

Describes this research group's 1st generation 6 DoF maglev stage, which uses a triangular flotor with 6 Lorentz actuators



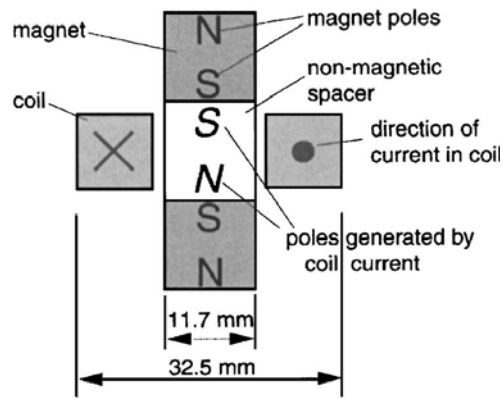
The flotor mass is a little more than 200 g.

The positioning resolution is 2 nm rms in the horizontal directions and 25 nm rms in the vertical direction. The rotational resolution of this stage is 300 nrad rms.

No-load power consumption is 15 mW per horizontal actuator and 320 mW per vertical actuator (gravity compensation).

The achievable resolution of the stage is mainly limited by noise in sensors, actuators, controller and D/A, A/D. The travel ranges are 300 μm in the x- and y-directions and 3.5 mrad rotation about the z-axis. The maximum velocity is 1 m/s, while the achieved acceleration is 2 g. The settling time of the stage is 10 ms, using a controller with a 90 Hz bandwidth.

Actuation: Uses 3 Lorentz actuators with two opposing magnets inside a coil (see below) for the horizontal actuation and 3 Lorentz actuators with a single magnet for the vertical actuation.



Because of small displacements, the actuators are assumed linear for control purposes. Force constant calculated from polynomial fit to integral equations (which have no closed form), experimentally validated to within 5%.

Sensing: 3 DoF by laser interferometry, 3 DoF by capacitive sensors underneath flotor. Capacitive sensors have higher noise, resulting in lower resolution in z-direction.

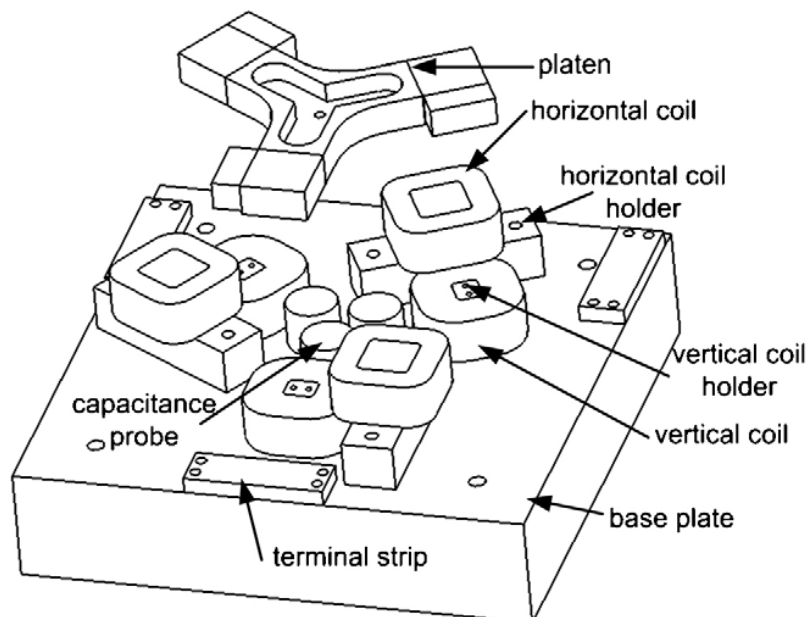
Control: Approaches system as six independent SISO systems, using simple (digital) lead-lag compensators, optimised with Matlab.

2. Design and precision construction of novel magnetic-levitation-based multi-axis nano scale positioning systems

Won-jong Kim, Shobhit Verma, Huzefa Shakir

Precision Engineering vol. 31 (Feb. 2007) p. 337–350

Describes the 2nd generation maglev stage by same research group. Also describes the abovementioned Delta stage, in comparison.

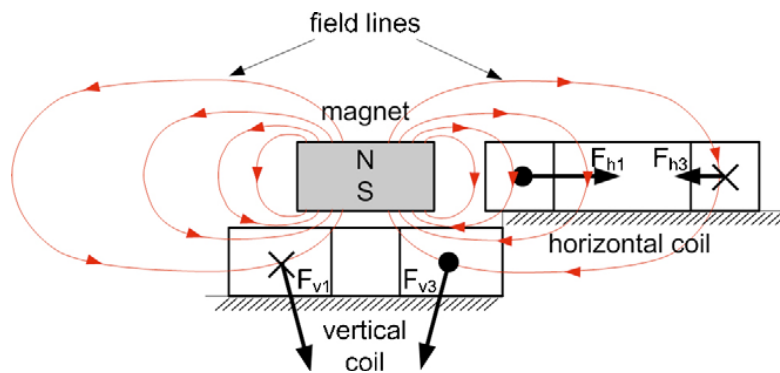


This second generation Y-stage has a larger travel range of 5 x 5 mm in the x- and y-directions, with a resolution of 3 nm resolution rms. In the z-direction the travel range is 0.5 mm and the rotational travel range is 1.7 mrad. The latter two are limited by the sensors used; the mechanical design would enable ranges of 7 mm and about 90 mrad, respectively.

The flotor mass is 270 g, with a payload of 2 kg. No-load power drain: 800 mW total.

Since there are no mechanical or electrical connections between flotor and base except for a thin ground wire for the capacitive sensors, the flotor can easily be removed and replaced.

Actuation: Uses three combined horizontal-vertical Lorentz actuators, with only one permanent magnet each. This enables simpler construction, fewer components and the flotor has no mechanical constraints to the base. However, horizontal actuation is more nonlinear, and because of partly cancelling forces, not very efficient.



Sensing: Similar to that of the 1st generation stage, uses interferometry (3 horizontal DoF) and capacitive sensing (3 vertical DoF).

Control: Similar to 1st generation, again assumes 6 independent SISO systems, controlled by lead-lag compensators. Actuator force constants are found numerically, and are then linearised around operating point. This procedure is discussed in more detail in [3]. The controllers have a bandwidth on the order of 100 Hz, and are optimised using Matlab.

According to this paper, the state of the art in piezo-actuated stages around 2000 is a 100 to 30 nm resolution over a 5 mm range using piezos, which is coarser than the current maglev stage. It further cites disadvantages including nonlinear voltage-displacement relation and high driving voltage. Higher resolutions (<1 nm) are achievable over smaller ranges using electrostatic or air bearings and voice coil actuation.

3. Novel Electromagnetic Actuation Scheme for Multiaxis Nanopositioning

Shobhit Verma, Huzefa Shakir, and Won-Jong Kim

IEEE TRANSACTIONS ON MAGNETICS, VOL. 42, NO. 8, AUGUST 2006, p. 2052-2062.

Describes the calculation of actuator forces and implemented control scheme for the Y-stage above. The forces were found analytically by evaluating 5-fold integrals in a large number of flotor positions. The actuator force constants are of course dependent on these positions, and a quadratic polynomial fit for these constants was found using the calculated and experimental data.

The control scheme uses a (real time C-programmed) non-linearity compensator for feedback linearisation. This way, simple SISO linear controllers (PID, lead-lag) can be used to stabilise and control the maglev stage, even over a travel range of 5 mm.

4. Design and control of a compact 6-degree-of-freedom precision positioner with linux-based real-time control

PhD thesis by Ho Yu (Promotor W.J. Kim)
Texas A&M University, Aug 2009

This thesis presents a 6 degree of freedom maglev positioner. It consists of a triangular flotor with 3-phase commutated x- and y-windings levitated over a Halbach magnet array. Because of this concept the travel range is very large, namely 200 x 220 mm. This can be further extended at will by using a larger magnet array. The horizontal velocity achieved is 17.5 mm/s, with an acceleration of 72.4 m/s². The rotational range around the z-axis is 0.2 rad, with a maximum angular velocity of 4.74 rad/s. The moving mass is 1.52 kg. The resolutions of this stage are 10 μm in the horizontal directions, 5 μm in the vertical direction and 17 μrad when tilting the flotor. The horizontal positioning noise is 6 μm rms.

Actuation: Two 3-phase windings in each horizontal direction provide the horizontal and levitation forces for the flotor. These windings are electronically commutated and form a planar motor in combination with the Halbach array.

Sensing: Three laser interferometers are used to measure the vertical motion and tilting motions around the x- and y-axes. Three 2-axis Hall sensors measure the lateral displacement and planar rotation.

Control: Both independent SISO controllers and a Linear Quadratic Gaussian MIMO controller are investigated.

5. Magnetically levitated planar actuator with moving magnets: Electromechanical analysis and design

PhD thesis by Jacob Willem Jansen
TU Eindhoven, Nov 2007

This thesis presents the theory and design of planar motor, using a Halbach array in the flotor and a herringbone-type array of elliptic coils in the stator plane. Its specifications are:

- Size of the translator 300x300 mm
- Levitated mass without magnets 4.0 kg
- Mechanical clearance (gap height) 1 - 2 mm
- Stroke in the xy-plane 200x200 mm
- Speed in the xy-plane 1.0 m/s
- Acceleration in the xy-plane 10 m/s²

Actuation: An electronically commutated herringbone array of coils in the stator forms a planar motor with the Halbach magnet array on the flotor.

Sensing: Coarse range uses encoders of an existing H-drive positioner (For experimental purposes only) while the fine range measurements are done using eight inductive sensors.

There is no mention of accuracy or resolution, which is probably not in the scope of the research. Control is also not discussed. However, this can be found in another PhD thesis:

6. Magnetically levitated planar actuator with moving magnets: Dynamics, commutation and control design

PhD thesis by C.M.M. van Lierop
TU Eindhoven, jan. 2008.

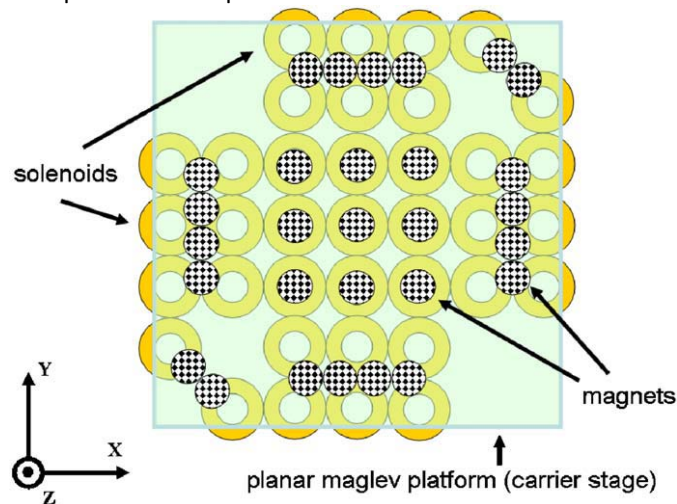
The rms-errors are $0.1\mu\text{m}$ and $1\mu\text{rad}$ in the translational and rotational directions respectively. Tracking errors are less than $30\mu\text{m}$ and 0.1 mrad .

Control: The system is decoupled and linearised using feedback linearisation. Then, 6 SISO controllers are used to stabilise the system. These consist of a lead-lag compensator and a low pass filter.

7. Design of a novel 6-DOF planar maglev system

Yi-Chih Lai, Jia-Yush Yen
Journal of Magnetism and Magnetic Materials 304 (march 2006) e386–e390

This paper does not state any specifications pertaining to range, weight or resolution but has an interesting, although complicated concept:



The position noise is around 1 mm, which is not really useful yet. This is due to non-optimised controllers and coarse sensors, the research focused mainly on keeping the platform in place under different force and moment perturbations.

Actuation: As depicted above, array of permanent magnets and coils.

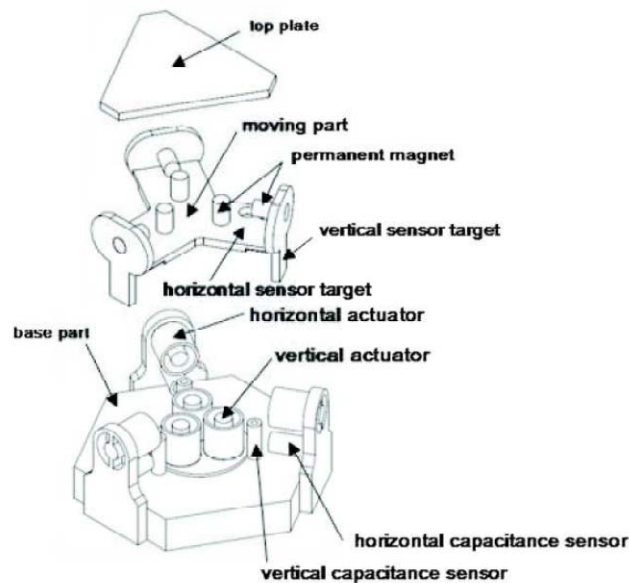
Sensing: Uses 4 optical LED sensors and 2 eddy current sensors for the 6 DoF.

Control: Also assumes six independent SISO systems, that are in this case stabilised (Apparently for static measurements) by simple PI controllers.

8. Modelling and Control of a High Precision 6-DOF Maglev Positioning Stage With Large Range of Travel

PhD thesis by Dengfeng Li
Florida Institute of Technology, Dec. 2008

This thesis presents a 6 degree of freedom maglev positioning stage using hybrid (reluctance + Lorentz force) actuators. The designed motion range is 1.1mm x 1mm x 1mm in translation and 13.3 mrad x 16.8 mrad x 13.0 mrad in rotation respectively. In a z-roll-pitch control experiment of a 6-DOF device, the positioning resolution is 250 nm and 0.5 μ rad in coarse measurement mode and 25nm in fine measurement mode respectively.



Actuation: 3 horizontal and 3 vertical hybrid actuators, the vertical actuators use permanent magnets to eliminate bias currents (repelling force)

Sensing: Capacitive sensors are used to measure all air gap lengths

Control: MIMO control scheme employing a passive 12-state observer (position and velocity) used for decoupling. The controllers themselves are PD or PID, and feedback linearisation and sliding mode control are also investigated.

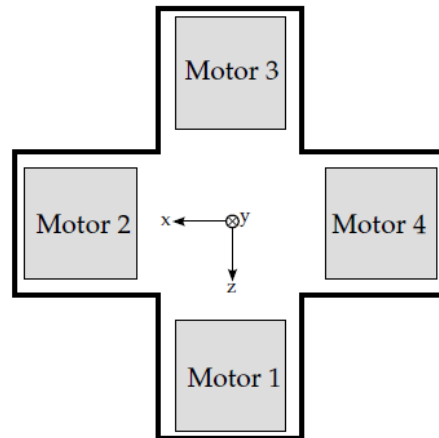
9. Path Following Using Transverse Feedback Linearization: Application to a Maglev Positioning System

Christopher Nielsen, Cameron Fulford and Manfredi Maggiore
Automatica, 2010

Deals mainly with path following control of a maglev stage. The stage presented here is 5 DoF, and uses linear guides to stabilise it. It is not a fully levitated stage. The stage has a range of 100 x 100 mm in x- and y-direction and 13 mm in vertical direction. The rotational ranges are 6 mrad around the x-axis and 28 mrad around the z-axis. The average path-following error with a properly tuned controller that was achieved is approximately 40 μ m.

Actuation: 4 iron-cored permanent magnet linear synchronous motors, as shown below.

Each motor can exert a horizontal and a vertical force. The system is overactuated.



Sensing: Not discussed in this paper.

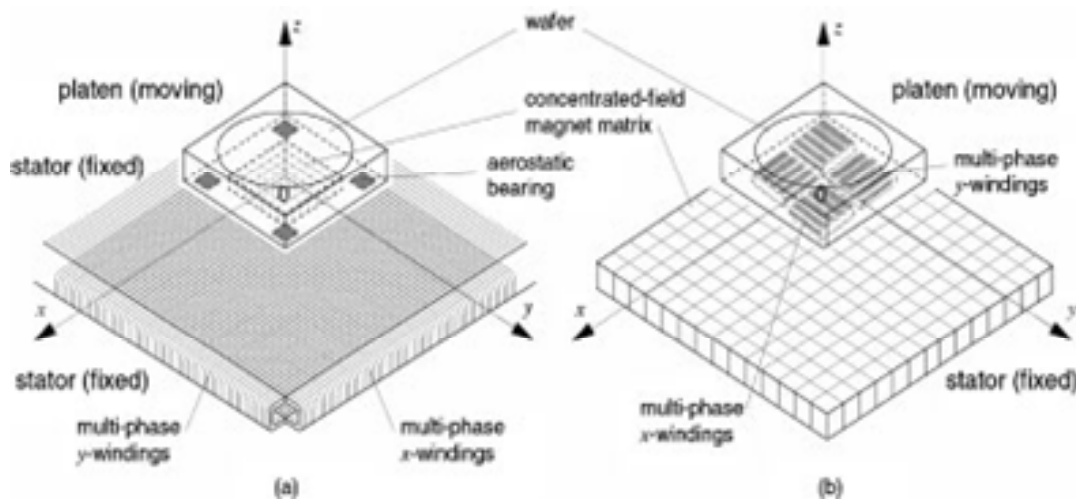
Control: MIMO path following control with feedback linearisation.

10. Controller design and implementation of six-degree-of freedom magnetically levitated positioning system with high precision

H Yu and W-J Kim

Proc. IMechE Vol. 222 Part I: **J. Systems and Control Engineering**, p 745-756, June 2008

Describes the same setup as [4], but the setup is further developed to have higher accuracy.



The flotor mass is 5.91 kg.

Angular resolution: Sub-microradian order

Nominal motor air gap (mm): 2.3

Vertical range (μm): 100

A position resolution of 20 nm with a position error of 10 nm root mean square was achieved. The experimentally demonstrated maximum travel range is 120 x 120 mm. A driving force of 22.87 N can be generated at a peak current density of 26 kA/m². Maximum travel velocity is 24.8 mm/s.

Actuation: Employs stator with Halbach magnet array and flotor with 3-phase windings.

Sensing: 3 laser interferometers measure three horizontal distances, three laser distance sensors at the underside of the flotor measure vertical distances (gap height).

Control: The system is controlled using 6 SISO lead-lag compensators with a bandwidth of 55 Hz. Plant is assumed linear, consisting only of inertia and magnetic spring constants.

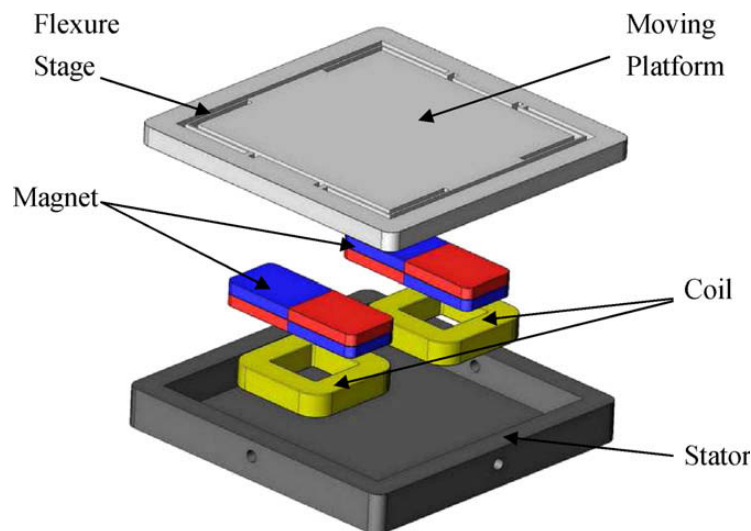
11. Implementation of a novel large moving range submicrometer positioner

Mei-Yung Chen , Huan-Wen Tzeng

Mechatronics 19 (2009) p. 1143–1151

This is a 2-DoF stage consisting of a platform suspended by flexures and actuated by voice coil motors. There is no magnetic levitation, but the range and accuracy are comparable. Does not have the disadvantages of piezo actuators and is open loop stable.

Travel range: 1000 μm in x-direction, 5 mrad around z-axis. Movement range is restricted by actuators and sensor range. Resolution and overshoot in the x-direction are both 100 nm.



Actuation: Two voice-coil motors drive the platform in one direction and can rotate it about the vertical axis.

Sensing: Position of the platform is measured with two eddy-current sensors that are mounted to it.

Control: MIMO LQR is applied using a self-tuning adaptive control scheme. This is necessary to enable the controller to compensate for thermal drift and model uncertainties.

12. The long-range scanning stage: a novel platform for scanned-probe microscopy

Mike Holmes, Robert Hocken, David Trumper

Journal of the International Societies for Precision Engineering and Nanotechnology 24 (2000) 191–209

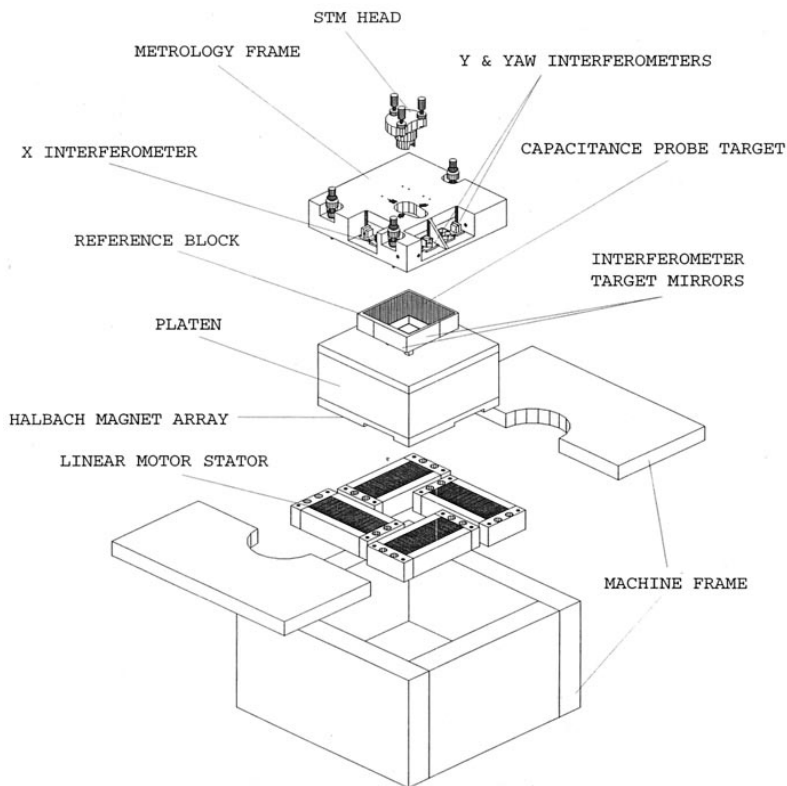
This research is somewhat older, but mentioned here for its very low noise. Relatively slow system.

Scanning stage for a AFM or STM microscope. This is a 6-DoF stage, which is magnetically levitated in oil to reduce vertical actuation forces. The oil also serves as damping and high-frequency coupling. The moving mass of the stage is 12 kg.

Range: 25 x 25 mm in xy-plane, 0.1 mm in z-direction.

Positioning noise: horizontal 0.6 nm 3 sigma , vertical 2.2 nm 3 sigma. Horizontal positioning accuracy is 10 nm. Maximal velocity 1 mm/s, power dissipation at this velocity is less than 1 W.

Needs accurately controlled ambient temperature to avoid thermal drift.



Actuation: The flotor has a Halbach magnet array mounted to the bottom surface, which forms a planar synchronous motor with the four 6-phase Lorentz coils at the bottom of the frame.

Sensing: To improve stability and accuracy, a separate metrology frame is used. This frame contains three capacitive sensors to measure the vertical displacements and three 4-pass laser interferometers to measure the horizontal displacements. Additional ultrasonic sensors are used to establish the initial position in horizontal direction.

Control: The linear motors are measured on a test stand, resulting in their force-current-position curves. These curves are used by the controller to decouple the vertical and horizontal forces and to calculate the desired current in each motor winding for a given position.

13. Electromagnetic Nanopositioner

PhD thesis by David P. Cuff
MIT, May 2006

Describes the development of a 1-DoF linear positioner suspended on rubber bearings. These replace metal flexures. Range 100 μm , maximum force 460 N, closed loop bandwidth 580 Hz. The resolution is not explicitly specified, but can be estimated from step responses to be on the order of 10 nm.

Actuation: Permanent magnet-biased reluctance actuator.

Sensing: Capacitive sensor measures position and velocity. A laser interferometer could not be used since it caused high frequency instabilities.

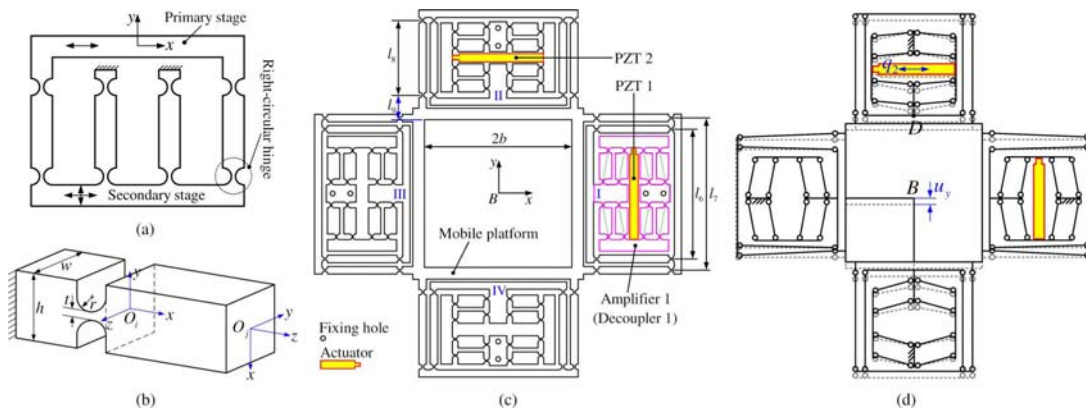
Control: Simple lead-lag compensator with additional integrator.

14. Development and Assessment of a Novel Decoupled XY Parallel Micropositioning Platform

Yangmin Li and Qingsong Xu

IEEE/ASME TRANSACTIONS ON MECHATRONICS, VOL. 15, NO. 1, FEBRUARY 2010, p. 125-135

Flexure-supported xy-positioning stage, uses piezo actuators.



The motion range is 117 x 117 μm , with a resolution of 400 nm. Accuracy is 230 nm, with a sigma of 120 nm. The device has been tested with velocities up to 30 $\mu\text{m/s}$, which is rather slow.

Actuation: 2 piezo transducers, with a stroke of 20 μm and a resolution of 20 nm.

Sensing: 2 laser distance sensors, which have a 40 nm resolution.

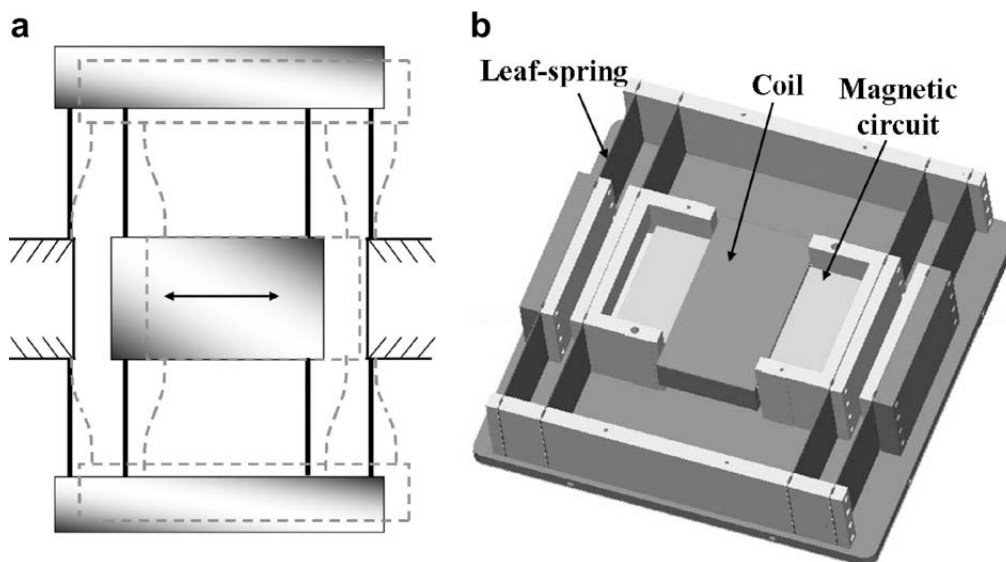
Control: The system is open loop stable but needs a controller to compensate for the (almost undamped) mechanical resonances and piezo nonlinearities such as creep and hysteresis. The system is modelled as a 2-DoF SISO system. The model is made using system identification, then Matlab is used to find the appropriate settings for the two controllers. These are lead-lag compensators.

15. Optimal design of high precision XY-scanner with nanometer-level resolution and millimeter-level working range

Dongwoo Kang , Kihyun Kim , Dongmin Kim , Jongyoup Shim , Dae-Gab Gweon , Jaehwa Jeong
Mechatronics 19 (2009) 562–570

This paper focuses mainly on design optimisation. Presents an xy-positioning stage suspended on leaf springs and actuated by voice coils. Movement range is 2 x 2 mm, with a 10 nm resolution. The first mechanical resonances of the stage are on the order of 25 Hz.

States that this scheme is easier to control than maglev/air bearing type stages and has better, more linear behaviour than piezo actuated stages.



Two of these mechanisms are mounted on top of each other to provide 2 DoF motion.

Actuation: 2 voice coil motors with leaf spring linear guides

Sensing: A laser Doppler vibrometer with a resolution of 2 nm was used to measure the displacement in the two directions.

Control: The stage was controlled using simple decoupled PID controllers.

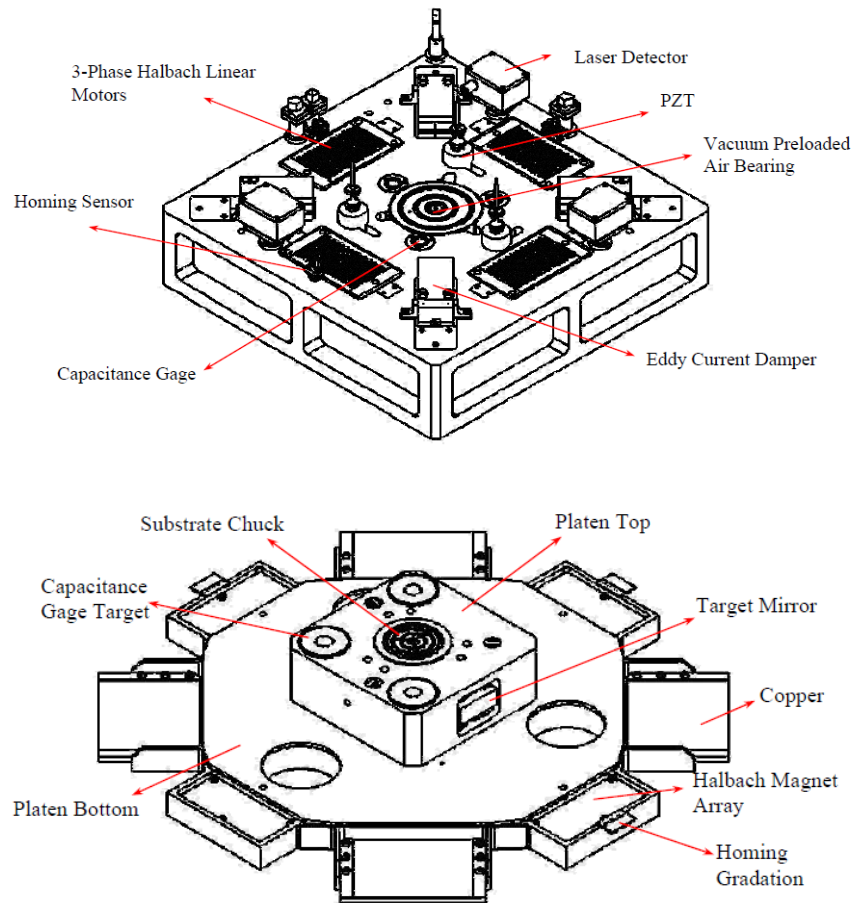
16. Multi-Scale Alignment And Positioning System II

PhD thesis by Ozkan Ozturk
University of North Carolina, 2008

Composite 6 DoF system intended for precise wafer-alignment and positioning to be used in nano-imprint lithography and similar processes. Uses various actuation principles for coarse and fine movement.

The system is designed to have a horizontal movement range of 10 x 10 mm, while the vertical movement ranges are 1.5 mm for the coarse stage and 40 μm for the fine stage. The horizontal

resolution should be 1 nm with a 2 nm error, but this could not be achieved due to temperature variations and mirror shape and alignment errors. The error was instead 120 nm in x- direction and 30 nm in y-direction. The horizontal velocity is 10 mm/s and the vertical position error less than 10 nm.



Actuation: Four 3-phase Halbach array motors for x- and y- motion and coarse z motion. The coils are mounted to the base, the magnet arrays are mounted to the mover. The fine z-direction is actuated by three piezo actuators with a travel range of 40 μm . The stage is not magnetically levitated but is suspended on a central air bearing. This air bearing is preloaded by a vacuum. The x- and y- directions are damped by eddy current dampers consisting of copper plates and permanent magnets.

Sensing: The x- and y- displacements are measured using three heterodyne two-pass interferometers, which have a resolution of 0.2 nm. Moiré fringe alignment is used to further increase the accuracy of wafer alignment.

The vertical displacements are measured by three purpose-built capacitive sensors that have sub-nanometer resolution. Optical sensors are used to measure the initial position in x- and y-directions.

Control: The system was tested using simple PID control, which will be improved later on. A computer routine incorporated into the controller takes care of the commutation of the Halbach linear motors. (This is presumably also the case for the other stages incorporating such motors) Control was not the research' main focus.

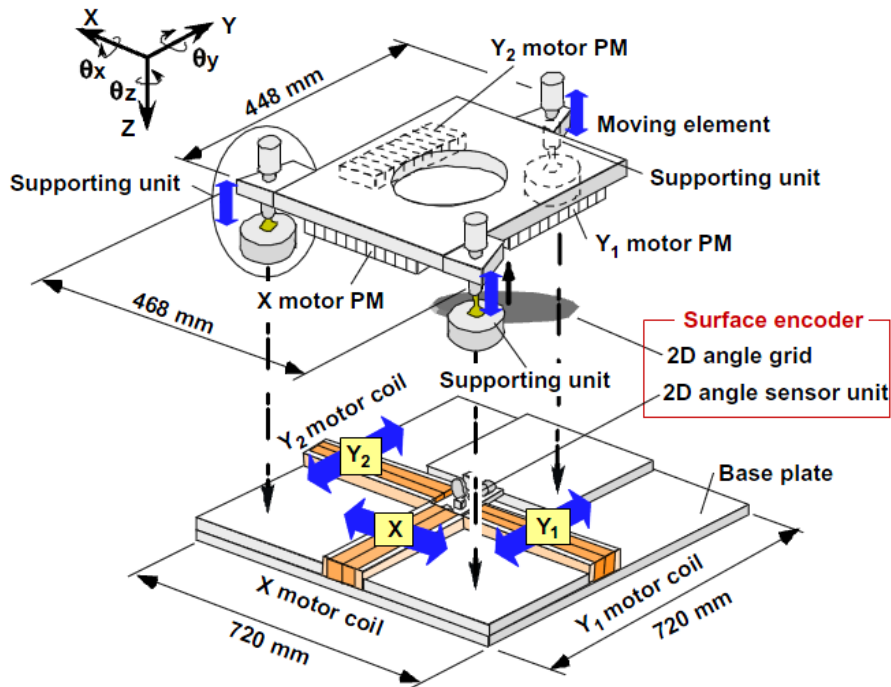
17. Precision positioning of a five degree-of-freedom planar motion stage

Shuichi Dejima, Wei Gao, Hiroki Shimizu, Satoshi Kiyono, Yoshiyuki Tomita
Mechatronics 15 (2005) 969–987

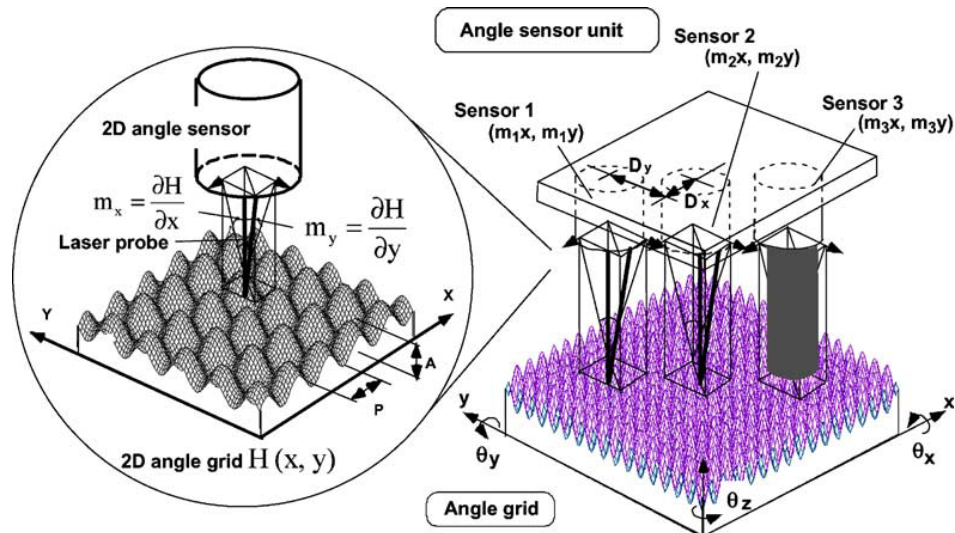
This paper presents a 5 degree of freedom hybrid stage. The mover is supported on three air bearings, and is actuated in the x- and y- directions by two-phase linear motors. Three piezo actuators provide vertical actuation, and rotation about the x- and y- axes. A special surface encoder is used as sensing element.

The mover structure consists of an aluminium block of 378 mm length, 393 mm width and 25 mm height, and has a mass of 24.9 kg. The total mass of the mover is 26 kg. The thrusts generated by the linear X- and Y-motors at rated current of 5 A are 27 N and 19 N, respectively.

The planar movement range of the stage is 200 x 200 mm. The piezos have a range of 34 μm to fine-adjust the vertical alignment of the mover. This provides an angular travel range about the x- and y- axes of approximately 5 mrad. The planar positioning resolution of the stage is 50 nm, with a 50 ms settling time. The angular resolutions are 0.14 mrad around the z-axis, and 0.058 mrad around the x- and y-axes, respectively. A horizontal velocity of 2.5 mm/s was reached.



Actuation: One two-phase electronically commutated linear motor for translation in the x-direction, two such motors actuate the y-translation. This also enables small rotations about the z-axis. The coils are mounted to the stator, the permanent magnets to the mover. Three piezo actuators provide vertical and tilting adjustment. The entire mover is supported on three air bearings.



Sensing: This stage uses a purpose-built surface encoder. A precision lathe is used to machine a fine 3D sinusoidal pattern into a disk, which is then mounted to the mover. The pitch of this pattern is 100 μm . Using a laser probe with a four quadrant photodiode, the slope of a point on this pattern can be measured in two directions independently. By placing 3 such probes at appropriate points on the stator, the displacements in x- and y- directions as well as the three rotations can be interpolated using geometrical relations. Note that these are relative measurements, much like an interferometer. The encoder achieves a horizontal resolution of 30 nm.

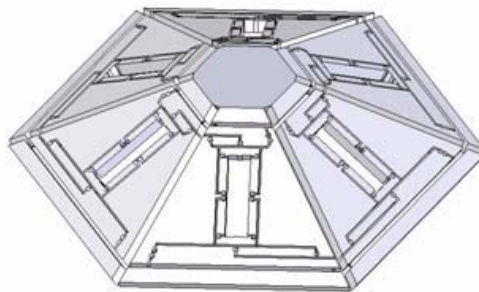
Control: Two MIMO PID-type controllers are used for the linear motors and piezo actuators, respectively. These controllers are based on decoupling of the system. The z-motion is not sensed in any way, and therefore has to be estimated from the voltages applied to the piezo actuators (essentially feed forward control).

18. The Design, Analysis and Fabrication of a Six-Axis Micropositioning Stage

Kao-Hui Lin and Ya-Hui Hu

Proceedings of the International MultiConference of Engineers and Computer Scientists 2008 Vol II

This paper describes a 6 DoF positioning stage based on aluminium flexures actuated by piezo transducers. The aluminium motion amplifiers are each made from a single piece, using microfabrication. Six of these are mounted together to a platform at the top, which can then be positioned with six degrees of freedom (see below).



The dimensions of the entire mechanism are 100 mm x 100 mm x 30 mm. The travel range of the translation is 50 μm in all directions, while the available rotation is about 9 mrad around all three

axes. The displacement resolution and the rotational resolution are 15.6 nm and 2.7 μ rad respectively.

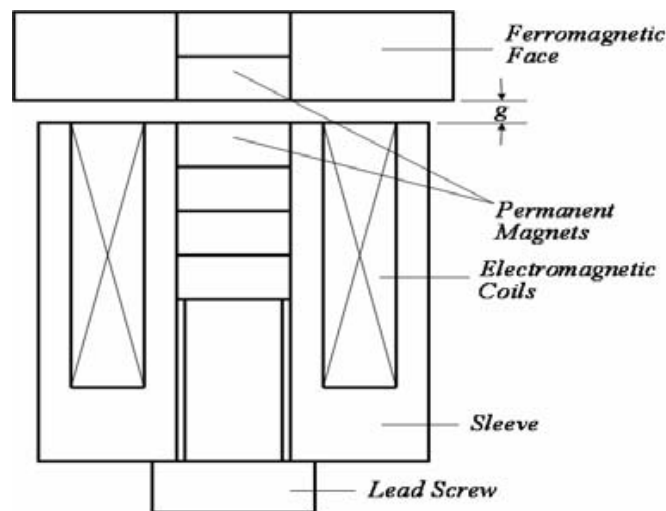
Actuation: Six piezo transducers mounted in the middle of the motion amplifiers.

Sensing, Control: Are not discussed in this paper. The mechanism has not been used in a closed loop, during the experiments a laser displacement sensor was used to measure the movement of the device.

19. Precise Motion Control of a Hybrid Magnetic Suspension Actuator with Large Travel

Dengfeng Li and Hector Gutierrez
Industrial Electronics, 2008

Paper describing in more detail the hybrid actuators used in the maglev stage discussed in [8].



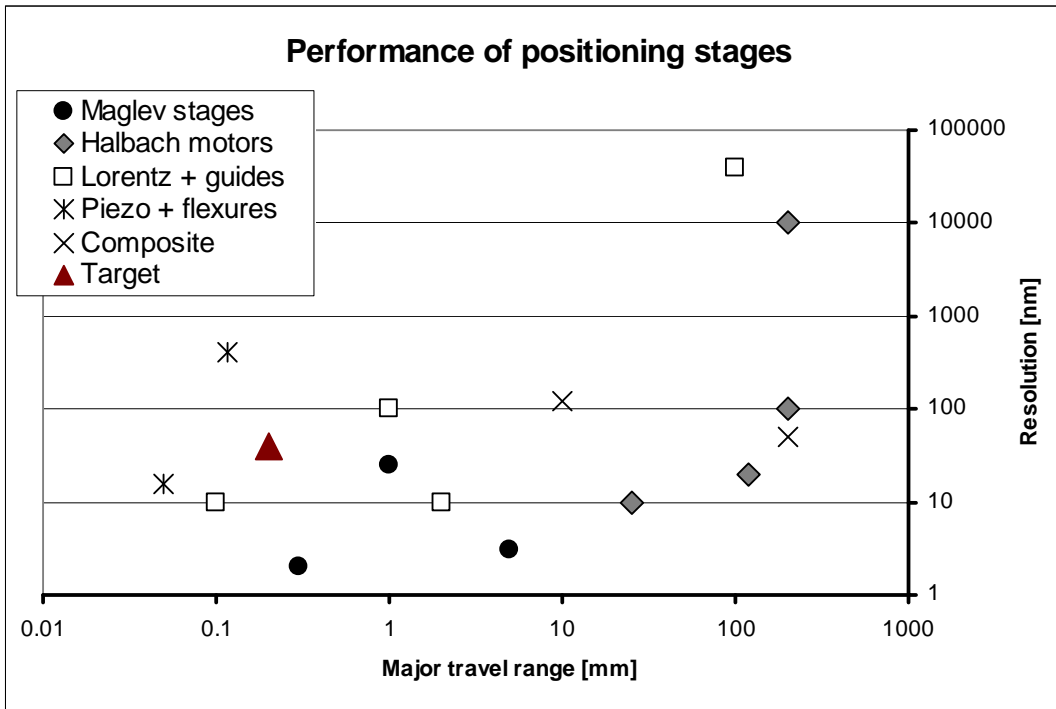
These actuators use two stacks of repelling permanent magnets that provide the levitation force to compensate gravity. The coil, located in the stator, provides an attractive force to stabilise the repulsion force and to make the actuator force controllable. This strategy enables a large movement and force range, since the coils and amplifiers do not have to supply the constant levitation force.

Sensing: A capacitive sensor is used to measure the mover displacement.

Control: The actuator force-displacement-current characteristics are measured, which are quadratic in both displacement and current. Based on these characteristics a transformation equation is found to linearise the feedback loop. This feedback linearisation is used with a MIMO PID controller. In later experiments a linear state observer is used to estimate the velocity and state feedback is used.

Overview of key figures

Research group	Technology	Travel range, x-y-z	Travel range, rotational	Resolution, x-y-z	Resolution, rotational	Travel velocity x-y-z	Year
Kim et al.	1 st generation 6 DoF maglev stage	300 x 300 μ m	3.5 mrad	2 nm x and y, 25 nm z	300 nrad	1 m/s	2005
Kim et al.	2 nd generation 6 DoF maglev stage	5 x 5 x 0.5 mm	1.7 mrad	3 nm x and y, 33 nm z			2007
Kim and Yu	Planar Halbach array motor	200 x 220 mm	0.2 rad	10 μ m x and y, 5 μ m z	17 μ rad	17.5 mm/s	2009
TU Eindhoven	Planar Halbach array motor, moving magnets	200 x 200 mm		100 nm x and y	1 μ rad	1 m/s	2007 / 2008
D. Li	Maglev stage with hybrid actuators	1.1 x 1 x 1 mm	13.3 x 16.8 x 13.0 mrad	25 nm x, y and z	0.5 μ rad		2008
Nielsen et al.	5 DoF Lorentz actuator + linear guides	100 x 100 x 13 mm	6 x 28 mrad	40 μ m			2010
Kim and Yu	Planar Halbach array motor	120 x 120 x 0.1 mm		20 nm x and y		24.8 mm/s	2008
Chen and Tzeng	Voice coil + flexures, 2 DoF	1 mm	5 mrad	100 nm			2009
Holmes et al.	Oil-suspended Halbach array actuator	25 x 25 x 0.1 mm		10 nm		1 mm/s	2000
Cuff	1 DoF Lorentz actuator, rubber suspension	100 μ m		10 nm			2006
Li and Xu	2 DoF piezo actuated with flexures	117 x 117 μ m		400 nm		30 μ m/s	2010
Kang et al.	2 DoF voice coil with leaf springs	2 x 2 mm		10 nm			2009
Ozturk	Composite linear motors + piezo	10 x 10 x 1.5 mm		120 nm x, 30 nm y, 10 nm z		10 mm/s	2008
Dejima et al.	5 DoF composite linear motors + piezo	200 x 200 mm	5 x 5 x 5 mrad	50 nm x and y	58 μ rad x and y, 140 μ rad z	2.5 mm/s	2005
Lin and Hu	6 DoF piezo + flexures	50 x 50 x 50 μ m	9 x 9 x 9 mrad	15.6 nm x, y and z	2.7 μ rad x, y and z		2008



B List of requirements for the three assembly steps

Adapted from [43]

Transport operation

Requirement Transport	Value	Reason
Range X x Y x Z	$\geq 20 \text{ mm} \times 20 \text{ mm} \times 10 \text{ mm}$	The slave robot's assembly working area will be about 20 mm x 20 mm, the parts initially scattered across it. The vertical range is less critical, but should be sufficient to easily move parts over each other and stack them.
Velocity X, Y and Z	$> 10 \text{ mm/s}$	Allows traversing the full workspace within two seconds. Allows approximately following 2 mm peak-to-peak user commands at 1 Hz. This following won't be necessarily sinusoidal, but enough to match the maximum velocities and end-point position tracking. To follow 1 Hz commands across the full range $>60 \text{ mm/s}$ would be needed.
Acceleration X, Y and Z	$> 30 \text{ mm/s}^2$	Allows traversing the full workspace within two seconds. Allows approximately following 2 mm peak-to-peak user commands at 1 Hz. This following won't be necessarily sinusoidal, but enough to match the maximum velocities and end-point position tracking. To follow 1 Hz commands across the full range $>400 \text{ mm/s}^2$ would be needed.
Minimum Incremental Motion (MIM) X, Y and Z	$< 100 \mu\text{m}$	$1/10^{\text{th}}$ of the assembly size, in order to position the part with sufficient accuracy for the pre-alignment step. This step should have a range several times the 100 μm MIM in order to correct possible mistakes without having to switch back to transportation mode.
Sensor resolution X, Y and Z	$< 20 \mu\text{m}$	A one fifth safety factor with respect to the MIM. Enables achieving "consistent and reliable" movements, as the concept of MIM requires. Using stepper motors or servo systems may make a sensor unnecessary for this step.
Rotational range Θ_z	360°	Manipulation and alignment of not-round parts requires full rotation around the Z axis.

Requirement Transport	Value	Reason
Rotational velocity Θ_z	90°/s	The rotational velocity and resolution are set to match the (estimated and un-scaled) human acting and observing capabilities. The user can move controllably at 90°/s, with a 1° resolution when performing coarse rotations. No scaling is used here since only a coarse alignment is expected.
Rotational MIM Θ_z	$\leq 1^\circ$	See above.
Perturbation rejection X, Y and Z	< 50 μm , above 3 Hz	Since the user can actuate controllably only up to 3 Hz, the system must ensure perturbation rejection for the higher frequencies, for a value smaller than the expected MIM. The upper limit is half the MIM, but smaller results in much better performance.
Perturbation rejection Θ_z	< 0.5°, above 3 Hz	Since the user can actuate controllably only up to 3 Hz, the system must ensure perturbation rejection for the higher frequencies, for a value smaller than the expected MIM. The upper limit is half the MIM, but smaller results in much better performance.
Perturbation rejection Θ_x and Θ_y	-	Is not significant in this phase since there is no contact. Also, this step is too coarse to correct small tilt errors, which is done in the final step.
Collision/emergency stop	0.2 μm	After (emergency) force sensing, the transporter should stop immediately. This puts an upper limit on the velocity in the vicinity of assembly region. A 200 nm stopping distance should prevent damage in these events. However, active obstacle avoidance is probably an easier way to prevent collision and damage.
Overshoot	0.2 μm	Maximum overshoot of the transporter for step responses in the assembly region, mainly to prevent collision. Here the same argument applies, collision can more easily be avoided by choosing the right transportation path.
Payload	-	Depends on the equipment that must be carried and the weight of the parts (which is probably insignificant).

Requirement Transport	Value	Reason
Driving Forces	-	Depends on the equipment that must be carried, and on the kind and magnitude of perturbations that must be rejected. Given the low acceleration requirements, the forces also stay low. For a 1 kg and the required acceleration of 30 mm/s ² , 30 mN is enough. No force measurement or control is required in this step. Depending on the system configuration, additional force is needed to overcome friction.

Pre-alignment operation

Requirement Pre-alignment	Value	Reason
Range X x Y x Z	≥ 1 mm x 1 mm x 1 mm	The working area has to cover the subassembly and parts sizes.
Velocity X, Y and Z	> 3.5 mm/s	Ensures following user commands at 1 Hz within the workspace. The following must be more accurate than in the transport phase due to the more complex motion patterns expected from the user.
Acceleration X, Y and Z	> 20 mm/s ²	Ensures following user commands at 1 Hz within the workspace, as above.
Minimum Incremental Motion (MIM) X, Y and Z	< 20 μm	1/10 th of the final mounting step range, in order to position the part with sufficient accuracy for this step.
Sensor resolution X, Y and Z	< 4 μm	A one fifth safety factor with respect to the MIM. Enables achieving “consistent and reliable” movements, as the concept of MIM requires. Using stepper motors or servo systems may make a sensor unnecessary for this step.
Rotational range Θ _z	360°	Manipulation and alignment of not-round parts requires full rotation around the Z axis. Same requirements as for transport phase, but in this phase scaling could be applied to enable more precise positioning.

Requirement Pre-alignment	Value	Reason
Rotational velocity Θ_z	90°/s	The rotational velocity and resolution are set to match the (estimated and un-scaled) human acting and observing capabilities. The user can move controllably at 90°/s, with a 1° resolution when performing coarse rotations. No scaling is used here since only a coarse alignment is expected. Also, the visual zooming doesn't act on the angles, and that is the only feedback the user has at this point since there is no contact with the environment.
Rotational MIM Θ_z	$\leq 1^\circ$	See above.
Perturbation rejection X, Y and Z	< 5 μm , above 3 Hz	Since the user can actuate controllably only up to 3 Hz, the system must ensure perturbation rejection for the higher frequencies, for a value smaller than the expected MIM. The upper limit is half the MIM, but smaller results in much better performance.
Perturbation rejection Θ_z	< 0.5°	Since the user can actuate controllably only up to 3 Hz, the system must ensure perturbation rejection for the higher frequencies, for a value smaller than the expected MIM. The upper limit is half the MIM, but smaller results in much better performance. (The actual specification will depend on the magnitude of the perturbations and on other system sections).
Perturbation rejection Θ_x and Θ_y	-	Is not significant in this phase since there is no contact. Also, this step is too coarse to correct small tilt errors, which is done in the final step.
Payload	-	Depends on the equipment that must be carried and the weight of the parts (which is probably insignificant).
Driving Forces	-	Depends on the equipment that must be carried, and on the kind and magnitude of perturbations that must be rejected. Given the low acceleration requirements, the forces also stay low. For a 1kg and the required acceleration of 30mm/s ² , 30mN is enough. No force measurement or control is required in this step.
Force resolution X, Y and Z	< 100 μN	If contact operations are to be carried out, this resolution should ensure no damage to the parts.

Mounting operation

Requirement Mounting	Value	Reason
Range X x Y x Z	$\geq 200 \mu\text{m} \times 200 \mu\text{m} \times 200 \mu\text{m}$	Scaling of the user range-to-MIM ratio (200:1), using half the maximum clearance (1 μm) as a reference for the MIM. Also allows correcting possible mistakes without having to switch back to pre-alignment mode.
Velocity X, Y and Z	$> 1 \text{ mm/s}$	Ensures following user commands at 1 Hz within the workspace.
Acceleration X, Y and Z	$> 5 \text{ mm/s}^2$	Ensures following user commands at 1Hz within the workspace.
Minimum Incremental Motion (MIM) X, Y and Z	40 – 100 nm	The MIM requirement is defined as a safety factor of 2 – 5 relative to the smallest tolerances. A smaller MIM leads to better performance and flexibility but is not needed in every case.
Sensor peak-to-peak noise X, Y and Z	$\leq 7 - 18 \text{ nm}$	Follows from the error budget for the mounting operation.
Motion tracking error, Linearity X, Y and Z	$< 10 \text{ nm per every } 100 \text{ nm}$	Accuracy to the full range is not necessary, due to the tele-operation mode. Relative accuracy or linearity like the one defined here is necessary for the user comfort (at least a 10% of the considered displacement in preliminary tests), and for control purposes.
Rotational range Θ_z	$\pm 1^\circ$	The MIM for the largest (2 μm) clearance, times the human hand range/resolution ratio (2:100°). Bigger ranges would be useful, this enables multiple scale factors for the rotation motion.
Rotational range Θ_x and Θ_y	$\pm 1^\circ$	Depends on the manufacturing, but sidewalls of 1° are common and should be corrected for low clearances. This alignment can be either passive (compliance) or active (actuated). It is expected for the gripper and base to be initially aligned to a value better than this, or for a coarse alignment stage to bring the system to an alignment within this value.

Requirement Mounting	Value	Reason
Rotational MIM Θ_z , Θ_x and Θ_y	.002°	With maximum parts size of 1 mm, and clearances of 200 nm, the angle MIM is defined as one fifth (safety factor) of the maximum allowable error when the part will still fit: $\text{atan}(200 \text{ nm}/1 \text{ mm}) / 5$. For 2 μm clearances, the MIM can be increased to .02°.
Perturbation rejection X, Y and Z	$\leq 14 - 35 \text{ nm}$, above 3 Hz	Since the user can actuate controllably only up to 3 Hz, the system must ensure perturbation rejection for the higher frequencies, for a value smaller than the expected clearance. The maximum values follow from the error budget for the mounting operation. See section ??
Perturbation rejection, Θ_z , Θ_x and Θ_y	$\leq .0008^\circ -$ 0.002°	Since the user can actuate controllably only up to 3 Hz, the system must ensure perturbation rejection for the higher frequencies, for a value smaller than the expected clearance. When a part size of 1 mm is assumed, a displacement of one end of 14 – 35 nm corresponds to a rotational perturbation rejection of $0.0008^\circ - 0.002^\circ$.
Payload Z	10 g	Passive structures for clamping, aligning, made of silicon, plastics or aluminium, small coils for actuation, sensor targets. Given the small size, 10 g should be enough for most of them. (10 g is the weight of a solid steel disc of 20 mm diameter by 4 mm height). Most likely, the moving mass will be lower than 4 grams.
Actuation force resolution X, Y and Z	< 100 μN	Has to prevent damage to small parts on silicon, photoresist or metals.
Actuation force ranges X, Y and Z	> 10 mN	Range/resolution ratio on wrist operation ($\sim 1:100$ between the force range and resolution in wrist operation). Enough also to hold and accelerate parts, overcome capillarity with small parts, wet glue capillarity, micro forces (van der Waals, statics), friction (assuming that the normal force can be controlled to the less than 1 mN resolution). Forced-fit or other high force tasks are not considered. The forces required to keep the controller bandwidth are not considered yet here.

Requirement Mounting	Value	Reason
Torque resolution Θ_z , Θ_x and Θ_y	10 $\mu\text{N}/\text{mm}$	Previously defined forces, in the whole base-space of 10 mm radius. No torque-tasks are defined.
Torque range Θ_z , Θ_x and Θ_y	1 mN/mm	Previously defined forces, in the whole base-space of 10 mm radius. No torque-tasks are defined.

Coarse stage requirements

The coarse stage will be used for both transportation and pre-alignment phases, where the haptic interface will take care of the proper scaling of user commands in each phase. Therefore, the requirements of both phases are combined to yield the requirements for the coarse stage. It should have the full 20 mm x 20 mm x 10 mm range for transportation, and the smallest MIM (20 μm) for pre-alignment. In the same way, from the requirements lists of both phases the largest ranges and best MIM's are kept. The overshoot and emergency stop requirements are transferred to the fine stage. The low (200 nm) values for these two requirements conflict with the coarse stage design, and the fine stage is far better specified to deal with these. Again, a semi-automatic transportation path is a far better alternative to prevent collision. The complete coarse stage requirement list is shown in the table below.

Requirement Coarse Stage	Value	Reason
Range X x Y x Z	$\geq 20 \text{ mm} \times 20 \text{ mm} \times 10 \text{ mm}$	The slave robot's assembly working area will be about 20 mm x 20 mm, the parts initially scattered across it. The vertical range is less critical, but should be sufficient to easily move parts over each other and stack them.
Velocity X, Y and Z	$> 10 \text{ mm}/\text{s}$	Allows traversing the full workspace within two seconds. Allows approximately following 2 mm peak-to-peak user commands at 1 Hz. This following won't be necessarily sinusoidal, but enough to match the maximum velocities and end-point position tracking. To follow 1 Hz commands across the full range $>60 \text{ mm}/\text{s}$ would be needed.
Acceleration X, Y and Z	$> 30 \text{ mm}/\text{s}^2$	Allows traversing the full workspace within two seconds. Allows approximately following 2 mm peak-to-peak user commands at 1 Hz. This following won't be necessarily sinusoidal, but enough to match the maximum velocities and end-point position tracking. To follow 1 Hz commands across the full range $>400 \text{ mm}/\text{s}^2$ would be needed.

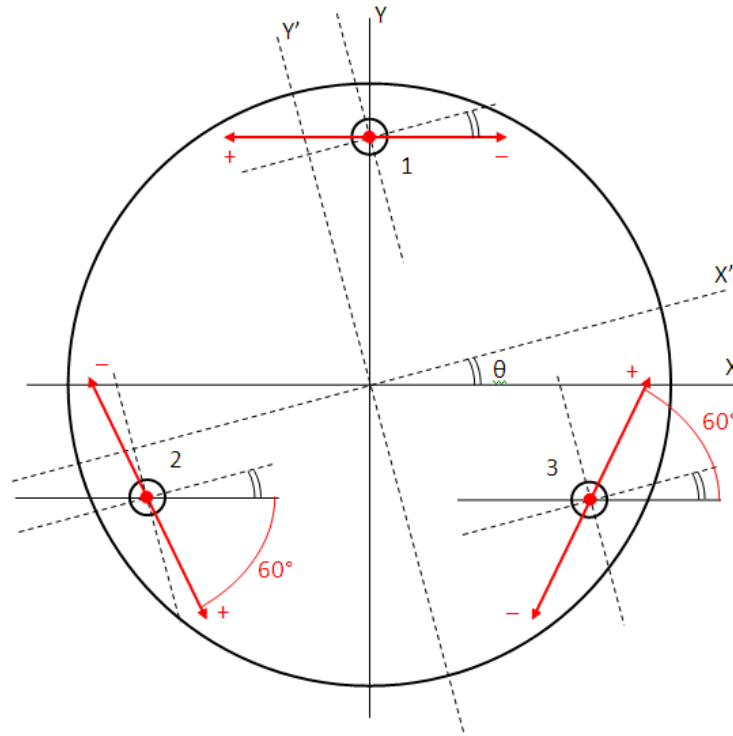
Requirement Coarse Stage	Value	Reason
Minimum Incremental Motion (MIM) X, Y and Z	< 20 μm	1/10 th of the final mounting step range, in order to position the part with sufficient accuracy for this step.
Sensor resolution X, Y and Z	< 4 μm	A one fifth safety factor with respect to the MIM. Enables achieving “consistent and reliable” movements, as the concept of MIM requires. Using stepper motors or servo systems may make a sensor unnecessary for this step.
Rotational range Θ_z	360°	Manipulation and alignment of not-round parts requires full rotation around the Z axis.
Rotational velocity Θ_z	90°/s	The rotational velocity and resolution are set to match the (estimated and un-scaled) human acting and observing capabilities. The user can move controllably at 90°/s, with a 1° resolution when performing coarse rotations. No scaling is used here since only a coarse alignment is expected. Also, the visual zooming doesn’t act on the angles, and that is the only feedback the user has at this point since there is no contact with the environment.
Rotational MIM Θ_z	$\leq 1^\circ$	See above.
Perturbation rejection X, Y and Z	< 5 μm , above 3 Hz	Since the user can actuate controllably only up to 3 Hz, the system must ensure perturbation rejection for the higher frequencies, for a value smaller than the expected MIM. The upper limit is half the MIM, but smaller results in much better performance. (The actual specification will depend on the magnitude of the perturbations and on other system sections).
Perturbation rejection Θ_z	< 0.5°, above 3 Hz	Since the user can actuate controllably only up to 3 Hz, the system must ensure perturbation rejection for the higher frequencies, for a value smaller than the expected MIM. The upper limit is half the MIM, but smaller results in much better performance. (The actual specification will depend on the magnitude of the perturbations and on other system sections).

Requirement Coarse Stage	Value	Reason
Perturbation rejection Θ_x and Θ_y	-	Is not significant in this phase since there is no contact. Also, this step is too coarse to correct small tilt errors, which is done in the final step.
Payload	-	Depends on the equipment that must be carried and the weight of the parts (which is probably insignificant).
Driving Forces	-	Depends on the equipment that must be carried, and on the kind and magnitude of perturbations that must be rejected. Given the low acceleration requirements, the forces also stay low. For a 1 kg and the required acceleration of 30 mm/s^2 , 30 mN is enough. No force measurement or control is required in this step. Depending on the system configuration, additional force is needed to overcome friction.
Force resolution	< 100 μN	If contact operations are to be carried out, this resolution should ensure no damage to the parts. Could be difficult to achieve with the coarse stage alone, so if contact is required during the pre-alignment phase, a dual stage control scheme may be necessary.

C Actuator force distribution

All actuation forces are distributed over the three dual actuators. The horizontal coils will supply force in the xy-plane and rotations about the z-axis. The vertical coils will provide the vertical levitation force and additional forces along the z-axis, as well as torques about the x- and y-axes. To find the force maxima for each controller, and for control purposes, the force distribution equations will be derived here.

The three horizontal coils of the actuators will be positioned at 120° angles relative to each other, at the points of an equilateral triangle. The force distribution of the horizontal actuators will therefore be as shown in the figure below. The sign convention of the actuator forces is chosen such that a positive force will give a positive (counter-clockwise) contribution to the resultant torque about the z-axis.



The force contribution of the three horizontal actuators to a force in an arbitrary direction can be found by decomposing the actuator forces along this direction. In the general case, for a force in the direction X', defined by an arbitrary angle θ, the force is given by

$$F_{X'} = -\cos \theta \cdot F_{1H} + \cos(60 + \theta) \cdot F_{2H} + \cos(60 - \theta) \cdot F_{3H}$$

Likewise, the force in the direction orthogonal to this, Y', is given by

$$F_{Y'} = \sin \theta \cdot F_{1H} - \sin(60 + \theta) \cdot F_{2H} + \sin(60 - \theta) \cdot F_{3H}$$

And the torque about the z-axis by

$$T_Z = R \cdot F_{1H} + R \cdot F_{2H} + R \cdot F_{3H}$$

where R is the distance from the actuator to the disk's centre, for now assumed to be 10mm.

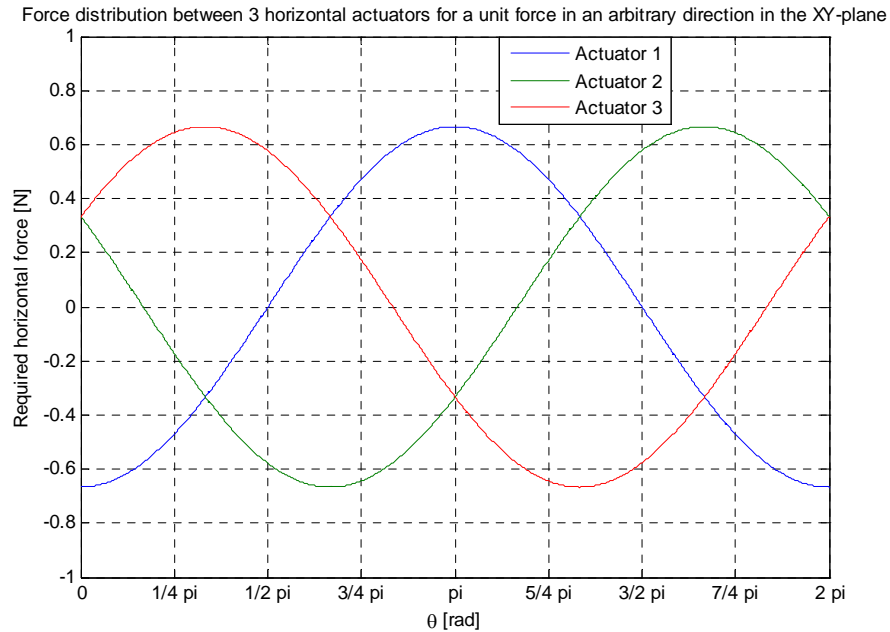
When a resultant force in the direction X' is needed, the resultant force in the orthogonal Y' direction and the torque T_z should be zero. This leads to the following system of equations

$$\begin{bmatrix} -\cos\theta & \cos(60+\theta) & \cos(60-\theta) \\ \sin\theta & -\sin(60+\theta) & \sin(60-\theta) \\ R & R & R \end{bmatrix} \begin{bmatrix} F_{1H} \\ F_{2H} \\ F_{3H} \end{bmatrix} = \begin{bmatrix} F_{X'} \\ 0 \\ 0 \end{bmatrix}$$

where F_{1H} , F_{2H} and F_{3H} are the three horizontal actuator forces. Solving for these forces as a function of the angle θ , we obtain

$$\begin{cases} F_{1H} = -\frac{2}{3}\cos\theta \cdot F_{X'} \\ F_{2H} = \frac{2}{3}\cos(\theta + 60) \cdot F_{X'} \\ F_{3H} = \frac{2}{3}\cos(\theta - 60) \cdot F_{X'} \end{cases}$$

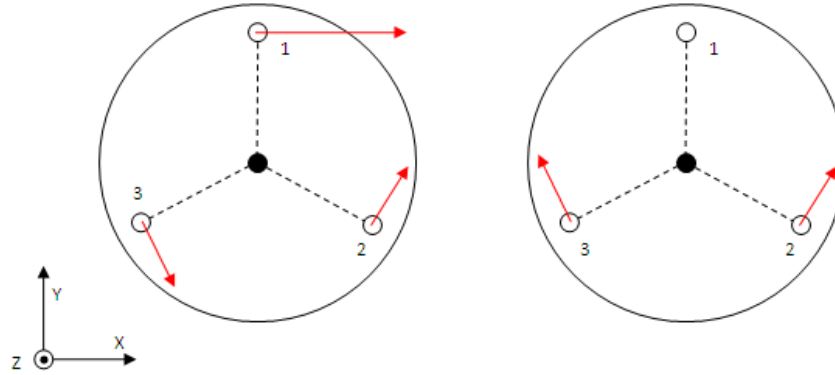
where R is cancelled out. The three actuator forces are plotted against θ in the following figure, to find the extreme cases of force distribution.



The actuator forces are sinusoidally distributed, of course shifted 120° in phase between actuators. Two extreme cases are:

- $\theta = 0^\circ$, X' coincides with the x-axis. The force generated by actuator 1 has to be twice that of actuators 2 and 3 and opposite in sign, so that the resulting torque is zero. Forces 2 and 3 have to be equal in magnitude, so the y-components cancel out.
- $\theta = 90^\circ$, X' coincides with the y-axis. Actuator 1 cannot contribute to the force in y-direction, and the forces of actuators 2 and 3 have to be equal in magnitude but opposite in sign.

These two cases are shown below. From the graph and equations we can observe that each actuator has to supply at worst two-thirds of the total required horizontal force.



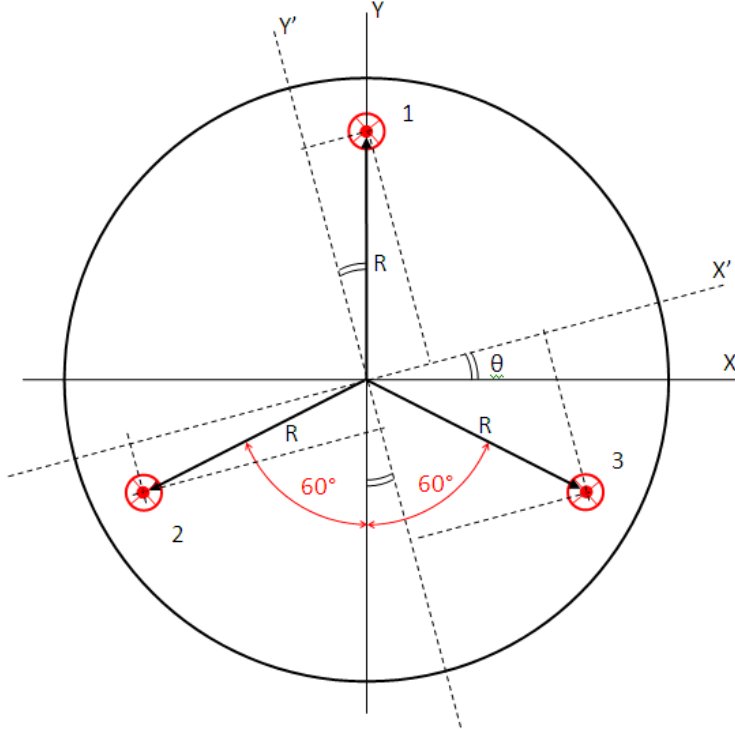
If the horizontal stage force is specified as a magnitude and an angle (polar coordinates), the above equations can be used by the controller to determine the force for each actuator. If, instead, the force is specified as an x- and y-component (Cartesian coordinates), these equations can be modified as follows:

$$\begin{bmatrix} -1 & \frac{1}{2} & \frac{1}{2} \\ 0 & -\frac{\sqrt{3}}{2} & \frac{\sqrt{3}}{2} \\ R & R & R \end{bmatrix} \begin{bmatrix} F_{1H} \\ F_{2H} \\ F_{3H} \end{bmatrix} = \begin{bmatrix} F_X \\ F_Y \\ 0 \end{bmatrix} \rightarrow$$

$$\begin{cases} F_{1H} = -\frac{2}{3} F_X \\ F_{2H} = \frac{1}{3} F_X - \frac{\sqrt{3}}{3} F_Y \\ F_{3H} = \frac{1}{3} F_X + \frac{\sqrt{3}}{3} F_Y \end{cases}$$

where $\theta = 0^\circ$ was substituted to state that X' and Y' coincide with the x- and y-directions, respectively.

In a similar way, the vertical actuator force distribution can be found for a torque around an arbitrary horizontal axis. This is shown in the figure below. The sign convention of the actuator forces is chosen such that a positive force will give a positive (upward) contribution to the resultant force in the z-direction.



The torque contribution of the three vertical actuators to a torque around an axis in an arbitrary direction can be found by decomposing the resultant actuator torques. In the general case, for a torque around an axis in the direction X' , defined by an arbitrary angle θ , this torque is given by

$$T_{X'} = R \cdot \cos \theta \cdot F_{1V} - R \cdot \cos(60 + \theta) \cdot F_{2V} - R \cdot \cos(60 - \theta) \cdot F_{3V}$$

Likewise, the torque orthogonal to this, around the Y' -axis, is given by

$$T_{Y'} = -R \cdot \sin \theta \cdot F_{1V} + R \cdot \sin(60 + \theta) \cdot F_{2V} - R \cdot \sin(60 - \theta) \cdot F_{3V}$$

And the resultant vertical force by

$$F_Z = F_{1V} + F_{2V} + F_{3V}$$

where R is again the distance from the actuator to the disk's centre.

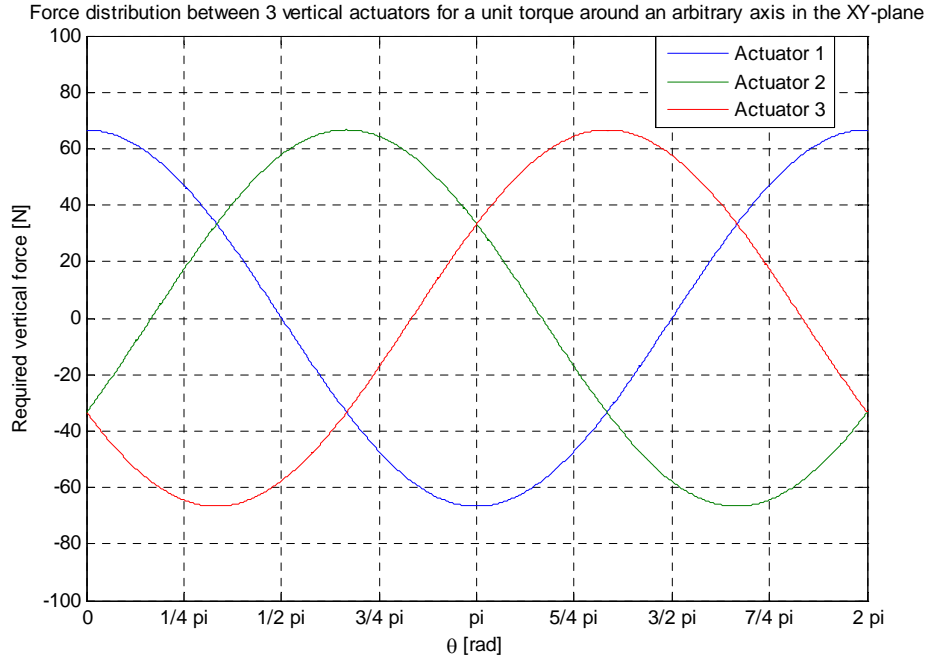
When a resultant torque around X' is needed, the resultant orthogonal torque Y' and the vertical force F_Z should be zero. This leads to the following system of equations

$$\begin{bmatrix} R \cos \theta & -R \cos(60 + \theta) & -R \cos(60 - \theta) \\ -R \sin \theta & R \sin(60 + \theta) & -R \sin(60 - \theta) \\ 1 & 1 & 1 \end{bmatrix} \begin{bmatrix} F_{1V} \\ F_{2V} \\ F_{3V} \end{bmatrix} = \begin{bmatrix} T_{X'} \\ 0 \\ 0 \end{bmatrix}$$

where F_{1V} , F_{2V} and F_{3V} are the three vertical actuator forces. Solving for these forces as a function of the angle θ , we obtain

$$\begin{cases} F_{1V} = \frac{2}{3R} \cos \theta \cdot T_X, \\ F_{2V} = -\frac{2}{3R} \cos(\theta + 60) \cdot T_X, \\ F_{3V} = -\frac{2}{3R} \cos(\theta - 60) \cdot T_X. \end{cases}$$

The three actuator forces are plotted against θ in the following figure, to find the extreme cases of force distribution.

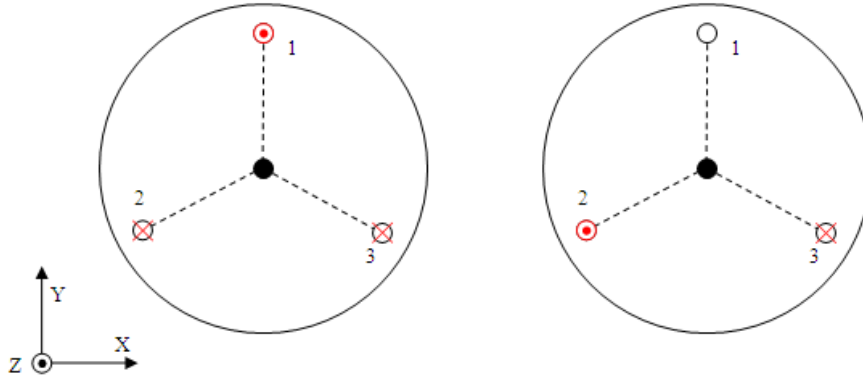


From the graph and the equations we can see that the force distribution for torques around X' is essentially the same as for forces in the X' direction, except for two things. The distribution is shifted 180° in phase, and the required force is greater by a factor $1/R$, in this case 100.

Two extreme cases are:

- $\theta = 0^\circ$, X' coincides with the x-axis. The force generated by actuator 1 has to be twice that of actuators 2 and 3 and opposite in sign, so that the resulting vertical force is zero. Forces 2 and 3 have to be equal in magnitude, so the y-components of the torques cancel out.
- $\theta = 90^\circ$, X' coincides with the y-axis. Actuator 1 cannot contribute to the torque around the y-axis, and the forces of actuators 2 and 3 have to be equal in magnitude but opposite in sign.

These two cases are shown below. From the graph and equations we can observe that each actuator has to supply at worst two-thirds of the total required torque, divided by the radius R (distance from actuators to the disk centre).



When the required torque is specified in polar coordinates, the above equations can be used by the controller. If the torque instead is specified in Cartesian coordinates, the equations have to be modified again by substituting $\theta = 0^\circ$:

$$\begin{bmatrix} R & -\frac{R}{2} & -\frac{R}{2} \\ 0 & \frac{R\sqrt{3}}{2} & -\frac{R\sqrt{3}}{2} \\ 1 & 1 & 1 \end{bmatrix} \begin{bmatrix} F_{1V} \\ F_{2V} \\ F_{3V} \end{bmatrix} = \begin{bmatrix} T_X \\ T_Y \\ 0 \end{bmatrix} \rightarrow \begin{cases} F_{1V} = \frac{2}{3R} T_X \\ F_{2V} = -\frac{1}{3R} T_X + \frac{\sqrt{3}}{3R} T_Y \\ F_{3V} = -\frac{1}{3R} T_X - \frac{\sqrt{3}}{3R} T_Y \end{cases}$$

To find the force distribution for vertical forces and torques about the vertical axis, the abovementioned systems of equations can be used, with the horizontal forces and torques set to zero:

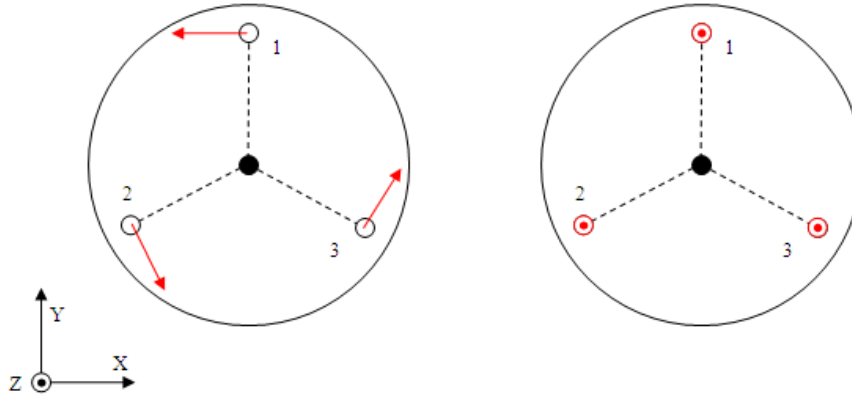
$$\begin{bmatrix} R \cos \theta & -R \cos(60 + \theta) & -R \cos(60 - \theta) \\ -R \sin \theta & R \sin(60 + \theta) & -R \sin(60 - \theta) \\ 1 & 1 & 1 \end{bmatrix} \begin{bmatrix} F_{1V} \\ F_{2V} \\ F_{3V} \end{bmatrix} = \begin{bmatrix} 0 \\ 0 \\ F_Z \end{bmatrix}$$

$$\begin{bmatrix} -\cos \theta & \cos(60 + \theta) & \cos(60 - \theta) \\ \sin \theta & -\sin(60 + \theta) & \sin(60 - \theta) \\ R & R & R \end{bmatrix} \begin{bmatrix} F_{1H} \\ F_{2H} \\ F_{3H} \end{bmatrix} = \begin{bmatrix} 0 \\ 0 \\ T_Z \end{bmatrix}$$

Solving for the actuator forces, the angle θ drops out and the forces are evenly distributed among the three actuators:

$$\begin{cases} F_{1V} = \frac{1}{3} F_Z \\ F_{2V} = \frac{1}{3} F_Z \\ F_{3V} = \frac{1}{3} F_Z \end{cases} \quad \text{and} \quad \begin{cases} F_{1H} = \frac{1}{3R} T_Z \\ F_{2H} = \frac{1}{3R} T_Z \\ F_{3H} = \frac{1}{3R} T_Z \end{cases}$$

This result agrees with what would be expected from the stage symmetry. These two situations are shown in the figure below:



Combining the equations for force and torque, the transformation matrix between required stage forces and actuator forces can be found, in polar coordinates:

$$\begin{bmatrix} -\frac{2}{3} \cos \theta & 0 & 0 & \frac{1}{3R} \\ \frac{2}{3} \cos(\theta + 60) & 0 & 0 & \frac{1}{3R} \\ \frac{2}{3} \cos(\theta - 60) & 0 & 0 & \frac{1}{3R} \\ 0 & \frac{2}{3R} \cos \varphi & \frac{1}{3} & 0 \\ 0 & -\frac{2}{3R} \cos(\varphi + 60) & \frac{1}{3} & 0 \\ 0 & -\frac{2}{3R} \cos(\varphi - 60) & \frac{1}{3} & 0 \end{bmatrix} \begin{bmatrix} F_{X'} \\ T_{X'} \\ F_Z \\ T_Z \end{bmatrix} = \begin{bmatrix} F_{1H} \\ F_{2H} \\ F_{3H} \\ F_{1V} \\ F_{2V} \\ F_{2V} \end{bmatrix}$$

where for the torques the angle φ is used for the torques to signify that the horizontal torque and force directions are independent quantities. This is however a somewhat awkward way to describe the system.

The same matrix in Cartesian coordinates, which is a lot simpler:

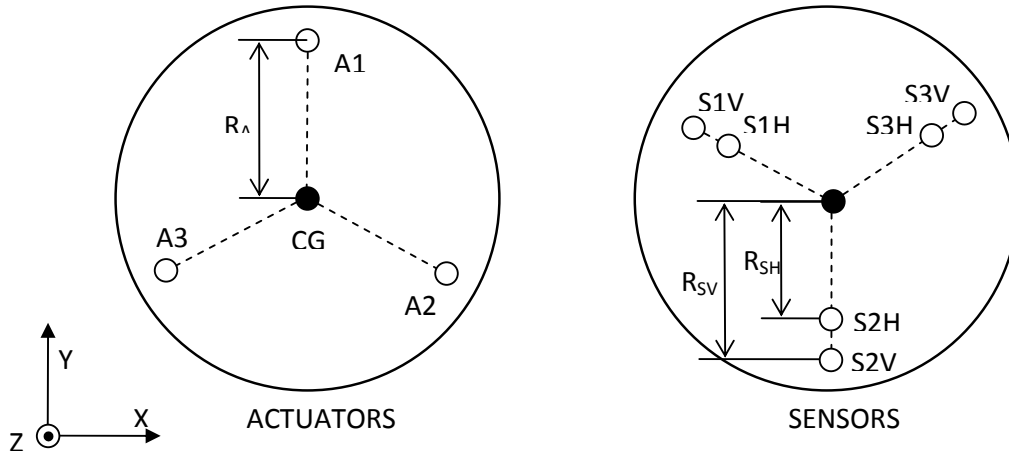
$$\begin{bmatrix} -\frac{2}{3} & 0 & 0 & 0 & 0 & \frac{1}{3R} \\ \frac{1}{3} & -\frac{\sqrt{3}}{3} & 0 & 0 & 0 & \frac{1}{3R} \\ \frac{1}{3} & \frac{\sqrt{3}}{3} & 0 & 0 & 0 & \frac{1}{3R} \\ 0 & 0 & \frac{1}{3} & \frac{2}{3R} & 0 & 0 \\ 0 & 0 & \frac{1}{3} & -\frac{1}{3R} & \frac{\sqrt{3}}{3R} & 0 \\ 0 & 0 & \frac{1}{3} & -\frac{1}{3R} & -\frac{\sqrt{3}}{3R} & 0 \end{bmatrix} \begin{bmatrix} F_X \\ F_Y \\ F_Z \\ T_X \\ T_Y \\ T_Z \end{bmatrix} = \begin{bmatrix} F_{1H} \\ F_{2H} \\ F_{3H} \\ F_{1V} \\ F_{2V} \\ F_{2V} \end{bmatrix}$$

D Derivation of coordinate transformation matrices

The overall system model has three coordinate transformation matrices:

- The AFT matrix, from CG forces to actuator forces
- The APT matrix, from CG positions to actuator positions
- The SPT matrix, from sensor positions to CG positions

The AFT and SPT matrices will also be used in the actual control system of the microslave stage. The matrices will be derived in this section. For the numbering convention of the actuators and sensors refer to the figure below.



It is assumed initially that the sensors and actuators lie on the vertices of equilateral triangles, centred around the moving mass CG. These two triangles are rotated 60° relative to each other. The actuators are 2-DoF, i.e. horizontal and vertical actuator forces act on the same point. The sensors are 1-DoF, i.e. the horizontal and vertical sensors have a different distance from the CG.

AFT matrix

The AFT matrix has already been derived in the previous section to calculate the maximum required actuator forces. It is used in both model and control system to calculate all actuator forces from the controller output, which are forces in CG coordinates. It is repeated here:

$$\{F_{ACT}\} = [AFT]\{F_{CG}\} \rightarrow$$

$$\begin{bmatrix} F_{1H} \\ F_{2H} \\ F_{3H} \\ F_{1V} \\ F_{2V} \\ F_{2V} \end{bmatrix} = \begin{bmatrix} -\frac{2}{3} & 0 & 0 & 0 & 0 & \frac{1}{3R_A} \\ \frac{1}{3} & -\frac{\sqrt{3}}{3} & 0 & 0 & 0 & \frac{1}{3R_A} \\ \frac{1}{3} & \frac{\sqrt{3}}{3} & 0 & 0 & 0 & \frac{1}{3R_A} \\ 0 & 0 & \frac{1}{3} & \frac{2}{3R_A} & 0 & 0 \\ 0 & 0 & \frac{1}{3} & -\frac{1}{3R_A} & \frac{\sqrt{3}}{3R_A} & 0 \\ 0 & 0 & \frac{1}{3} & -\frac{1}{3R_A} & -\frac{\sqrt{3}}{3R_A} & 0 \end{bmatrix} \begin{bmatrix} F_X \\ F_Y \\ F_Z \\ T_X \\ T_Y \\ T_Z \end{bmatrix}$$

In the actual device, $R_A = 12$ mm. The AFT matrix then becomes

$$\{F_{ACT}\} = [AFT]\{F_{CG}\} \rightarrow$$

$$\begin{bmatrix} F_{1H} \\ F_{2H} \\ F_{3H} \\ F_{1V} \\ F_{2V} \\ F_{2V} \end{bmatrix} = \begin{bmatrix} -0.667 & 0 & 0 & 0 & 0 & 27.8 \\ 0.333 & -0.577 & 0 & 0 & 0 & 27.8 \\ 0.333 & 0.577 & 0 & 0 & 0 & 27.8 \\ 0 & 0 & 0.333 & 55.6 & 0 & 0 \\ 0 & 0 & 0.333 & -27.8 & 48.1 & 0 \\ 0 & 0 & 0.333 & -27.8 & -48.1 & 0 \end{bmatrix} \begin{bmatrix} F_x \\ F_y \\ F_z \\ T_x \\ T_y \\ T_z \end{bmatrix}$$

APT matrix

This matrix is needed in the model to calculate the position dependent actuator forces. We assume that the effect of rotations on the actuator forces is negligible. The transformation matrix is then a 9 x 6 matrix. Referring again to the figure above, we have the following relations between disk CG displacements and actuator target x-translations:

$$\begin{cases} X_1 = -\cos(0) \cdot x - \sin(0) \cdot y + \psi \cdot R_A \\ X_2 = \cos(60) \cdot x - \sin(60) \cdot y + \psi \cdot R_A \\ X_3 = \cos(60) \cdot x + \sin(60) \cdot y + \psi \cdot R_A \end{cases}$$

For the y-translations:

$$\begin{cases} Y_1 = -\sin(0) \cdot x - \cos(0) \cdot y \\ Y_2 = \sin(60) \cdot x + \cos(60) \cdot y \\ Y_3 = -\sin(60) \cdot x + \cos(60) \cdot y \end{cases}$$

And for the z-translations:

$$\begin{cases} Z_1 = z + R_A \cdot \cos(0) \cdot \varphi + R_A \cdot \sin(0) \cdot \theta \\ Z_2 = z - R_A \cdot \cos(60) \cdot \varphi + R_A \cdot \sin(60) \cdot \theta \\ Z_3 = z - R_A \cdot \cos(60) \cdot \varphi - R_A \cdot \sin(60) \cdot \theta \end{cases}$$

When we again assume that there are no misalignments, this is in matrix form:

$$\{x_{ACT}\} = [APT]\{x_{CG}\}$$

$$\begin{bmatrix} x_1 \\ y_1 \\ z_1 \\ x_2 \\ y_2 \\ z_2 \\ x_3 \\ y_3 \\ z_3 \end{bmatrix} = \begin{bmatrix} -1 & 0 & 0 & 0 & 0 & R_A \\ 0 & -1 & 0 & 0 & 0 & 0 \\ 0 & 0 & 1 & R_A & 0 & 0 \\ \frac{1}{2} & -\frac{\sqrt{3}}{2} & 0 & 0 & 0 & R_A \\ \frac{\sqrt{3}}{2} & \frac{1}{2} & 0 & 0 & 0 & 0 \\ 0 & 0 & 1 & -\frac{R_A}{2} & \frac{\sqrt{3}R_A}{2} & 0 \\ \frac{1}{2} & \frac{\sqrt{3}}{2} & 0 & 0 & 0 & R_A \\ -\frac{\sqrt{3}}{2} & \frac{1}{2} & 0 & 0 & 0 & 0 \\ 0 & 0 & 1 & -\frac{R_A}{2} & -\frac{\sqrt{3}R_A}{2} & 0 \end{bmatrix} \begin{bmatrix} x \\ y \\ z \\ \varphi \\ \theta \\ \psi \end{bmatrix}$$

SPT matrix

The SPT matrix is needed in both the model and control system to convert the measured sensor positions to the displacement of the moving disk in CG coordinates. When the sensors are numbered as above, we have the following relations between sensor target displacements and CG displacements for the three vertical sensors:

$$\begin{cases} V_1 = z + R_{SV} \cdot \cos(60) \cdot \varphi + R_{SV} \cdot \sin(60) \cdot \theta \\ V_2 = z - R_{SV} \cdot \cos(0) \cdot \varphi + R_{SV} \cdot \sin(0) \cdot \theta \\ V_3 = z + R_{SV} \cdot \cos(60) \cdot \varphi - R_{SV} \cdot \sin(60) \cdot \theta \end{cases}$$

and for the three horizontal sensors:

$$\begin{cases} H_1 = -\cos(60) \cdot x - \sin(60) \cdot y + \psi \cdot R_{SH} \\ H_2 = \cos(0) \cdot x - \sin(0) \cdot y + \psi \cdot R_{SH} \\ H_3 = -\cos(60) \cdot x + \sin(60) \cdot y + \psi \cdot R_{SH} \end{cases}$$

Here two different radii are specified to allow placing the sensors at separate locations. Random numbers can in a later stage be added to the angles to represent misalignments. For now however, we assume the ideal case. The above equations then have the following matrix form:

$$\{x_{SENS}\} = [SPT]^{-1} \{x_{CG}\}$$

$$\begin{bmatrix} H_1 \\ V_1 \\ H_2 \\ V_2 \\ H_3 \\ V_3 \end{bmatrix} = \begin{bmatrix} -\frac{1}{2} & -\frac{\sqrt{3}}{2} & 0 & 0 & 0 & R_{SH} \\ 0 & 0 & 1 & \frac{R_{SV}}{2} & \frac{\sqrt{3}R_{SV}}{2} & 0 \\ 1 & 0 & 0 & 0 & 0 & R_{SH} \\ 0 & 0 & 1 & -R_{SV} & 0 & 0 \\ -\frac{1}{2} & \frac{\sqrt{3}}{2} & 0 & 0 & 0 & R_{SH} \\ 0 & 0 & 1 & \frac{R_{SV}}{2} & -\frac{\sqrt{3}R_{SV}}{2} & 0 \end{bmatrix} \begin{bmatrix} x \\ y \\ z \\ \varphi \\ \theta \\ \psi \end{bmatrix}$$

The SPT matrix needed for the simulation model converts the sensor positions to CG positions and is therefore the inverse of this matrix:

$$\{x_{CG}\} = [SPT] \{x_{SENS}\}$$

$$\begin{bmatrix} x \\ y \\ z \\ \varphi \\ \theta \\ \psi \end{bmatrix} = \begin{bmatrix} -\frac{1}{3} & 0 & \frac{2}{3} & 0 & -\frac{1}{3} & 0 \\ -\frac{\sqrt{3}}{3} & 0 & 0 & 0 & \frac{\sqrt{3}}{3} & 0 \\ 0 & \frac{1}{3} & 0 & \frac{1}{3} & 0 & \frac{1}{3} \\ 0 & \frac{1}{3R_{SV}} & 0 & -\frac{2}{3R_{SV}} & 0 & \frac{1}{3R_{SV}} \\ 0 & \frac{\sqrt{3}}{3R_{SV}} & 0 & 0 & 0 & -\frac{\sqrt{3}}{3R_{SV}} \\ \frac{1}{3R_{SH}} & 0 & \frac{1}{3R_{SH}} & 0 & \frac{1}{3R_{SH}} & 0 \end{bmatrix} \begin{bmatrix} H_1 \\ V_1 \\ H_2 \\ V_2 \\ H_3 \\ V_3 \end{bmatrix}$$

In the actual system this matrix will have to be adapted to match the microslave geometry. In particular, the angles will be different than assumed here, namely:

$$\begin{cases} V_1 = z + R_{SV} \cdot \cos(70) \cdot \varphi + R_{SV} \cdot \sin(70) \cdot \theta \\ V_2 = z - R_{SV} \cdot \cos(10) \cdot \varphi - R_{SV} \cdot \sin(10) \cdot \theta \\ V_3 = z + R_{SV} \cdot \cos(50) \cdot \varphi - R_{SV} \cdot \sin(50) \cdot \theta \end{cases}$$

and

$$\begin{cases} H_1 = -\cos(68) \cdot x - \sin(68) \cdot y + \psi \cdot R_{SH} \\ H_2 = \cos(8) \cdot x + \sin(8) \cdot y + \psi \cdot R_{SH} \\ H_3 = -\cos(50) \cdot x + \sin(50) \cdot y + \psi \cdot R_{SH} \end{cases}$$

We then have the inverse matrix

$$\{x_{SENS}\} = [SPT]^{-1} \{x_{CG}\}$$

$$\begin{bmatrix} H_1 \\ V_1 \\ H_2 \\ V_2 \\ H_3 \\ V_3 \end{bmatrix} = \begin{bmatrix} -0.37 & -0.93 & 0 & 0 & 0 & R_{SH} \\ 0 & 0 & 1 & 0.34R_{SV} & 0.94R_{SV} & 0 \\ 0.99 & 0.14 & 0 & 0 & 0 & R_{SH} \\ 0 & 0 & 1 & -0.98R_{SV} & -0.17R_{SV} & 0 \\ -0.62 & 0.79 & 0 & 0 & 0 & R_{SH} \\ 0 & 0 & 1 & 0.64R_{SV} & -0.77R_{SV} & 0 \end{bmatrix} \begin{bmatrix} x \\ y \\ z \\ \varphi \\ \theta \\ \psi \end{bmatrix}$$

which becomes, with sensor radii of 11.9 mm for the vertical and 5 mm for the horizontal sensors

$$\{x_{SENS}\} = [SPT]^{-1} \{x_{CG}\}$$

$$\begin{bmatrix} H_1 \\ V_1 \\ H_2 \\ V_2 \\ H_3 \\ V_3 \end{bmatrix} = \begin{bmatrix} -0.37 & -0.93 & 0 & 0 & 0 & 0.005 \\ 0 & 0 & 1 & 0.0041 & 0.0112 & 0 \\ 0.99 & 0.14 & 0 & 0 & 0 & 0.005 \\ 0 & 0 & 1 & -0.0117 & -0.0020 & 0 \\ -0.62 & 0.79 & 0 & 0 & 0 & 0.005 \\ 0 & 0 & 1 & 0.0076 & -0.0092 & 0 \end{bmatrix} \begin{bmatrix} x \\ y \\ z \\ \varphi \\ \theta \\ \psi \end{bmatrix}$$

And finally, the sensor coordinate transformation matrix is the inverse of this matrix:

$$\{x_{CG}\} = [SPT]\{x_{SENS}\}$$

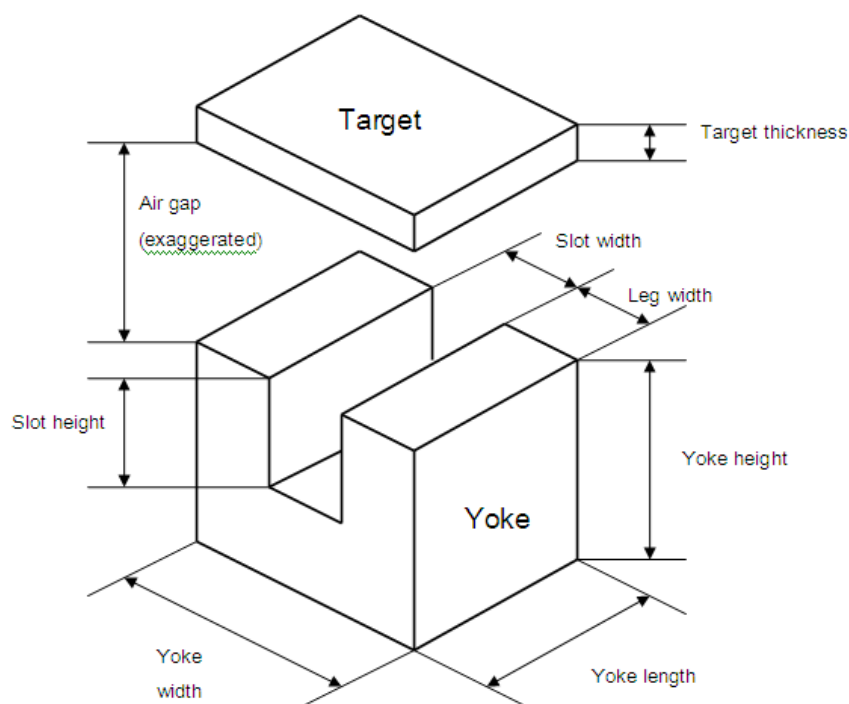
$$\begin{bmatrix} x \\ y \\ z \\ \varphi \\ \theta \\ \psi \end{bmatrix} = \begin{bmatrix} -0.249 & 0 & 0.660 & 0 & -0.411 & 0 \\ -0.618 & 0 & 0.096 & 0 & 0.522 & 0 \\ 0 & 0.333 & 0 & 0.333 & 0 & 0.333 \\ 0 & 19.5 & 0 & -55.4 & 0 & 35.8 \\ 0 & 52.4 & 0 & -9.50 & 0 & -42.9 \\ 66.7 & 0 & 66.7 & 0 & 66.7 & 0 \end{bmatrix} \begin{bmatrix} H_1 \\ V_1 \\ H_2 \\ V_2 \\ H_3 \\ V_3 \end{bmatrix}$$

E Finite element modelling of reluctance actuators

Preliminary calculations on Reluctance Actuators

First, to obtain some insight into the order of magnitude of the forces and dimensions involved, the simplest actuator geometry will be considered. This is a single vertical (or horizontal, but then the force requirements are lower) reluctance actuator consisting of an iron U-shape wound with a coil and an iron target. Permanent magnets used for biasing purposes are not yet considered here.

Due to the required small size and weight of the flotor, the target dimensions will be limited. This means magnetic saturation of the iron will probably occur in the target first. As a first approximation, a target with a surface area of $4 \times 5 \text{ mm}^2$ and a 1 mm thickness will be assumed. This will ensure the target and corresponding yoke with copper windings will not be too large. The required maximal force is 100 mN static, 10 mN dynamic. The target will be incorporated into the flotor disk. The main yoke dimensions are shown in the sketch below.



The required travel range is at least $200 \mu\text{m}$, while the linearity should be as good as possible over this range to simplify the control scheme. The air gap has to be sufficiently large to accommodate the travel range, $100 \mu\text{m}$ in both directions. A larger air gap will lead to a smaller maximum force, but a more linear behaviour. For now, a $500 \mu\text{m}$ gap will be considered.

The maximum allowed current density J is assumed to be 4 A/mm^2 , which is a commonly used value for coils, transformers and the like. This is probably a conservative estimate, since the surface-to-volume ratio of these small actuator coils will be much higher than that of a power transformer. Therefore, values of $5 - 6 \text{ A/mm}^2$ should be possible (6 for wires in free air), but to be on the safe side in this phase of the calculations a value of 4 will be used.

The maximum attainable reluctance force in the actuator is limited by this maximum current density and saturation of the iron. The magnetic saturation is greatly simplified for these preliminary

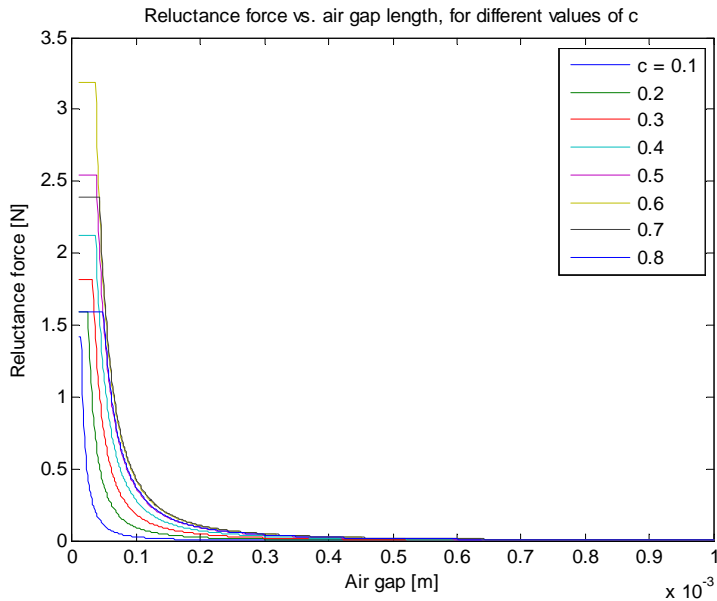
calculations, a straight cut-off at 1 T is assumed. This is also a conservative estimate. Although the saturation of the iron has to be considered here, the reluctance of the yoke and target can still be neglected with respect to the reluctance of the air gap (as long as the iron is not saturated).

For a U-shaped iron yoke with two air gaps the flux density is given by $B = \mu_0 \frac{NI}{2s}$ where NI is the applied magneto motive force (mmf, in ampere-turns) and s is the air gap length. The maximum NI is independent of the actual number of turns or maximum wire current, since the product of these terms is constant and is limited by the maximum J . This yields $NI_{\max} = J \cdot A_c \cdot K_b$ where K_b is the winding bulk factor, here assumed to be 0.8. A_c is the total winding cross-sectional area, defined by the slot width and height.

The windings can be wound around one or both legs, the latter configuration will lead to a more symmetric flux distribution. The winding method does not affect the maximum number of turns or NI .

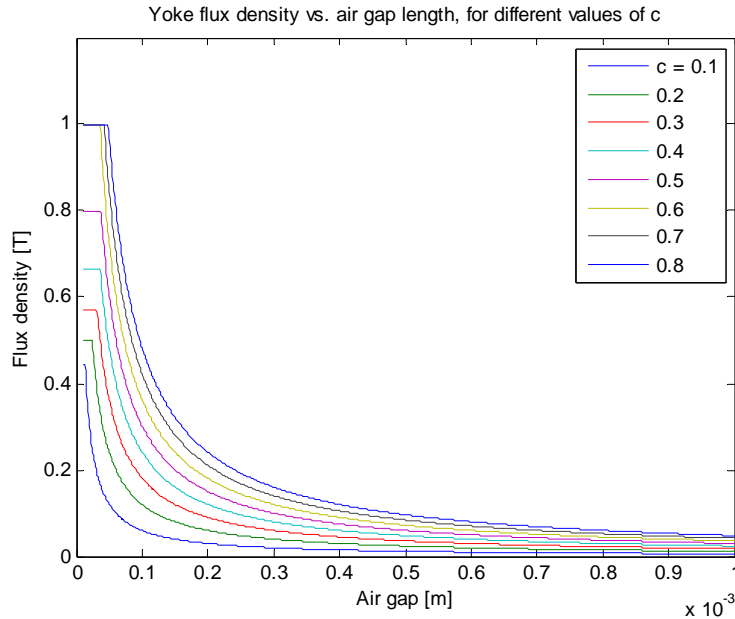
The maximum reluctance force now follows as $f_{\max} = \frac{B^2 A_a}{\mu_0} = \frac{1}{4} \mu_0 A_a \frac{(NI_{\max})^2}{s^2}$ where A_a is the cross-sectional area of one air gap.

The yoke height h can be varied in this setup, as well as the slot width. The latter is considered first, with a fixed yoke height of 10 mm and a slot height of 6 mm. The slot width can be defined in terms of the yoke width as $w_s = c \cdot w_y$ where w_y is the yoke width. A wider slot will allow a larger NI_{\max} , but the air gap area A_a will decrease, so there will be an optimum somewhere. The parameter c is varied from 0.1 to 0.8 in steps of 0.1 in the following calculation. The maximum force, limited by current and saturation, is then plotted for each value of c against the air gap length.



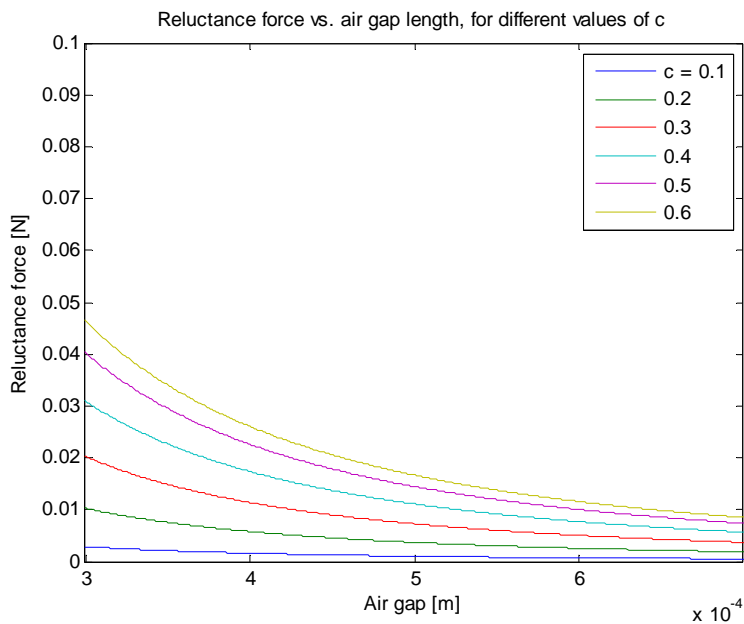
From this plot it follows that saturation will not be a problem for forces of the required magnitude, and that a value of 0.6 is roughly the optimum for the factor c with respect to maximal force (this is independent of the actual yoke dimensions). Also it is clear the actuator is highly nonlinear, since the force varies inversely with the square of the air gap length. For $c > 0.6$ an additional effect is that the

cross-section of the yoke legs becomes smaller than that of the target, so in that case it is the yoke that saturates first. The flux density in the yoke is shown in the following plot:



It can be seen that saturation ($B > 1$ T) occurs in this geometry only for gap lengths smaller than $100 \mu\text{m}$, when the force is far too large and the gap too small. This point will never be reached under operating conditions of the stage, so saturation will not be a problem. Also the effect that the target saturates before the yoke does for $c \leq 0.6$ can be observed.

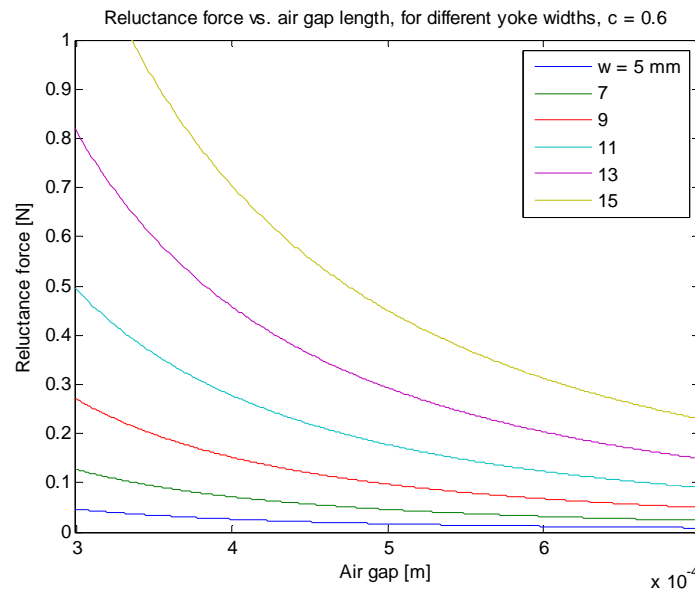
Zooming in on the first plot, we can see what happens around the operating point when $s = 500 \mu\text{m}$. This is shown below. To achieve gravity compensation, a static force of 100 mN should be generated.



When an air gap of $500 \mu\text{m}$ is considered along with the required travel range of $200 \mu\text{m}$ around this point, it becomes clear that this actuator can not supply the required force, and is still very nonlinear

(20 – 30% nonlinearity over this range). Therefore, at least one of the actuator dimensions has to be increased.

Now setting $c = 0.6$ and varying the yoke width yields the following results:

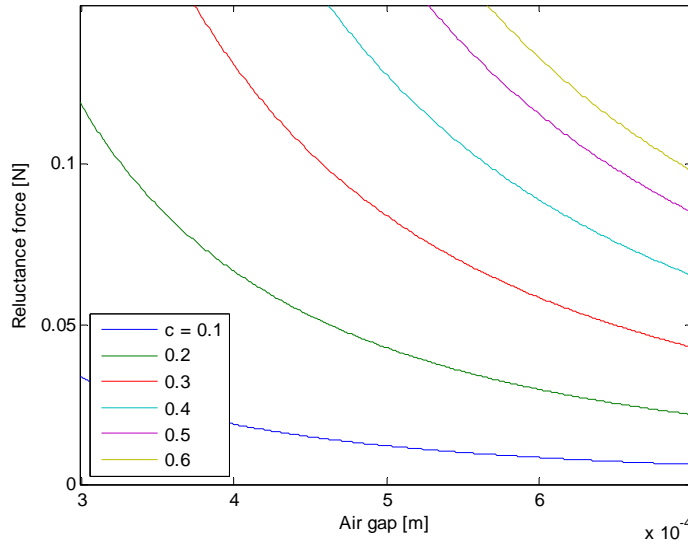


From this plot and the equations it follows that the maximum attainable force varies with the 3rd power of the yoke width. (If c is not varied, NI and A_o go as w_y , while f goes as the square of NI and linearly with A_o .) Similar calculations show that the maximum force varies linearly with yoke length and with the square of the yoke height, when all other parameters are kept constant. This is also follows from the force and flux density equations.

Therefore, an actuator that is strong enough can easily be constructed this way, by slightly increasing each dimension. Especially increasing the width would improve the force, but may lead to an actuator target that is too large for the application. Varying the height would be less critical.

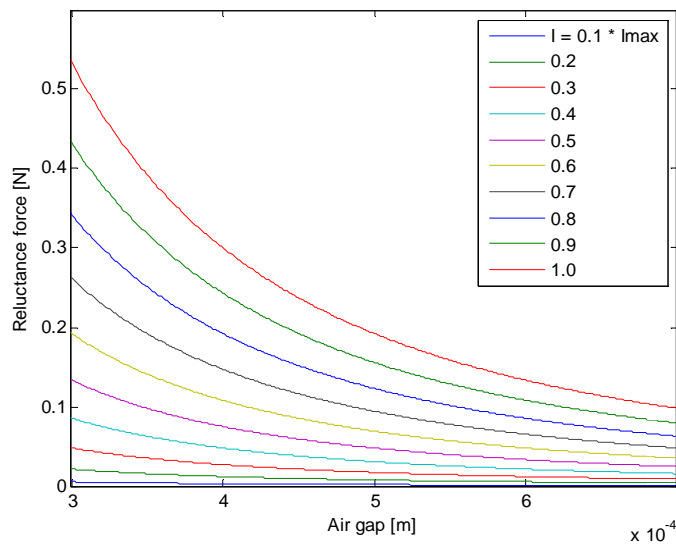
If all dimensions are slightly increased, an actuator with a yoke of 7 mm wide by 5 mm long, and which is 15 mm high, will be able to deliver a force of 150 mN over almost the entire range. The target is correspondingly enlarged to 7 x 5 x 1 mm. This is shown below.

Reluctance force vs. air gap length, for different values of c , yoke dimensions $7 \times 5 \times 15$ mm



The force can of course still be varied by varying the actuator current, and goes as the square of this current. This yields the following force characteristic for this actuator:

Reluctance force vs. air gap length, for different values of coil current I



Differential actuator

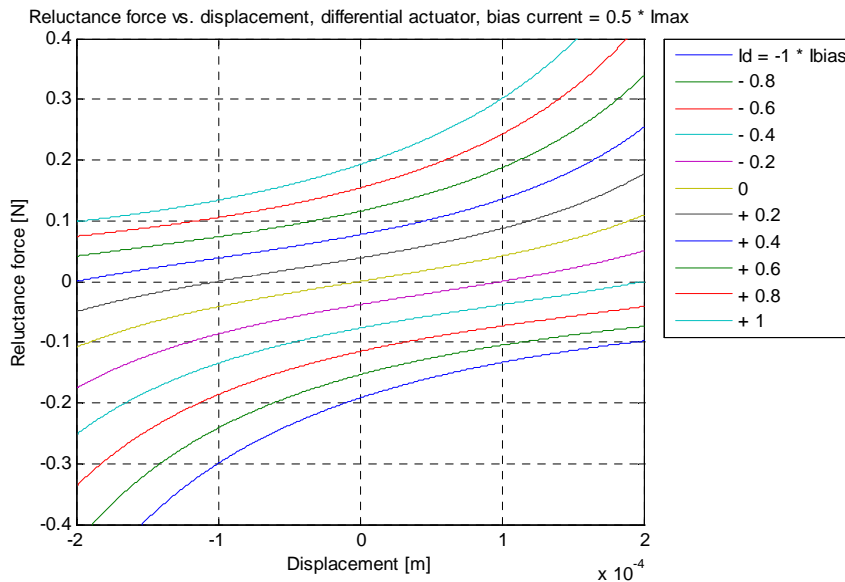
All in all, this type of actuator is very nonlinear in both current and displacement, and therefore far from ideal for this application. Also, the actuator can generate forces in one direction only. This would mean that the gravitational force has to be used to move the flotor downwards. The required accelerations are a fraction of the gravitational acceleration, so this would be possible. However, this is of course not controllable, and wouldn't work at all for the horizontal actuators. A better approach would be to use a symmetric or differential actuator, which has two yokes opposing each other and a target on either side of the levitated disk.

The flux density in one actuator is still governed by the equation $B = \mu_0 \frac{NI}{2s}$ but since the symmetric actuator is operated in differential mode, it is more convenient to write this as

$B^+ = \mu_0 \frac{N(I_0 + I_d)}{2(s_0 - s_d)}$ where I_0 is the bias current, I_d the differential current, s_0 the air gap length of the operating point and s_d the displacement from this operating point. This is the equation for the top actuator, the bottom actuator flux density then is given by $B^- = \mu_0 \frac{N(I_0 - I_d)}{2(s_0 + s_d)}$. These equations can still be used to check for saturation.

The actuator forces are given by $f^+ = \frac{1}{4} \mu_0 A_a \frac{N^2 (I_0 + I_d)^2}{(s_0 - s_d)^2}$ and $f^- = \frac{1}{4} \mu_0 A_a \frac{N^2 (I_0 - I_d)^2}{(s_0 + s_d)^2}$, the resulting force is the difference of these two, $f = f^+ - f^-$. Note that although in these equations N is used, the actual number of turns is unimportant at this stage since the product NI still is a constant.

When both halves of the actuator have a yoke that is 7 x 5 mm and 15 mm high, the following results are obtained:



In this case the bias current is set to half the maximal current, which ensures the largest force range without overloading the coils. The maximum allowed NI is about 160 ampere-turns, so the bias NI_{bias} is 80 ampere-turns. The behaviour of the actuator is more linear than that of a single actuator, but non-linearities are still present. In practise this will be worse since the magnetisation curve of iron is not a straight line. In the operating point, where the air gap is 500 μm and the resultant force 100 mN, the differential current is then about 0.5 times the bias current. This means the top actuator runs at 75 % of its current capability and the bottom actuator at about 25 %.

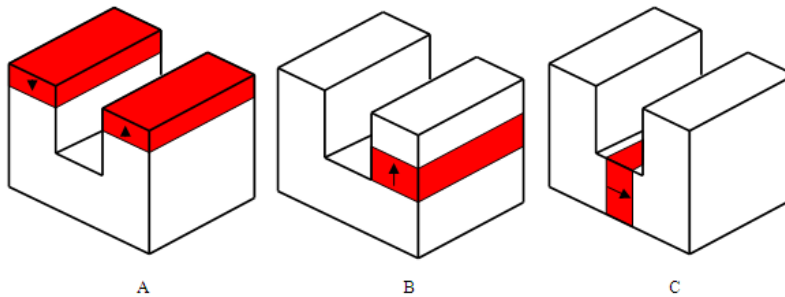
Permanent magnet biased differential actuator

Since the bias flux is constant, it can be supplied by permanent magnets. Because these are passive components, the required electrical power can be lower, improving the actuator efficiency, reducing thermal issues and decreasing the actuator size or increasing its force capabilities. It is even possible to use a stronger magnet in the top actuator, so that the resulting force is not zero but just large enough to compensate the weight of the flotor. Another way to achieve this is by making the lower air gap (at zero displacement of the flotor) slightly wider than the upper one. In that case, the actuators have to supply a differential force of only 10 mN.

When a NdFeB permanent magnet is used, the effective air gap length increases by the thickness of the magnet, because this material has a relative permeability that is close to unity. The presence of the larger air gap increases the reluctance of the magnetic circuit, which leads to a more linear actuator behaviour. This also has the additional advantage that the actuator inductance is reduced, which makes the actuator faster (smaller electrical time constant). Commercially available magnets have an internal remanent flux density on the order of 1.3 T. This results in a flux density in the yoke that is an order of magnitude greater than when no permanent magnets are used. This enables far greater forces, and a far more linear force characteristic. Calculations show that saturation is still not

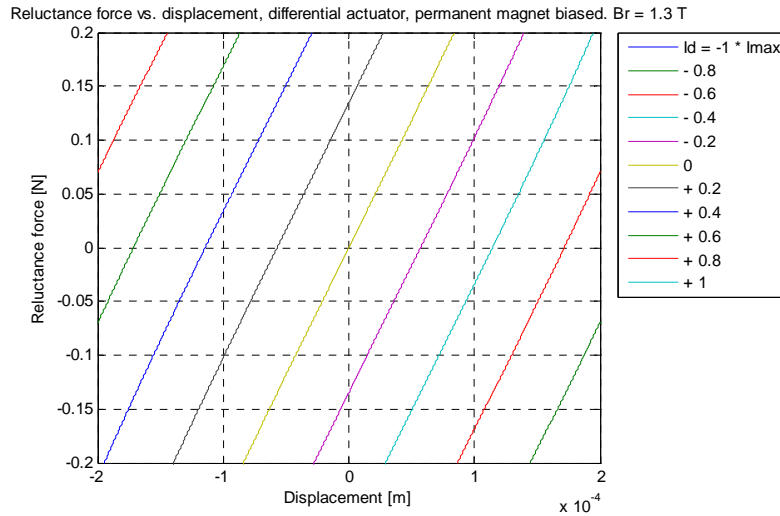
a problem. The equivalent magneto motive force is given by $mmf_{eq} = \frac{B_r \cdot l_m}{\mu_0}$ where l_m is the magnet length. Commercially available magnets can have lengths of $\frac{1}{2}$ or 1 mm, which is sufficient for this application.

A number of possible geometries to incorporate a permanent magnet in the yoke are shown below:

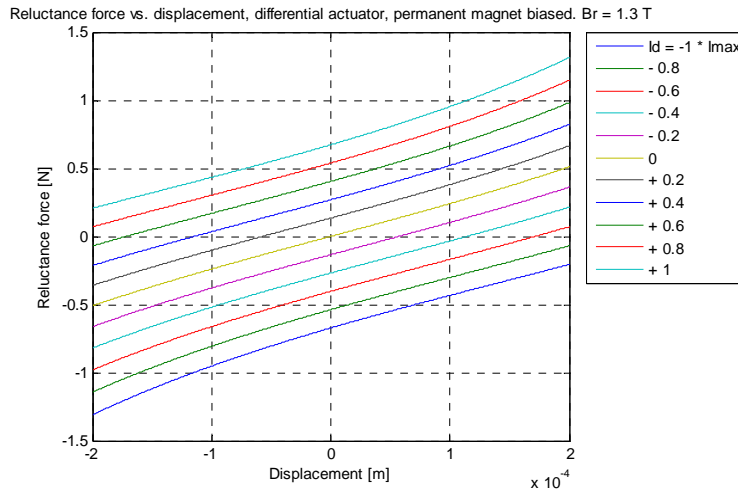


A configuration like (A) will probably lead to large flux leakage, so it would be better to put the magnet between two iron parts, like in configuration (B). To ensure a symmetric flux distribution, this configuration could also use two magnets. However, configurations with two magnets are more complicated and may lead to an effective air gap that is too large, reducing the available force. Therefore, configuration (C) is probably preferable, needing only one magnet and being symmetrical. It has the additional advantage that the dimensions of the yoke legs are decoupled from the dimensions of the magnet, which is not available in arbitrary sizes.

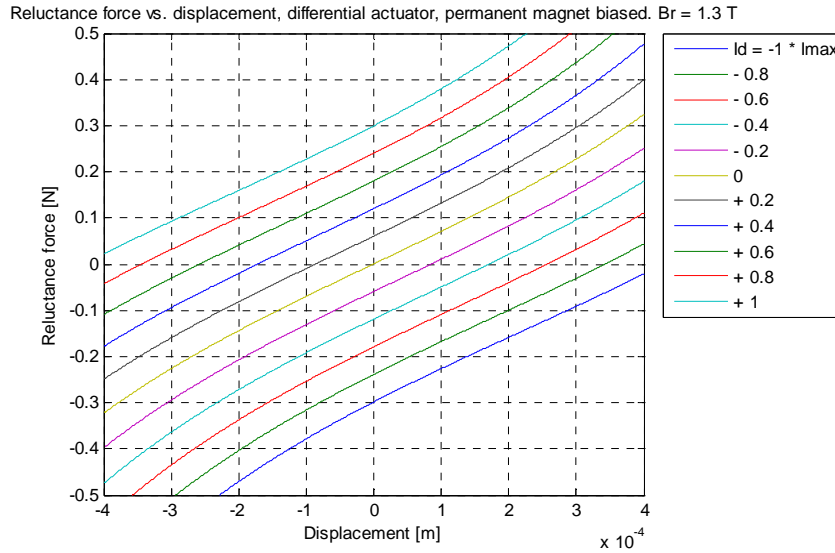
The equivalent (bias) mmf of a magnet of 0.5 mm thickness in this setup is about 520 ampere-turns, which is indeed almost nine times the bias mmf that could be reached without permanent magnets. This results in the following force characteristic:



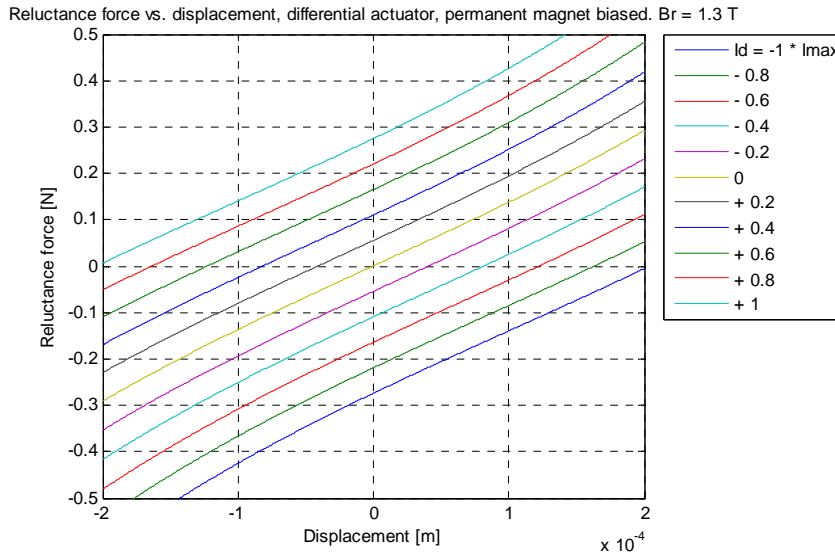
The force characteristics are much steeper, and the force range is dramatically increased. The full force range is shown in the figure below. The maximum force is now increased to 1.3 N, which is about ten times overspecified. This has the disadvantage, however, that the actuator stiffness becomes more negative, so it would be more difficult to stabilise in a control loop.



The overspecification means that the yoke could be made smaller, or the air gap length increased. The latter option will enable a larger travel range, but at the expense of force range. Linearity will improve on the original travel range, but the extended travel range will be less linear. Shown below is the force characteristic when the air gap is increased to 1 mm on either side, with a travel range of 800 μm :

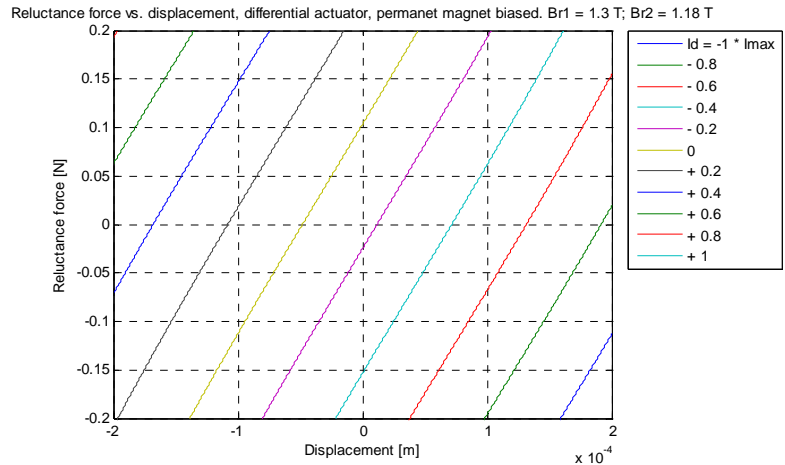


Another option is to reduce the yoke and target sizes but keep the same force range as the actuator without permanent magnets. If the target size is reduced to the original 5 x 4 mm, but yoke height is kept at 15 mm, we obtain the following results:



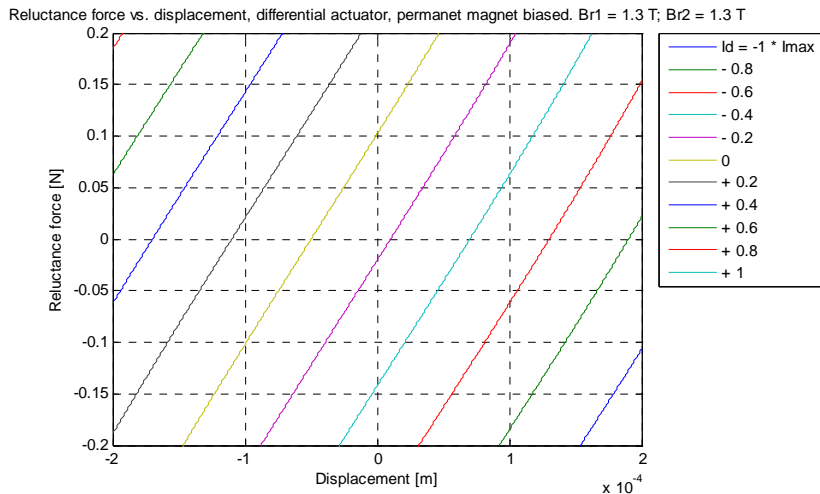
However, flux leakage could be a serious issue with such small dimensions. FEM calculations will have to be used to determine this.

In order to compensate the gravity force, so that the nominal current in the operating point is zero, a weaker permanent magnet (of the same dimensions) could be used in the bottom actuator. For instance, when the top magnet remanent flux density B_r is 1.3 T and the bottom magnet B_r is 1.18 T, the resultant force is exactly 100 mN in the operating point when the coil currents are zero. This is shown in the plot below, with the yoke dimensions returned to 7 x 5 mm and a 0.5 mm air gap:



However, the properties of the magnets would have to be exactly right, and magnets are not available for every value of B_r . This value is also subject to tolerances, which would make tuning of the setup to exact gravity compensation difficult.

A better solution is to use two identical actuators, but with different air gaps. For instance, if the top air gap is kept at $500 \mu\text{m}$, but the bottom gap is increased to $600 \mu\text{m}$, we get the following results:



This is almost identical to the previous plot, but much easier to practically realise.

A point to note for the permanent magnet biased actuators is that the target may get stuck to the yoke when it comes too close. As the displacement gets bigger, there will be a certain point where the coil and magnet of one actuator are no longer able to counter the permanent magnet reluctance force of the other. At that point the net reluctance force can not be controlled anymore and can only be in one direction. This causes instability. Therefore, it is important that this point lies (preferably far) outside the travel range of the flotor. Mechanical stops could also be used to prevent the target getting stuck to the yoke.

Horizontal actuators

These can be made using the same principles, but can be much smaller since the force requirements are much lower (5 mN dynamic, no static force). However, this would require vertically mounted targets, which interferes with the demand that the flotor be a flat disk. These targets could be made smaller, for instance about 2 by 5 mm would be sufficient, with a yoke height of 8 mm. However,

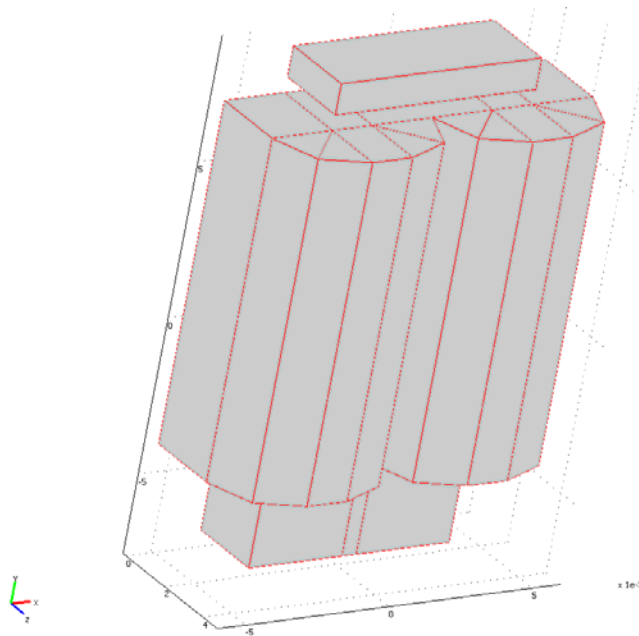
manufacturing of such small actuators may pose difficulties, and flux leakage will probably become an important factor, for which more detailed calculations would be necessary.

FEM Calculations

All (analytical) calculations so far are based on a lot of simplifications. These include:

- the iron has zero reluctance and hysteresis (dynamic behaviour) is not considered
- all flux passes through the iron, i.e. no flux leakage at air gap or magnets
- the flux crosses the air gap perpendicularly and has a uniform distribution
- saturation of the iron occurs at 1 T, as a straight cut-off

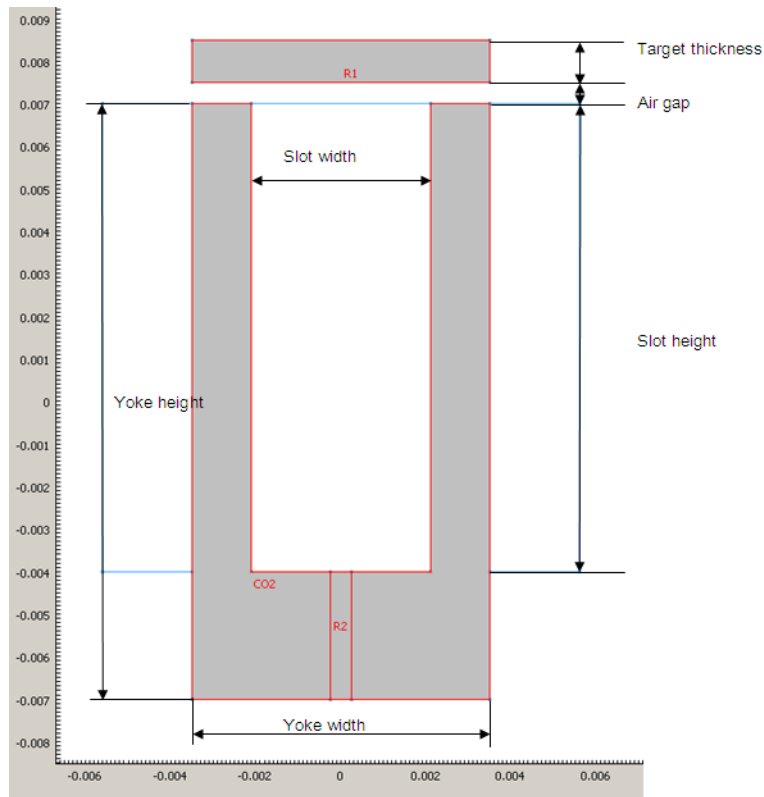
In order to obtain more detailed results, finite element calculations are carried out for the reluctance actuators. First of all, a model of the actuator is made using the AC/DC module of the COMSOL package. An overview of the actuator model geometry is shown below:



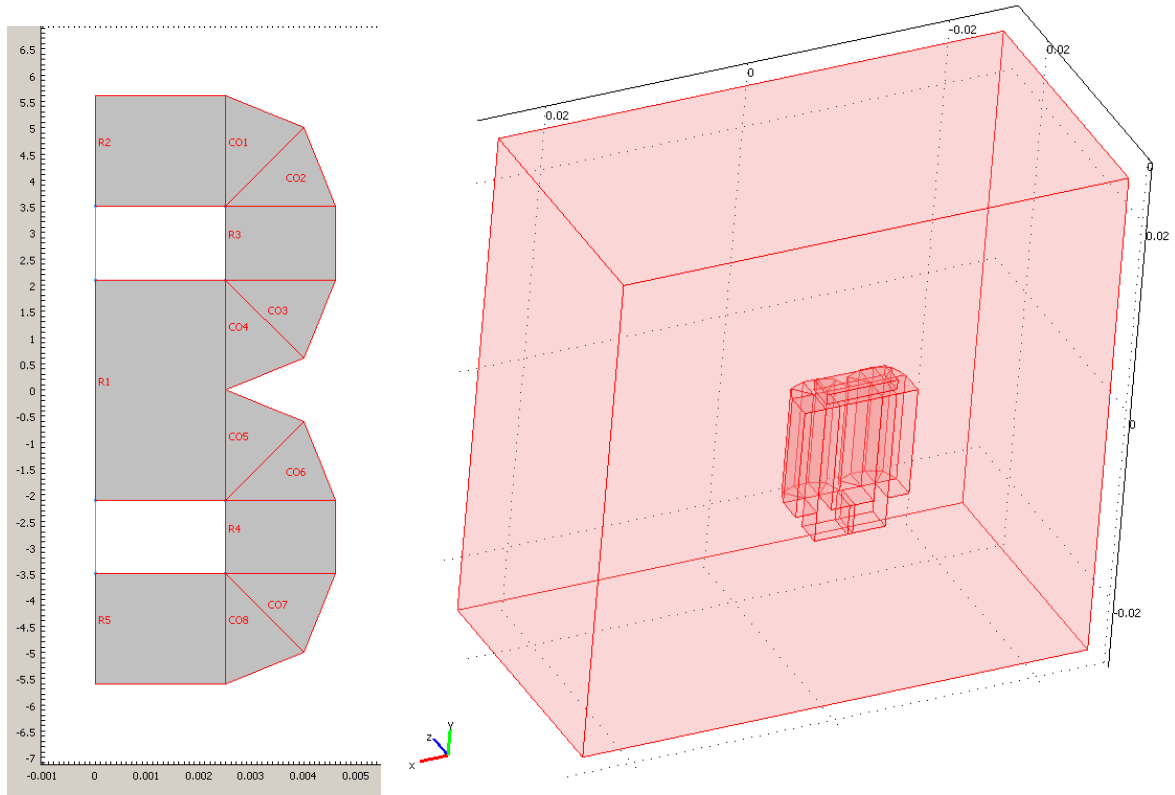
In this figure, the actuator yoke with magnet is shown, surrounded by the coils. A ferromagnetic target is positioned at a small distance above the yoke.

Since the actuator is symmetrical about the XY-plane, a half model is used to reduce calculation time. The model could be further reduced by exploiting symmetry about the YZ-plane as well, but this does not provide a closed flux path and therefore leads to erroneous results.

The model is built up as follows: In the XY-plane the yoke, magnet and target cross-sections are drawn, as shown below. The yoke is defined by the composite geometry CO1, the target by rectangle R1 and the magnet by rectangle R2. In this chapter, the dimensions are named in the same way as in the analytic calculations. For now, a yoke geometry of 7 by 5 mm, with a height of 14 mm is kept to be able to directly compare FEM results to the analytic results. A magnet of 3 x 5 mm and 0.5 mm thickness is used. Later on, these dimensions are varied in a parametric analysis to find the optimum geometry. The air gap is set to 0.5 mm here.



This geometry is then extruded in the z-direction over a distance of 2.5 mm, which is half the yoke length. Next, a cross-section of the coil geometry is drawn in the XZ-plane as shown below. The four quarter-circular sections of the windings are each divided into two triangular sections. This is done so that a simple constant current density condition can be used for each coil domain, where the current flows in a straight line, parallel to the wires. Subdividing into two triangular sections instead of just one improves the model accuracy. The coil cross-section is then extruded in the y-direction along the slot height to obtain the coil geometry.

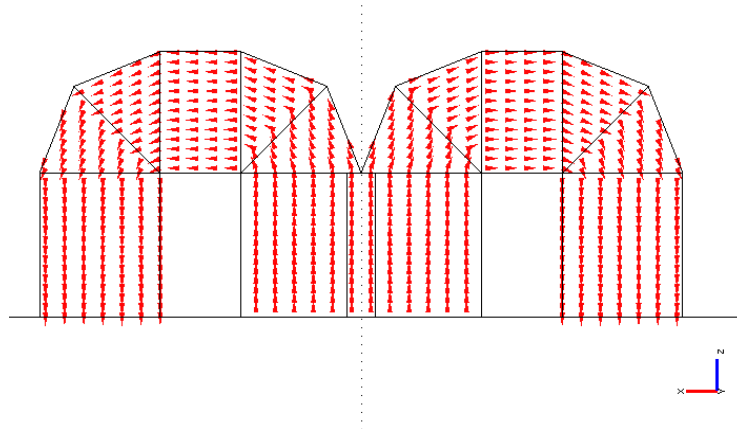


Finally, a rectangular block of 50 x 50 x 25 mm is drawn around the actuator to represent the air and non-ferromagnetic materials around the actuator and to define the external model boundaries. This results in the complete model geometry shown above on the right.

Boundary conditions

A magnetic insulation condition is applied to all external boundaries. At the boundaries of the air volume except for the symmetry plane ($z = 0$) the distance from the actuator is assumed to be large enough that there are no magnetic field lines present in this area. The symmetry plane itself also has a magnetic insulation condition because in this plane the field lines are assumed to be all in-plane. That is, the magnetic field has no z -component here because of the model symmetry.

A constant current density, equal to that used in the analytic calculations ($3.2 \cdot 10^{-6} \text{ A/m}^2$) is applied to all coil segments, in the direction of the wires. This is shown below:



Further parameters are:

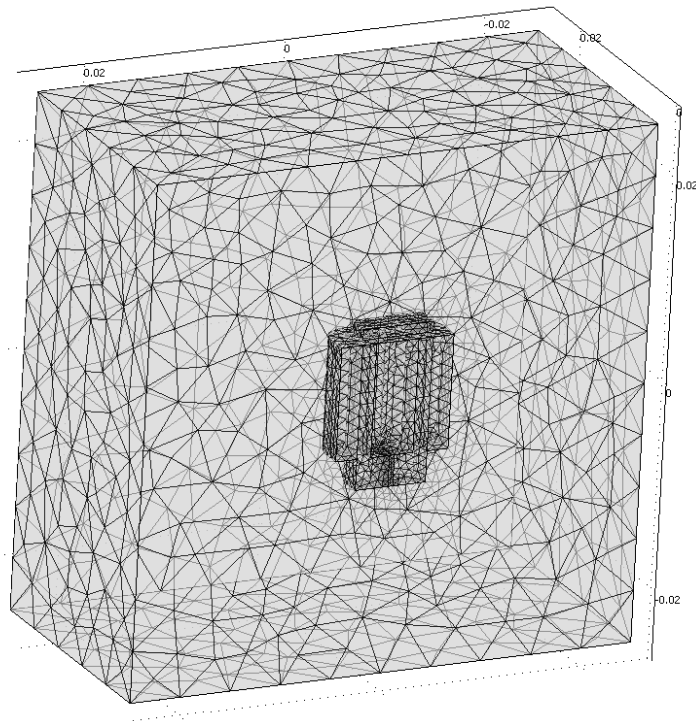
- Relative magnetic permeability. This is assumed to be 1 for the air, non-ferromagnetic coil material and for the neodymium magnet. The relative permeability of the iron yoke and target is assumed to be 5000, where a linear behaviour is assumed. In this phase of the calculations the magnetic saturation of the iron is not yet taken into account.
- Permanent magnet remanent flux density: This is set to the value specified by the supplier of the magnets, namely 1.37 T.

Meshing

The accuracy of the FEM results depends of course on the meshing of the model. In general, the results are more accurate the finer the mesh is. However, computation time increases exponentially with the number of elements, so an optimum element size has to be found. This was done experimentally, as follows: The model is solved using COMSOL, and then exported to an .m file, to be run in Matlab. This way, the model geometry can be varied by editing the .m file, as will be done later on in the parametric analysis.

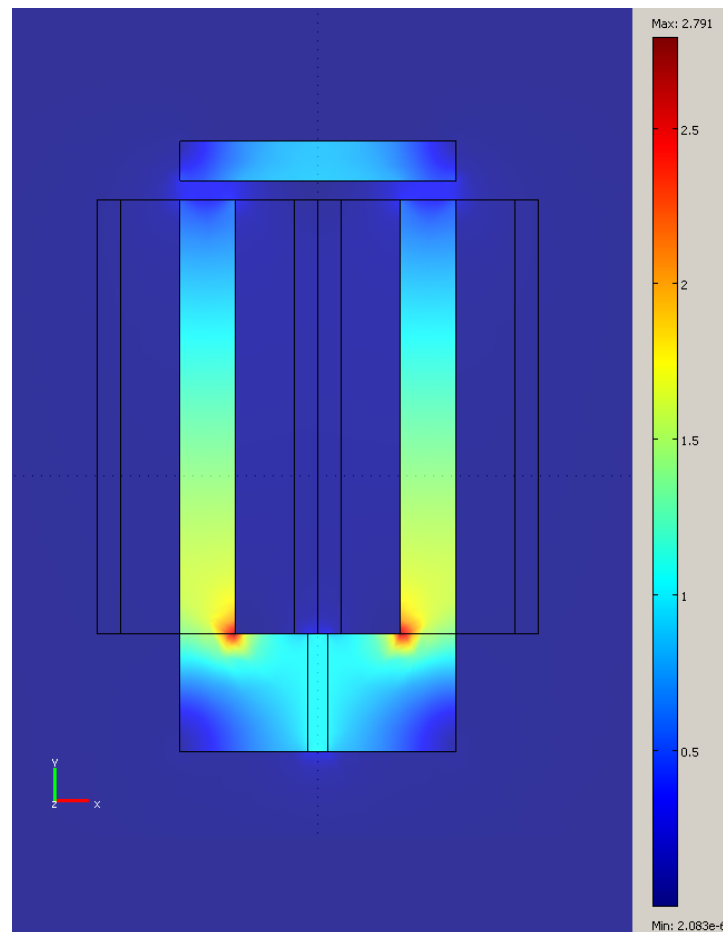
When the model geometry is altered slightly (dimensions increased by a micrometer or so), the results should stay almost the same. However, a slightly different geometry results in a different mesh, and when the meshing is too coarse, the results of the two runs will differ significantly. Therefore, the meshing was refined until the results of the altered and unaltered geometries were within 0.5 % of each other.

This resulted in minimum element sizes of $0.5 \cdot 10^{-3}$ m for the magnet, $1.0 \cdot 10^{-3}$ m for the yoke and target, and $1.5 \cdot 10^{-3}$ m for the coils. The air volume has no fine details away from the actuator, so here the element size could be left at the default value of $1/10^{\text{th}}$ of the largest dimension (in this case 5 mm). The resulting meshed model is shown below. The computation time for this model was about 30 seconds, for approximately 170,000 degrees of freedom.



Solution and postprocessing

The model was solved using the standard linear solver for time-independent (static) problems FGMRES, for a magnetostatic analysis with currents (emqa). In the figure below, the magnetic flux intensity in the actuator is plotted in the XY-plane. Because of the high magnetic permeability of the iron, most flux stays in the yoke and target. There is some leakage around the magnet and at the air gap, but it is not large. An important result is the peak value of the flux, which is almost 2.8 T. This is not a realistic value, since most iron will saturate at about 1.7 T. Because saturation was not considered here, there is no upper limit on the flux density in the iron and all magnetic field lines will take the shortest possible path through the iron. This leads to the high flux density at the corners of the yoke. To obtain the reluctance force acting on the target, the y-component of the Maxwell stress tensor is integrated over all six sides of the target volume.



Force characteristic – single actuator

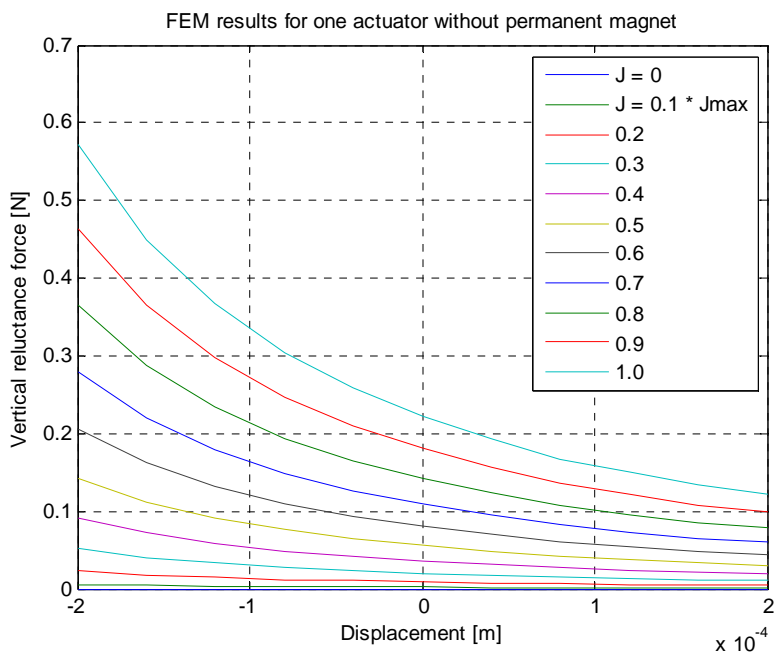
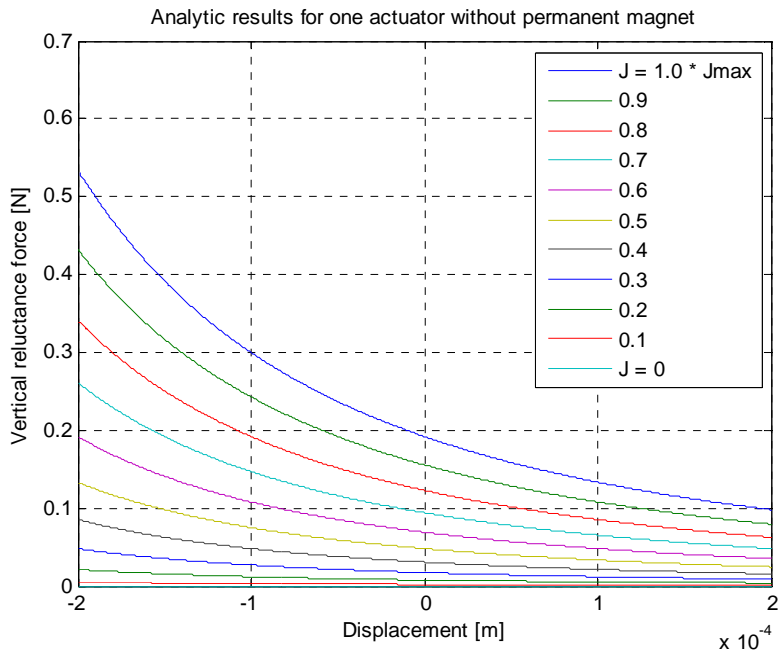
The .m file of the model is placed in a nested loop using Matlab, in which the air gap length and current density are varied, to obtain the force characteristic. The air gap is varied in 11 steps from 300 to 700 μm , and the current density in 11 steps from -3.2 to $+3.2 \cdot 10^6$ A/m^2 . This leads to a total of 121 points to be evaluated. The number of points in each loop has to be odd, so that a zero-displacement (gap = 500 μm) line is obtained as well as a zero-current line. These lie in the middle of

the investigated range. The current is varied from the negative maximum value to the positive maximum value. This is done because the flux generated by the coils counteracts the permanent magnet flux in the former case and contributes to it in the latter case.

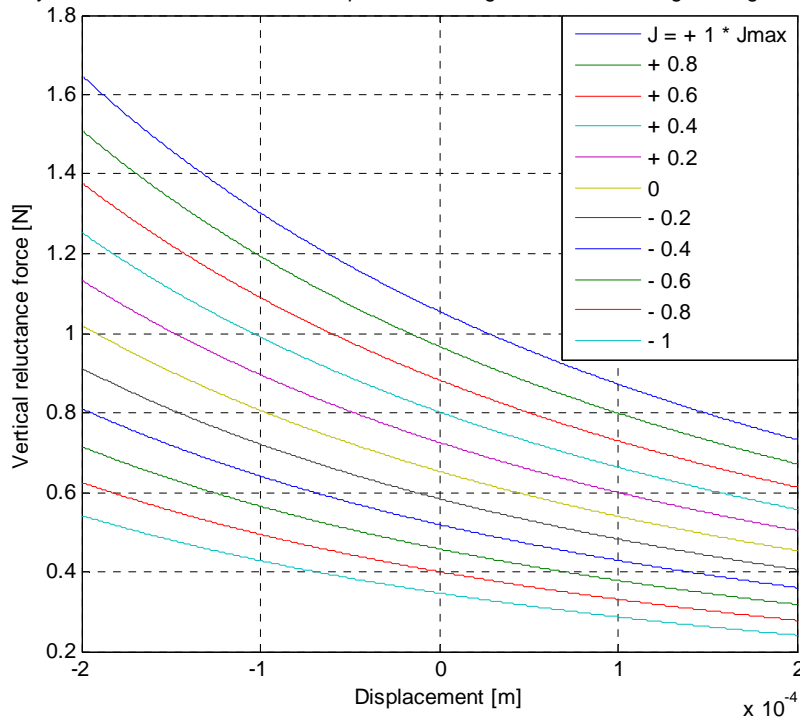
This loop is run three times, for actuators without, and with a 0.5 mm and 1.0 mm thick magnet respectively. In the case of the actuator without the permanent magnet, only a positive current density is considered, since it will yield the same results when the current in the coils is flowing the other way around. On the following pages, the analytic results and FEM results for the three actuator types are compared. The analytic results are shown in the upper figures, the FEM results in the lower figures.

The curves for the actuator without a permanent magnet have the same shape for both calculations. The reluctance force is quadratic both in displacement and current density. However, the FEM results show a reluctance force that is between 10% (at minimum air gap) and 20% (at maximum air gap) higher than in the analytic results. The opposite would be expected, due to flux leakage around the air gap that was neglected in the analytic calculations. This is maybe due to the way COMSOL determines the magnetic flux resulting from a current density or the reluctance force resulting from this flux. This actuator type, without a permanent magnet, will not be used in the final setup but is included here to help validate the FEM model. The maximum flux density in the yoke is on the order of 200 mT, so a nonlinear FEM calculation including iron saturation is not needed here.

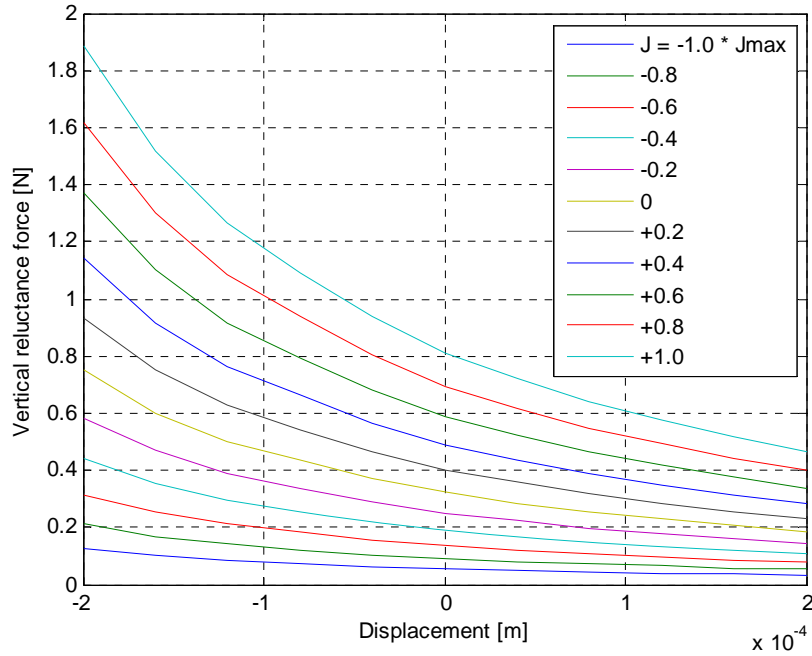
The curves for the actuators with permanent magnets do look different for both calculations. The overall shape is still the same, but the reluctance force at minimum air gap is larger in the FEM results (as before, about +15%), and smaller at maximum air gap (about -45%). Especially this last result is a large difference. The possible reason for this is that when the air gap is larger, the magnet 'sees' a larger reluctance in the magnetic circuit and flux leakage will increase at the magnet, and possibly also at the gap. A second difference is that for negative current densities the reluctance force approaches zero more closely than predicted by the analytic calculations. As in the model without the magnet, the coils generate a larger flux, and thus are able to almost cancel the magnet flux when $J = -J_{max}$. Combined with the flux leakage at the magnet itself, this causes the almost zero force at $J = -J_{max}$.



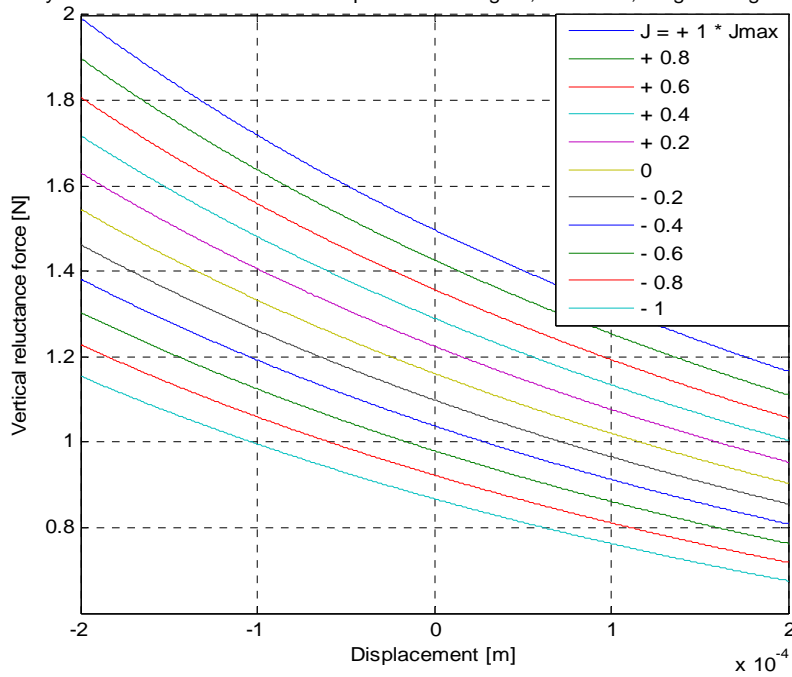
Analytic results for one actuator with permanent magnet, $B_r = 1.37$, magnet length = 0.5 mm



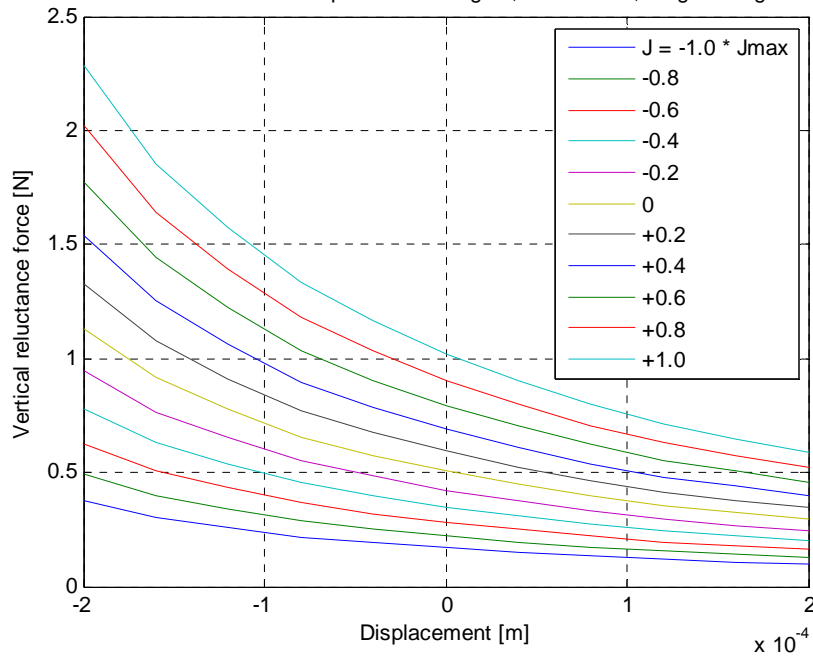
FEM results for one actuator with permanent magnet, $B_r = 1.37$ T, magnet length = 0.5 mm



Analytic results for one actuator with permanent magnet, $B_r = 1.37$, magnet length = 1 mm



FEM results for one actuator with permanent magnet, $B_r = 1.37$ T, magnet length = 1.0 mm



Force characteristic – differential actuator

From the results for a single actuator, the behaviour of a differential actuator can be obtained. Here we assume that flux from one yoke will not go through the other yoke or its target, meaning there is no magnetic crosstalk between the actuators. This seems to be a safe assumption since there is almost no magnetic flux going around the target, and the two targets will be at least 3 mm apart in the differential setup.

Obtaining the differential characteristic is done by subtracting from the reluctance force in each point of the graph the corresponding reluctance force in the complementary point. For example, when the air gap of one actuator is $700\ \mu\text{m}$, the displacement is $+200\ \mu\text{m}$ and therefore the air gap of the other actuator has to be $500 - 200 = 300\ \mu\text{m}$. In the same way, because of the differential drive configuration, when current density is $+J_{\text{max}}$ in one actuator, it has to be $-J_{\text{max}}$ in the other, and so on. This way all points can be found, yielding the graphs displayed on the following pages. The analytic results are again shown in the upper figures, the FEM results in the lower ones.

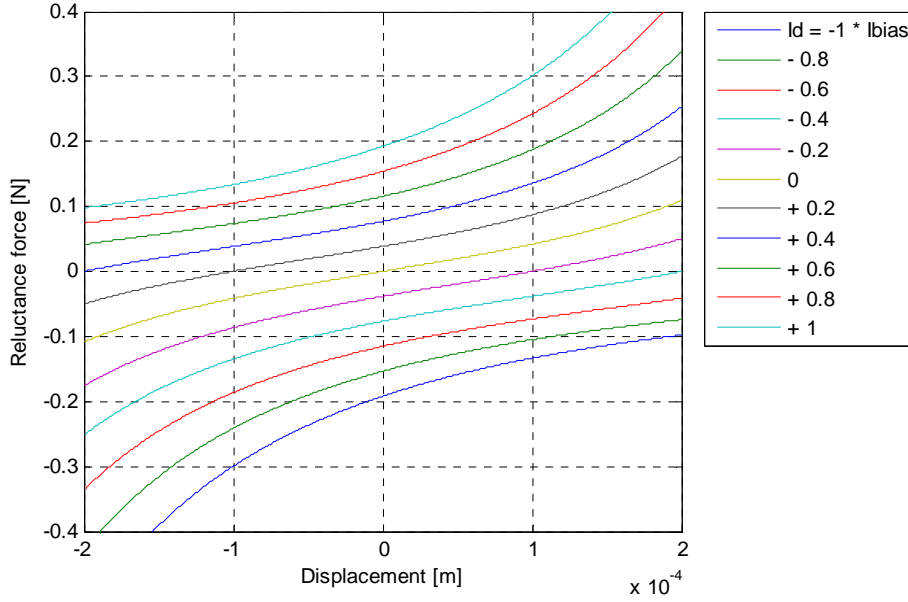
The differential actuator without permanent magnets again shows the same results for both calculations, with an about 15% higher force result for the FEM calculations.

In the differential actuators with magnets, the flux leakage at larger air gap lengths results in a far more nonlinear behaviour according to the FEM calculations. This is also caused by the fact that the force in one actuator, when the current in its coils opposes the magnet flux, is almost zero. The other actuator (running at maximum positive current density) then dominates the behaviour of the entire system, and its nonlinearity is not compensated by the first actuator.

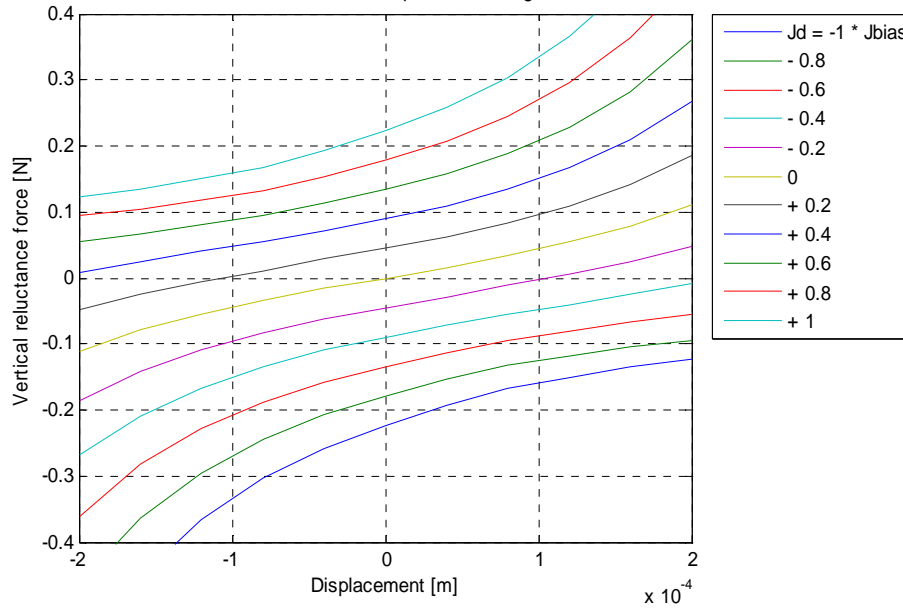
Furthermore, the fact that for negative current densities the force in a single actuator becomes smaller in the FEM calculations than in the analytic calculations results in a larger force-current constant of the actuator. This can be seen in the graphs, the lines for two given current densities are further apart.

Although the FEM results indicate nonlinearity for this type of actuator, and the analytic calculations did not, the actuator is still more or less linear over the motion range needed in this application. This range is $\pm 100\ \mu\text{m}$, while a range of $\pm 200\ \mu\text{m}$ was investigated. The conclusion still holds that a stronger, thicker magnet, which causes a larger effective air gap, makes the actuator less nonlinear.

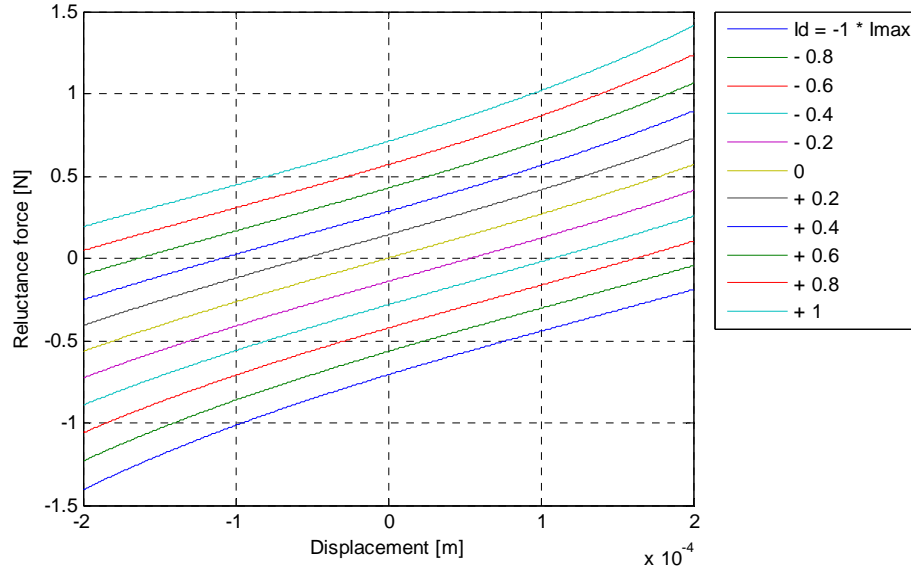
Analytic results for differential actuator without permanent magnet, bias current = $0.5 \cdot I_{max}$



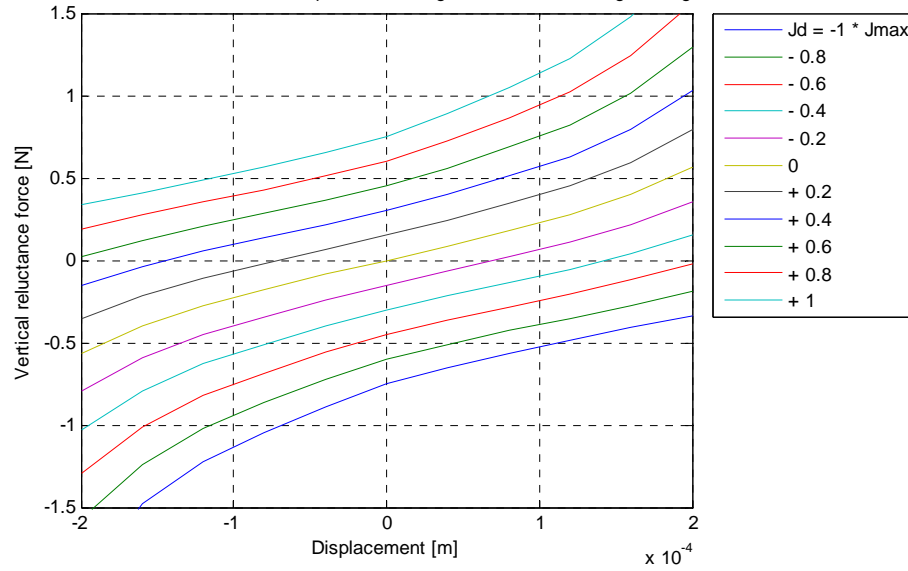
FEM results for differential actuator without permanent magnet, $J_{bias} = 0.5 \cdot J_{max}$



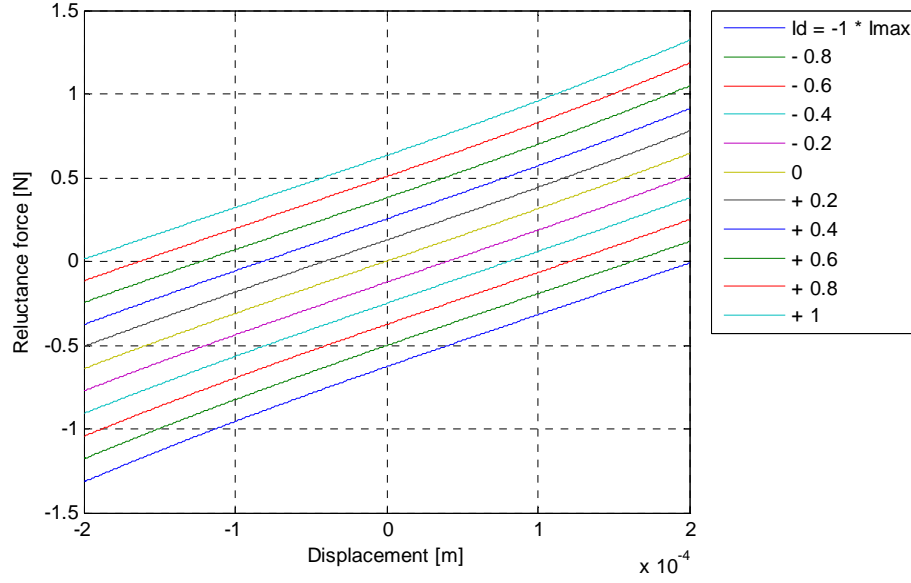
Analytic results for differential actuator with permanent magnet, $B_r = 1.37$ T, magnet length = 0.5 mm



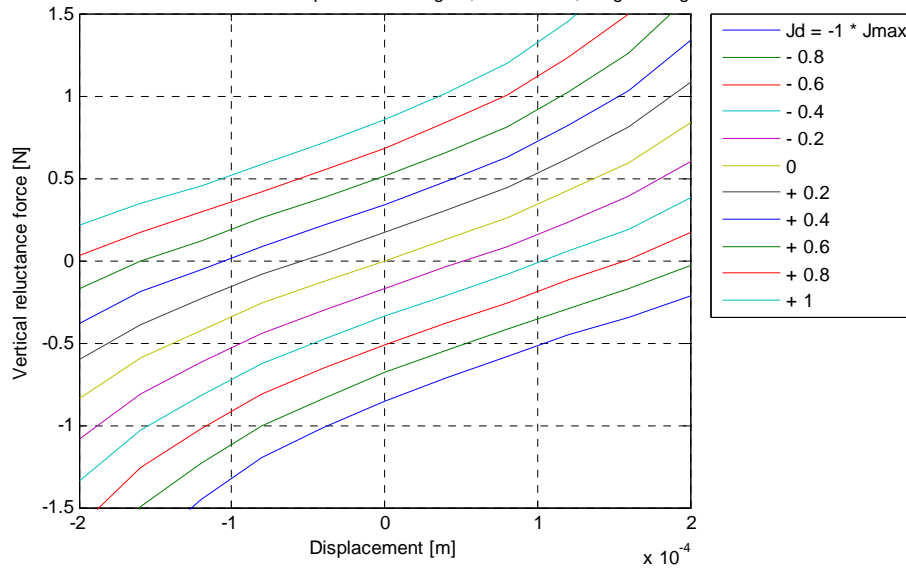
FEM results for differential actuator with permanent magnet, $B_r = 1.37$ T, magnet length = 0.5 mm



Analytic results for differential actuator with permanent magnet, $B_r = 1.37$ T, magnet length = 1 mm



FEM results for differential actuator with permanent magnet, $B_r = 1.37$ T, magnet length = 1.0 mm



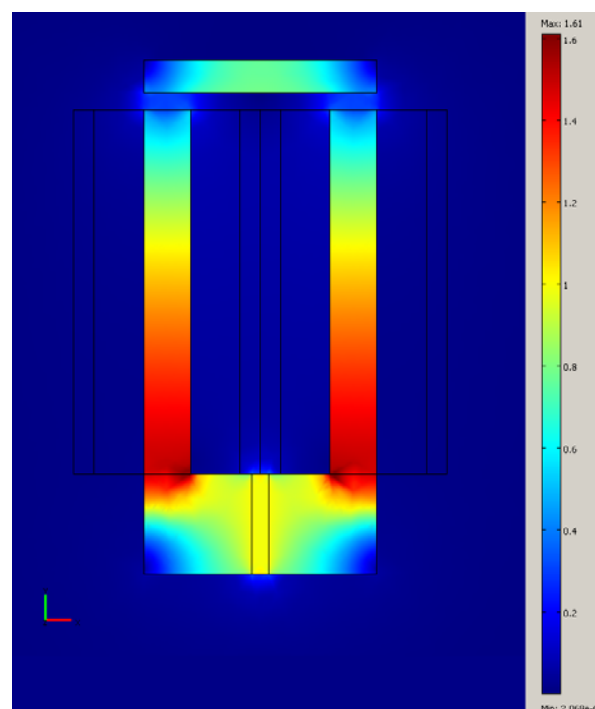
Force characteristic – Nonlinear model

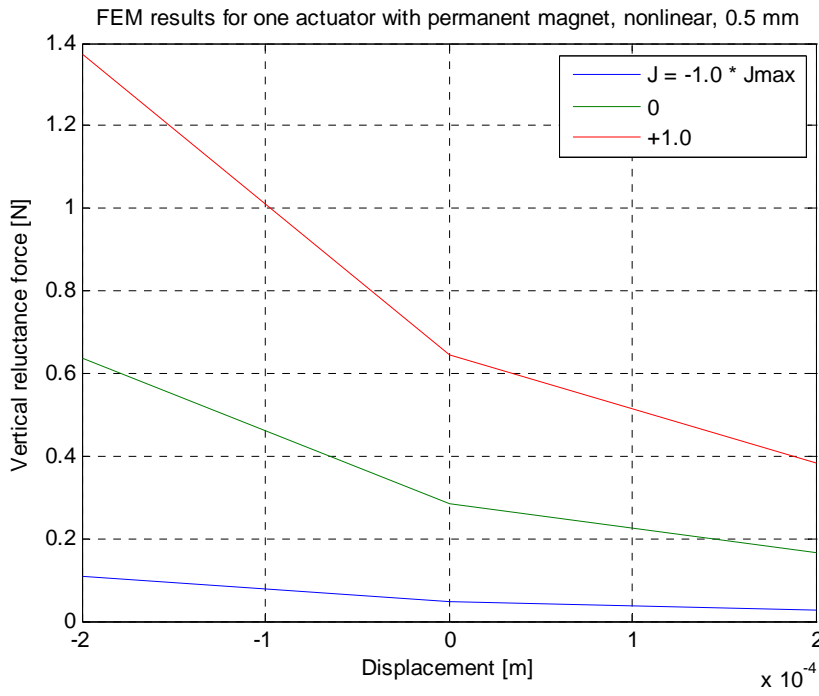
Because the flux distribution showed peaks well in excess of 2 T, it is logical to assume that in the permanent magnet biased actuators magnetic saturation will occur. The model used so far will therefore be inaccurate, and needs to be refined. In order to do this, the constant (linear) magnetic permeability of the iron parts in the model is replaced by the behaviour of soft iron, which has a nonlinear magnetic permeability, depending on the flux density. This nonlinear dependency is available in the COMSOL material library, as Soft Iron. The flux distribution of the basic actuator model with saturation is shown on the next page.

The iron in the yoke clearly becomes saturated at the corners, where the flux density is 1.6 T. Because the magnetic permeability of saturated iron is almost equal to that of air, the flux leakage increases significantly. The flux distribution is now much more even than in the linear model, and it can be observed that it gradually becomes less along the yoke legs. This is due to flux leakage along the legs. Also considerable leakage shows around the permanent magnet, and at the air gaps.

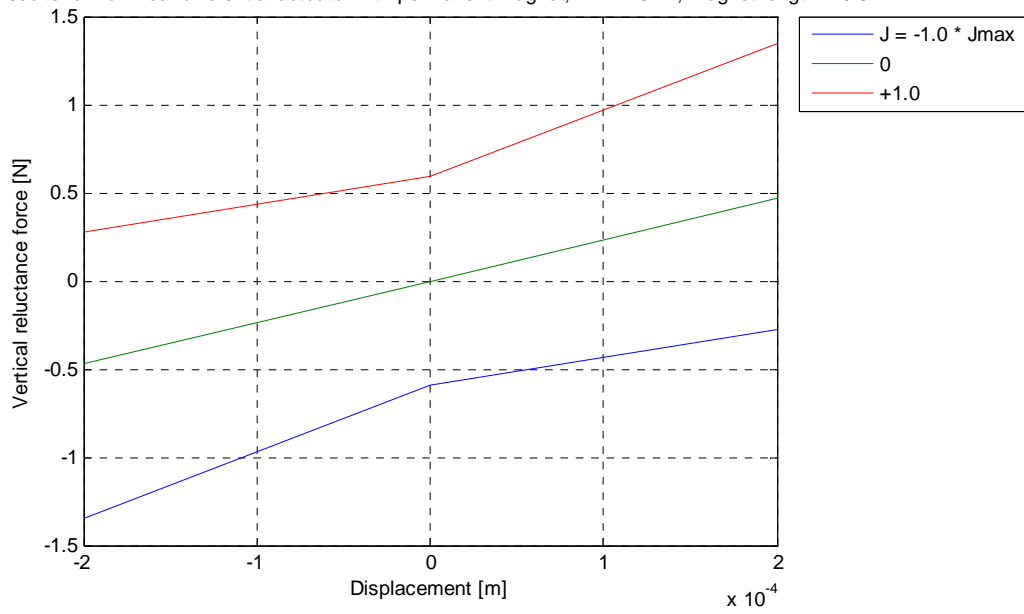
All this results in a reluctance force that is some 60% of the force obtained in the linear model. To check the effect on the actuator force characteristic, the nonlinear model is also placed in a for loop, as before. However, the nonlinear model requires many more iterations for each solution (120 vs. 10 or 11), so the computation time per point is increased from 30 seconds to about 5 minutes. Owing to this, the nonlinear model is evaluated in only 9 points for each magnet thickness, namely at maximum, minimum and zero current, at maximum, minimum and zero displacement, and all possible combinations thereof.

The results for these computations are shown on the next pages. Due to the limited number of points, only very general conclusions can be drawn about the shape of the graphs. However, they seem to be consistent with the results of the linear model, but are consistently approximately 60% lower in force. This result can be used to make predictions about the final actuator geometry and its resultant force.

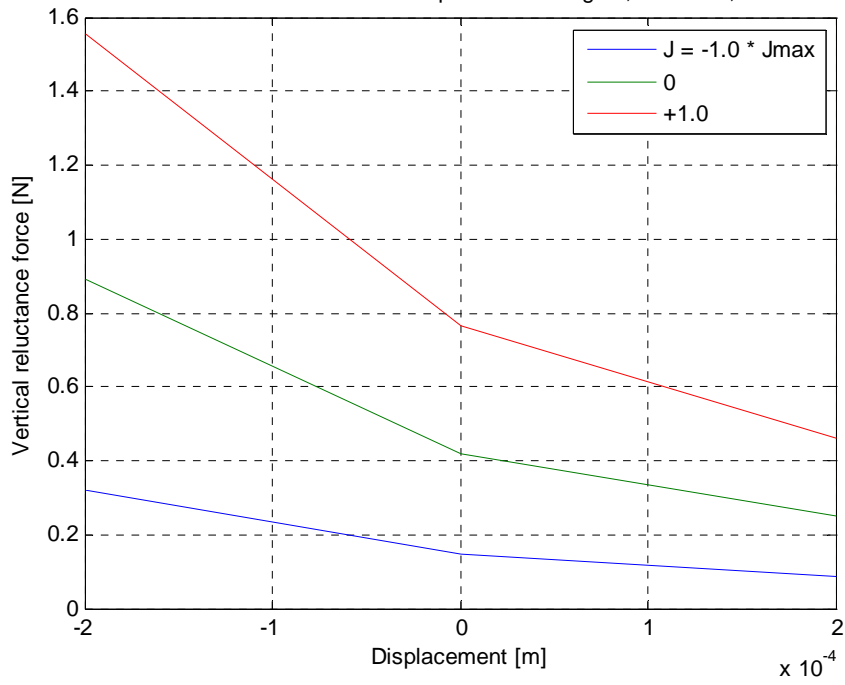




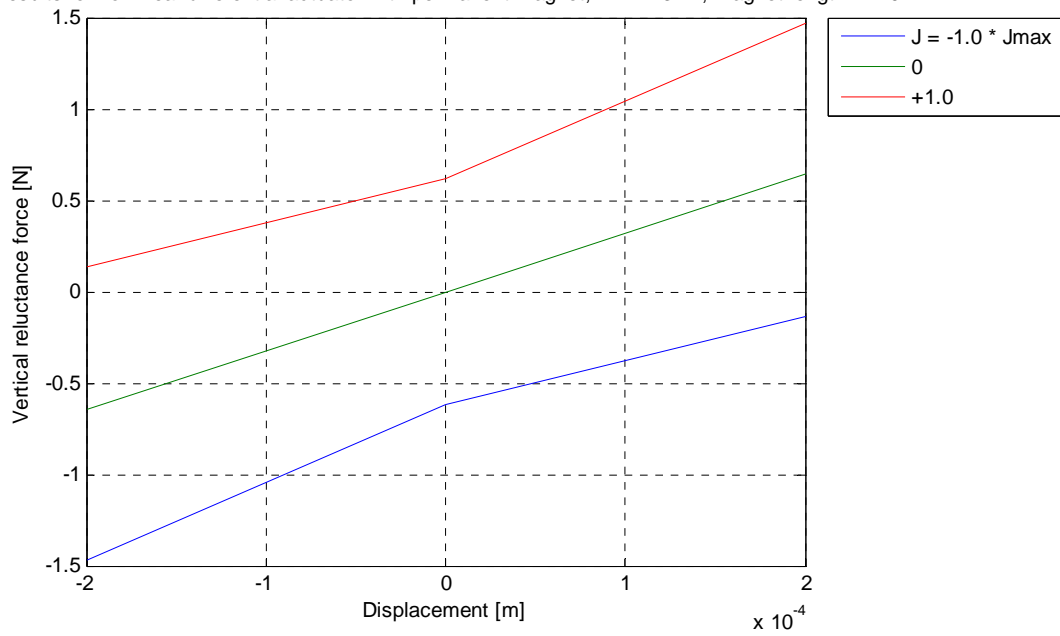
FEM results for nonlinear differential actuator with permanent magnet, $B_r = 1.37$ T, magnet length = 0.5 mm



FEM results for one actuator with permanent magnet, nonlinear, 1.0 mm



FEM results for nonlinear differential actuator with permanent magnet, $B_r = 1.37$ T, magnet length = 1.0 mm



Force characteristic – Varying slot width factor

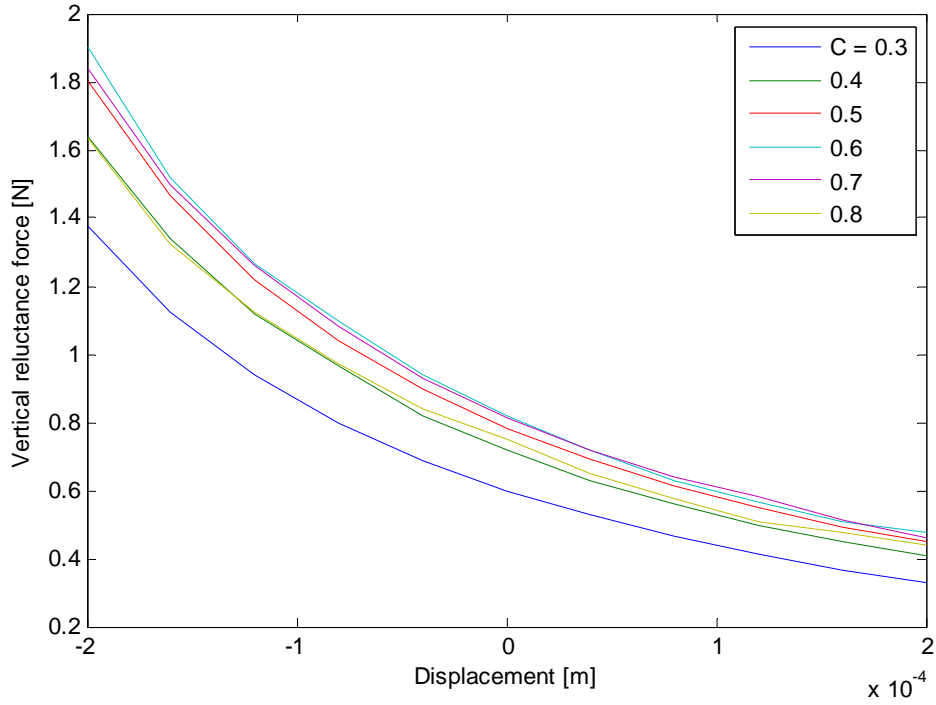
After the initial FEM calculations to establish the force characteristic, the COMSOL model was made fully parametric, so that all dimensions and constants could be varied using a Matlab .m file. This approach was used to find the optimum geometry for the actuators.

Like in the analytic calculations, the slot width factor c was varied, to find its optimum. The analytic calculations showed an optimum value of 0.6 for c . Using the linear FEM model, the maximum reluctance force (at maximum current density) was calculated for 11 air gap lengths, again varying from 300 to 700 μm . This was repeated for different values of c and two magnet thicknesses, namely 0.5 and 1.0 mm. The results of these calculations are shown on the next page. The results agree with the analytic calculations, and confirm that 0.6 is the optimum value for c .

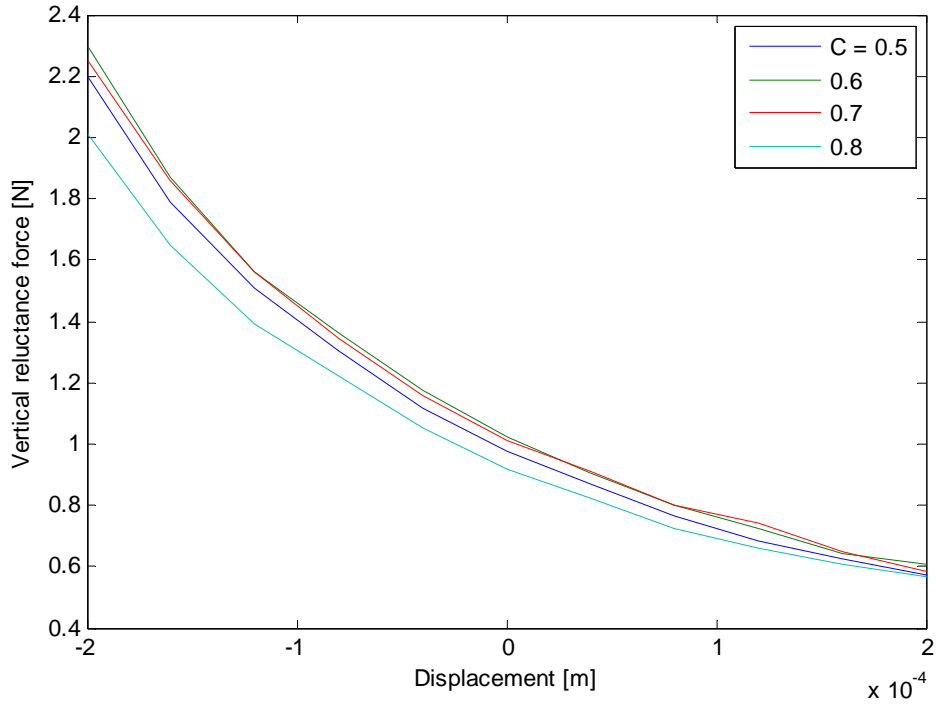
However, it is likely that saturation of the iron plays an important role in determining the optimum c , since at larger slot widths there will be less iron available for the magnetic flux, while the increased copper cross-section will allow for a larger NI product. Therefore, the calculations were repeated using the nonlinear soft iron model. Due to increased calculation time, the number of points in the displacement interval was reduced to 5. The value of 0.8 for c was also not considered, because it was clear from the initial calculations that it was not the optimum value, and because of the resulting thin yoke required finer meshing. This led to more than 350,000 degrees of freedom to be solved for, which would have required a computation time of more than 20 minutes per point.

The results of using the nonlinear model show that the optimum value of c is in fact 0.5, so a little more iron is required than would be expected based on the linear FEM and analytic calculations. In order to find a more accurate value for the optimum more refined calculations would have to be carried out, where the interval 0.4 – 0.6 for c would be evaluated in, for instance, 5 points.

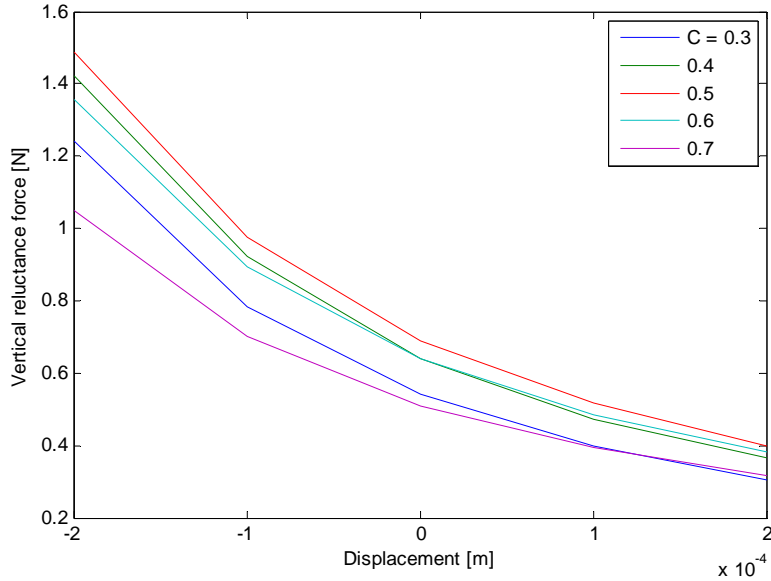
FEM results for varying slot width factor c , permanent magnet thickness = 0.5 mm, linear model



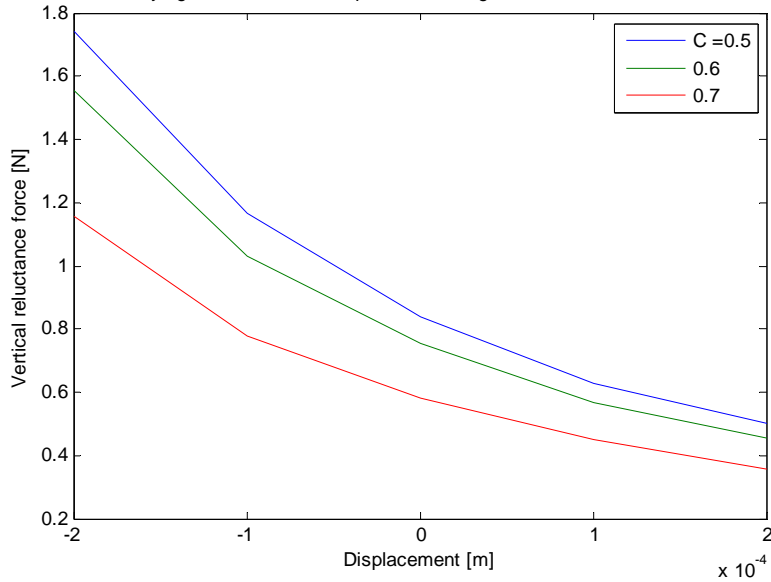
FEM results for varying slot width factor c , permanent magnet thickness = 1.0 mm, linear model



FEM results for varying slot width factor c , permanent magnet thickness = 0.5 mm, Nonlinear model



FEM results for varying slot width factor c , permanent magnet thickness = 1.0 mm, Nonlinear model



Force characteristic – Extended legs model

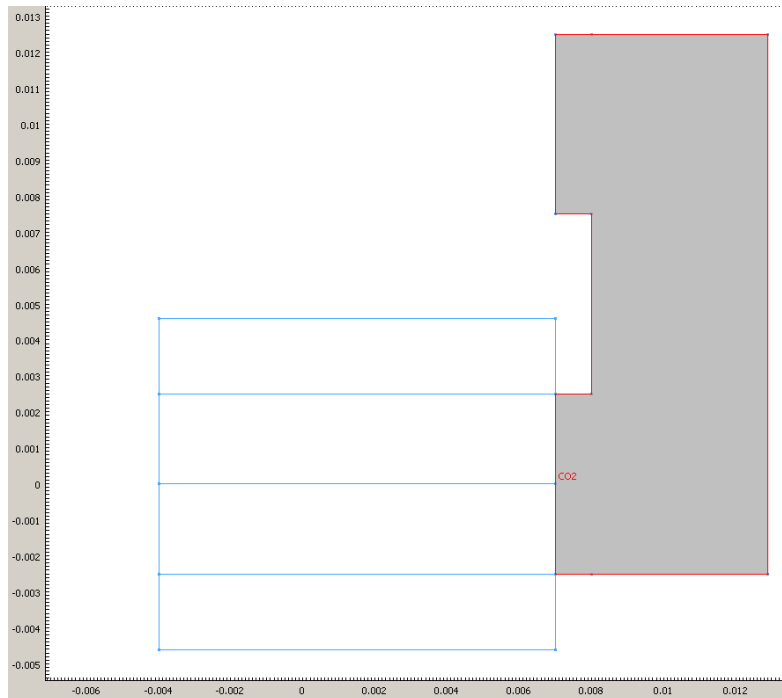
To make a differential actuator, like discussed above, two actuators of the type just investigated would have to be placed above each other. However, the top actuator then has to be above the levitating disk, which renders that part of the disk useless for the manipulation and positioning of parts to be assembled. Moreover, the height of the actuator would be a considerable hindrance to the tool in accessing the area around it. Since three such actuators are needed, a different solution has to be found for the top actuators.

One method is to place the actuator not above but beside the levitating disk, and extend the iron yoke to guide the magnetic flux to an iron target on the disk. These extended legs then have a hook-

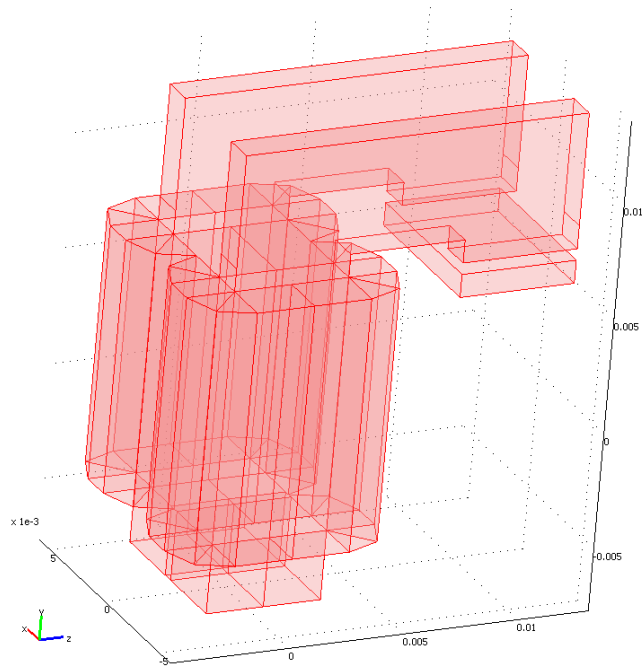
shape, like shown in the actuator geometry below. It can be expected that the extended yoke will provide an additional flux leakage path, which will reduce the available reluctance force.

Therefore, an additional COMSOL model has to be made, to investigate this effect. Since the model now is no longer symmetrical about the XY-plane, the full model has to be used. To obtain this model, as a first step the half model for the bottom actuator, without the extended legs, is mirrored in the XY-plane. This step yields a full model for the standard actuator, which can also be used to investigate the validity of using a half model. In the operating point of the actuator, with an air gap of 500 μm and maximum current density, the half model yields a vertical reluctance force of 405 mN. The full model yields a force of 814 mN, which is almost exactly twice that. This indicates the half model and its boundary conditions are indeed valid.

To make the extended legs model, first the ferromagnetic target is removed and the extended leg geometry is drawn as a composite object of three rectangles in the YZ-plane, as shown on the following page. The legs extend one millimeter above the coils, and then 15 mm in the z-direction. At the end of the legs, a 1 mm thick protrusion is made to help focus the magnetic field lines onto the target in its new position, and thus reduce stray flux. Initially the legs are made 5 mm high, to provide sufficient stiffness to the actuator.

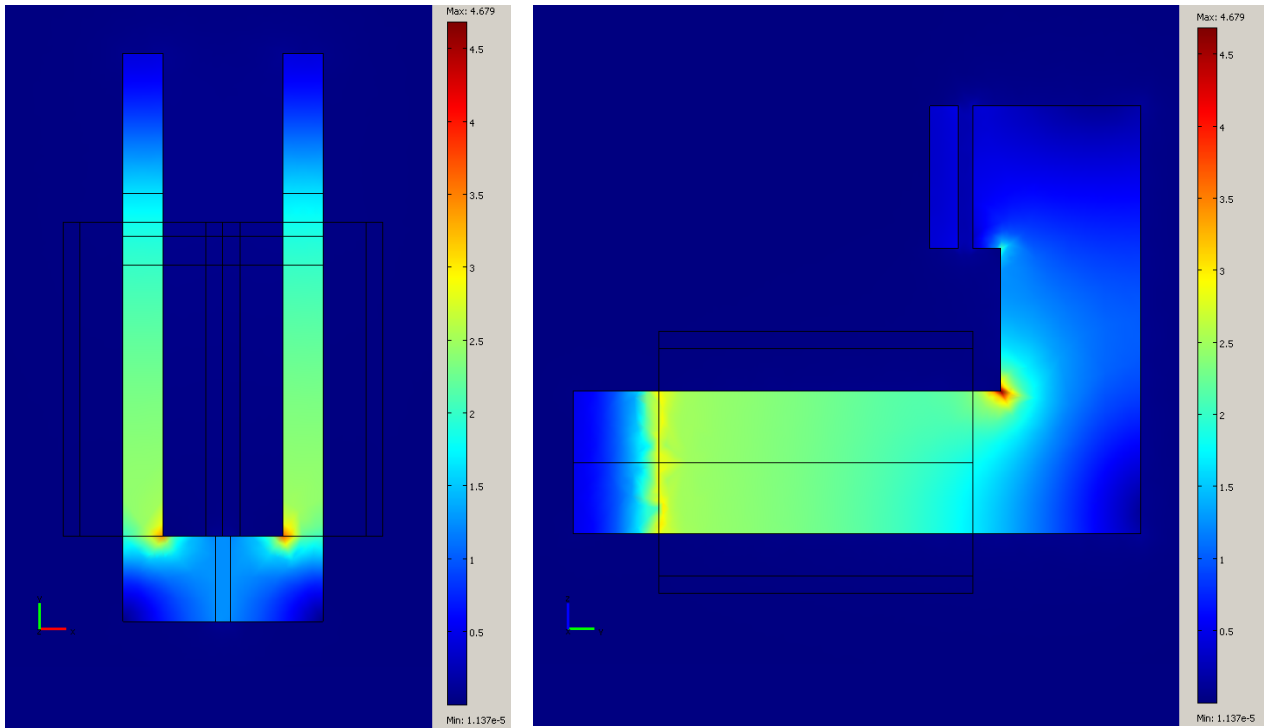


This geometry is then extruded twice along the y-axis, corresponding to the position of the existing yoke legs. Then, a new ferromagnetic target is made at its new position, again with an air gap of 500 μm . This results in the complete model, shown on the next page with the air volume surrounding it removed for clarity:



The magnetic flux density distribution of the linear solution of this model is shown in the following two figures, below. The cross-sections are in the XY-plane in the middle of the yoke, and in a plane parallel to the YZ-plane in the middle of one of the legs, respectively. There is indeed considerable flux leakage between the extended legs, and again the flux concentrations at the corners of the iron show up.

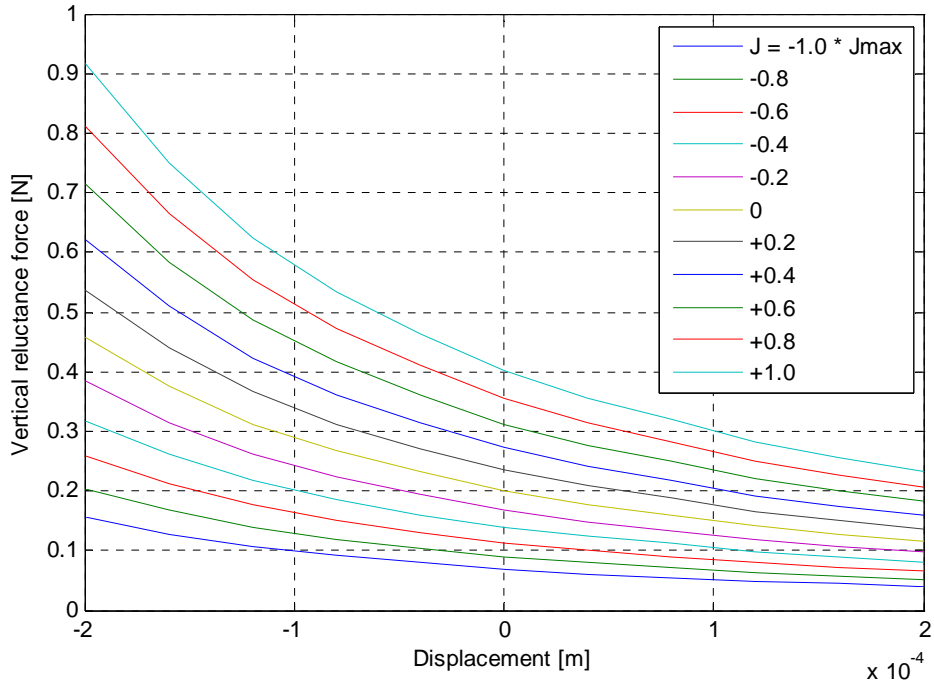
Due to the increased leakage, the maximum reluctance force is reduced from 814 mN to 376 mN, when all other parameters are kept the same. This loss depends on the amount of overlapping area between the two legs. If the height of the extended portion is reduced from 5 to 2.5 mm, the reluctance force increases somewhat to 456 mN, which is still almost a factor two lower than the standard actuator.



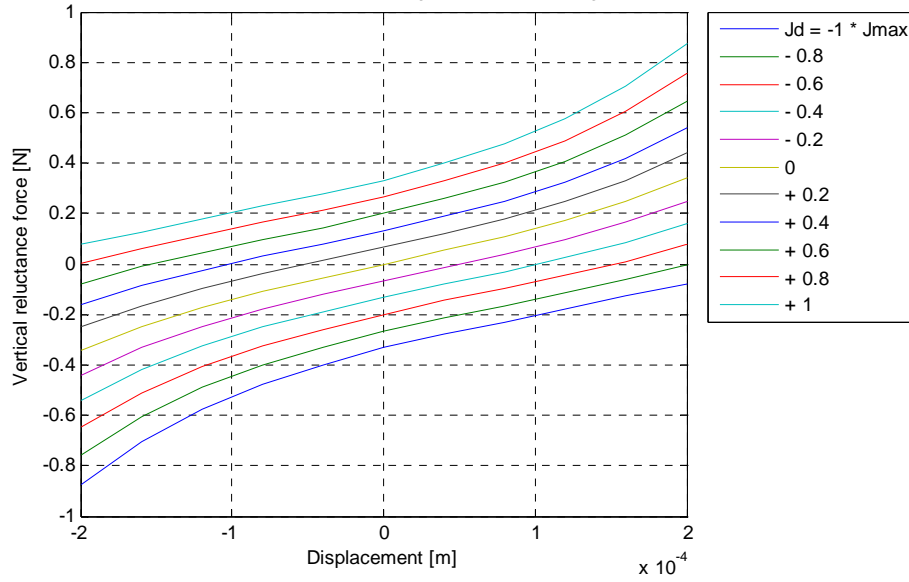
To check whether the force characteristic of these actuators is similar to that of the standard actuator, the model is once again placed in a for-loop in an .m file. The current and displacement are again varied in 11 steps, yielding a total of 121 data points. This procedure is repeated for actuators with 5 mm high and 2.5 mm high leg extensions.

The results of this analysis are shown on the following pages, showing a behaviour that is indeed very similar to that of the standard actuator. The force is also in these figures roughly a factor 2 lower than for the standard actuator, and the one with 2.5 mm high legs has a somewhat higher force capability.

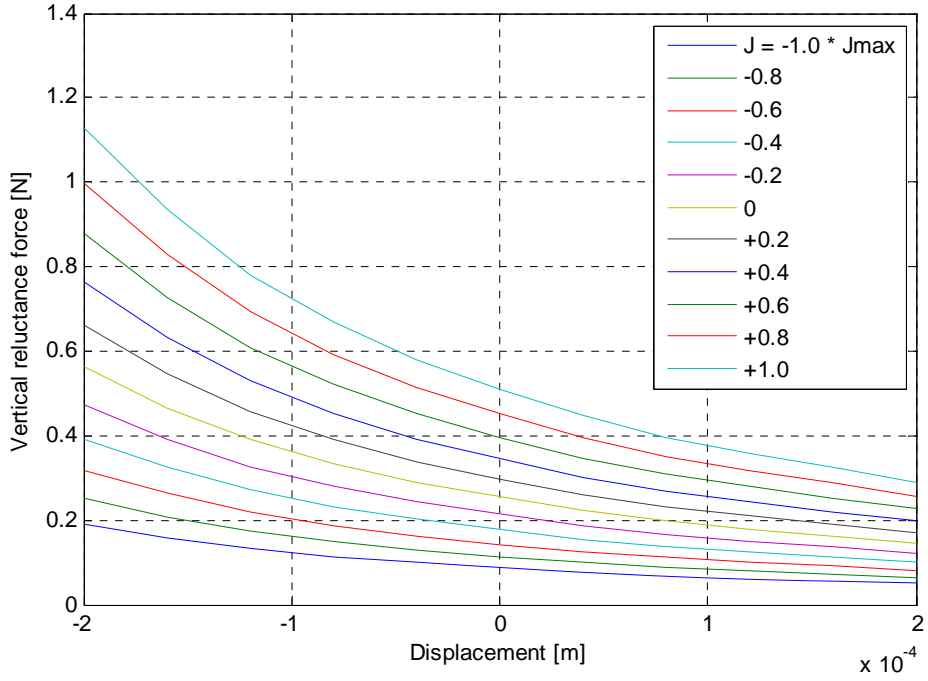
FEM results for single actuator with permanent magnet 1.0 mm, ext. legs, 1.4 x 5.0 mm x 15 mm



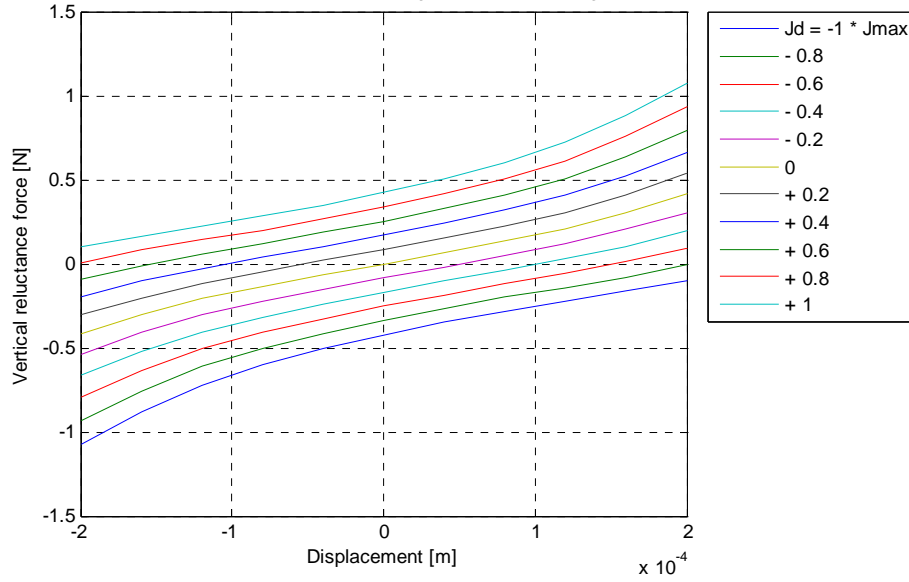
FEM results for differential actuator with permanent magnet 1.0 mm, ext. legs, 1.4 x 5.0 mm x 15 mm



FEM results for single actuator with permanent magnet 1.0 mm, ext. legs, 1.4 x 2.5 mm x 15 mm



FEM results for differential actuator with permanent magnet 1.0 mm, ext. legs, 1.4 x 2.5 mm x 15 mm



Parametric analysis

Now that some details are known about the reluctance actuators, a parametric analysis of the actuator dimensions can be carried out to obtain the optimum geometry. In general, the actuator will be stronger as the dimensions of yoke and corresponding target are increased. However, the actuator and especially the target should be kept as small as possible, to limit the portion of the levitating disk that can't be used for assembly tasks. The goal of the parametric analysis is therefore to find the minimum actuator dimensions for which the available force is still sufficient.

From the requirements calculations it is known that a vertical actuator has to be able to supply at least 37 mN over its entire motion range. To be on the safe side, this requirement is extended to 50 mN. For simplicity's sake, and to reduce the required computation time, the parametric analysis will be carried out using the linear, not saturating model, for the standard half actuator model without extended legs. Furthermore, the target will be at its nominal position in the middle of the motion range in this analysis, meaning that the air gaps are kept constant at 500 μm .

To be able to use the data from this analysis for the actual actuators, some additional data is needed. From the previous calculations it can be observed that when the target is displaced 100 μm away from the yoke, to the end of its designed motion range, the maximum available reluctance force is decreased by a factor 2 at most. Furthermore, including ferromagnetic saturation, which will occur in practical actuators, reduces the force by a factor 1.7. This means that the force requirement for the lower actuator has to be multiplied by both factors to obtain an actuator that can supply a force of 50 mN over its entire range. Consequently, all actuator geometries that can supply a force of 170 mN in this parametric analysis are suitable for the lower actuator.

The upper actuator will have a force that is reduced by a further factor 2 because of the flux leakage through the extended legs. Therefore, actuator geometries able to supply at least 340 mN in this analysis can be used (with added leg extensions) for the upper actuator.

Initially, the model .m file was made fully parametric, and placed in a triple nested for-loop. In these loops, the yoke width, length and height are varied in 6 steps, leading to a total of 216 possible configurations. The width was varied from 6 to 11 mm, the length from 3 to 8 mm, and the height from 10 to 20 mm.

The magnet thickness was chosen to be 1.0 mm instead of 0.5 mm. This has to do with the manufacturing tolerances of the magnets, which are on the order of 100 μm and therefore a 0.5 mm magnet cannot be guaranteed to have the specified dimensions. This would affect the actuator characteristics too much.

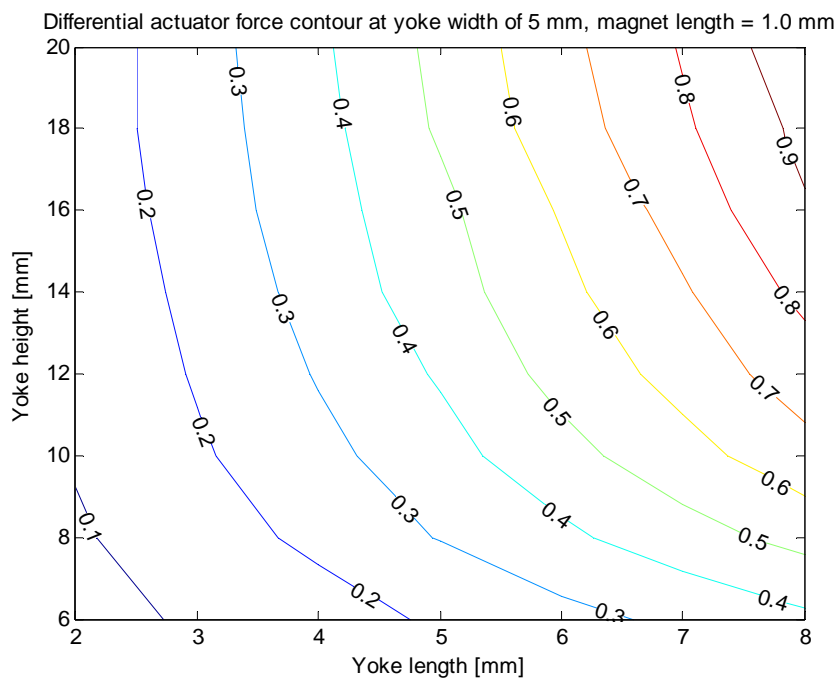
Even though the optimum slot width factor was found to be 0.5, it is kept at 0.6 in this analysis. The reason for this is ease of manufacturing the actuator yokes, which will become apparent in the chapter explaining the experimental setup. The difference in maximum force between $c = 0.5$ and $c = 0.6$ is not that great to outweigh this advantage.

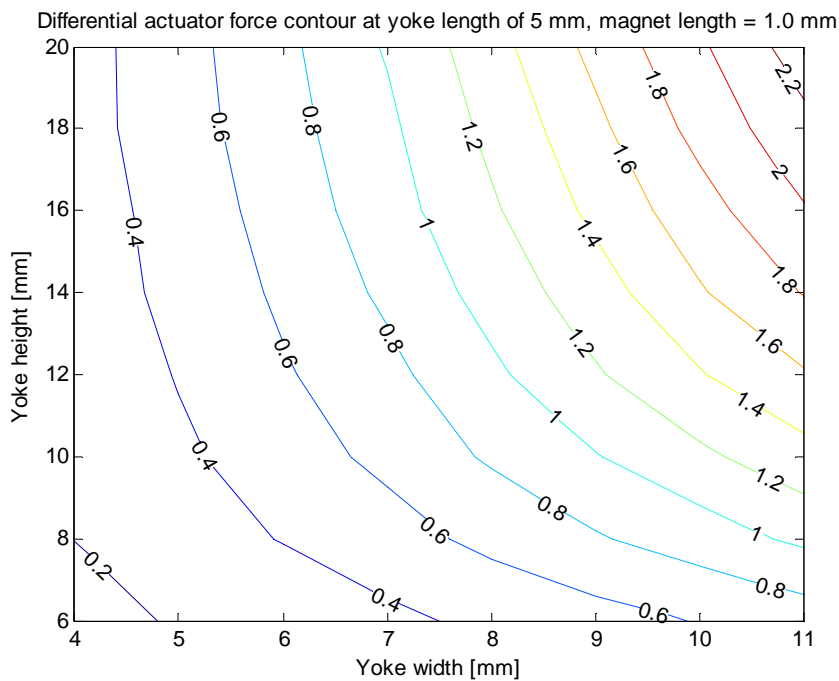
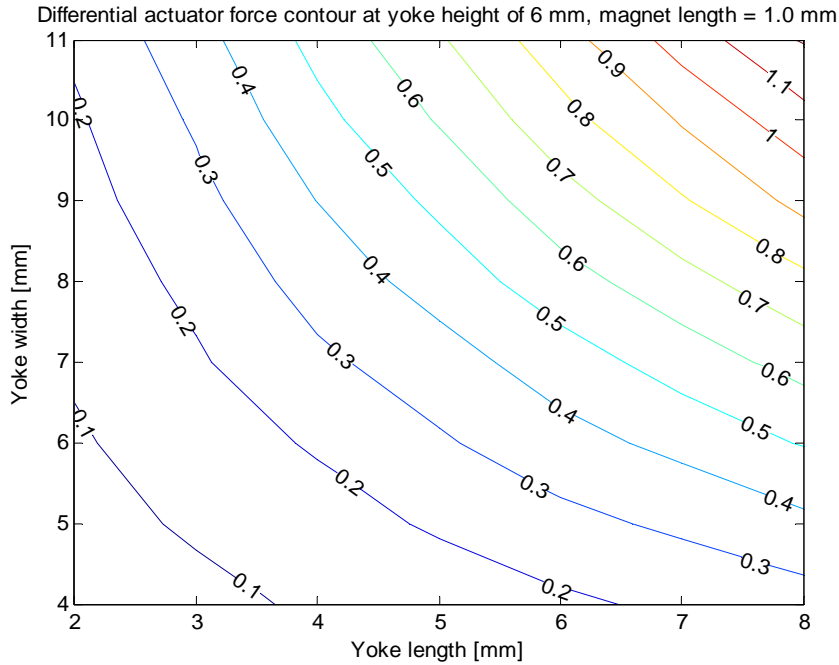
During the analysis, it was found that defining a fixed element size would lead to meshing problems, especially for yokes with large aspect ratios. For tall, narrow leg geometries some tetrahedral elements would become almost two-dimensional. To solve this problem, the element size of each subdomain was set to be equal to the smallest dimension of that subdomain. This way, the element size was changing with the geometry during the analysis, leading to more accurate results.

The entire parametric analysis was run twice, once with maximum positive current density and once with maximum negative current density. Subtracting the two sets of results then yields the available reluctance force in a differential actuator setup.

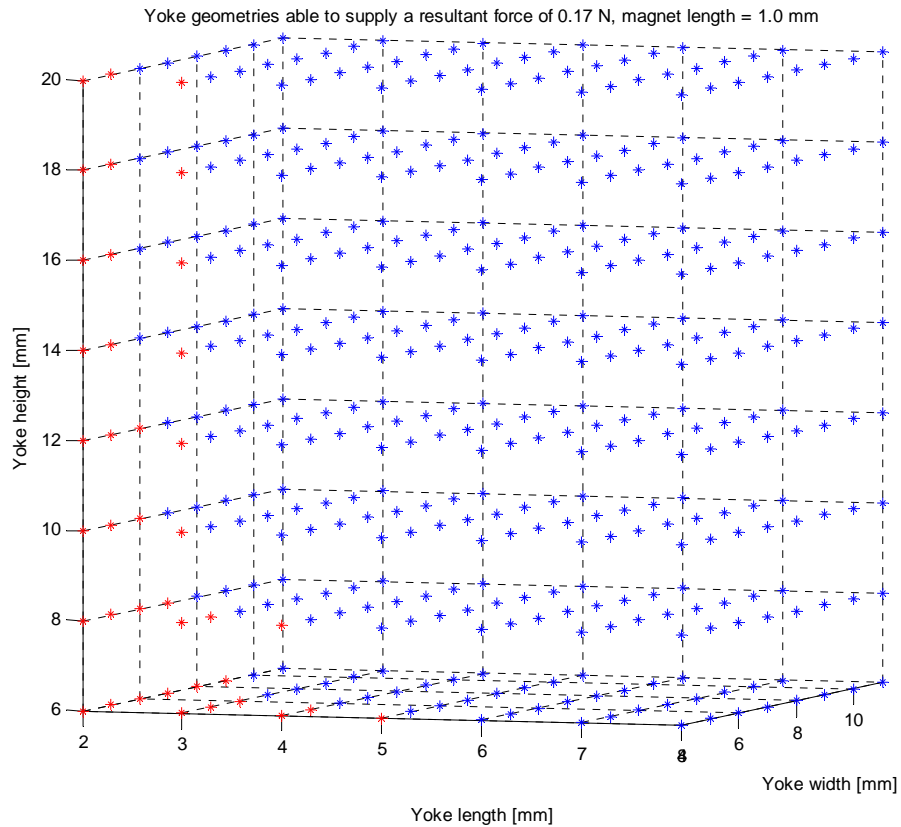
The first set of results indicated that all investigated actuator geometries were capable of supplying the required reluctance force of 170 mN. In other words, the lower limit of actuator sizes had not been found. Therefore, the range of sizes to be investigated was extended in further calculations to include actuator widths of 4 and 5 mm, lengths of 2 mm, and heights of 6 and 8 mm. The total number of points investigated eventually was therefore $8 \times 7 \times 8 = 448$. For the smaller widths, the model .m file had to be adapted to accommodate for the different numbering of the geometry surfaces. This is a result of the way COMSOL does this numbering, and the fact that when the magnet is 1 mm thick and the yoke width becomes less than 6 mm, surfaces of the magnet and coils get a different orientation relative to each other.

The final results of the parametric analysis are plotted on the following pages. Contour plots of the maximum available force at certain actuator dimensions show that this force indeed increases with all three dimensions, but that it is not useful to increase the yoke height above 10 mm. The added flux by the extra coil windings is then about the same as the flux loss due to leakage between the yoke legs. The nearly vertical contours in the last two contour plots show that above 10 mm height, the available force is almost constant.





In the following two plots, all investigated points have been plotted, with their colour depending on whether the corresponding geometry is capable of delivering the required force or not. Useful geometries are plotted in blue; geometries that fail to meet the requirement are plotted in red. An optimum geometry corresponds to a blue point that lies next to one or more red points, indicating that particular geometry is one of the smallest possible actuator sizes for the requirement.

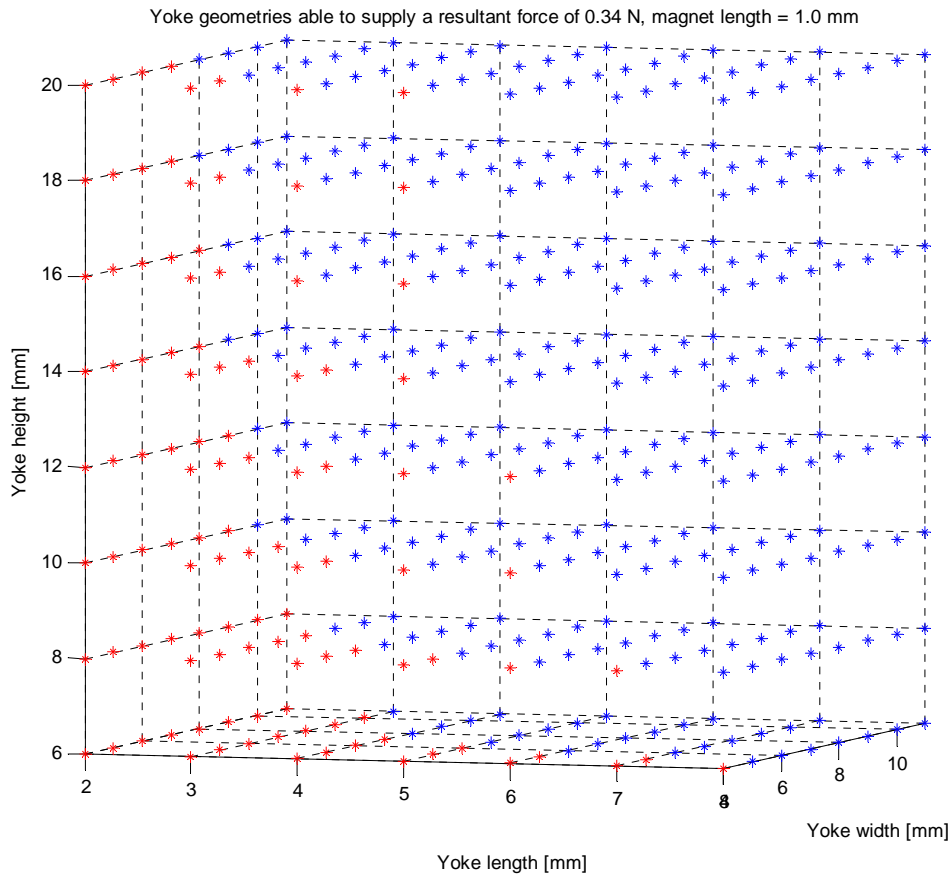


This plot shows which geometries meet the 170 mN force requirement for the lower actuator. It can be seen that above 10 mm yoke height there are no blue points above red points, meaning that above this height the force no longer increases.

The actuator geometries that can be practically made also depend on the available magnet sizes. Two types of cuboid permanent magnets have been ordered from HKCM, they are 3 x 5 x 1 mm and 3.5 x 2 x 1 mm, respectively. The yoke length has to be equal to one of the magnet dimensions (other than the 1 mm thickness), so this would allow for the lower actuator the following geometries:

Width [mm]	Length [mm]	Height [mm]
5	3	10
5	3.5	10
5	5	6
7	3	6

Here actuators that are 2 mm long are not considered, because this would require an impractical width of 10 or 8 mm. When manufacturing is considered, actuators that are 5 mm wide are most practical. This allows building the yoke from a stack of five 1 mm thick plates, one of which is the magnet and the other four are soft iron. Furthermore, keeping the actuator low is advantageous and as we will see further on, a 5 x 5 mm target size is also a good choice for the upper actuator. Having two targets that are exactly the same size will also simplify aligning the two actuators and their targets relative to each other in the final device. Therefore, a yoke that is 5 mm wide and long and 6 mm high is selected for the lower actuator. In terms of surface area needed on the levitating disk, there is no appreciable difference between a 7 x 3 mm and a 5 x 5 mm target.



This plot shows which actuator configurations meet the force requirement for the upper actuator of 340 mN. Based on the available magnets, there are three possible geometries that can be readily made:

Width [mm]	Length [mm]	Height [mm]
5	5	10
7	3	10
7	3.5	10

Because of the additional considerations stated above, the first configuration is selected. In both actuators, a 3 x 5 x 1 mm magnet is used. Now that the required actuator geometries are known, a test setup and manufacturing procedure can be designed.

Conclusions

Extensive FEM calculations have been carried out for the reluctance actuators using the COMSOL package. The results of these calculations are in good agreement with results from analytic calculations, but the actuator force characteristic is less linear than was expected. However, over a 200 μm movement range this poses no problem.

Considering ferromagnetic saturation of the iron parts in the model yielded a factor 1.7 reduction of the available force. Adding extended legs to the actuator to make it suitable to be placed above the levitating disk further reduces this by a factor 2. The optimum slot width factor was found to be 0.5 when saturation was considered, instead of 0.6 for the linear FEM and analytic calculations.

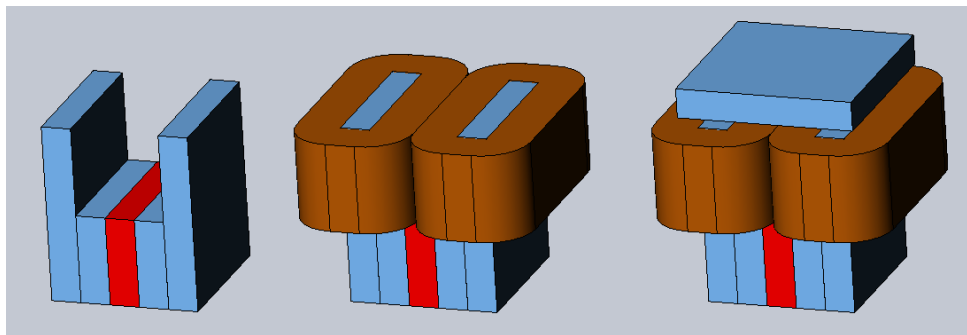
A parametric analysis was carried out to find the smallest possible actuator sizes that can supply enough force for the levitating disk positioning stage. Based on the actuator force characteristics and the abovementioned factors, these sizes could be determined from the parametric analysis. The required sizes ($w \times l \times h$) for the lower and upper actuator have been determined as $5 \times 5 \times 6$ mm and $5 \times 5 \times 10$ mm, respectively.

Description of experimental setup for reluctance actuator tests

This section describes an experimental setup that can be used to test the force-current-displacement characteristics of the reluctance actuators that have been designed previously. It will make use of three MICOS micropositioning stages to accurately set the displacement. A laser distance sensor is used to accurately measure the actuator target displacement, and a mini S-beam load cell will measure the reluctance force.

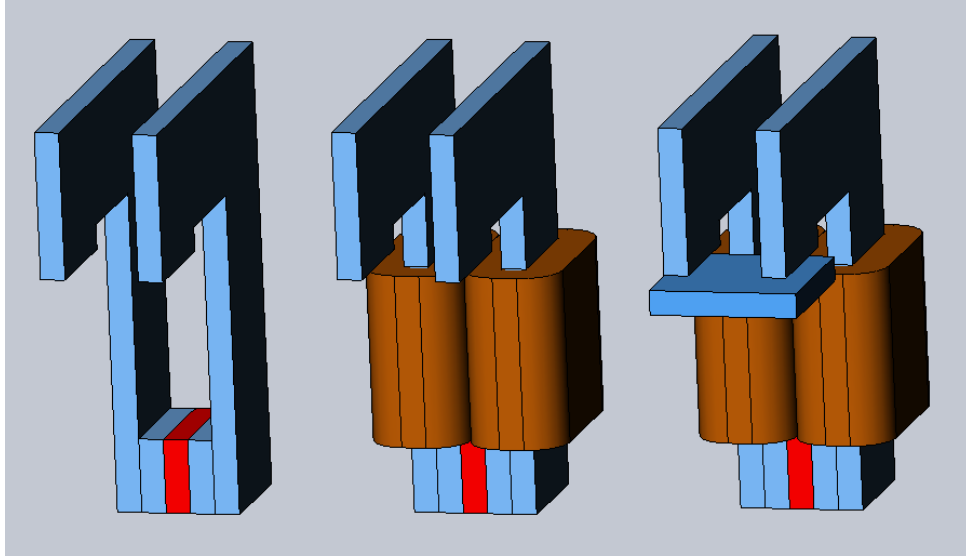
In the FEM calculations, the required sizes ($w \times l \times h$) for the lower and upper actuator have been determined as $5 \times 5 \times 6$ mm and $5 \times 5 \times 10$ mm, respectively. Both actuators use a $3 \times 5 \times 1$ mm magnet. The actuator sizes have been chosen such that they can be easily assembled from 1 mm thick steel or soft iron parts, which can be cut from sheet metal.

The construction of the lower actuator is shown below. The permanent magnet is shown in red, the iron plates blue. The target is made slightly bigger than the yoke dimensions, namely 6×6 mm instead of 5×5 mm, to accommodate for lateral displacements. During assembly the actuator components are held together by the reluctance force of the magnet attracting the iron parts, until they are clamped in the final setup.

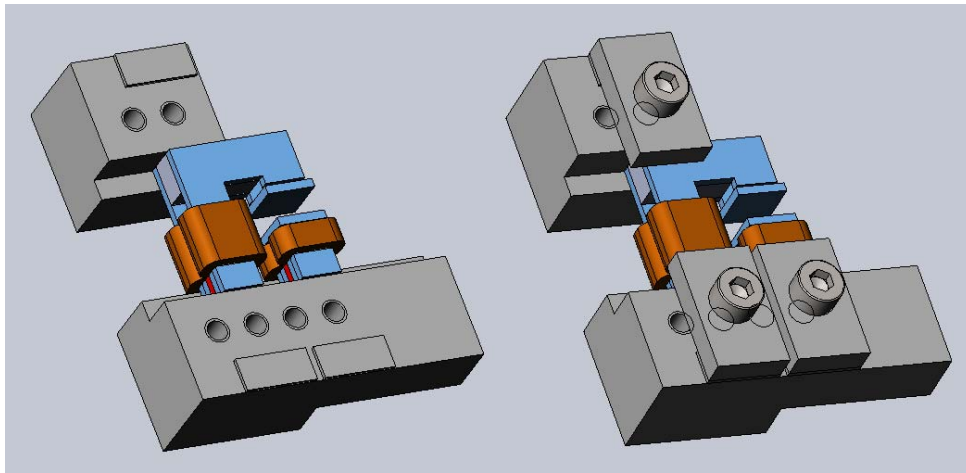


The upper actuator, shown below, is constructed in a similar manner, but has a somewhat more complicated geometry. The extended legs are chosen to be 5 mm high, even though this will cause a somewhat larger flux leakage. This is done to ensure the stiffness of the actuator, theoretically the vertical deformation is at worst $0.2 \mu\text{m}$ in this configuration. Conversely, when the legs would have a 2.5×1 mm cross-section to reduce leakage, this increases to more than $1.4 \mu\text{m}$. Since the actuator force depends quadratically on displacement, this will make the actuator more difficult to control.

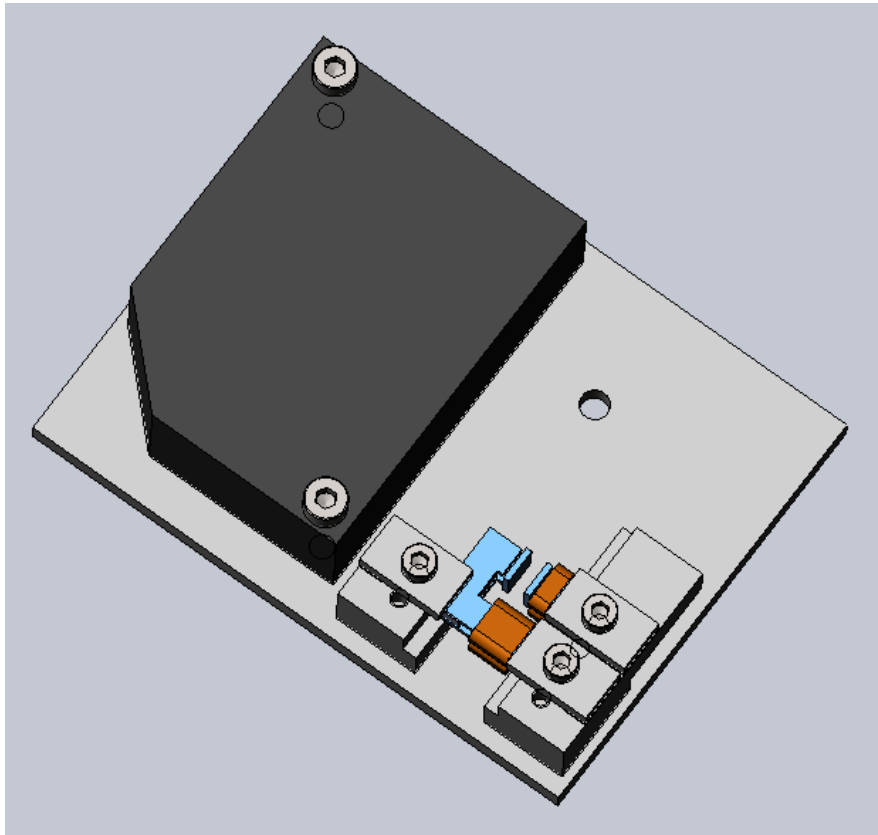
The actuator legs are also made 2 mm longer than in the original design. This is to be able to clamp the two actuators on the same ground plane, greatly simplifying the manufacturing and aligning procedure.



The actuators are placed in grooves in clamping blocks, which are mounted to a baseplate (not shown here). An aluminium spacer is inserted between the legs of the upper actuator, and the actuators are aligned and clamped with the help of shims and M3 screws, as shown below. To prevent unwanted flux leakage, these screws have to be of a non-ferromagnetic material such as brass. At this stage of assembly the targets are not yet present.

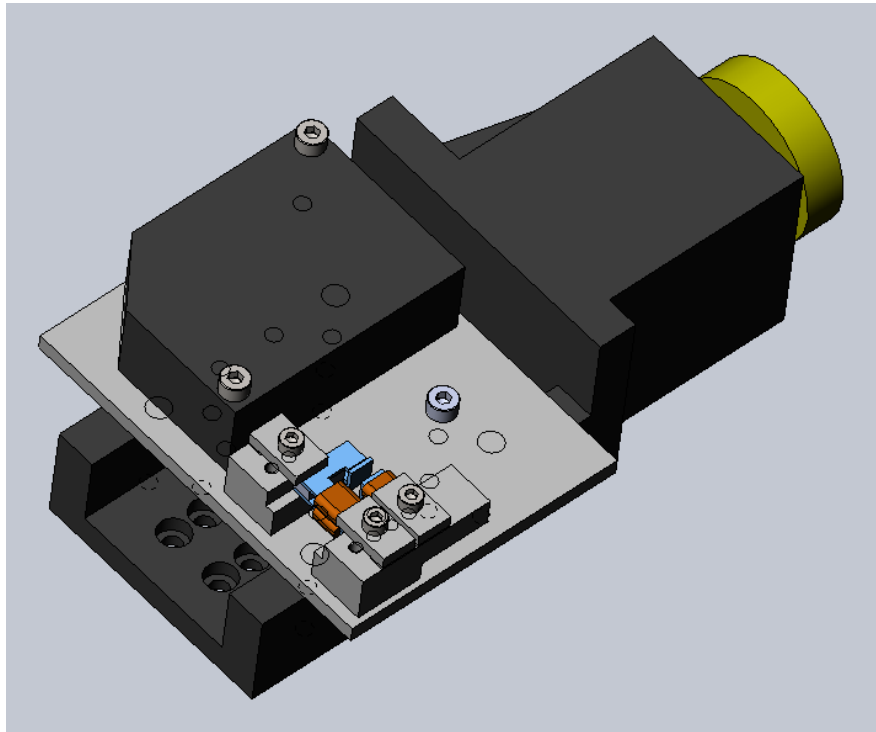


The baseplate subassembly, which is shown below, holds the actuator clamps and also the laser distance sensor. This sensor is a IDL 1401-5 from Micro-Epsilon which has a static resolution of 600 nm, over a measurement range of 5 mm. The distance it can measure lies between 20 and 25 mm, so a 20 mm offset is needed. The sensor is mounted in such a way that its laser beam hits the target of the upper actuator exactly in the centre. In this way measurement errors due to tilting of the target (Abbe errors) are prevented.

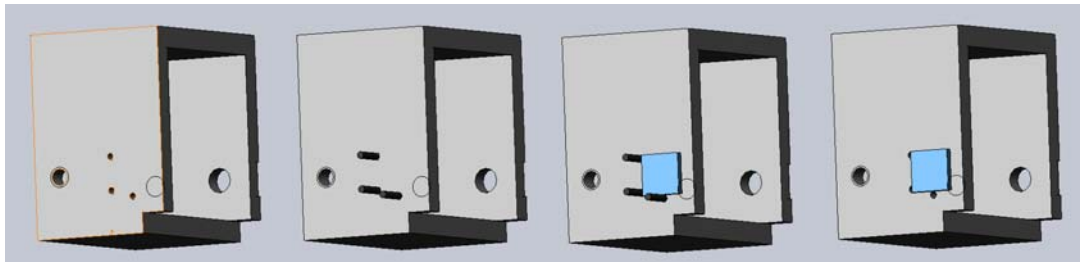


The baseplate subassembly is itself mounted to a MICOS LS-65 positioning stage. This type of stage works with a stepper motor and screw spindle and has a travel range of 26 mm. The positioning resolution is in the micrometer range, although the backlash inherent to this type of stage limits the accuracy when the stage has to reverse direction of motion. The assembly of baseplate and MICOS stage is shown on the following page.

This positioning stage will move the entire subassembly in the x-direction, which is in this setup the horizontal lateral displacement. This displacement is relative to the targets, which are mounted on a holder (discussed further on). During the experiments, the displacement will be 100 – 200 μm in both directions, corresponding to the intended lateral motion range of the levitating disk. The effect of lateral displacements on the reluctance force can be determined this way.

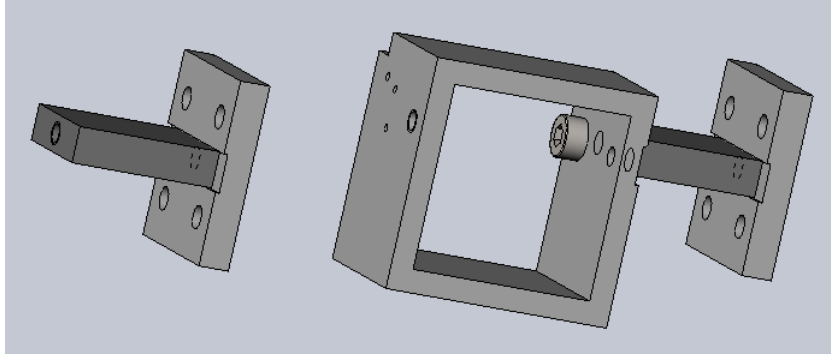


The actuator targets will be mounted to the target holder using epoxy resin or a similar glue. To ensure that the targets will be aligned to each other, even though they are on opposite sides of the holder, three small holes are drilled in the face holding the target. During assembly and curing of the glue, three pins will be inserted through these holes, to serve as a kinematic mount for the targets on both sides. Later on, these pins will be removed. This procedure is illustrated below.

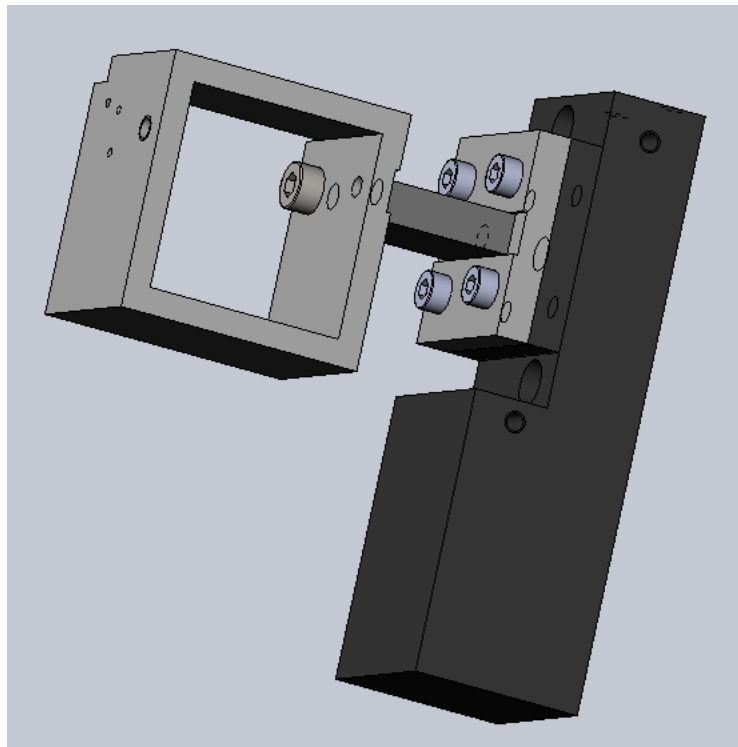


The target holder is made from a piece of aluminium square pipe, which has a 30 x 30 x 3 mm cross section. This hollow part will fit around the lower actuator clamping block, and this will ensure that the force sensor can be mounted in a position that is coaxial to the actuator targets. Then, the reluctance force will be in line with the heart of the sensor, and there will be no parasitic torques interfering with the measurements.

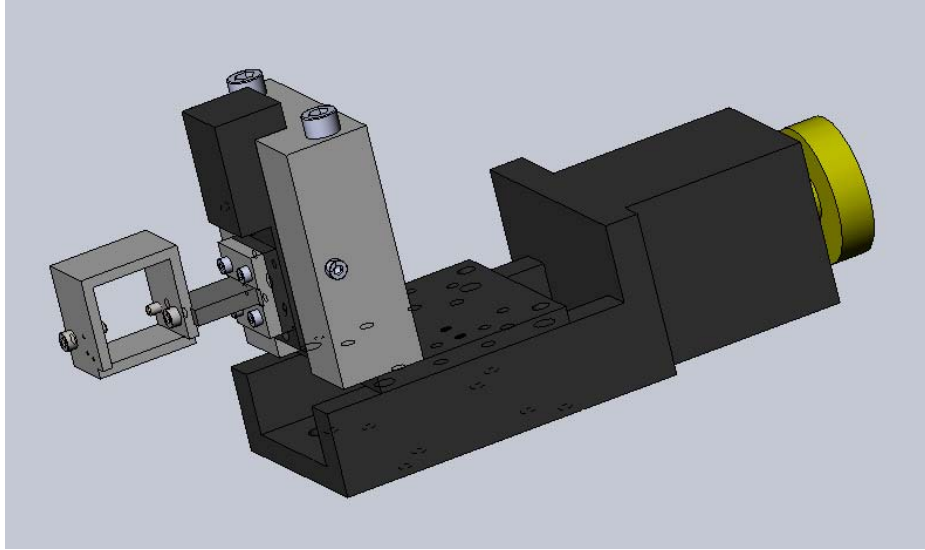
The force sensor is a FUTEK Type LSB-200 miniature S-beam load cell which has a 2 pound (9 N) range. It is mounted in an alignment groove in the target holder on one side, and in a similar groove in an adapter plate on the other side. This is shown below. The target holder will load the force sensor with a small parasitic torque due to its weight. This will affect the measurements, but since it is a constant effect, it can be compensated for.



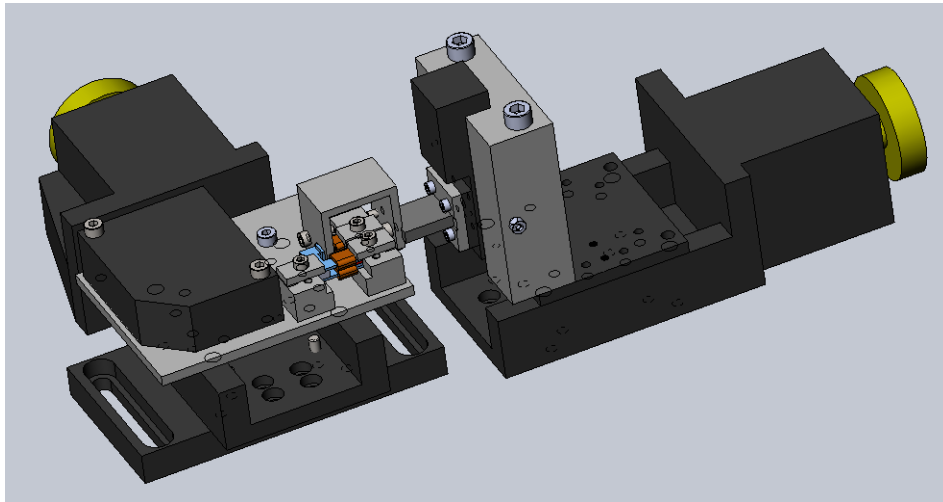
The adapter plate is then screwed to the moving part of a MICOS VT-21 positioning stage. This is a smaller positioning stage, with a travel range of 10 mm. It will be used as the vertical positioning stage here (z-direction), moving the targets (via their holder and the force sensor) relative to the actuators. This will allow investigation of the effect of vertical lateral displacement of the targets on the reluctance force. The motion range investigated here will again be 100 – 200 μm to both sides. The subassembly of vertical stage, force sensor and target holder is shown on the following page.



To enable displacement in the direction of the reluctance force (y-direction), and thereby measure the force-displacement characteristics of the actuator, a second MICOS LS-65 stage is used. This is placed at a 90° angle relative to the other LS-65 stage, and the entire subassembly of target holder, force sensor and VT-21 stage is mounted on it by means of an adapter block. This is shown on the next page.

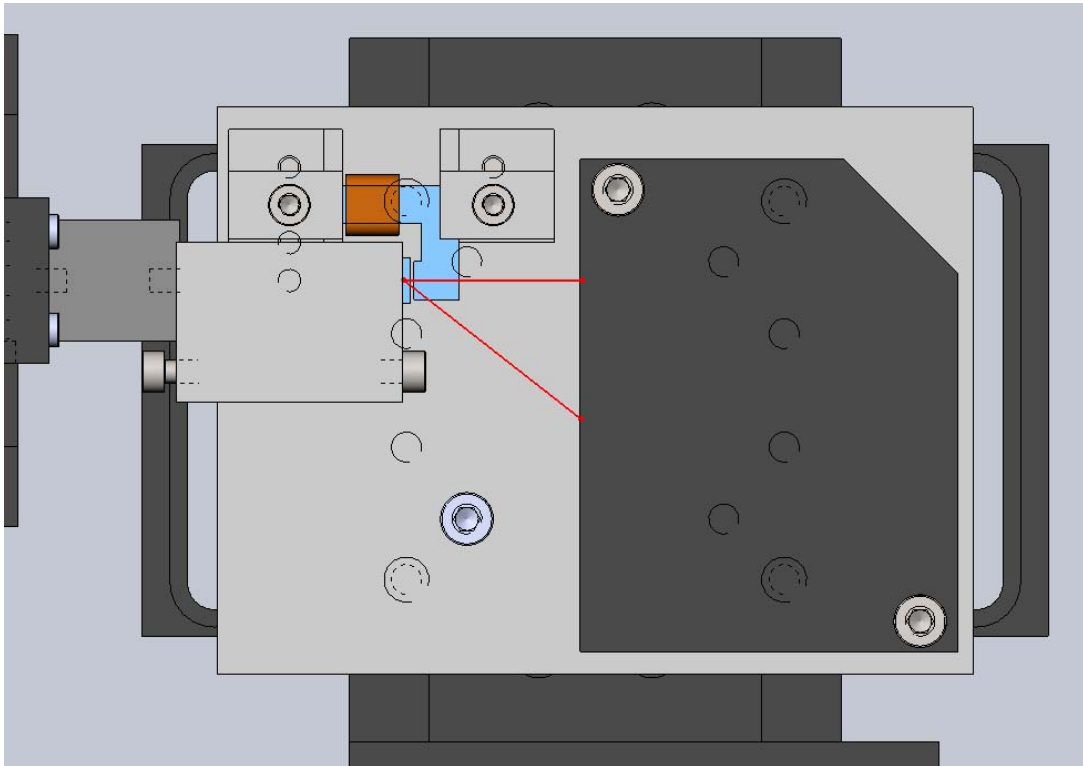


The two LS-65 stages form the base of the complete setup, and are mounted to an optical table with a standard 1" hole grid using adapter plates. The following figure shows the complete setup. Two M3 screws are added to the target holder to function as adjustable end stops. This will prevent the targets getting stuck to one of the (permanent magnet biased) actuators when they get too close, and sensor overloading.



During the experiments, the stiffness of the whole loop comprising the three stages, force sensor and adapter blocks will have to be determined. This stiffness will have an effect on the measurements. However, the displacement sensor is able to determine the exact position of the targets relative to the actuators once it is calibrated. Any unwanted displacement in the y-direction due to this finite stiffness can therefore be measured and the correct force-displacement characteristics determined.

The last figure shows in red the path of the laser beam that is used to measure the displacement of the upper target.



References

Active magnetic bearings, chapter 3:
Hardware Components
Alfons Traxler and Eric Maslen, 2009

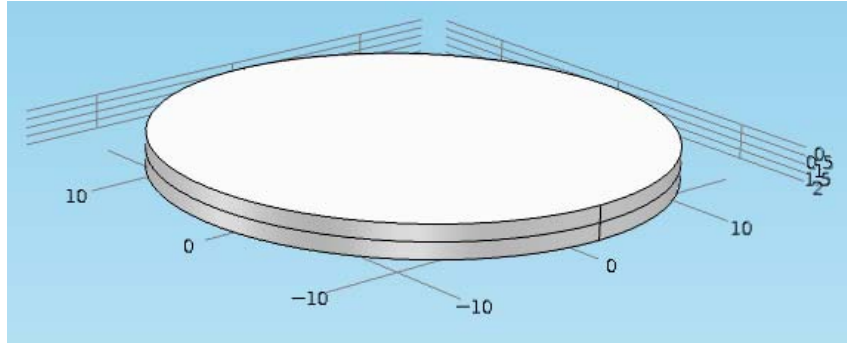
MSD Lecture notes, ch.6:
Electromagnetic Actuators
Rob Munnig Schmidt, 2010

www.monstermagnet.de

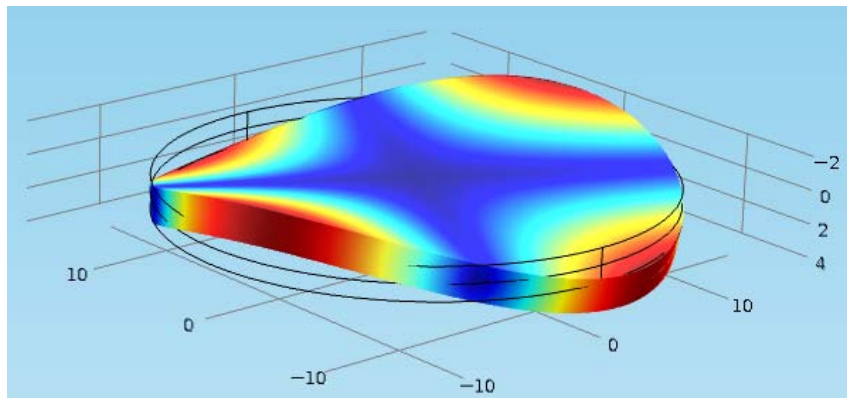
Online permanent magnet catalogue

F Modal analysis of moving part

The first geometry that was investigated is a simple disk, 30 mm in diameter. It consists of a 1 mm aluminium layer and a 1 mm steel layer. This is the reference geometry.



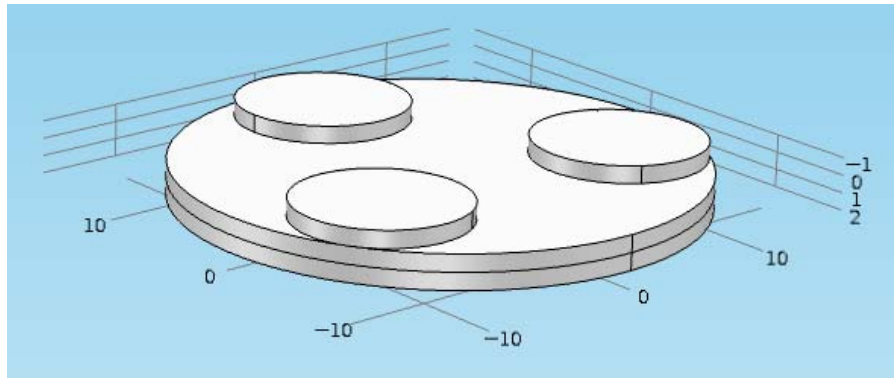
Since aluminium and steel have nearly the same specific stiffness, the eigenfrequencies are almost the same as a pure aluminium disk of the same dimensions. The first two mode shapes have again a four-fold symmetry:



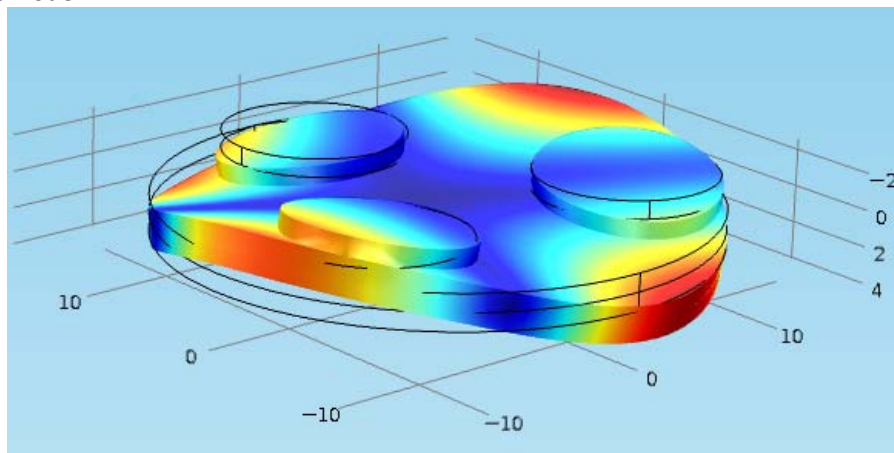
The first six eigenfrequencies of this geometry are

Mode number	Eigenfrequency [kHz]
1	10.2
2	10.2
3	17.4
4	23.3
5	23.3
6	38.2
Mass	7.5 gram

Next, the magnets are added to the geometry. In this stage of the design it was assumed that the distance of the actuators to the centre could be as small as 10 mm, and that the overall diameter could be 30 mm.



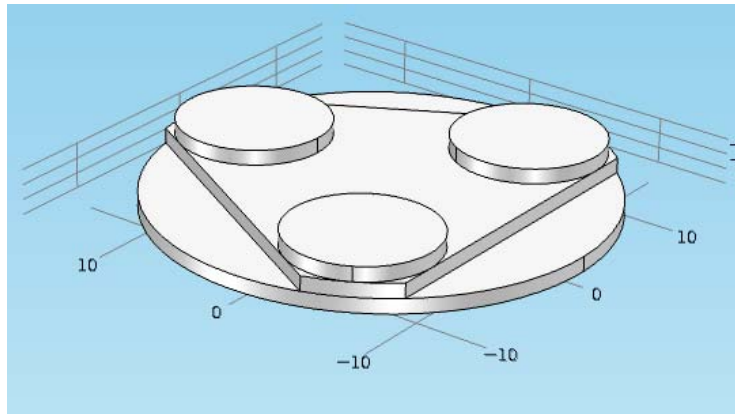
The mode shapes are almost identical to those of the disk alone. Most eigenfrequencies have actually increased, where it would be expected that adding mass would lower them. However, in most mode shapes the magnets do not take part in the motion, i.e. they are located on the areas with the smallest displacements (nodes). The magnets break the symmetry of most structural modes (especially the first two), which makes the structure stiffer. This can be seen in the deformed shape of the first mode:



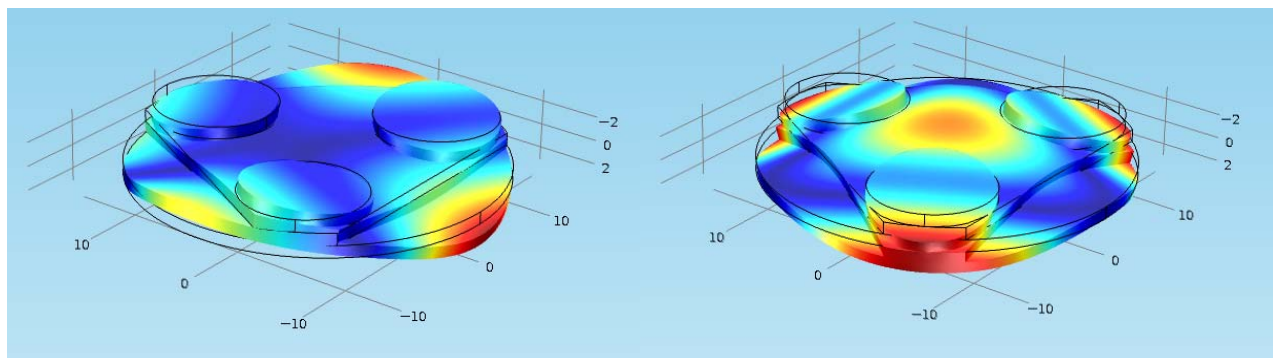
The first six eigenfrequencies of this geometry are

Mode number	Eigenfrequency [kHz]
1	11.1
2	11.1
3	17.2
4	26.3
5	27.6
6	41.3
Mass	9.2 gram

In the next design steps parts of the steel disk are removed to reduce the mass. The main dimensions remain unchanged. First, the material at the edge of the disk is removed:



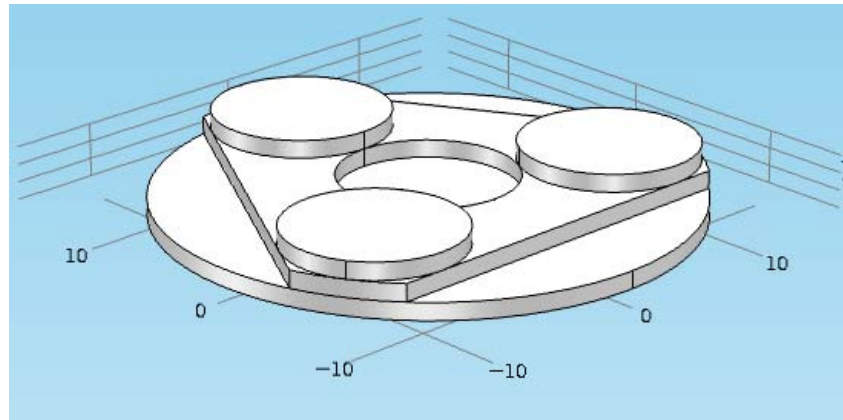
This makes the three-fold symmetry of the disk even more apparent, while the first two modes have a four-fold symmetry (below, left). The eigenfrequency of these modes increases. Conversely, the 3rd mode shape has an axial symmetry (below, right), and its frequency is lowered due to the increased mass (magnets) and reduced stiffness in this direction.



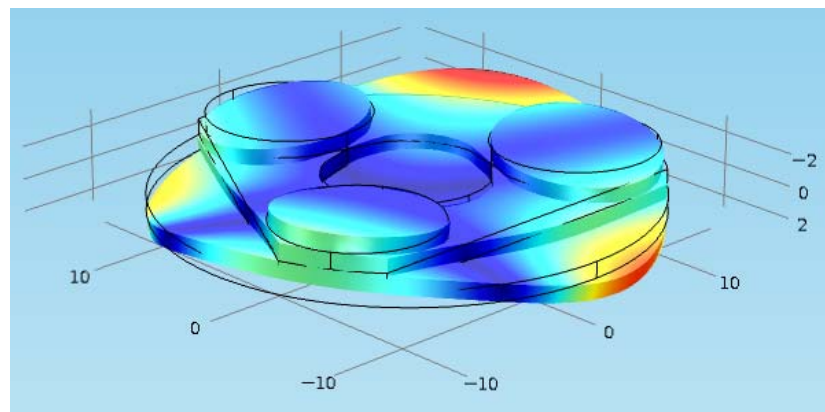
The first six eigenfrequencies of this geometry are

Mode number	Eigenfrequency [kHz]
1	12.7
2	12.7
3	16.7
4	28.9
5	30.2
6	38.3
Mass	7.4 gram

Next, a hole is made in the middle of the steel part. This reduces the mass but lowers the stiffness as well.



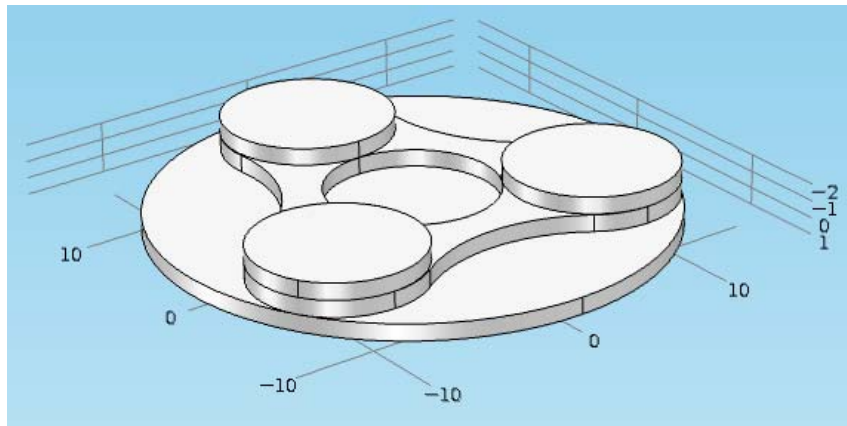
The eigenfrequencies are somewhat lower than in the previous step, but still higher than for a simple disk. A first eigenfrequency of around 10 kHz is anyway acceptable in this design. The mass is now below 7 grams, which is also acceptable.



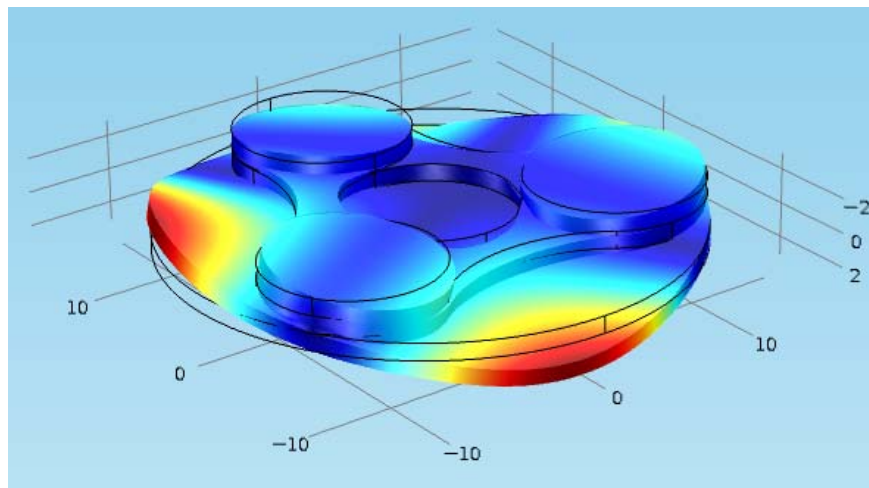
The first six eigenfrequencies of this geometry are

Mode number	Eigenfrequency [kHz]
1	11.6
2	11.6
3	16.1
4	28.4
5	30.4
6	35.7
Mass	6.8 gram

Since the steel part makes up most of the moving mass, in the next step as much of this material as possible is removed, while still retaining a more or less rigid link between the three magnets. This results in the following geometry:



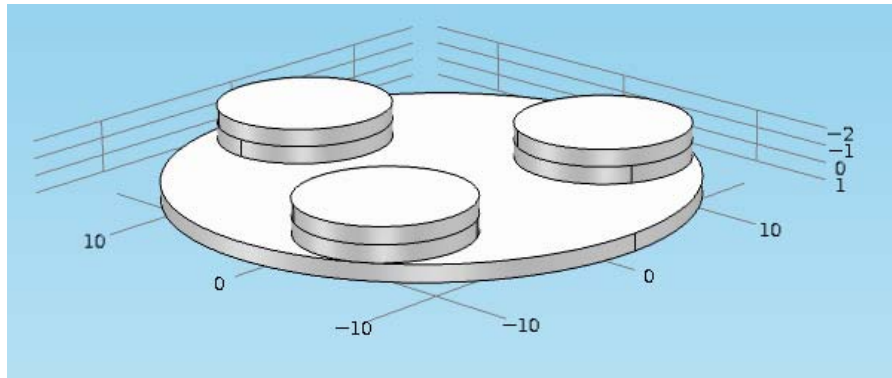
Since the stiffness is now decreased further, and the magnets start behaving more as independent masses, the eigenfrequencies are lowered once more. The first one is still above 10 kHz however, so this would still be acceptable.



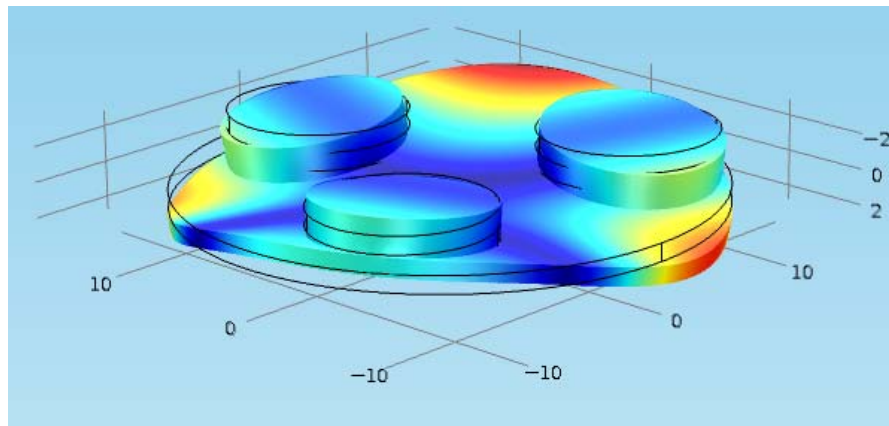
The first six eigenfrequencies of this geometry are

Mode number	Eigenfrequency [kHz]
1	10.2
2	10.2
3	14.2
4	22.3
5	24.3
6	27.2
Mass	6.1 gram

When the amount of steel is reduced to the absolute minimum, namely three disks with the same dimensions as the magnets, we obtain the following geometry:



The eigenfrequencies are now dramatically lowered, because the bending stiffness of the disk is greatly reduced. The three magnets with their steel shielding disks now behave more as three point masses on a relatively flexible disk, the eigenfrequencies are almost halved.



The first six eigenfrequencies of this geometry are

Mode number	Eigenfrequency [kHz]
1	5.8
2	5.8
3	6.6
4	15.0
5	20.3
6	20.6
Mass	5.5 gram

At this point in the design process it became apparent that the moving part needed to be increased in diameter, to make room for the six sensors. Therefore, the distance between the actuators and disk centre was increased to 12 mm and the diameter became 36 mm. If the above geometry would be made with these dimensions, the eigenfrequencies would be even lower:

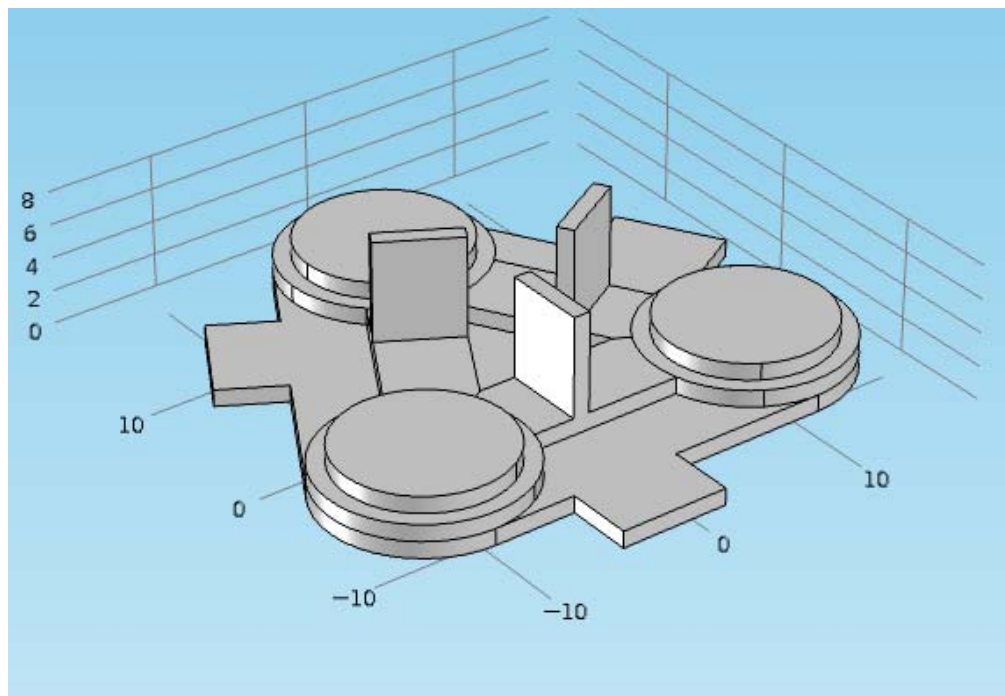
Mode number **Eigenfrequency [kHz]**

1	4.1
2	4.1
3	5.2
4	10.6
5	13.5
6	14.4

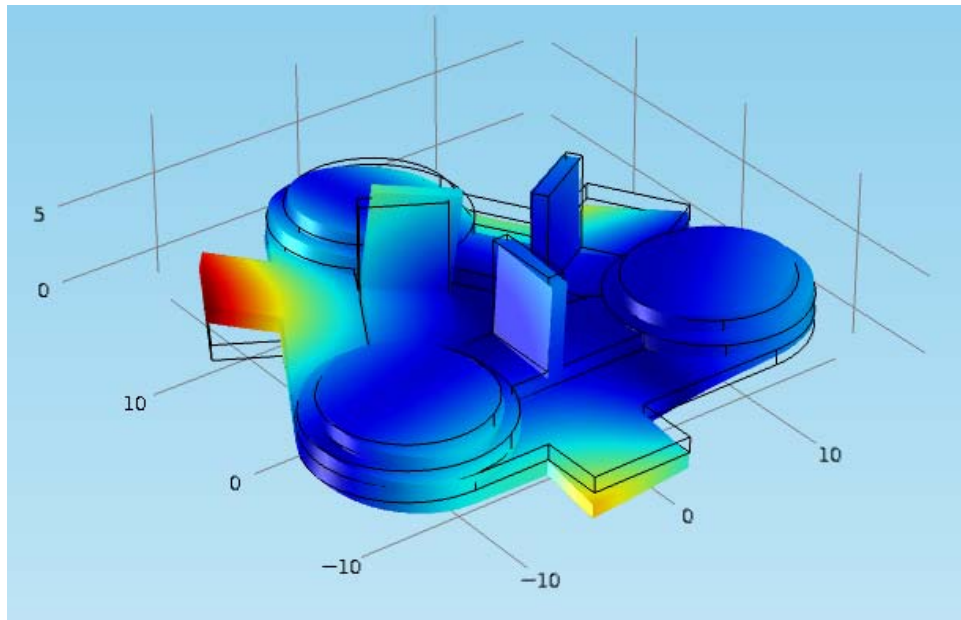
Mass 6.2 gram

Less than 0.8 grams would then be still available to increase the stiffness of the structure. In addition, to provide sufficient magnetic shielding, the steel disks need to be bigger in diameter than the magnets, and sensor targets still need to be added. In short, this would yield a moving part that is either too compliant or too heavy.

Since the assembly area needs to be only 20 mm in diameter, some material at the disk edge could be removed, leaving only the vertical sensor targets. The ribs between the magnets were made from aluminium instead of steel and were integrated with the horizontal sensor targets. The resulting total mass could be kept as low as 7.1 grams. This yielded a moving part structure with the following geometry:



This part is considerably stiffer than the previous one. It shows that the ribs between the magnets are necessary to obtain sufficiently high eigenfrequencies. The sensor targets introduce additional structural modes, but these have eigenfrequencies that lie above 20 kHz and do not affect system performance.

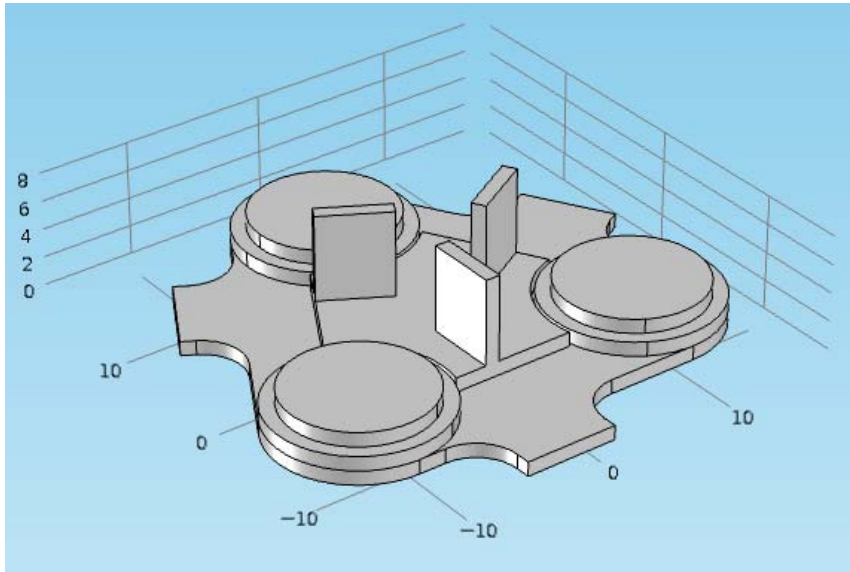


The first six eigenfrequencies of this geometry are

Mode number	Eigenfrequency [kHz]
1	7.7
2	7.7
3	8.9
4	16.0
5	19.7
6	20.1
Mass	7.1 gram

This would theoretically be acceptable for the microslave stage moving part. However, in this form the moving part is not manufacturable. The aluminium structure, including the ribs and sensor targets must be milled from a single block of aluminium, and therefore fillets are needed in certain corners. The hole in the middle, between the three ribs, has to be removed. Finally, there must be a small clearance between the ribs and the magnetic shields, so the position of the latter can be adjusted during assembly. (Necessary to align magnets to coils.) The latter feature will decrease the stiffness somewhat and consequently lower the eigenfrequencies.

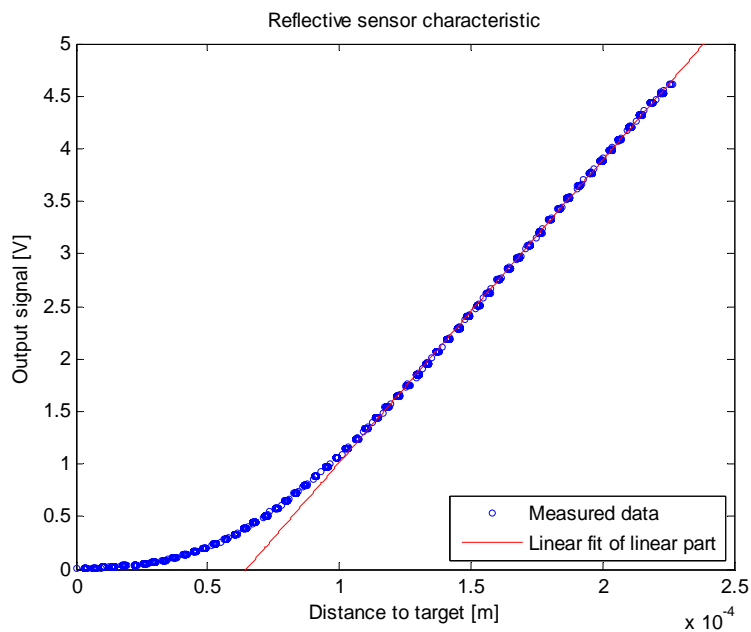
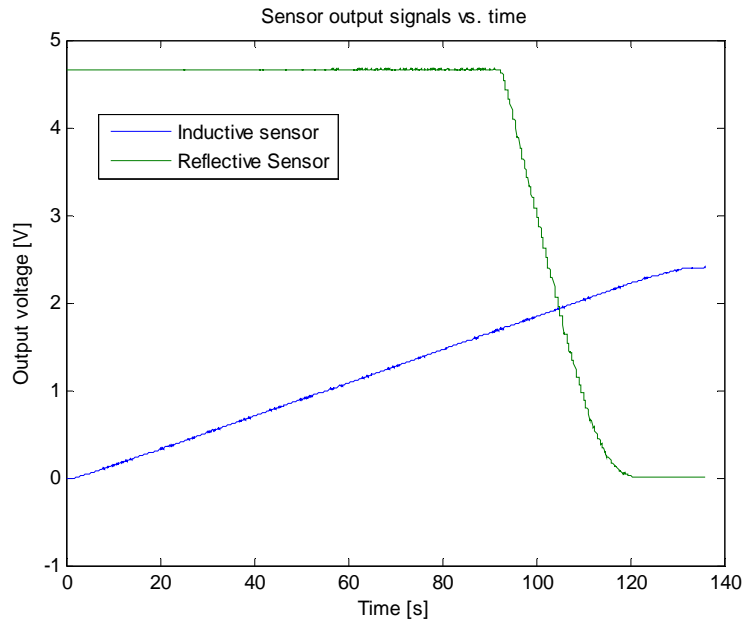
This leads to the final geometry displayed below. Its first eigenfrequency is 7.0 kHz, and the mass is increased to 7.3 grams. This is slightly more than the originally specified maximum of 7 grams, but still acceptable. More details about its geometry and mode shapes is given in chapter 6.



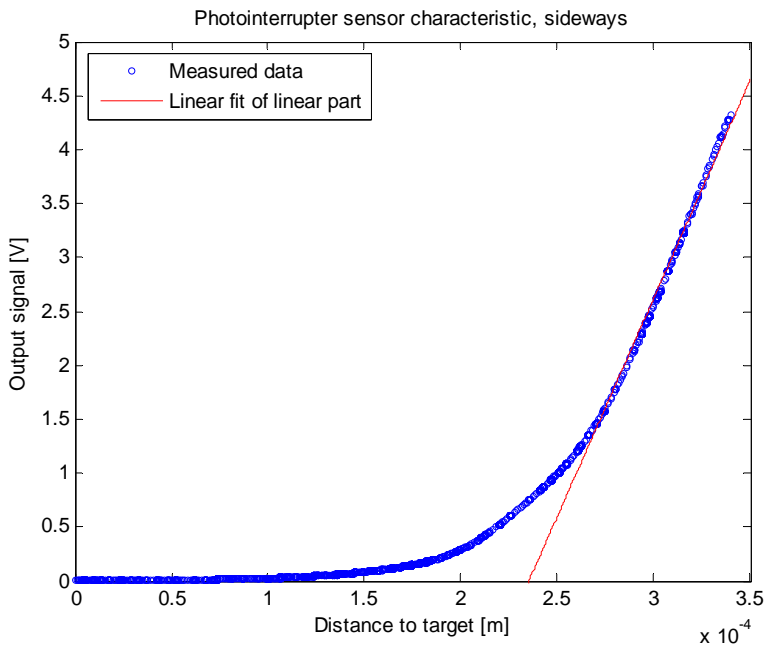
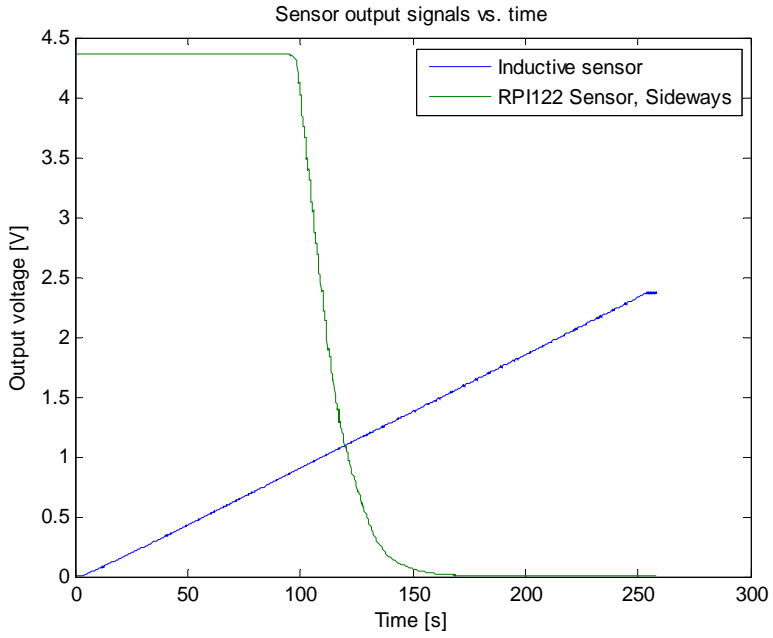
G Sensor tests measurement data

Initial sensor range tests

Displayed in the six graphs below are the measurement data of the initial tests of both types of optical sensor. The first graph on each page shows the optical sensor output and inductive (reference) sensor output vs. time. During the measurement the target moved with small steps relative to the sensors. The second graph on each page shows the optical sensor characteristic that derives from the measurement data, as well as a linear fit.

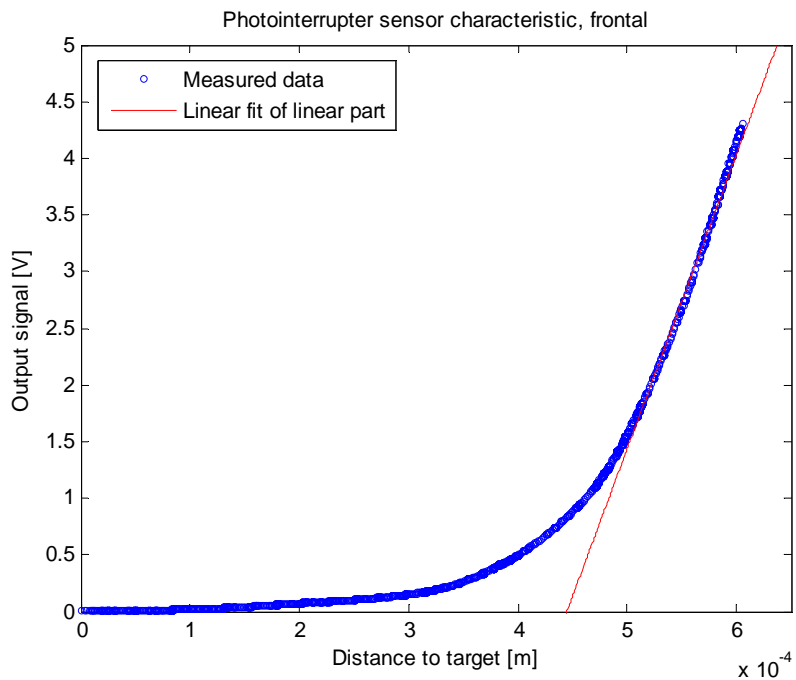
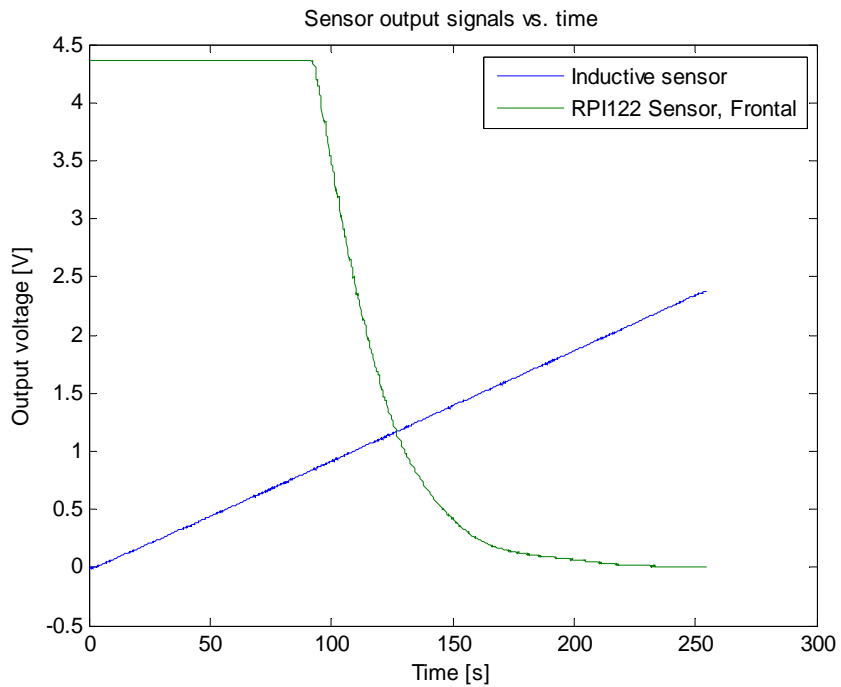


Sensitivity, linearised: 29 mV/ μm
Standoff: about 100 μm , Range 120 μm .



Sensitivity, linearised: 40 mV/ μm

Standoff (relative to total darkness): about 270 μm , range : 80 μm



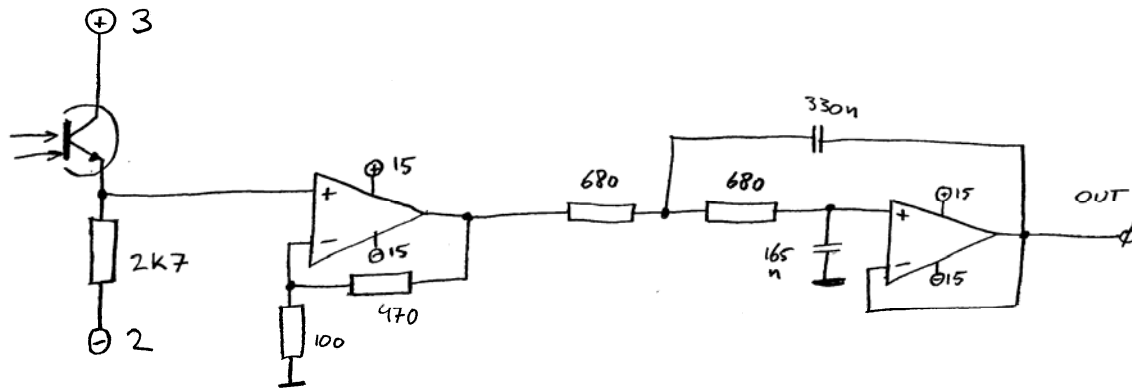
Sensitivity, linearised: 26 mV/ μm

Standoff (relative to total darkness): about 500 μm , range : 100 μm

Summary of Optical Sensor Range and Noise Measurements

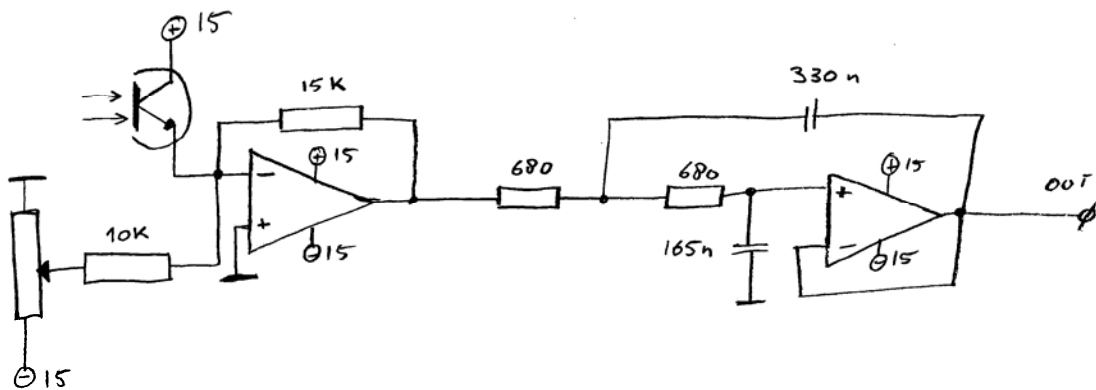
After the initial experiments and a lot of testing, three configurations were tried for the sensor readout electronics. These are (current sources not shown):

- Diagram 1#.



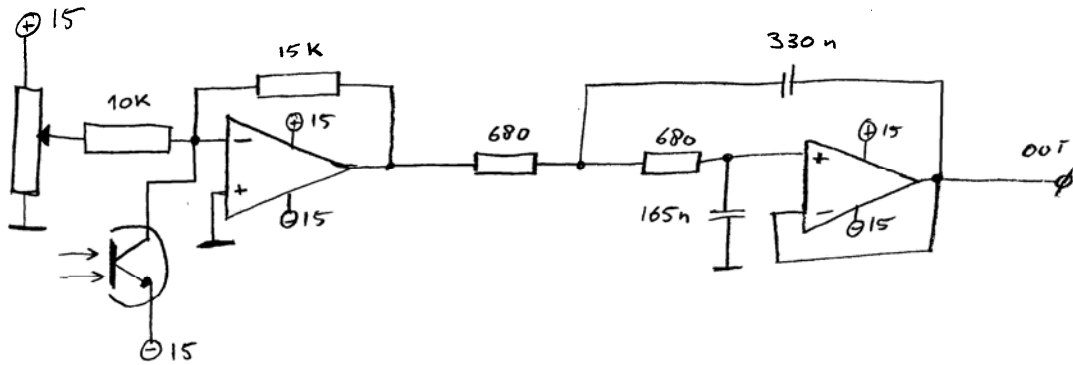
Phototransistor fed by dual, low voltage supply. Photocurrent to voltage conversion by an emitter resistor, followed by a non-inverting amplifier and filter. The disadvantages of this setup are:

- Needs two additional supply voltages for the PHT (extra components, added noise sources)
 - Emitter resistance causes varying collector-emitter voltage, resulting in poor linearity
 - No possibility for zero adjustment except by altering PHT supply voltages
- Diagram #2A.



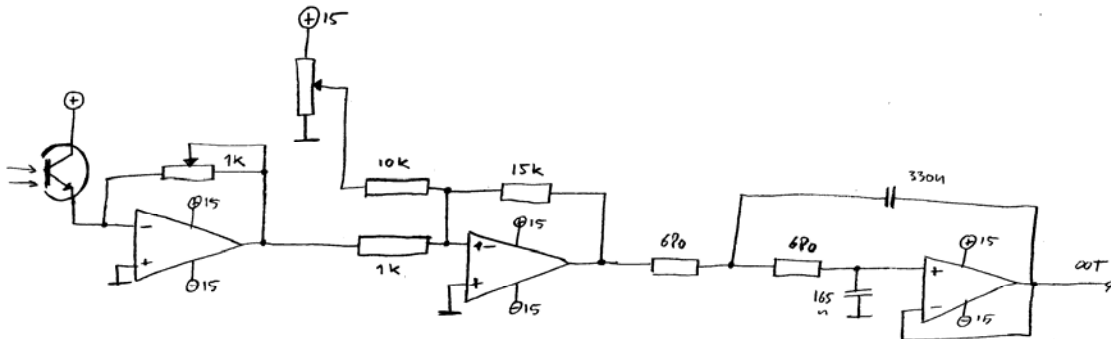
Phototransistor fed by single supply, directly connected to transresistance amplifier. The filter is identical to the previous setup. When the reflective type sensor is used, the PHT supply can 15V and no additional supply voltages are needed. Zero adjustment is possible, as well as gain adjustment. The amplifier is inverting, this results in an inverted sensor characteristic (maximum output voltage at minimum target distance).

- Diagram #2B.



Identical to diagram #2B except for PHT polarity. The PHT is fed from the negative supply, so the output characteristic is no longer inverted. This setup proved to be the best configuration.

- Diagram #3.



Setup similar to diagram #2A, but with separate inverting amplifier stage for zero adjustment. Because of the two series connected inverted amplifiers the sensor characteristic is non-inverted without having to invert PHT supply polarity. The extra amplifier stage introduces extra noise, however.

During the initial tests various configurations were tried for the current source. It was found that an active, opamp controlled current source had the lowest noise levels and temperature sensitivity. This type CCS was used during all subsequent experiments, except for one test with an integrated current source (type LT 3092), which proved to be very noisy.

A test parameter that could be varied was the current flowing in the sensor IR LED, it was found that a larger current resulted in a relatively lower noise level in the output (because the absolute noise current stays constant).

On the following pages, range and noise test results are summarised for the two sensor types and the various electronic setups described above. Sensor supply voltages, amplifier gain settings and current settings are indicated in each case. The tests where an LT3092 CCS or an improved DAQ system was used are indicated as well.

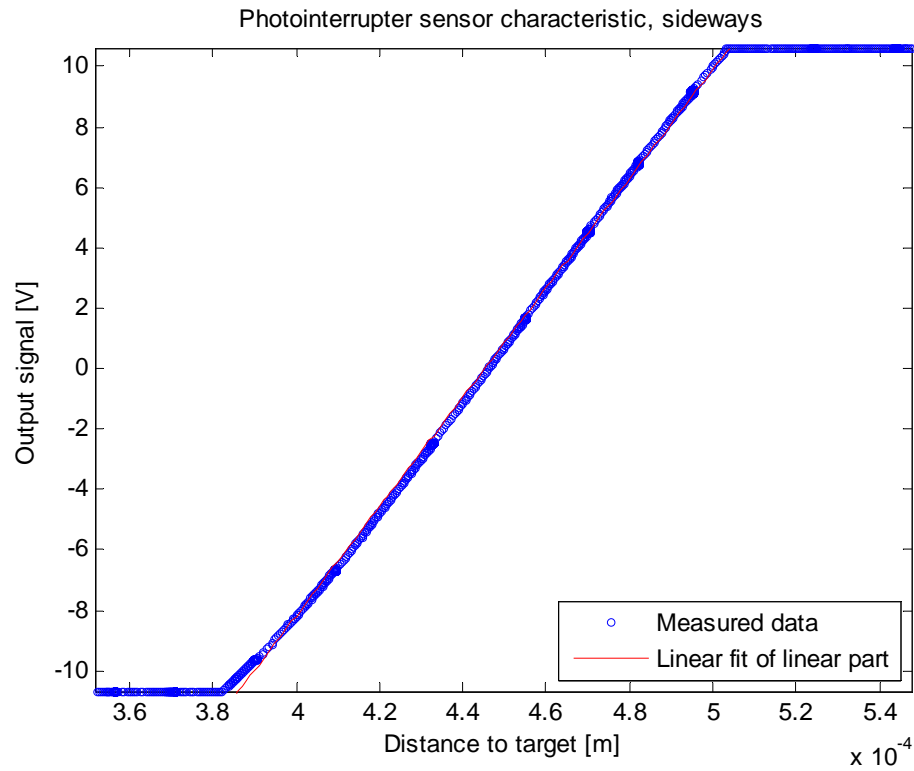
RPI-122 Photo-interrupter

- **Sideways configuration, Readout acc. to Diagram #1**

Emitter resistance 560 Ω

Supply voltages +6 and -1.5 V

Amplifier gain 11



Linear range approx. 120 μm

Sensitivity 180 mV/ μm

Range	RMS position noise [nm]:	Peak-to-peak position noise [nm]:
Full	3.0	25
Mid	2.6	22
Low	2.0	22

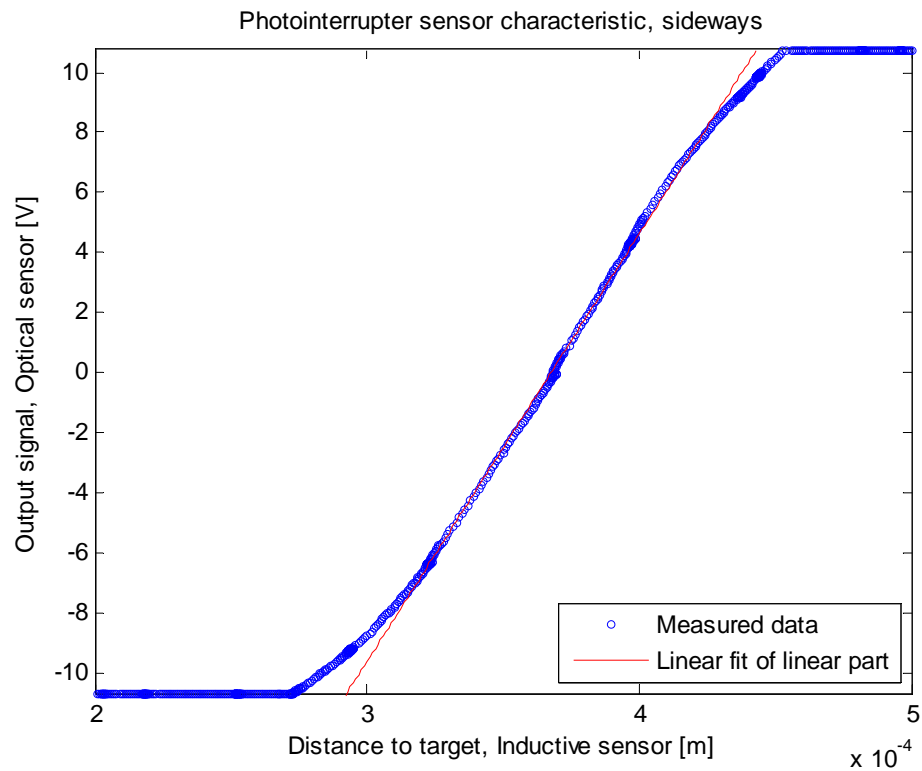
RPI-122 Photo-interrupter

- **Sideways configuration, Readout acc. to Diagram #1**

Emitter resistance 3300 Ω

Supply voltages +11 and -9 V

Amplifier gain 1.7



Linear range approx. 130 μm

Sensitivity 140 mV/ μm

Range	RMS position noise [nm]:	Peak-to-peak position noise [nm]:
Full	3.3	30
Mid	3.2	27
Low	2.5	22

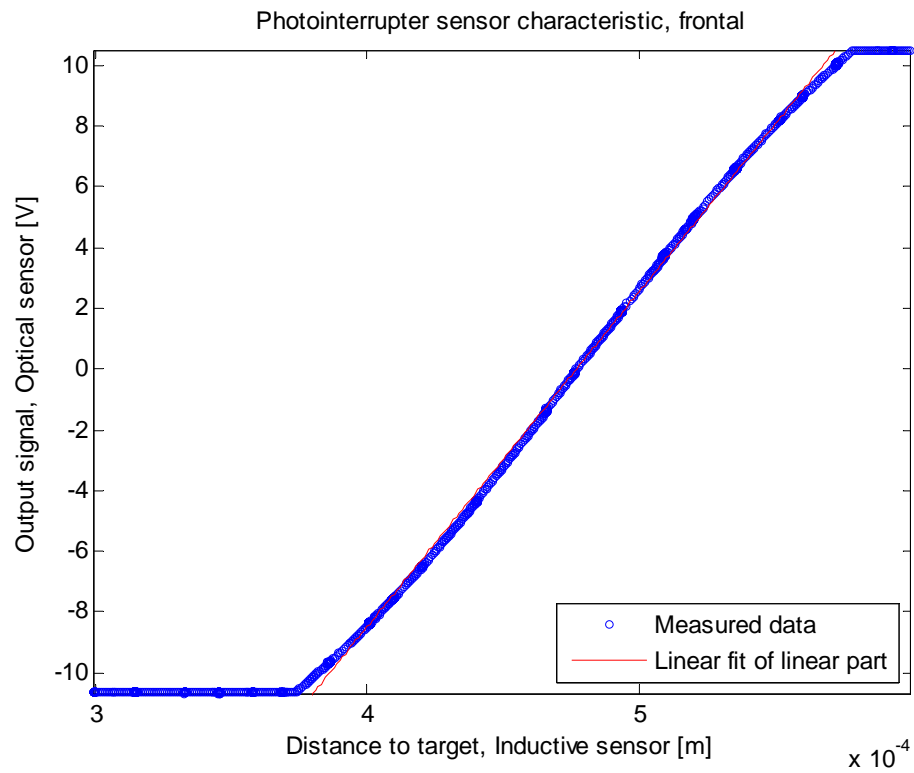
RPI-122 Photo-interrupter

- **Frontal configuration, Readout acc. to Diagram #1**

Emitter resistance 560 Ω

Supply voltages +6 and -1.5 V

Amplifier gain 11



Linear range approx. 180 μm

Sensitivity 104 mV/ μm

Range	RMS position noise [nm]:	Peak-to-peak position noise [nm]:
Full	5.5	47
Mid	4.6	39
Low	3.7	32

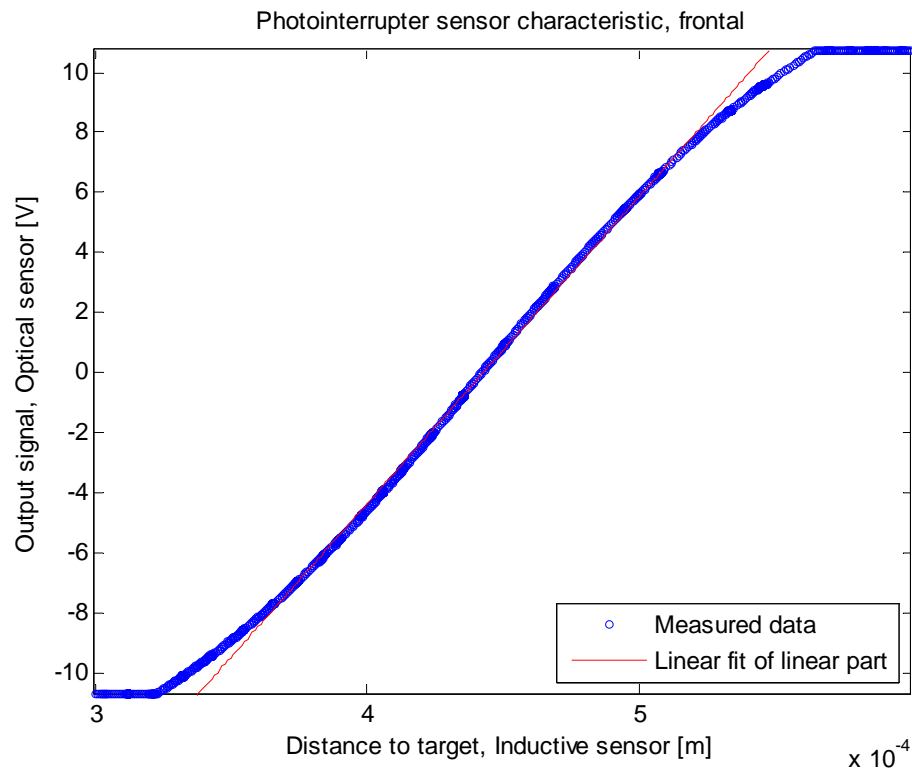
RPI-122 Photo-interrupter

- **Frontal configuration, Readout acc. to Diagram #1**

Emitter resistance 3300 Ω

Supply voltages +11 and -9 V

Amplifier gain 1.7



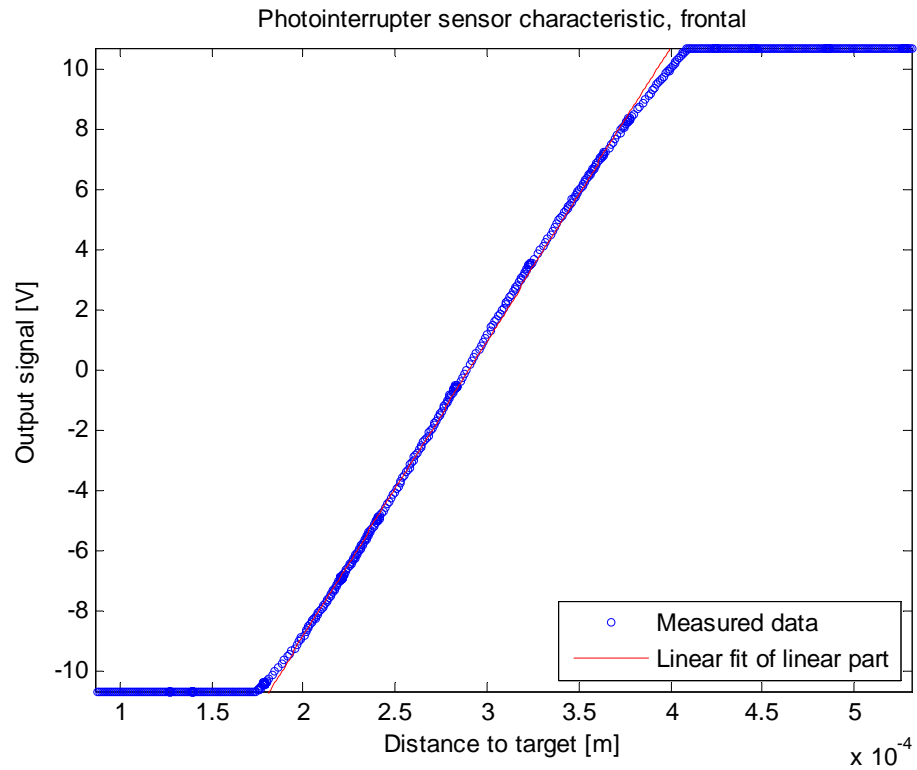
Linear range approx. 160 μm

Sensitivity 102 mV/ μm

Range	RMS position noise [nm]:	Peak-to-peak position noise [nm]:
Full	4.3	36
Mid	4.0	35
Low	3.3	28

SFH-9201 Reflective sensor

- **Readout acc. to Diagram #1**
 Emitter resistance 2700 Ω
 Supply voltages +3 and -2 V
 Amplifier gain 6

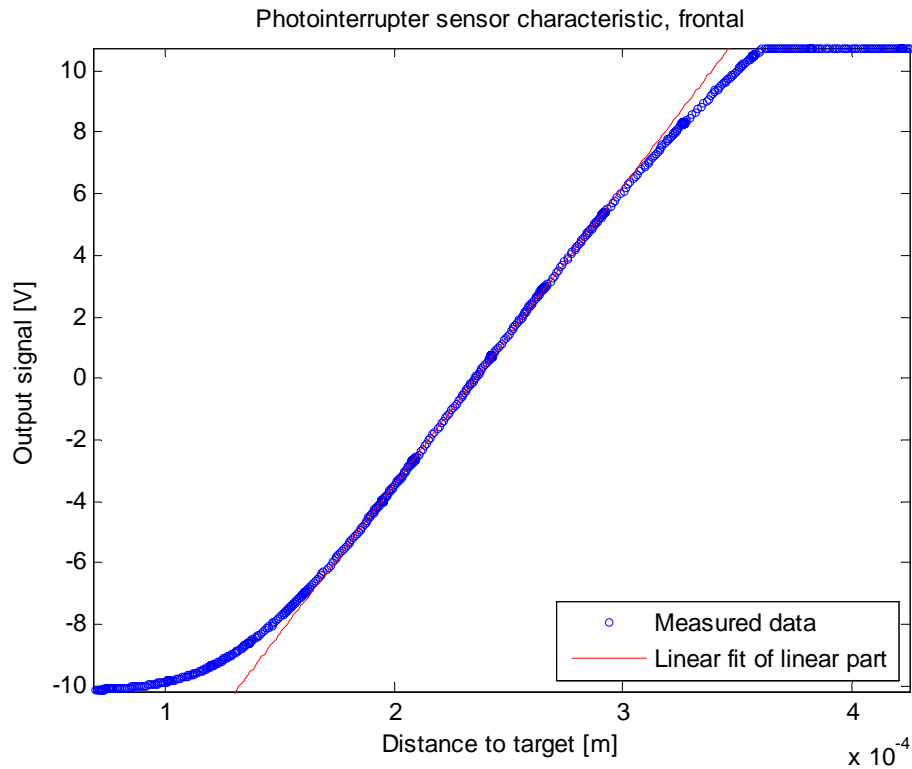


Linear range approx. 190 μm
 Sensitivity 98 mV/ μm

Range	RMS position noise [nm]:	Peak-to-peak position noise [nm]:
Full	4.8	40
Mid	4.1	36
Low	3.3	26

SFH-9201 Reflective sensor

- **Readout acc. to Diagram #1**
 Emitter resistance 10000 Ω
 Supply voltages +8 and -7 V
 Amplifier gain 1.5



Linear range approx. 170 μm
 Sensitivity 97 mV/ μm

Range	RMS position noise [nm]:	Peak-to-peak position noise [nm]:
Full	4.2	35
Mid	3.9	31
Low	3.3	27

SFH-9201 Reflective sensor

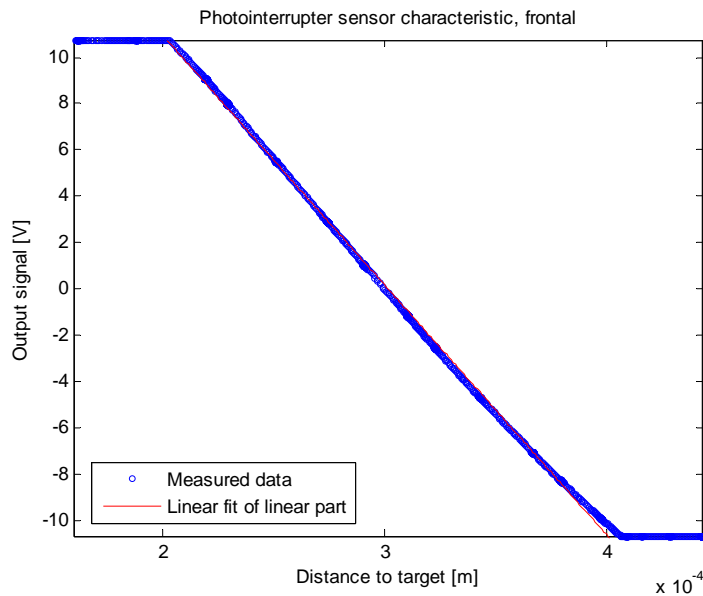
- **Readout acc. to Diagram #2A**

Several measurements were carried out with this setup, to determine the effect of the current source setting. The transresistance amplifier gain was adjusted accordingly. The following settings were tried:

LED current 15 mA

Transresistance gain 33 V/mA

Offset voltage -4.2 V



Linear range approx. 200 μm

Sensitivity -108 mV/ μm

With USB-6211

Range	RMS position noise [nm]:	Peak-to-peak position noise [nm]:
-------	--------------------------	-----------------------------------

Full	6.2	53
------	-----	----

Mid	5.3	43
-----	-----	----

Low	4.2	36
-----	-----	----

With PXI-4464 board

Range	RMS position noise [nm]:	Peak-to-peak position noise [nm]:
-------	--------------------------	-----------------------------------

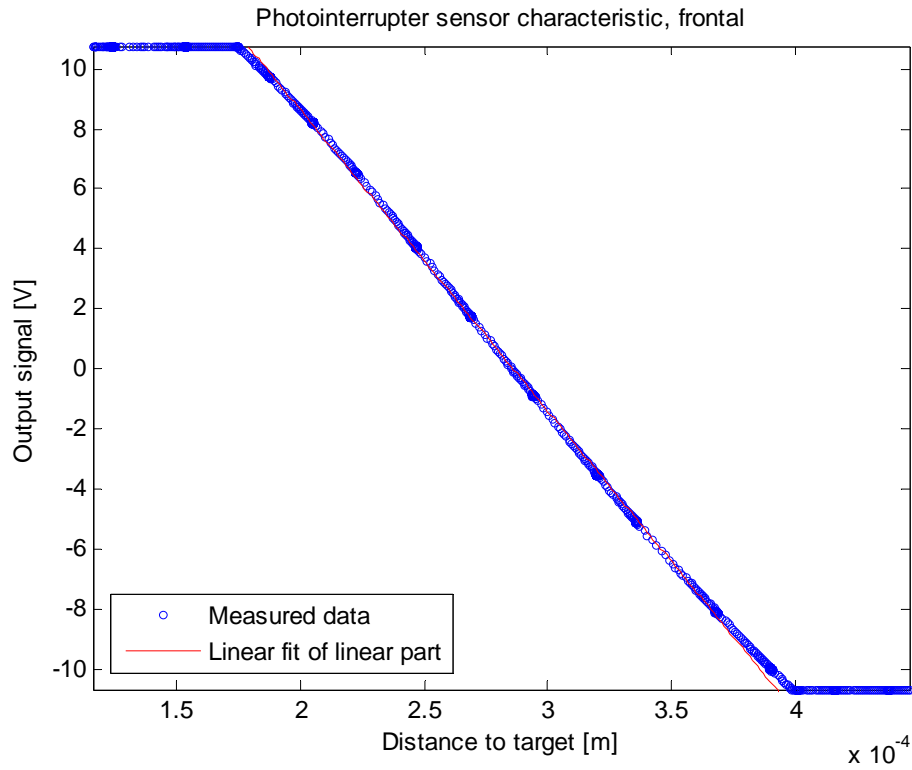
Full	5.7	46
------	-----	----

Mid	4.8	38
-----	-----	----

Low	3.3	28
-----	-----	----

SFH-9201 Reflective sensor

- **Readout acc. to Diagram #2A**
 LED current 30 mA
 Transresistance gain 15 V/mA
 Offset voltage -9 V



Linear range approx. 200 μm
 Sensitivity -100 mV/ μm

With USB-6211

Range	RMS position noise [nm]:	Peak-to-peak position noise [nm]:
Full	5.1	39
Mid	4.3	36
Low	3.5	30

With PXI-4464 board

Range	RMS position noise [nm]:	Peak-to-peak position noise [nm]:
Full	4.0	32
Mid	3.2	26
Low	2.0	17

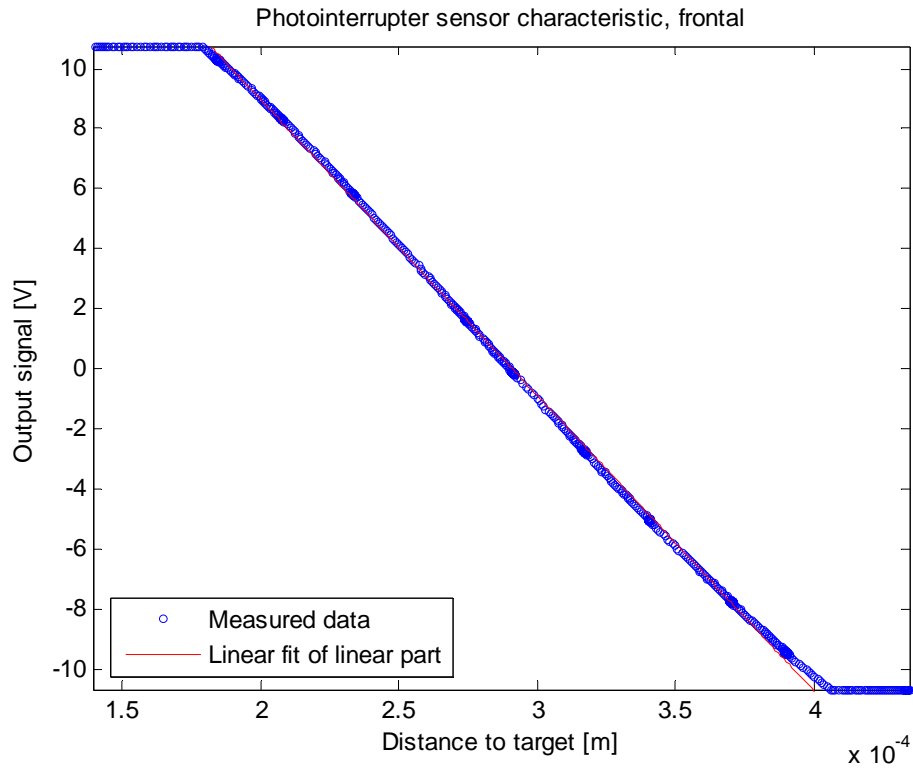
SFH-9201 Reflective sensor

- **Readout acc. to Diagram #2A**

LED current 45 mA

Transresistance gain 10 V/mA

Offset voltage -13.6 V



Linear range approx. 200 μm

Sensitivity -99 mV/ μm

With USB-6211

Range	RMS position noise [nm]:	Peak-to-peak position noise [nm]:
Full	4.4	35
Mid	3.9	33
Low	3.3	26

With PXI-4464 board

Range	RMS position noise [nm]:	Peak-to-peak position noise [nm]:
Full	3.3	30
Mid	2.5	21
Low	1.6	14

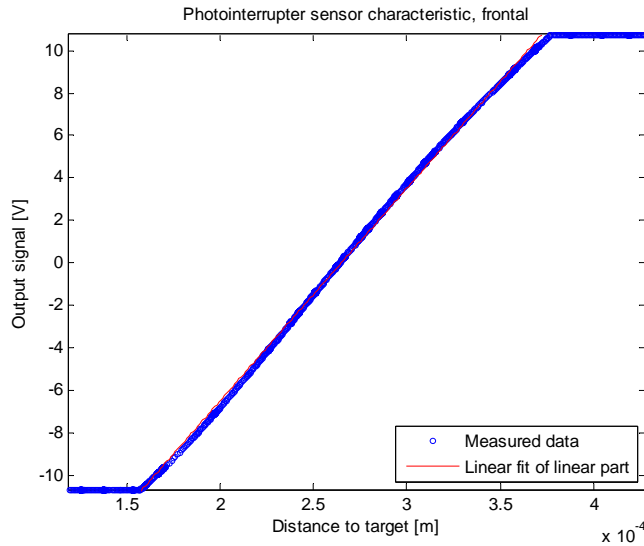
SFH-9201 Reflective sensor

- **Readout acc. to Diagram #2B, reversed polarity**

LED current 45 mA

Transresistance gain 10 V/mA

Offset voltage +13.6 V



Linear range approx. 200 μm

Sensitivity 100 mV/ μm

This measurement shows exactly the same linearity, range and sensitivity as the previous one, but this time the polarity is “logical”.

With PXI-4464 board

Range RMS position noise [nm]: Peak-to-peak position noise [nm]:

Full	3.3	28
Mid	2.5	20
Low	1.6	15

Also the noise levels are (almost) the same as before.

With PXI-4461 board and LT3092 Current source

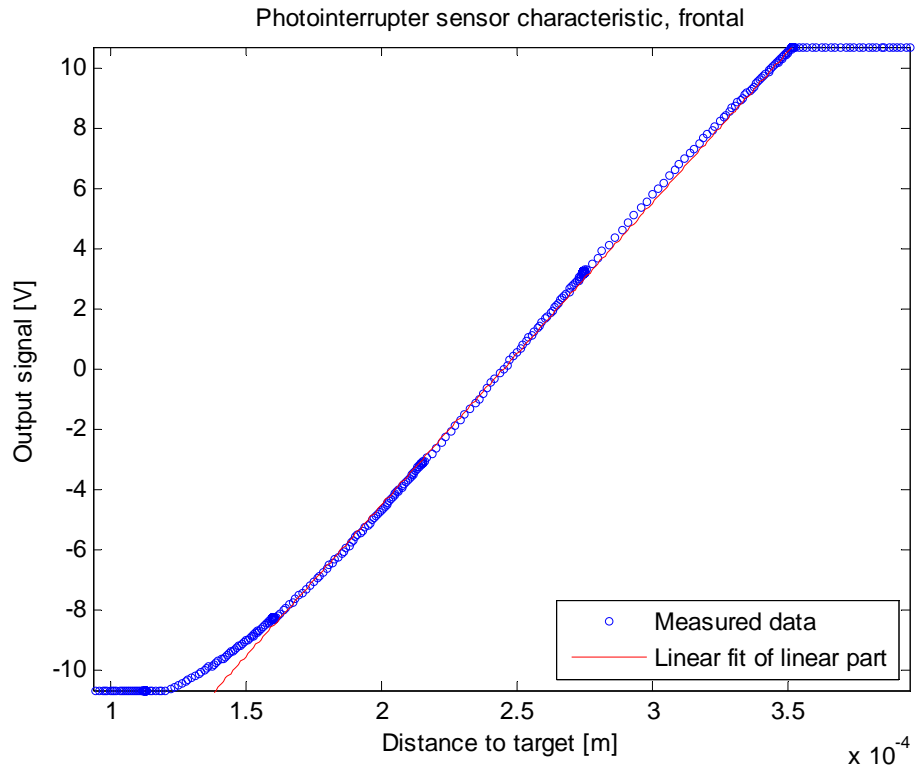
Range RMS position noise [nm]: Peak-to-peak position noise [nm]:

Full	10	80
Mid	6.1	58
Low	2.6	23

This is a considerable worsening of performance.

SFH-9201 Reflective sensor

- Readout acc. to Diagram #3

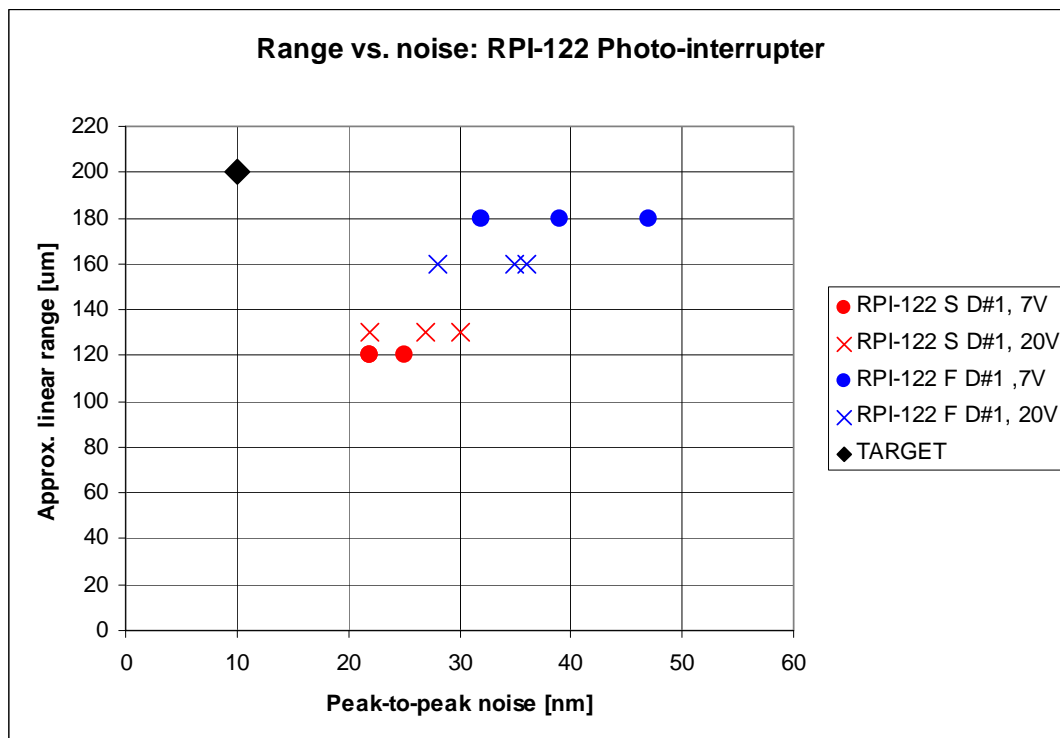


Linear range approx. 200 μm
Sensitivity 100 mV/ μm

Range	RMS position noise [nm]:	Peak-to-peak position noise [nm]:
Full	5.0	43
Mid	4.6	39
Low	3.4	30

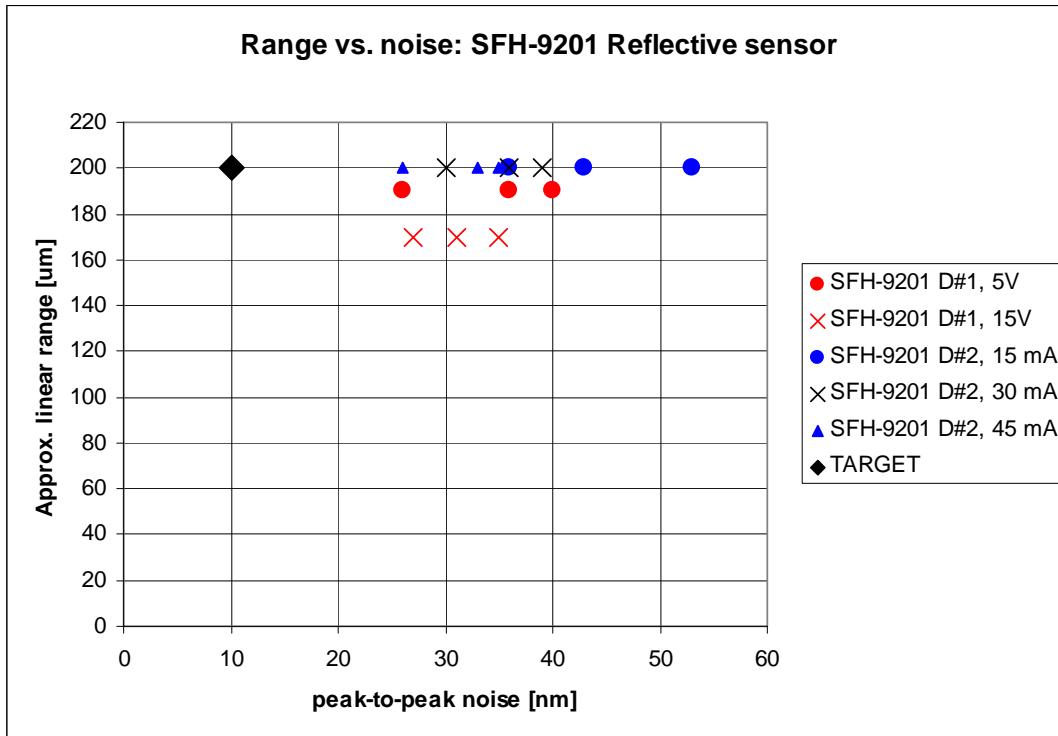
In the following graphs, the achieved sensor range is plotted versus the peak-to-peak noise to summarise the above measurements. The data is divided across three graphs for clarity.

The first graph shows the results of the photo-interrupter measurements. These were done using the readout electronics according to diagram #1 only. Blue symbols show the photo-interrupter in frontal configuration, red ones the sideways configuration. The points lie more or less on the same line through the origin, meaning that there is a trade-off between range and noise. A 180 μm range was the most that could be achieved with this type sensor. Noise levels down to 25 nm p-p are possible, but only over smaller ranges.

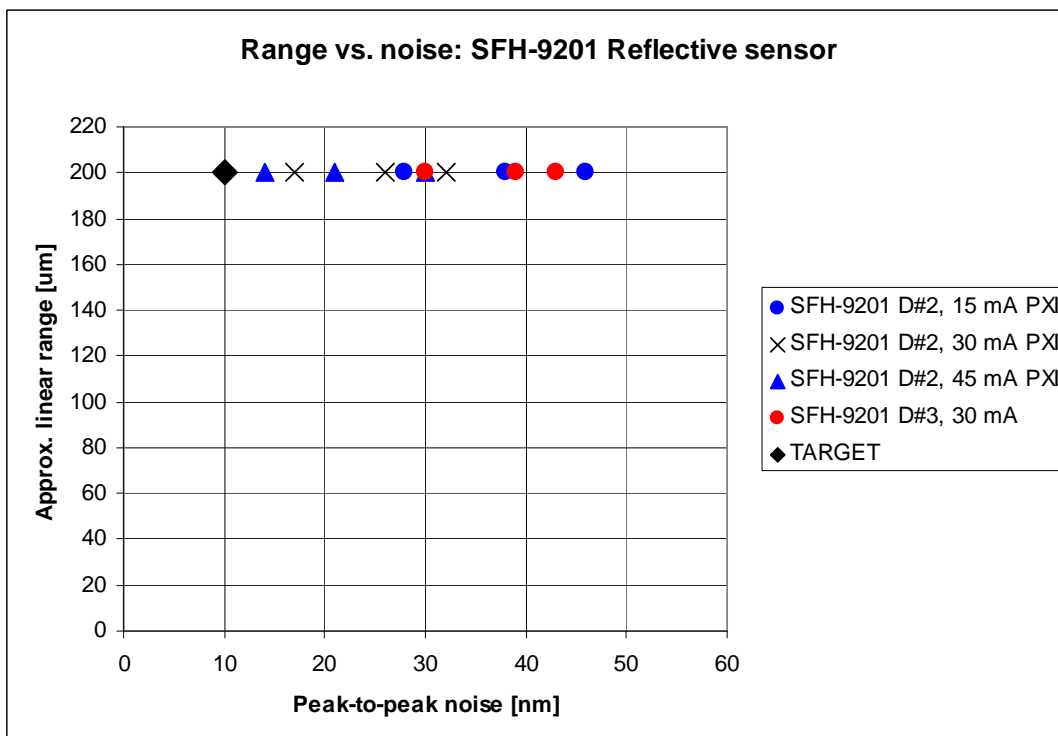


The second graph shows the same results for the reflective sensor. These measurements were done with readout electronics according to diagram #1 (red symbols) and according to diagram #2 (transresistance amplifier, blue symbols). The red symbols indicate a similar trade-off between range and noise as before, although the slope appears to be somewhat steeper. This would indicate a better performance of this sensor than the RPI-122. However, a 200 μm linear range still could not be achieved with this setup.

The transresistance amplifier setup shows considerable improvement over these results. The linear range is now 200 μm and as the LED current is increased, points on the graph move to the left. This indicates that noise performance can be improved without adversely affecting the range. This is limited, however, by the maximum permissible LED current and the noise caused by the DAQ unit used.



The final graph shows the results of the same measurements taken with the PXI-4644 DAQ board (blue symbols), as well as those of an experiment with readout electronics according to diagram #3 (red symbols). The latter results indicate a somewhat worse noise performance at the same LED current when compared to those with diagram #2, therefore this setup was not investigated further.



The measurements with the PXI board, however, show a considerable improvement. All data points have shifted to the left when compared to the previous data obtained with the USB-6211 board. The best performance achieved was a 14 nm peak-to-peak noise, which is almost the desired performance of 10 nm. However, this occurs only in the lower part of the range, since in the same measurement at the upper part of the range, the noise goes up to 30 nm p-p. Using the PXI board made this effect even more clear than before. This indicates two possible noise sources:

1. Stray light. The sensor is more sensitive to this when the gap between it and its target is larger. During the measurements the setup was shielded from stray light, but this shielding was far from perfect.
2. Noise in the light emitted by the sensor LED. This has a greater effect when more of this light is reflected back to the sensor, i.e. in the upper part of the range. This noise, in turn, can have two possible causes:
 - a. Noise in the LED itself. This is a property of the sensor and can't be improved.
 - b. Noise in the current source feeding the LED. This can be remedied up to a certain limit by decreasing the current noise, by redesigning or by selecting a suitable integrated circuit current source. The LT3092 was clearly not suitable in terms of noise performance. Another possibility is replacing the zener diode by a low-noise, low-drift integrated voltage reference.

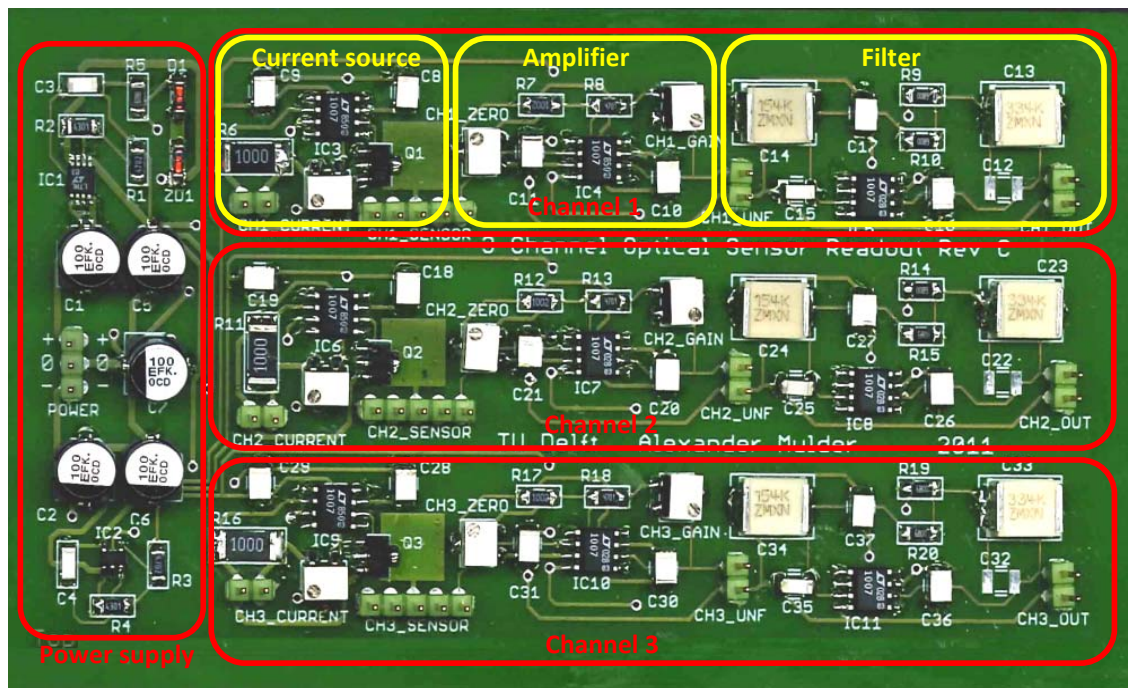
H Sensor readout board manual

Specifications

Power supply voltage	±15 V DC
Power supply current	200 mA max
Output voltage range	±10 V
Output impedance	< 70 Ω
Filter bandwidth	1 kHz
Output sensitivity	100 mV/μm (With SFH-9201 sensor, used in the near range)
Output noise, peak-peak	1.5 – 2.8 mV (Equivalent to 15 – 28 nm, ditto, LED current 45 mA)

Overview

The sensor readout board is a low noise, three channel board that provides power to the sensor and amplifies its output signal. It is primarily designed for use with the Osram type SFH-9201 reflective sensor, but can also be used with other optical sensors that consist of a LED and phototransistor (including photo-interrupters). The fully built-up board is shown below; the main functional blocks are indicated by rectangles.



The board consists of a low-noise power supply block (left) and three identical sensor readout channels. The power supply is symmetrical, to enable an output voltage with the industry standard voltage range of ±10 V. Each channel consists of a constant current source that powers the sensor LED, an amplifier that converts the phototransistor current to an output voltage, and a 2nd order Butterworth filter to improve the signal-to-noise ratio. To enable sensor calibration and the use of various sensor types, the LED current, amplifier gain and zero are adjustable per channel. The channels are fully independent, so in applications that do not require all three channels only the relevant channels have to be built up. The board is designed to fit inside a Hammond type 1455J1601 encasing (Farnell order no. 4272845).

Circuit description

- **Power supply**

The board is fed from an external symmetric power supply of ± 15 V DC. The current drain from this supply is, depending on the sensor current settings, up to 200 mA per board. The external supply should be connected to the three pole pinheader labelled "POWER".

Note: Always make sure that the polarity and voltage of the power supply are correct! The input voltage should never exceed ± 16 V DC. The polarity of the supply lines is indicated on the board.

IC1 and IC2 are stabiliser ICs that reduce the noise levels on the supply lines to a few hundred μ V. The output voltages are set to ± 14.5 V by resistors R1 and R2 (positive supply) and R3 and R4 (negative supply). Bypass and buffer capacitors are provided to further reduce noise and improve stability. Each opamp is provided with two 100 nF decoupling capacitors to reduce crosstalk between channels.

A diode/zenner series combination provides the reference voltage V_{REF} (6.3 V DC) for the constant current sources. This combination is chosen for its low temperature coefficient.

- **Constant current sources**

IC3, IC6 and IC9 are the opamps that actively control the current passed by the three transistors (Q1, Q2 and Q3). This current is approximately equal to V_{REF} / R_E where the emitter resistance R_E is the sum of a 100 Ω resistor and the resistance of the trimmer labelled "CHx_CURRENT". With this trimmer the current feeding the sensor LED can be adjusted between approximately 10 and 60 mA, depending on the application and sensor type. Turning the trimmer screw clockwise increases the current.

Note: The LED maximum current and power dissipation, specified in the sensor datasheet, should never be exceeded!

During adjustment the LED current can be monitored by measuring the voltage across the 100 Ω measurement resistors R6, R11 and R16 (1 V corresponds to a current of 10 mA). This voltage is available on the pinheaders labelled "CHx_CURRENT", next to the trimmers.

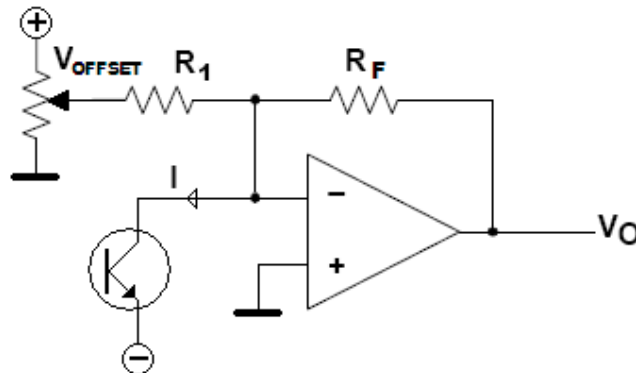
Note: The current source outputs of any channels that are not in use should never be left open. This will result in parasitic oscillations in the opamp and transistor, which causes excessive dissipation and interference in the other channels. Unused channels should have a resistor of around 100 Ω connected between the collector of the transistor and ground (pin 2 and 3 on the sensor connectors)

- **Transresistance amplifiers**

IC4, IC7 and IC10 are opamps connected as so-called transresistance amplifiers. The inverting input of such an amplifier is a virtual earth node. Any current (i.e. the position dependent phototransistor collector current) applied to this node is directly converted to a voltage at the amplifier output. The amplifier gain (in V/A) is equal to the opamp feedback resistance R_F (R8, R13 and R18 in series with trimmers). The trimmers labelled "CHx_GAIN" can be used to adjust the amplifier gain so the desired part of the sensor range is translated to an output voltage range of ± 10 V. The gain adjustment range is approximately 5 – 50 V/mA. Turning the trimmer screw clockwise increases the gain. The sensor itself should be connected to the five-pole pinheaders marked "CHx_SENSOR".

At the virtual earth node an offset voltage is added to the signal (via R7, R12 and R17) to make the output voltage range symmetrical around 0 V. The offset voltage, and therefore the 0 V point, can be

adjusted with the trimmers labelled “CHx_ZERO”. Turning the trimmer screw clockwise makes the amplifier output voltage more negative.



Simplified transresistance amplifier diagram. When I is the phototransistor current, the output voltage is given by

$$V_o = -R_F \left(-I + \frac{V_{Offset}}{R_1} \right)$$

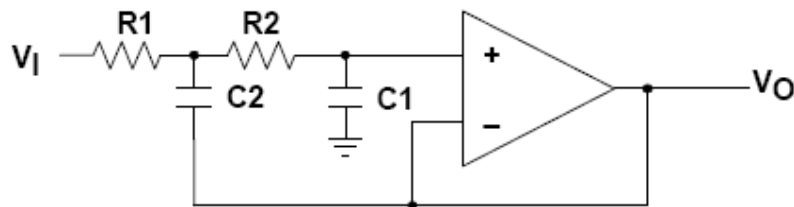
Note: When connected to the board, the sensor’s collector-emitter voltage is always 15 V. If other sensor types than the SFH-9201 are used, this value should be checked against the maximum collector-emitter voltage and power dissipation specified in the sensor’s datasheet.

If desired, the unfiltered signal (i.e. amplifier output) is available at the pinheaders labelled “CHx_UNF”.

- **Filters**

The filters are used to reduce the noise level on the output signal by limiting the output bandwidth. They are built around opamps IC5, IC8 and IC11, and are 2nd order Sallen-Key low-pass filters with a Butterworth characteristic. The impedance of the filter components is kept low (on the order of 1 kΩ) to reduce the noise generated by the filter itself. The opamp type LT1007 is optimised for low noise with component impedances in this range. The filter gain is unity in the passband.

With the component values given in the diagram, the filter crossover frequency is 1 kHz. If another frequency f_0 is needed, the component values can be recalculated with the following equations:



$$RC = \frac{1}{2\pi f_0}$$

$$R = 1k\Omega; \quad C = RC / C$$

$$R_1 = R_2 = \frac{\sqrt{2}}{2} \cdot R$$

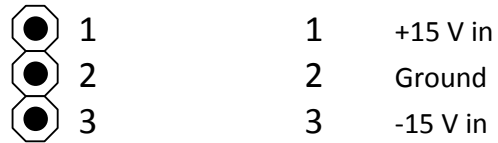
$$C_1 = C$$

$$C_2 = 2 \cdot C$$

Setting $R = 1 \text{ k}\Omega$ determines the filter impedance. Some experimenting with component values may be needed to arrive at values that lie in the E12-series, capacitors are usually only available in these values. Filter capacitors with non-E12 values can also be made by connecting two capacitors in parallel; extra solder pads for capacitors of different physical sizes are provided on the circuit board. The filtered output signal is available at the pinheaders labelled "CHx_OUT".

Pinout

- Pinheaders (Top View)



POWER



CHx_CURRENT



CHx_SENSOR



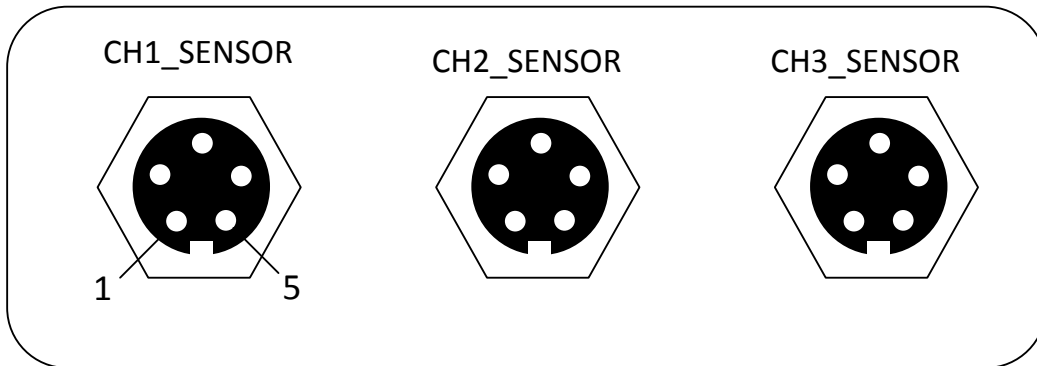
CHx_UNF



CHx_OUT

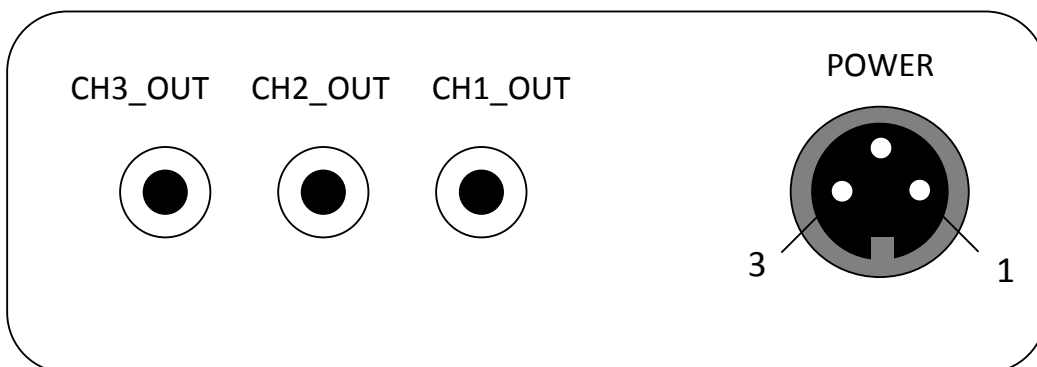
- External connectors (Front view)
These are the front and rear panels of the encasing as it was built for the microslave application.

FRONT PANEL



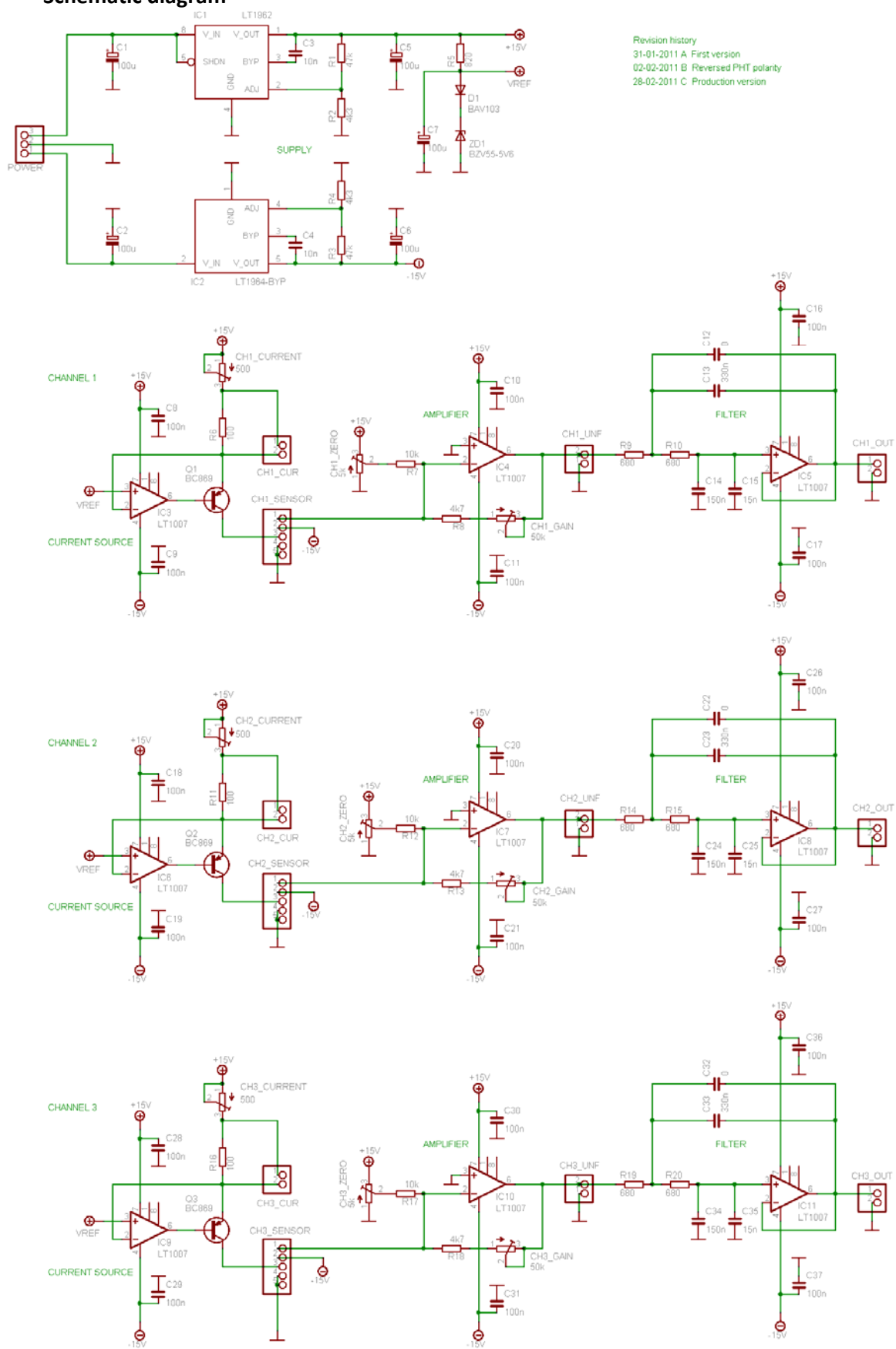
- 1 Shielding (Ground)
- 2 Cathode (Ground)
- 3 Anode (Current source out)
- 4 Emitter (-15 V)
- 5 Collector (Amplifier in)

REAR PANEL



- 1 +15 V in
- 2 Ground
- 3 -15 V in

Schematic diagram



Revision history
 31-01-2011 A First version
 02-02-2011 B Reversed PHT polarity
 28-02-2011 C Production version

Parts list

Part name	Value	Type, package	Function	Farnell order no.	Pc. per board
Capacitors					
C1,C2,C5,C6,C7	100 μ F	25V electrolytic, Case style D8	PSU buffer cap	1850109	5
C3,C4	10 nF	100V PEN, 1206	PSU bypass cap	1657968	2
C8,C9,C10,C11,C16,C17					
C18,C19,C20,C21,C26,C27					
C28,C29,C30,C31,C36,C28	100 nF	25V PEN, 1210	Opamp decoupling	1100602	18
C13,C23,C33	330 nF	50V PET, 2824	SK Filter cap	1753066	3
C14,C24,C34	150 nF	50V PET, 2824	SK Filter cap	1753062	3
C15,C25,C35	15 nF	25V PEN, 1206	SK Filter cap	1100601	3
Resistors					
R1,R3	47 k Ω	250mW, 1206	PSU voltage set	1653133	2
R2,R4	4.3 k Ω	250mW, 1206	PSU voltage set	1653140	2
R5	820 Ω	500mW, 1206	Vref series res	1576627	1
R6,R11,R16	100 Ω	1W, 2512	Current sense res	1653199	3
R7,R12,R17	10 k Ω	250 mW, 1206	Amplifier input res	1653050	3
R8,R13,R18	4.7 k Ω	500 mW, 1206	Amplifier feedback res	1576638	3
R9,R10,R14,R15,R19,R20	680 Ω	500 mW, 1206	SK Filter res	1576626	6
Potentiometers					
P1,P4,P7	500 Ω	250 mW, 13 turn, YJ case	Current adjust	1141344	3
P2,P5,P8	5 k Ω	250 mW, 13 turn, YJ case	Zero adjust	1141347	3
P3,P6,P9	50 k Ω	250 mW, 13 turn, YJ case	Gain adjust	1141350	3
Semiconductors					
D1		BAV103, 250 mA, SOD80	Vref temp. compensation	1612356	1
ZD1	5,6 V	BZV55, 500 mW, SOD80	Vref	1757825	1

Part name	Value	Type, package	Function	Farnell order no.	Pc. per board
Semiconductors, cont'd					
Q1,Q2,Q3		BC869-25, SOT89	Current source transistor	1757901	3
IC1		LT1962, MSOP8	Positive regulator	1663518	1
IC2		LT1964-BYP, SOT23-5	Negative regulator	1663815	1
IC3,IC4,IC5,IC6,IC7,IC8,IC9 IC10,IC11		LT1007, SOIC8	Opamps	1136622	9
Connectors					
		50x1 pinheader, for all pcb connectors		1822168	1
		Two pole plug, pcb output		1593458	3
		Three pole plug, pcb power		1593459	1
		Five pole plug, pcb sensor		1593461	3
		SMB connector, chassis mount, for output signal		1169644	3
		Five pole circular connector, chassis mount, for sensor		1122354	3
		Five pole circular connector, plug, for sensor		1122335	3
		Three pole circular connector, chassis mount, power		1122372	1
		Three pole circular connector, plug, power		1122365	1

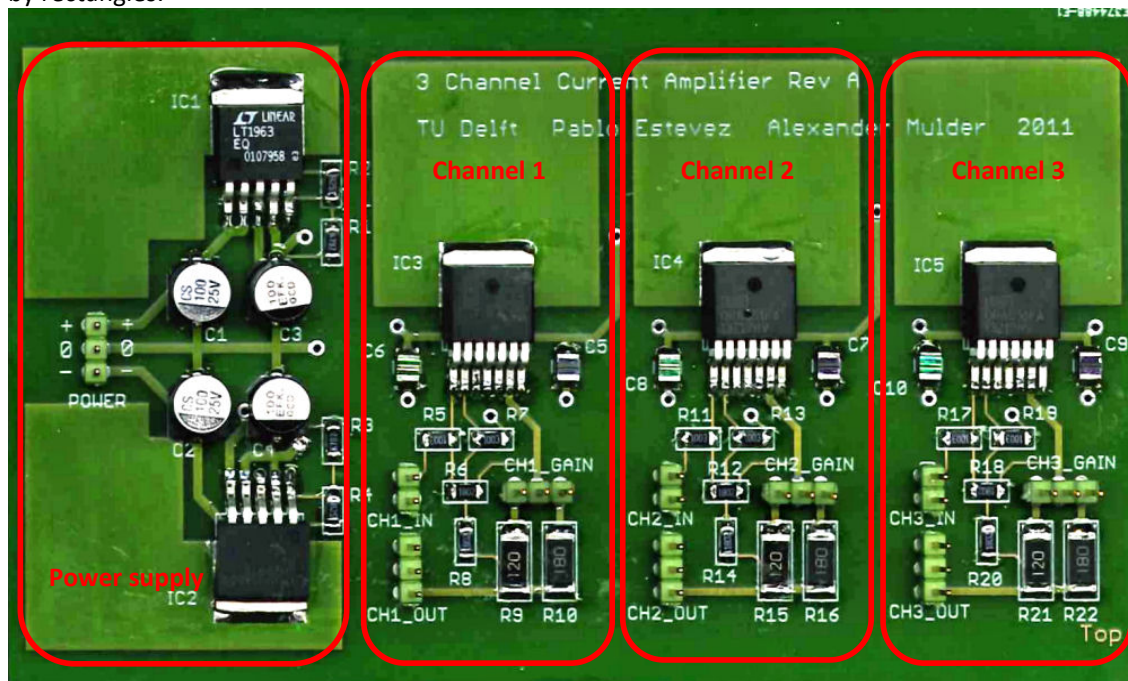
I Current amplifier board manual

Specifications

Power supply voltage	± 9 V DC
Power supply current	500 mA max
Input voltage range	± 10 V
Output current range	± 100 mA / ± 150 mA selectable
Transconductance gain	10 mA/V / 15 mA/V selectable
Output noise, peak-peak	75 μ A

Overview

The current amplifier board is a low noise, three channel board that provides a voltage controlled constant current to the actuator coils. It is primarily designed for use with the actuator coils of the microslave stage but can also be used in other applications such as small voice coil actuators, up to currents of 200 mA. The fully built-up board is shown below; the main functional blocks are indicated by rectangles.



The board consists of a low-noise power supply block (left) and three identical current amplifiers. The power supply is symmetrical to enable a bidirectional output current range. The input voltage is the industry standard voltage range of ± 10 V. Each channel is a Widlar bilateral opamp current source built around an OPA 551 power opamp. Two output current ranges are selectable by means of a jumper setting per channel. The channels are fully independent, so in applications that do not require all three channels only the relevant channels have to be built up. The board is designed to fit inside a Hammond type 1455J1601 encasing (Farnell order no. 4272845).

NOTE: Revision A of the circuit board has a trace layout error: Pins 1 and 2 of the three power opamps are interchanged. When building up these boards this should be corrected! A corrected version of the board has been designed (Rev B), Eagle and Gerber files are available for reordering if necessary.

Circuit description

The current amplifier board is made in two versions that have the same schematic diagram but different component values. One version is designed specifically for the horizontal actuator coils, the other for the vertical coils. Depending on the application, component values can be altered to obtain the correct output current range.

- **Power supply**

The board is fed from an external symmetric power supply of ± 9 V DC. The current drain from this supply is, depending on the amplifier gain settings and instantaneous output current, up to 500 mA per board. The external supply should be connected to the three pole pinheader labelled "POWER".

Note: Always make sure that the polarity and voltage of the power supply are correct! The polarity of the supply lines is indicated on the board.

IC1 and IC2 are stabiliser ICs that reduce the noise levels on the supply lines to a few hundred μ V. The supply voltages are set by resistors R1 and R2 (positive supply) and R3 and R4 (negative supply). The supply voltage is determined by the following equation:

$$V_o = 1.21V \cdot \left(1 + \frac{R_1}{R_2} \right)$$

where R1 (R3 in the negative supply) is typically 47 k Ω . The supply voltage should be chosen as low as possible to reduce the power dissipation in the amplifiers, but should be at least 3 V higher than the maximum expected output voltage across the coils to prevent amplifier saturation. The board driving the vertical coils has a ± 8 V supply, while the horizontal coils amplifier supply is ± 5 V. Buffer capacitors are provided to further reduce noise and improve stability. Each opamp is provided with two 1 μ F decoupling capacitors to reduce crosstalk between channels.

Note: The external supply voltage can be any value smaller than ± 20 V, but should not be more than 4 V higher than the value chosen for the board supply, to reduce power dissipation in the stabiliser ICs.

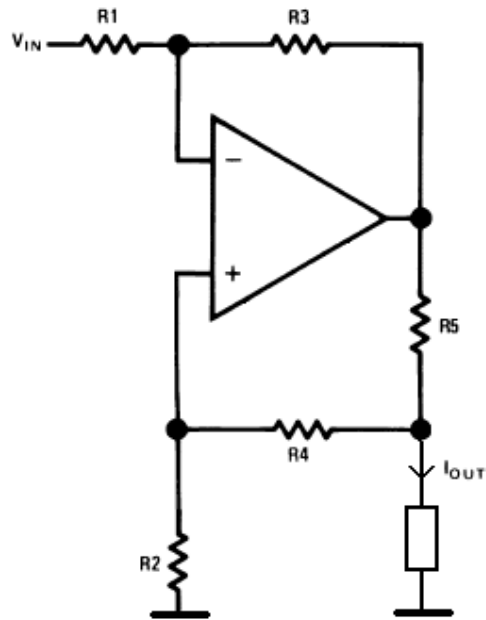
- **Current amplifiers**

The current amplifiers are built around power opamps IC3, IC4 and IC5. A simplified schematic diagram of the current amplifier is given below. The opamp forms an inverting amplifier together with R1 and R3 for V_{in} . Since the gain of this amplifier is smaller than unity, the input voltage V_{in} can be higher than the supply voltage, as long as the amplifier doesn't saturate.

The opamp output voltage causes a current to flow through R5 and the load. This current would still depend on voltage drop variations across the load (In this case, dynamic effects because of the coil self-inductance), so an additional feedback path is needed. This is provided by R2 and R4. Any variations in the voltage across the load are added to the opamp input voltage with gain $R2/(R2 + R4)$. For this voltage, the opamp forms a non-inverting amplifier with gain $(R3 + R1)/R1$. Because $R1 = R3$ and $R2 = R4$, the opamp output follows the voltage variations across the load.

This means that for a fixed value of V_{in} the voltage across R5 is kept constant by the opamp, and consequently the current through it is constant. Since $(R4 + R2) \gg R5$ the load current can be assumed equal to the current through R5, and therefore also constant. The load current can be controlled by varying V_{in} , the (transconductance) gain is given by $R3/(R1 \cdot R5)$.

On the current amplifier board two resistors of unequal value are provided for R5. One of these can be connected to the opamp at a time by means of a jumper, so that the current amplifier gain is selectable between two values. In the microslave application these are 10 mA/V and 15 mA/V, so that the input voltage range of ± 10 V is translated to an output current range of ± 100 mA or ± 150 mA, respectively.



To redesign the current amplifier for other applications the following equations can be used:

$$I_{out} = -V_{in} \left(\frac{R_3}{R_1 R_5} \right)$$

$$R_1 = R_2$$

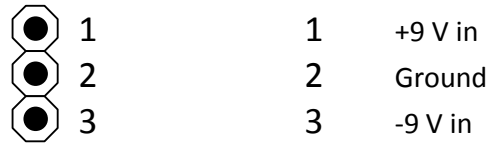
$$R_3 = R_4$$

$$R_1 + R_3 \ll R_5$$

Note: When redesigning the current amplifier care should be taken that the maximum power dissipation of the opamp and current sense resistor (R5) is not exceeded. If necessary the supply voltage can be lowered to achieve this. The maximum output current of the OPA551 is 200 mA. R1, R2, R3 and R4 should have a tolerance of 1 % or less on their resistance values.

Pinout

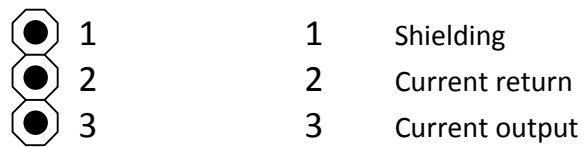
- Pinheaders (Top View)



POWER

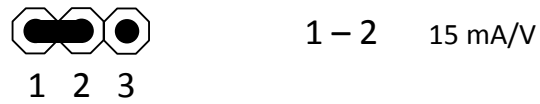


CHx_IN



CHx_OUT

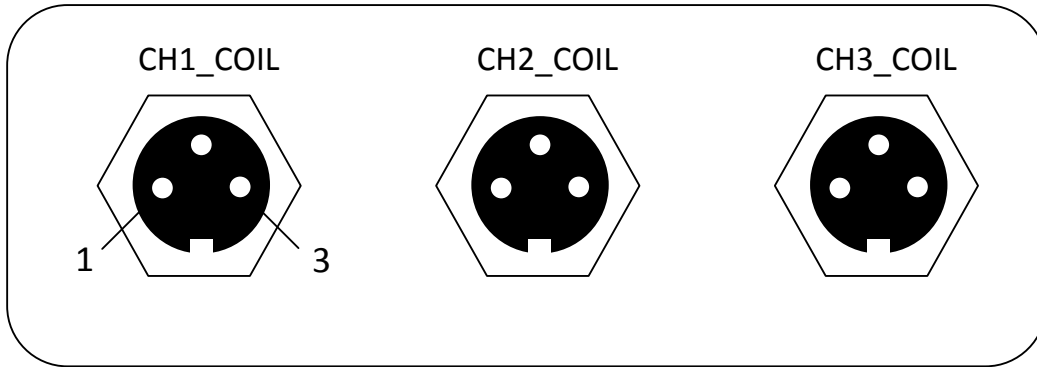
- Jumpers (Top View)



CHx_GAIN

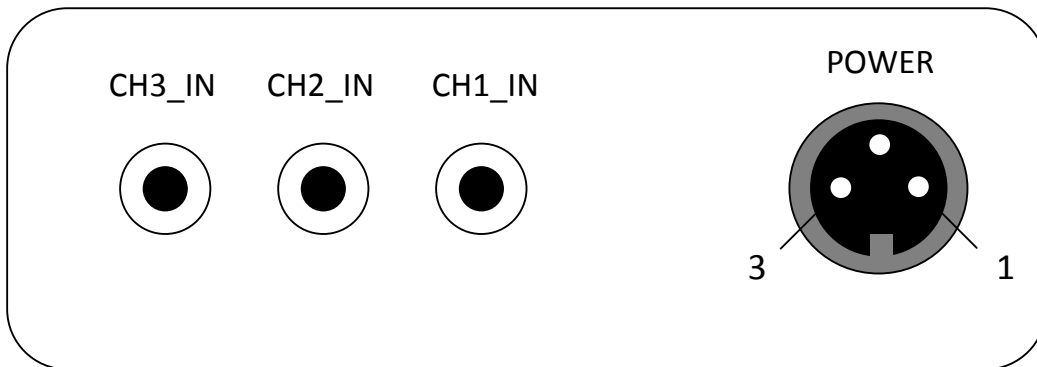
- External connectors (Front view)
These are the front and rear panels of the encasing as it was built for the microslave application.

FRONT PANEL



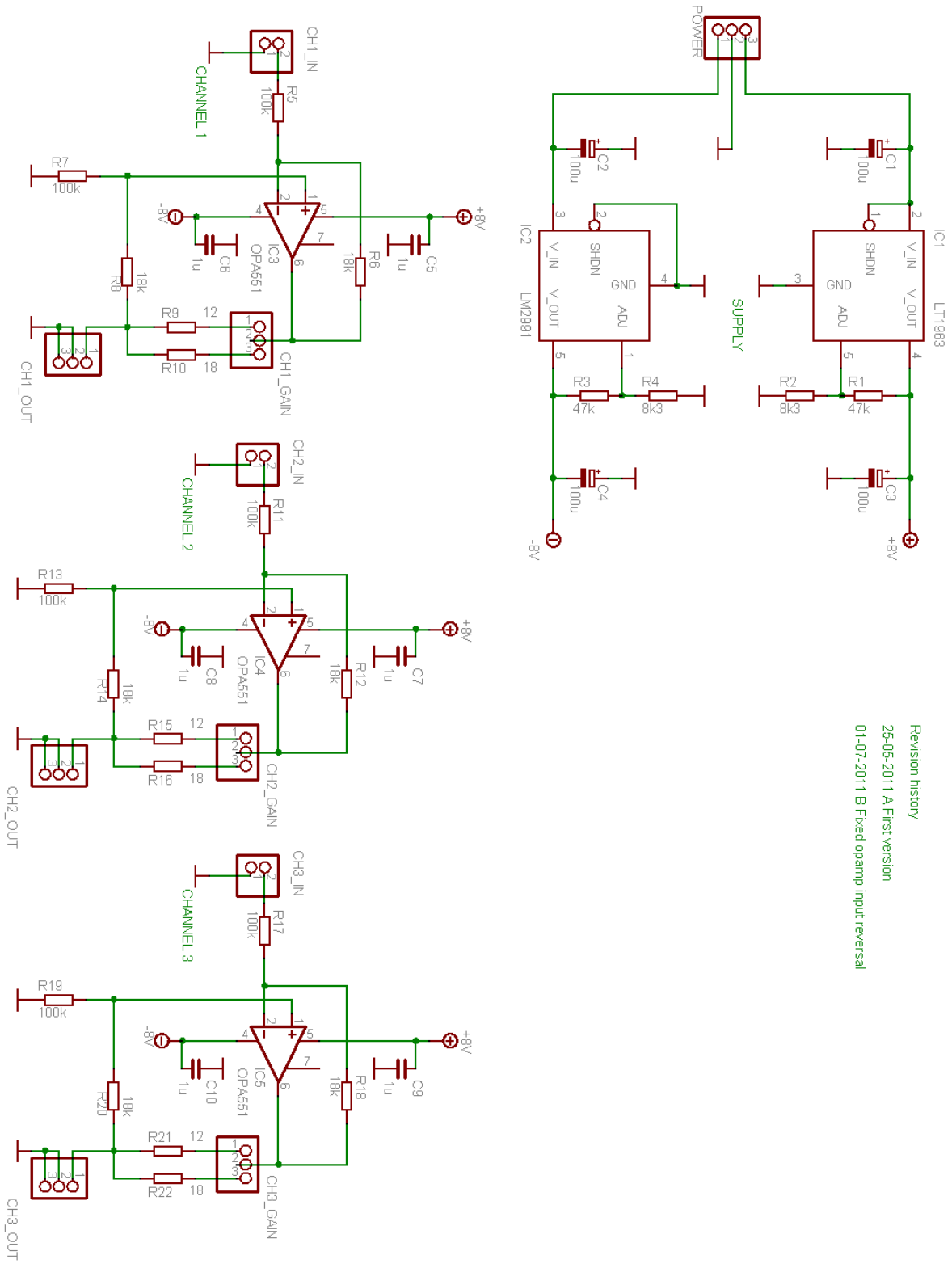
- 1 Shielding
- 2 Current return
- 3 Current output

REAR PANEL



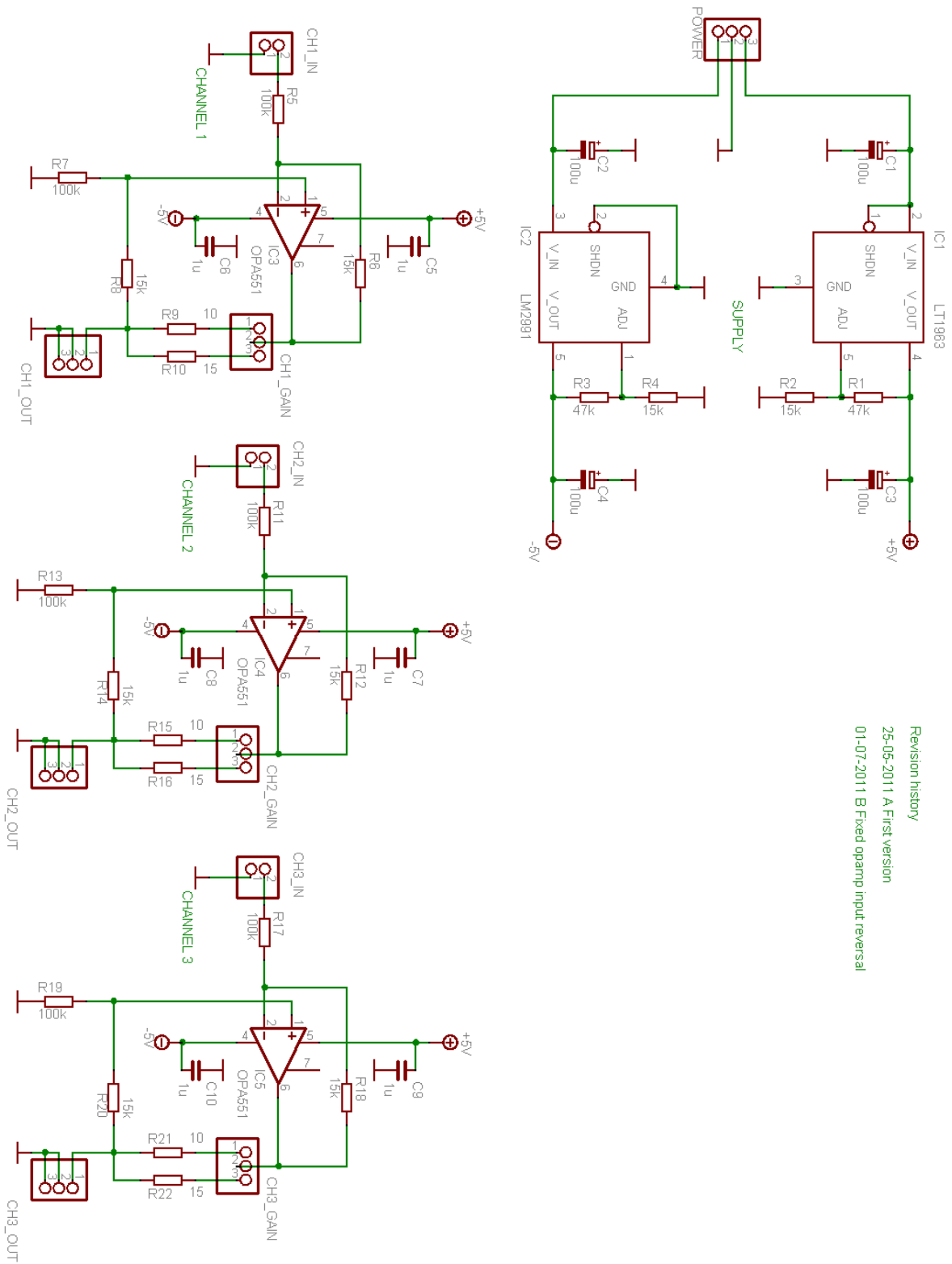
- 1 +9 V in
- 2 Ground
- 3 -9 V in

Schematic diagram – 8V version (vertical coils)



Revision history
 25-05-2011 A First version
 01-07-2011 B Fixed opamp input reversal

Schematic diagram – 5V version (horizontal coils)



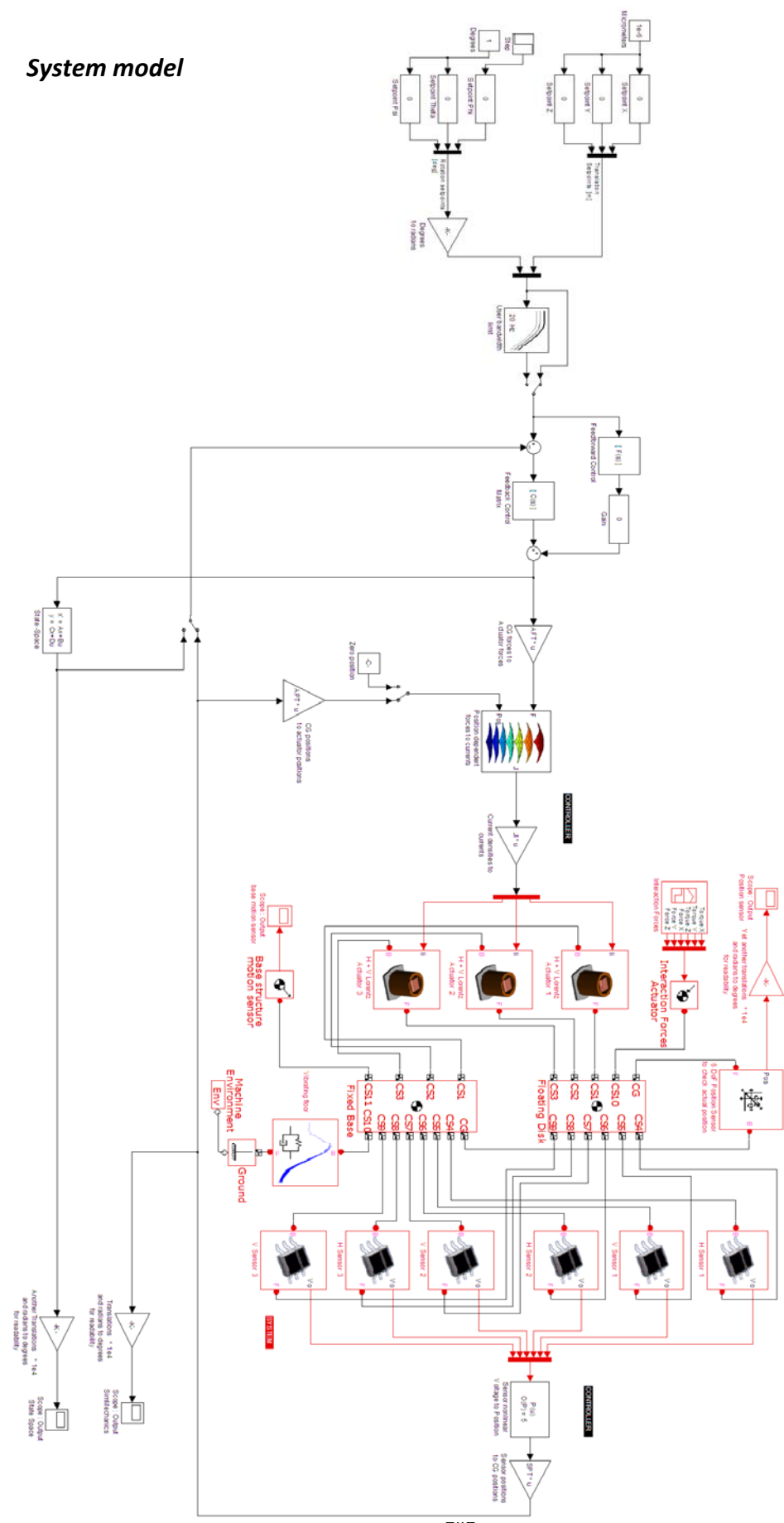
Revision history
 25-05-2011 A First version
 01-07-2011 B Fixed opamp input reversal

Parts list

Part name	Value	Type, package	Function	Farnell order no.	Pc. per board
Capacitors					
C1,C2,C3,C4	100 μ F	25V electrolytic, Case style D8	PSU buffer cap	1850109	4
C5,C6,C7,C8,C9,C10	1 μ F	16V PEN, 1210	Opamp decoupling	9694315	6
Resistors - 8V version					
R1,R3	47 k Ω	250mW, 1206	PSU voltage set	1653133	2
R2,R4	8.25 k Ω	250mW, 1206	PSU voltage set	1653178	2
R5,R7,R11,R13,R17,R19	100 k Ω	250mW, 1206, 1%	Opamp input res	1469975	6
R6,R8,R12,R14,R18,R20	18 k Ω	250 mW, 1206, 1%	Opamp feedback res	1653074	6
R9,R15,R21	12 Ω	1W, 2512	Current sense res 150 mA	1265169	3
R10,R16,R22	18 Ω	1W, 2512	Current sense res 100 mA	1265175	3
Resistors - 5V version					
R1,R3	47 k Ω	250mW, 1206	PSU voltage set	1653133	2
R2,R4	15 k Ω	250mW, 1206	PSU voltage set	1653067	2
R5,R7,R11,R13,R17,R19	100 k Ω	250mW, 1206, 1%	Opamp input res	1469975	6
R6,R8,R12,R14,R18,R20	15 k Ω	250 mW, 1206, 1%	Opamp feedback res	1653067	6
R9,R15,R21	10 Ω	1W, 2512	Current sense res 150 mA	1265166	3
R10,R16,R22	15 Ω	1W, 2512	Current sense res 100 mA	1265173	3
Semiconductors					
IC1		LT1963, D2PAK-5	Positive regulator	1273634	1
IC2		LM2991, D2PAK-5	Negative regulator	1564648	1
IC3, IC4, IC5		OPA551, D2PAK-7	Power Opamps	1651888	3
Connectors					
		50x1 pinheader, for all pcb connectors		1822168	1
		Two pole plug, pcb input		1593458	3
		Three pole plug, pcb power and output		1593459	4

Part name	Value	Type, package	Function	Farnell order no.	Pc. per board
Connectors, cont'd					
		SMB connector, chassis mount, for input signal		1169644	3
		Three pole circular connector, chassis mount, for coil		1122352	3
		Five pole circular connector, plug, for sensor		1122333	3
		Three pole circular connector, chassis mount, power		1122372	1
		Three pole circular connector, plug, power		1122365	1

J System model

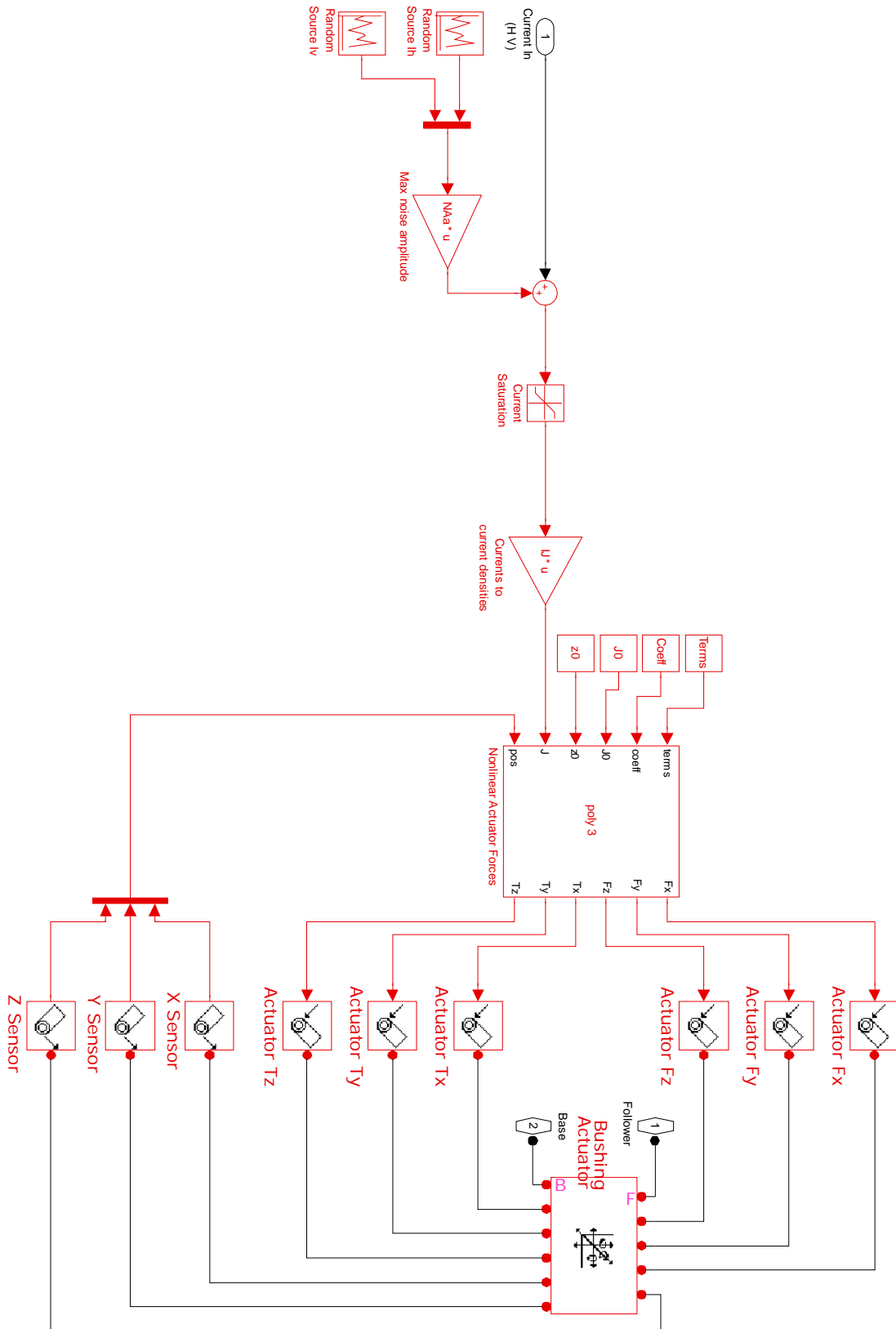


CS10.10

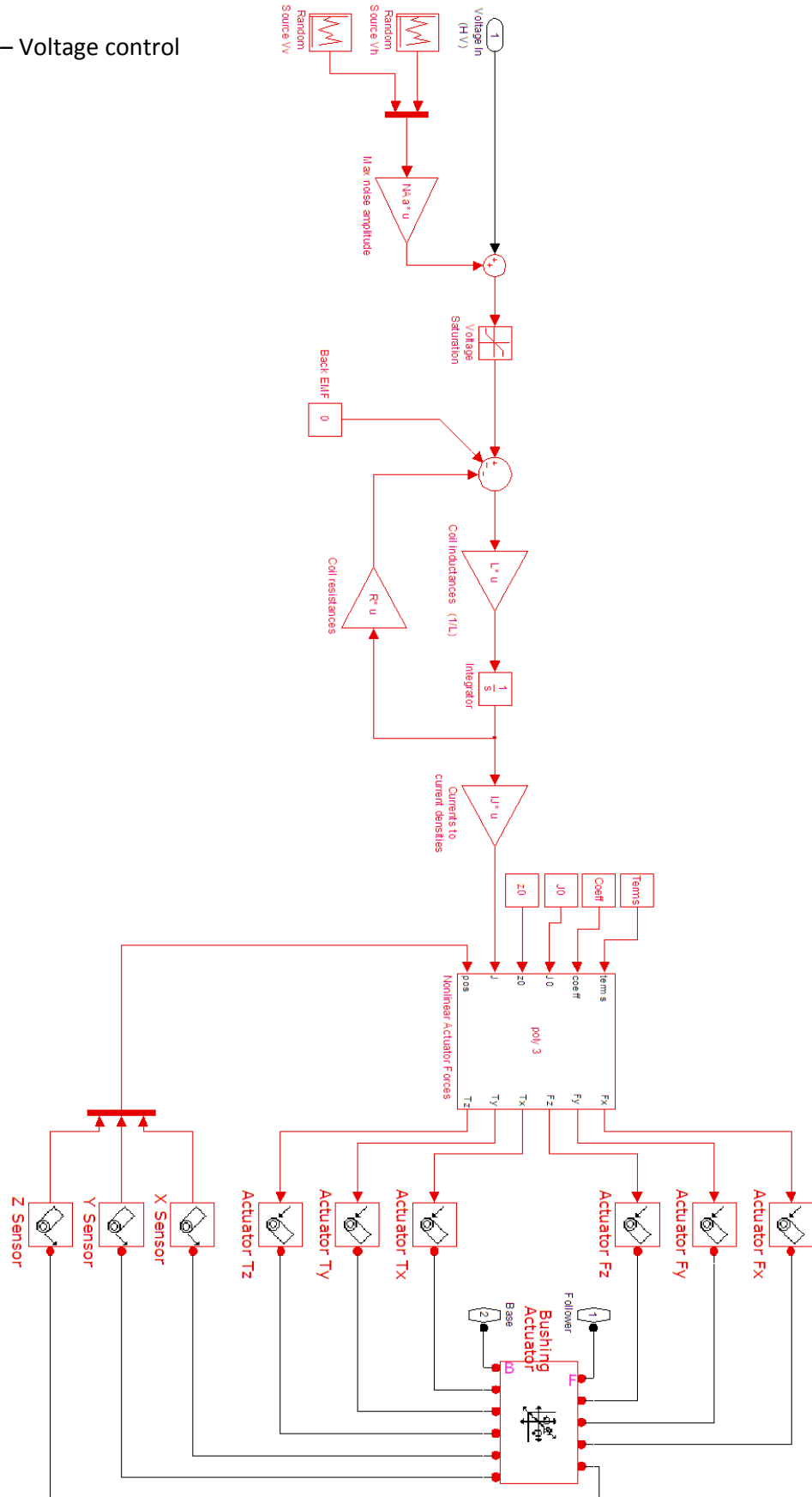
CS10.10

CS10.10

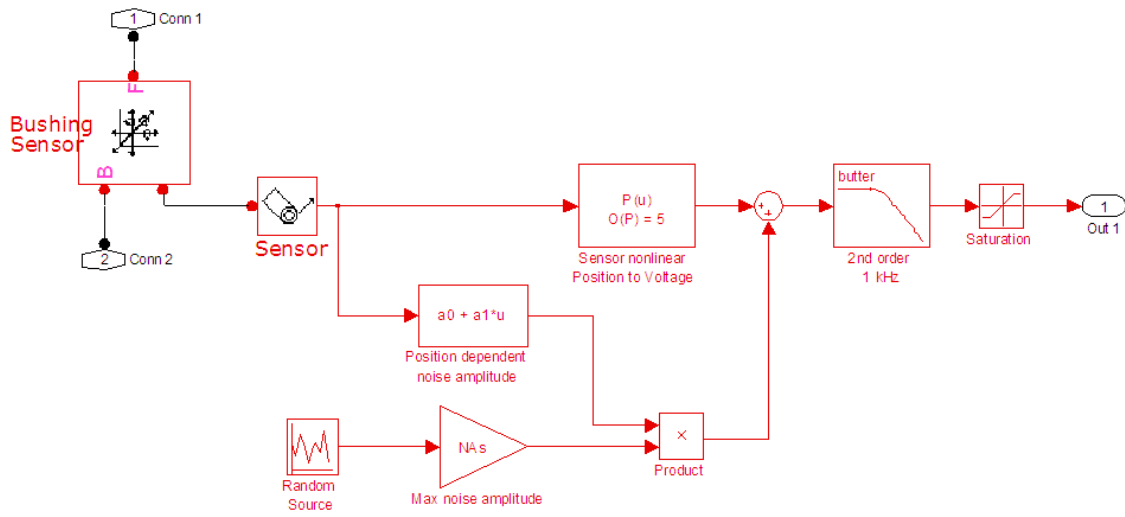
Actuator model – Current control



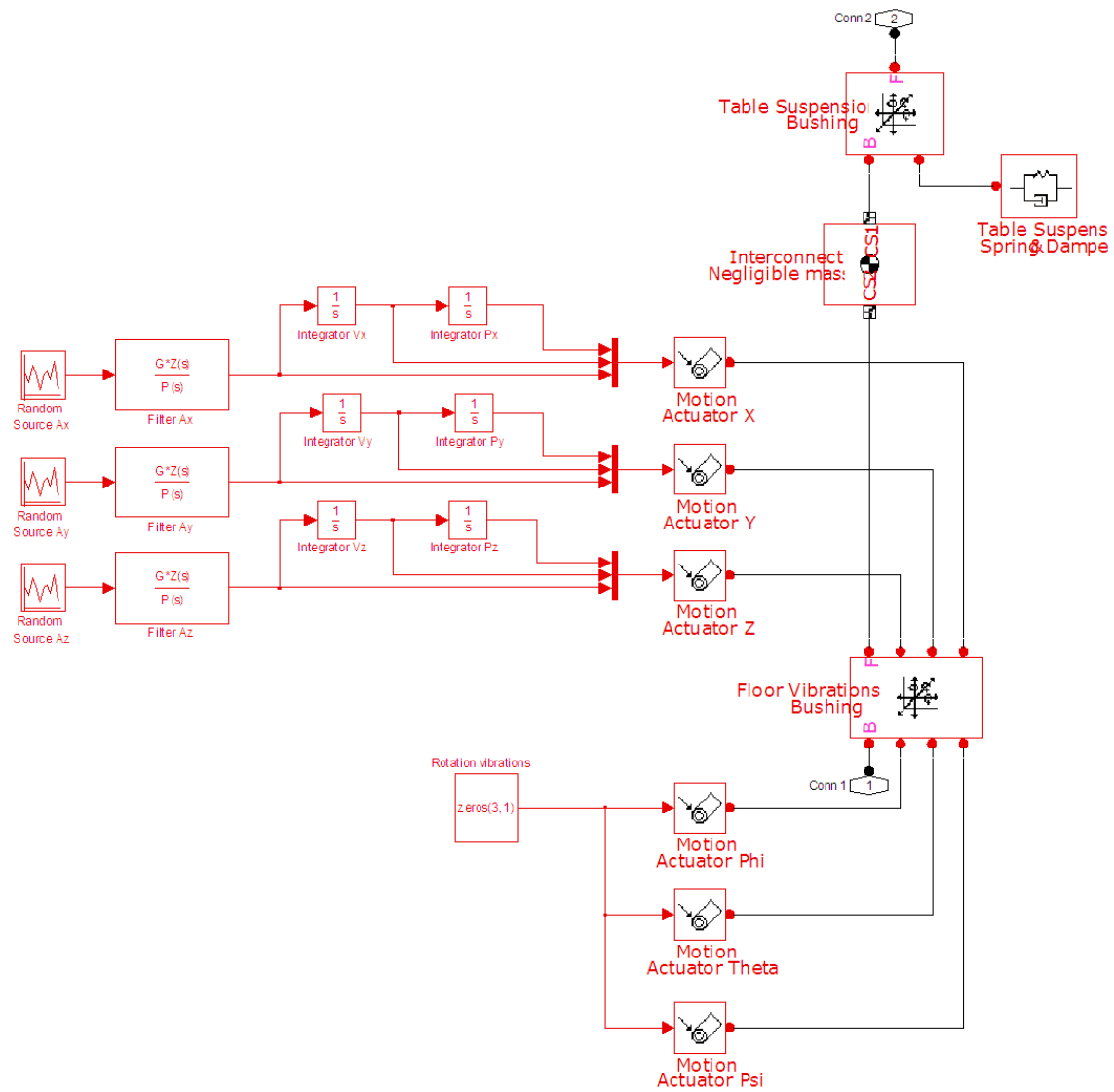
Actuator model – Voltage control



Sensor model



Floor and Suspension model



K Mechanical design drawings